Institute of Geological Sciences
Polish Academy of Sciences

Doctoral dissertation

Micro- to nanoscale constraints on fluid-induced alteration processes of zircon, monazite and xenotime – experiments and nature

Charakterystyka indukowanych przez fluidy przeobrażeń cyrkonu, monacytu i ksenotymu w mikro- i nanoskali – eksperymenty oraz przyroda

Fabian Tramm

Supervisor
Dr hab. Bartosz Budzyń

ING PAN

Fabian

Acknowledgments

I would like to thank my supervisor and doctoral father Bartosz Budzyń for his guidance during my studies, his helpful feedback and his position as a scientific compass from the early stages to the final success of a finished PhD study. His expertise and friendly support, during conceptualization and the editorial progress of my work, helped me in many ways to learn and improve my fundamentals of scientific and concice research.

Special thanks goes to Richard Wirth, a specialist in transmission electron microscopy (TEM), who helped with interpretation of the complex textures observed in nanoscale and gave editorial advice regarding data presentation. His supervision provided fascinating insights in the TEM instrument and I am very grateful for his participation in this work. Further thanks go to Ania Schreiber for sample preparation and methodological advice.

Gabriela Kozub-Budzyń and Jiří Sláma are thanked for processing and consultation regarding electron probe microanalysis (EPMA) and laser ablation inductively coupled plasma mass spectrometry (LA-ICPMS).

Raman microspectroscopy represents a large focus in this work. For teaching the fundamentals of Raman spectroscopy and guidance during measurements, handling of the instrument, processing of data and consultation during interpretation of results Grzegorz Rzepa deserves special thanks.

Furthermore, Jakub Dybaś is kindly thanked for consultation with difficult questions regarding Raman data and fluorescence effects, and supervision during measurments.

I would like to acknowledge Mirosław Jastrzębski for providing the pegmatite sample from which the investigated zircon and xenotime were discovered.

Chris Barnes is thanked for help in english grammar.

This study was financially supported by the Polish National Science Centre (Narodowe Centrum Nauki) research grant no. 2017/27/B/ST10/00813.

OŚWIADCZENIE

Świadomy odpowiedzialności prawnej oświadczam, że niniejsza rozprawa doktorska została napisana przeze mnie samodzielnie i nie zawiera treści uzyskanych w sposób niezgodny z obowiązującymi przepisami.

Oświadczam również, że przedstawiona rozprawa nie była wcześniej przedmiotem procedur związanych z uzyskaniem stopnia doktora w wyższej uczelni lub innej jednostce naukowej.

Oświadczam ponadto, że niniejsza wersja pracy jest identyczna z załączoną wersją elektroniczną.

DECLARATION

Aware of legal responsibility, I hereby declare that this thesis has been written solely by myself and does not contain content obtained in a manner inconsistent with applicable regulations.

I also declare that the presented dissertation has not previously been the subject of procedures related to obtaining a doctoral degree at a university or other scientific unit.

I further declare that this version of the work is identical to the attached electronic version.

22.09.2023

Data / Date

Fabian

Podpis autora / Signature

Abstract

This study investigates alteration processes of xenotime, monazite and zircon in microscale down to nanoscale. The investigations include evaluation of the natural cases of alteration of zircon, monazite and xenotime, and monazite and xenotime from products of laboratory experiments conducted under P-T conditions of 200 MPa / 350 °C, 400 MPa / 450 °C, 600 MPa / 550 °C, 800 MPa / 650 °C and 1000 MPa / 750 °C. The main goal of this study is focused on evaluation of textural, structural and compositional characteristics using a variety of analytical methods on unaltered and altered domains to improve our understanding of alteration processes that affect zircon, monazite and xenotime.

The first part of this study focuses on an altered zircon-xenotime intergrowth from pegmatite from Piława Górna (Góry Sowie Block SW Poland). Investigations were conducted at microscale and submicron-scale with transmission electron microscopy (TEM) and laser ablation inductively coupled plasma mass spectrometry (LA-ICPMS). The strongly altered zircon and xenotime demonstrate distinct domains related to fluid-induced coupled dissolution-reprecipitation processes that resulted in development of micro- to nanoporosity in both zircon and xenotime, and diffusion-reaction processes in the metamict zircon core. Secondary inclusions include fluorapatite, unknown layered Fe-silicates, fibrous Fe-oxides, solid solutions of coffinite-thorite and uraninite-thorianite, uraninite and secondary U-rich zircon. The fluid supplied zircon and xenotime with Ca and Fe, while mobilizing U, Th and Pb.

The second part of this study focuses on Raman microspectroscopic study of monazite and xenotime from the products of laboratory experiments using 488 nm, 532 nm, 633 nm and 780 nm excitation lasers in combination with compositional measurements using electron probe microanalysis (EPMA) and LA-ICPMS. Additional Raman microspectroscopy was conducted on altered monazite from Ankazobe (Madagascar), altered xenotime from pegmatite from Piława Górna, and synthetic REE-phosphates ($LaPO_4$–$LuPO_4$ and YPO_4). Monazite spectra (532 nm) display shifts of the $v_1(PO_4)$ symmetric stretching band from 969–981 cm^{-1} to 962–965 cm^{-1}, formation of a new band at ca. 861–869 cm^{-1} and broad fluorescence peaks at ca. 2028 cm^{-1} and ca. 3287 cm^{-1}. Raman spectra of xenotime from experimental products display characteristic features in the form of fluorescence effects in the range of 200–700 cm^{-1} caused by Ho^{3+} ($^5S_2 \rightarrow {}^5I_8$) and Er^{3+} ($^4S_{3/2} \rightarrow {}^4I_{15/2}$) electronic transitions. Raman spectra of Y-rich fluorcalciobritholite display characteristic changes of fluorescence effects at the range of 1500–3000 cm^{-1} with a significant increase in the fluorescence peak at ca. 2600 cm^{-1} caused by Sm^{3+} ($^5D_0 \rightarrow {}^7F_3$), and is accompanied by a new band at 974 cm^{-1} (488 nm) and 964 cm^{-1} (633 nm). Fluorescence effects remain a difficult artefact in Raman microspectroscopy of xenotime, whereas, at the same time they enable differentiation of xenotime and Y-rich fluorcalciobritholite in hyperspectral mapping.

TEM investigation of microscale to submicron-scale alterations of xenotime and zircon from pegmatite from Piława Górna are in good agreement with its geochemical characteristics and emphazise the importance to identify nanoinclusions and their abundances which otherwise remain undetected with microscopic methods. The spectral characteristics of unaltered and altered monazite and xenotime enable identification of structural changes, presence of secondary phases and expand the Raman database. Results of both analytical approaches, TEM nanoscale evaluation and application of Raman microspectroscopy provide complementary information to petrochronological interpretation and timing of various processes that affected the rock during its formation and when transformed or reworked during tectonometamorphic events.

Streszczenie

Niniejsza praca prezentuje badania procesów przeobrażeń ksenotymu, monacytu i cyrkonu zachodzących w skali od mikro do nanoskali. Przedmiotem badań są cyrkon, monacyt i ksenotym przeobrażone w warunkach naturalnych oraz monacyt i ksenotym z produktów eksperymentów laboratoryjnych przeprowadzonych w warunkach 200 MPa / 350°C, 400 MPa / 450°C, 600 MPa / 550° C, 800 MPa / 650°C oraz 1000 MPa / 750°C. Głównym celem pracy jest kompleksowa charakterystyka teksturalna, strukturalna i składu chemicznego nieprzebrażonych oraz przeobrażonych domen minerałów przy użyciu szeregu metod analitycznych, w celu poszerzenia naszej wiedzy w zakresie procesów przeobrażeń cyrkonu, monacytu i ksenotymu.

Pierwsza część niniejszej pracy prezentuje badania przobrażeń zarejestrowanych przez cyrkon i ksenotym z pegmatytu z Piławy Górnej (Blok Gór Sowich, SW Polska). Badania przeprowadzono w skali mikro i submikronowej za pomocą transmisyjnej mikroskopii elektronowej (TEM) oraz laserowej ablacji w połączeniu ze spektrometrią mas z indukcyjnie wzbudzoną plazmą (LA-ICPMS). Silnie przeobrażone cyrkon i ksenotym zawierają domeny związane z indukowanymi przez fluidy procesami *coupled dissolution-reprecipitation*, czego rezultatem jest obecność mikroporów i nanoporów w cyrkonie i ksenotymie, oraz procesy *diffusion-reaction* w zmetamiktyzowanym jądrze cyrkonu. Wrostki minerałów wtórnych obejmują fluoroapatyt, niezidentyfikowane, wzbogacone w Fe krzemiany warstwowe, włókniste tlenki Fe, roztwory stałe coffinitu z thorytem i uraninitu z thorianitem, uraninit oraz wzbogacony w U wtórny cyrkon. Wapń i Fe zostały dostarczone do cyrkonu i ksenotymu przez fluidy, które jednocześnie mobilizowały U, Th i Pb.

Druga część pracy przedstawia wyniki badań monacytu i ksenotymu z produktów eksperymentów laboratoryjnych przy użyciu mikrospektroskopii Ramana z laserami wzbudzającymi 488 nm, 532 nm, 633 nm i 780 nm, w połączeniu z analizą składu chemicznego przy użyciu mikrosondy elektronowej (EPMA) oraz LA-ICPMS. Ponadto badania mikrospektroskopii Ramana przeprowadzono na przeobrażonym monacycie z Ankazobe (Madagaskar), przeobrażonym ksenotymie z pegmatytu z Piławy Górnej oraz syntetycznych fosforanach REE ($LaPO_4$–$LuPO_4$ i YPO_4). Widma monacytu (532 nm) prezentują przesunięcie symetrycznego pasma rozciągającego $v_1(PO_4)$ od 969–981 cm^{-1} do 962–965 cm^{-1}, nowe pasmo ok. 861–869 cm^{-1} oraz szerokie pasma fluorescencji ok. 2028 cm^{-1} i ok. 3287 cm^{-1}. Widma Ramana ksenotymu z produktów eksperymentalnych wykazują charakterystyczne cechy w postaci efektów fluorescencji w zakresie 200–700 cm^{-1}, związanych z przejściami elektronowymi Ho^{3+} ($^5S_2 \rightarrow {}^5I_8$) oraz Er^{3+} ($^4S_{3/2} \rightarrow {}^4I_{15/2}$). Widma Ramana wzbogaconego w Y fluorcalciobritholitu wykazują charakterystyczne zmiany efektów fluorescencji w zakresie 1500–3000 cm^{-1} ze znacznym wzrostem piku fluorescencji ok. 2600 cm^{-1}, spowodowanego przez Sm^{3+} ($^5D_0 \rightarrow {}^7F_3$), oraz obecność nowego pasma 974 cm^{-1} (488 nm) i 964 cm^{-1} (633 nm). Efekty

fluorescencji mogą stanowić utrudnienie w zastosowaniu mikrospektroskopii Ramana w badaniach ksenotymu, a jednocześnie umożliwiają identyfikację ksenotymu i wzbogaconego w Y fluorcalciobritholitu przy użyciu obrazowania hiperspektralnego.

Wyniki badań przeobrażeń ksenotymu i cyrkonu przy zastosowaniu TEM w skali mikro do submikronowej w pegmatycie z Piławy Górnej są zgodne z ich charakterystyką geochemiczną i podkreślają znaczenie identyfikacji nanoinkluzji i ich liczebności, na co nie pozwalają metody mikroskopowe. Charakterystyka spektralna nieprzeobrażonego i przeobrażonego monacytu i ksenotymu umożliwia identyfikację zmian strukturalnych, obecności faz wtórnych oraz rozszerza dostępną bazę danych Ramana. Wyniki obu podejść analitycznych, badań TEM przeprowadzonych w nanoskali oraz mikrospektroskopii Ramana dostarczają istotne informacje dla interpretacji petrochronologicznych i czasu trwania różnych procesów, które miały wpływ na skałę podczas jej powstawania, późniejszych przeobrażeń lub transformacji w trakcie zdarzeń tektonometamorficznych.

Table of contents

Appendices (on DVD)

Supplementary Tables A1–A3

Supplementary Tables B1–B8

List of abbreviations

REE – rare earth elements (Sc, La–Lu)

HREE – heavy rare earth elements (Gd–Lu)

LREE – light rare earth elements (La–Eu)

APT – atom probe tomography

EPMA – electron probe microanalysis

EDS – energy dispersive spectrometry

LA-ICPMS – laser ablation inductively coupled plasma mass spectrometry

SEM – scanning electron microscope

SEM-FIB – scanning electron microscope - focused ion beam

SHRIMP – sensitive high resolution ion microprobe

SIMS – secondary ion mass spectrometry

WDS – wavelength dispersive spectrometry

FWHH – full width at half height

TCA – true component analysis

wt.% – weight percentage

ppm – parts per million

apfu – atoms per formula unit

Ab – albite $NaAlSi_3O_8$

Aln – Y-rich allanite-(Ce) $(Ce,Ca,Y)_2(Al,Fe^{3+})_3(SiO_4)_3(OH)$

Ap – apatite	$Ca_5(PO_4)_3(F,Cl,OH)$
Blt – blatonite	$(UO_2)CO_3 \cdot H_2O$
Cheralite	$CaTh(PO_4)_2$
Cof – coffinite	$USiO_4 \cdot nH_2O$
Fcbri – fluorcalciobritholite	$(Ca,REE)_{10}(SiO_4,PO_4)_6F_2$
Hing – hinganite-(Y)	$Y_2(\square)Be_2Si_2O_8(OH)_2$
Kfs – K-feldspar	$KAlSi_3O_8$
Mnz – monazite-(Ce)	$CePO_4$
Ms – muscovite	$KAl_2(AlSi_3O_{10})(OH)_2$
Qz – quartz	SiO_2
Scy – REE-rich steacyite	$(K,\square)(Na,Ca)_2(Th,U)Si_8O_{20}$
Tho – thorianite	ThO_2
Thr – thorite	$ThSiO_4$
Urn – uraninite	UO_2
Xtm – xenotime-(Y)	YPO_4
YFcbri – Y-rich fluorcalciobritholite	
Zrn – zircon	$ZrSiO_4$
Zrn2 – secondary zircon	

1. Introduction

Zircon ($ZrSiO_4$) is a common accessory mineral present in a wide range of environments such as igneous rocks, metamorphic rocks and sediments (Corfu et al. 2003; Harley and Kelly 2007; Nemchin et al. 2013). Likewise, monazite-(Ce) ($CePO_4$, henceforth monazite) forms as an accessory mineral in similar geological environments (Overstreet 1967; Williams et al. 2007, 2017; Kylander-Clark 2017). Xenotime-(Y) (YPO_4, henceforth xenotime) forms in metamorphic and igneous rocks (Hawkins and Bowring 1999; Spear and Pyle 2002), as well as in diagenetic environments (Rasmussen 2005; Vallini et al. 2005; Rasmussen et al. 2010), however, it is less abundant in Earth’s crust than zircon and monazite. The presence of zircon, monazite and xenotime in a wide range of envrionments, the capability to incorporate high amounts of U in zircon and xenotime (Smits 1989; Krogh 1993; Förster 1998, 2006; McNaughton and Rasmussen 2018) and Th (and U) in monazite (Parrish 1990; Williams et al. 2007), and low diffusion rates of Pb (Cherniak and Watson 2001; Cherniak et al. 2004; Cherniak 2006, 2010) make them suitable to constrain the U-(Th-)Pb age of the processes they form in.

Zircon, monazite and xenotime find applications in thermometry (Kingsbury et al. 1993; Gratz and Heinrich 1997; Andrehs and Heinrich 1998; Pyle et al. 2001; Seydoux-Guillaume et al. 2002a; Watson and Harrison 2005; Watson et al. 2006; Ferry and Watson 2007; Siégel et al. 2018; Volante et al. 2020) and bear potential to use their chemical fingerprint to estimate their provenance (Hoskin and Schaltegger 2003; Hoskin 2005; Yang et al. 2006; Dawood and Abd El-Naby 2007; Grimes et al. 2007, 2015; Bouvier et al. 2012; McNaughton and Rasmussen 2018; Chen et al. 2019; Dröllner et al. 2023). Zircon, monazite and xenotime are also considered as potential materials for long term disposal of nuclear waste due to their high chemical stability in most geological environments (Sales et al. 1983; Ewing and Lutze 1991; Ewing 1999, 2001; Lumpkin 2006; Vance et al. 2011).

The chemical stability of zircon, monazite and xenotime can be significantly affected by various alteration processes. Decay of U and Th leads to self-irradiation and consequently damage in the crystal structure, which can result in amorphization (i.e. metamictization) that is commonly observed in zircon (Nasdala et al. 1995, 2001; Ewing et al. 2003; Geisler et al. 2007; Budzyń et al. 2018; Ende et al. 2021). Monazite and xenotime can accumulate moderate degrees of radiation damage, but do not become metamict (Meldrum and Boatner 1997; Meldrum et al. 1998; Urusov et al. 2012; Seydoux-Guillaume et al. 2018; Nasdala et al. 2020). Radiation-damaged crystal structure enhances element transport, which can result in modification of the original geochemical signature, disturbance of the geochronological record and overprint of crystallization temperatures. Further processes that can strongly affect zircon, monazite and xenotime involve fluid-induced alteration mechanisms, which may result in compositional changes. The effects of alteration in micro- and nanoscale were investigated extensively in zircon (Williams and Jercinovic 2002; Corfu et al. 2003; Geisler et al. 2007; Austrheim et al. 2008; Nasdala et al. 2010), monazite (Broska and Siman 1998; Finger et al. 1998; Seydoux-Guillaume et al. 2002c, 2003, 2012, 2015, 2017, 2018; Harlov et al. 2007, 2011; Budzyń et al. 2010, 2011, 2015, 2017, 2021, 2022; Hetherington et al. 2010; Williams et al. 2011; Grand'Homme et al. 2016, 2018) and xenotime (Broska et al. 2005; Hetherington and Harlov 2008; Hetherington et al. 2008, 2010; Majka et al. 2011; Ondrejka et al. 2016; Švecová et al. 2016; Budzyń et al. 2017, 2018, 2023a, b). Common results of such alteration include formation of micro- to nanoporosity, secondary inclusions and partial to complete recrystallization of the primary phase induced by fluid-mediated coupled dissolution-reprecipitation processes (Putnis 2002, 2009; Putnis et al.

2005; Putnis and Putnis 2007; Geisler et al. 2007; Putnis and Austrheim 2010, 2013; Harlov et al. 2011; Ruiz-Agudo et al. 2014; Villa and Hanchar 2017; Budzyń et al. 2018).

The combination of different alteration mechanisms of zircon, monazite and xenotime, such as radiation damage and fluid-induced coupled dissolution-reprecipitation processes, can result in a distorted mineral structure creating a mosaic of a highly disrupted lattice and recrystallized “repaired” altered domains. This structural discordance can yield important information to recognize and evaluate different alteration processes. Raman microspectroscopy serves as a versatile tool to investigate the structural properties of zircon, monazite and xenotime such as structural disorder due to radiation damage, effects of annealing or recrystallization due to alteration based on broadening and narrowing of Raman bands (Nasdala et al. 1995, 2001, 2002, 2018; Ruschel et al. 2012; Švecová et al. 2016; Ginster et al. 2019; Anderson et al. 2020; Budzyń et al. 2021, 2023a, b; Ende et al. 2021).

This study investigates the alteration processes recorded by zircon, monazite and xenotime using various analytical methods, from microscale to nanoscale, to constrain their textural, compositional and structural characteristics. The study consists of two main parts. The first part focuses on microscale and, particularly, nanoscale investigations of altered zircon and xenotime from a pegmatite from Piława Górna (the Góry Sowie Block, NE Bohemian massif, SW Poland), which underwent several stages of late- to post-magmatic alteration. Trace element composition of zircon and xenotime were evaluated using laser ablation inductively coupled plasma mass spectrometry (LA-ICPMS), whereas submicron scale investigations were performed using a scanning electron microscope equipped with focused ion beam (SEM-FIB) and transmission electron microscopy (TEM). This part of the study aims to expand our understanding of fluid-induced alteration mechanisms, which enhance element mobilization, breakdown of primary phases and formation of secondary phases at micro- to nanoscale. Nanoscale observations of the zircon and xenotime were expected to provide new insights and review earlier interpretations of the alteration mechanisms which affect xenotime and zircon. The combined observations in micro- and nanoscale provide information of fluid composition, inward and outward element transport, potential fluid-pathways and micro- to nanopore development. This part of the dissertation has been published in Tramm et al. (2021).

The second part of this study focuses on Raman microspectroscopy conducted on monazite and xenotime from laboratory experiments (experimental products from Budzyń and Kozub-Budzyń 2015; Budzyń et al. 2015, 2017), altered monazite from Ankazobe (Madagascar) and xenotime from pegmatite from Piława Górna. Major and trace element composition of unaltered and potentially altered domains of monazite and xenotime were investigated using electron probe microanalysis (EPMA) and LA-ICPMS. Structural characterization of the monazite, xenotime and synthetic REE (rare earth elements) phosphates ($LaPO_4$–$LuPO_4$ and YPO_4) has been conducted using Raman microspectroscopy with 488 nm, 532 nm, 633 nm and 780 nm excitation lasers at a broad range, and hyperspectral mapping has been performed in selected domains using 532 nm and 633 nm lasers. The goals of this part of the study are focused on evaluation of altered domains of monazite and xenotime based on combined Raman microspectroscopic, textural and compositional evaluations. Structural changes from radiation damage are reflected in band broadening, and structural recovery by recrystallization or annealing are reflected in band narrowing. Evaluation of unaltered and potentially altered domains in monazite and xenotime from experiments and nature should therefore be reflected in distinctive Raman data and may even bear the potential to recognize and interpret individual alteration mechanisms related to element mobilisation. Collection of Raman spectra with various excitation lasers will enable identification of primary Raman features from fluorescence effects and other artefacts, and will provide an assessment of the usability of different excitation lasers for Raman microspectroscopy of monazite and xenotime. Hyperspectral maps and EPMA-WDS X-ray element maps of selected domains in monazite and xenotime combine textural, structural and compositional information and provide an approach to bring data of various microanalytical methods into context with each other. Interpretation of the hyperspectral maps can set an overview of the applicability of Raman microspectroscopy as a tool to improve evaluation of monazite and xenotime with addition of structural information in future geological or petrological studies. The analytical data and interpretations from this study contribute to the expansion of the Raman database of monazite and xenotime, which will serve as reference in future petrochronological studies of monazite and xenotime involving Raman microspectroscopy.

2. A brief summary of previous works on zircon, monazite and xenotime

2.1. Zircon

Zircon is an accessory mineral that has versatile applications in petrochronology as it forms in a wide range of geological settings under broad P-T conditions while recording various geochemical signatures. The geochemistry of zircon varies depending on the environment in which it is formed, which allows to estimate the origin of the source lithology and the U-Pb age(s) (Morton and Hallsworth 1999; Belousova et al. 2002; Hay and Dempster 2009; Rubatto 2017). During formation of zircon, nonformula elements are incorporated via various substitution mechanisms. Incorporation of U, Th and other tetravalent elements such as Ti, Sn or Hf occur by simple substitution ($M^{4+} = Zr^{4+}$, Frondel 1953), whereas more complex coupled substitution mechanisms are required for pentavalent or trivalent ions such as REE^{3+}, i.e. $LaPO_4$–$LuPO_4$, Y^{3+} or Sc^{3+} (Hoskin and Schaltegger 2003). These include the following substitutions:

(i) at one structural site

$M^{3+} + M^{5+} = 2\ Zr^{4+}$ (Es'kova 1959)

(ii) at two structural sites

$M^{3+} + P^{5+} = Zr^{4+} + Si^{4+}$ (Speer 1980; Halden et al. 1993)

$M^{n+} + n(OH)^{-} + (4-n)H_2O = Zr^{4+} + (SiO_4)^{4-}$ (Caruba and Iacconi 1983)

(iii) at an interstitial site

${}_{int}(Mg,Fe)^{2+} + 3\ M^{3+} + P^{5+} = 3\ Zr^{4+} + Si^{4+}$ (Hoskin 2000)

${}_{int}(Al,Fe)^{3+} + 4\ M^{3+} + P^{5+} = 4\ Zr^{4+} + Si^{4+}$ (Hoskin 2000)

with M representing metal ions.

Different processes by which zircon is formed result in a wide variety of textures (Corfu et al. 2003). Igneous zircon commonly demonstrates oscillatory zoning due to heterogeneous distribution of REE in the melt during zircon formation (Corfu et al. 2003; Hoskin and Schaltegger 2003), but can also form patchy zoning caused by strain during magmatic formation (Paquette et al. 1995; Corfu et al. 2003), or caused by metamictization or fluid-mediated alteration (Nasdala et al. 2001; Geisler et al. 2007; Budzyń et al. 2018). Textures of metamorphic or hydrothermal zircon commonly are result of an overgrowth from exsolution of fluids (Hay and Dempster 2009; Rubatto 2017), whereas diagenetic zircon can develop an irregular (or sawtooth-shaped) texture at low P-T conditions (Rasmussen 2005; Hay and Dempster 2009). These examples demonstrate the broad range of zircon textures present in the Earth’s crust, thus, detailed textural evaluation of zircon combined with geochemical characterisation are required to determine source provenance to correctly interpret zircon age data and distinguish formation processes.

The incorporation of Ti into zircon during crystallization has been experimentally shown to be temperature dependent and pressure independent, demonstrating that it can be used as a geothermometer to constrain conditions of zircon crystallization or saturation (Watson and Harrison 2005; Watson et al. 2006; Ferry and Watson 2007). The Ti-in-zircon thermometry founds increasing importance in petrogenetic models, however, Siégel et al. (2018) pointed out that careful evaluation of zircon origin, as autocryst (formed from melt), xenocryst (inherited from a different source) or antecryst (formed from a preceding melt of similar composition), needs to be done to correctly estimate and attribute calculated temperatures.

Many previous studies have used various approaches to estimate the origin and the igneous or hydrothermal nature of zircon formation using trace element composition (Hoskin and Schaltegger 2003; Hoskin 2005; Grimes et al. 2007; Bouvier et al. 2012; El-Bialy and Ali 2013). Discrimination of zircon provenance from oceanic or continental crust is possible with the characteristic fingerprint of Hf and Y in relation to U/Yb (Grimes et al. 2007, 2015; El-Bialy and Ali 2013), whereas zircon light rare earth elements (LREE) composition can provide information of igneous or hydrothermal origin (Hoskin and Schaltegger 2003; Hoskin 2005; Bouvier et al. 2012).

Zircon contains relatively high amounts of U (up to several wt.%, Hoskin and Schaltegger 2003) and low concentrations of common Pb incorporated during its crystallization (Krogh 1993; Watson et al. 1997), which makes it a good mineral for U-Pb geochronology. Crystalline zircon is chemically stable and diffusion of Pb is limited due to a high closure temperature ≤ 900 °C (Cherniak and Watson 2001; Cherniak 2010), which enables maintaining the isotopic U and Pb signature over a long period of time. A consequence of the high actinide content in zircon, however, is accumulation of structural damage due to self-radiation. This process can lead to complete “metamictization”, i.e. the amorphization of zircon structure, which significantly enhances properties for fluid-induced alteration (Nasdala et al. 1995, 2001; Meldrum et al. 1998; Ewing et al. 2003; Geisler et al. 2007; Ende et al. 2021). Metamictization is dependent on the number of recoil events occurring during the α-decay of radioactive elements distorting the mineral structure, which is in direct correlation with the content of alpha emitters (U, Th or Pu), their half-life and the time for the damage to accumulate. In case of zircon, the damage results in displaced atoms caused by recoil of nuclei during the ejection of α-particles into the zircon structure, which results in local distortion and a decrease in density (Meldrum et al. 1998; Trachenko et al. 2002). The damaged texture then may be characterized by a matrix of amorphous zircon in which parts of crystalline zircon remain, but over time the matrix expands and gradually overlaps leading to complete amorphization (Meldrum et al. 1998; Geisler et al. 2003a, b, c, 2007). Mechanisms that oppose metamictization of zircon and repair a radiation-damaged crystal structure are temperature-dependent annealing processes, which occur at relatively low temperatures starting from ca. 200 °C (Geisler et al. 2001, 2003a; Nasdala et al. 2001, 2002). The reason why understanding metamictization of zircon is important lies in its enhancing properties for fluid-mediated alteration, which can modify the zircon composition, disturb the geological age, affect the Ti-in-zircon thermometry records or change REE contents hindering conclusive estimation of provenance and/or origin of zircon.

Processes of zircon alteration induced by fluids, such as diffusion-reaction (Geisler et al. 2002, 2003a, c, 2007; Nasdala et al. 2010; Soman et al. 2010; Seydoux-Guillaume et al. 2015; Zamyatin et al. 2017) or coupled dissolution-reprecipitation processes (Putnis 2002, 2009; Putnis et al. 2005; Geisler et al. 2007; Putnis and Putnis 2007; Putnis and Austrheim 2010, 2013; Ruiz-Agudo et al. 2014; Villa and Hanchar 2017; Budzyń et al. 2018), typically result in textural and compositional changes. These alteration mechanisms may lead to recrystallization of the mineral or replacement with a secondary phase(s). The diffusion-reaction process is induced by a hydrous fluid (H^+), which penetrates structurally damaged zircon and supports its structural recovery, but results in development of nanoporosity and element transport that can lead to mobilization of U, Th and Pb, among other elements such as Zr, Si, Hf and REE, and enrichment of nonformula elements supplied by the fluid (Silver and Deutsch 1963; Pidgeon et al. 1966, 1995; Sinha et al. 1992; Geisler et al. 2003a, 2007; Schmidt et al. 2006). The coupled dissolution-reprecipitation processes affecting zircon result in pseudomorphic recrystallization. The crystalline phase, however, possesses a lower volume that results in formation of nanoporosity, which convolute into micropores from pore-ripening to minimize surface energy (Putnis 2002, 2009; Putnis et al. 2005; Geisler et al. 2007; Putnis and Austrheim 2010, 2013; Ruiz-Agudo et al. 2014). These pores may be partially to completely filled with inclusions of secondary phases or residual fluids. Typical consequences of coupled dissolution-reprecipitation processes include re-equilibration of zircon and mobilisation of trace elements such as U, Th, Pb or REE, but also introduction of foreign elements from fluid medium into the structure (Tomaschek et al. 2003; Geisler et al. 2003a, b, c, 2007; Seydoux-Guillaume et al. 2015, 2017; Budzyń et al. 2018; Kelly et al. 2020; Harlov et al. 2023).

Alteration processes induced by aqueous fluids or melt result in various compositional and textural changes at microscale and submicron scale, therefore, investigation of the altered zircon at nanoscale is important to bring microscopic observations into context with submicron processes, such as development of patchy zoning in nanoscale caused by various degrees of metamictization, recrystallization of altered zircon, development of nanoporosity and formation of secondary nanoinclusions (Geisler et al. 2007; Schmidt et al. 2006; Seydoux-Guillaume et al. 2015, 2017; Valley et al. 2015). Alteration of metamict zircon in fluid-experiments at low to moderate temperature conditions (200–500 °C) demonstrated enhanced mobility of Zr, U, Th and Pb and emphasised that zircon alteration can occur already at low temperature range (ca. 260–300 °C) in low-grade metamorphic rocks (Schmidt et al. 2006). Zircon from a U-rich pegmatite assemblage (Iveland-Evje, South Norway), demonstrate radiation damage, which caused swelling of the zircon structure and lead to radial cracking, providing pathways for fluid-induced alteration (Seydoux-Guillaume et al. 2015). In this case, the alteration resulted in nanopores surrounded by a halo of low density zircon, whereas the pore-walls were coated with denser zircon enriched in U and Ca provided by fluids (Seydoux-Guillaume et al. 2015). Potential initial pathways for fluids are related to nano-structural defects of zircon, which greatly enhance permeability of zircon towards fluids (Seydoux-Guillaume et al. 2017).

Investigations of Hadean and Archean crystalline zircons by atom-probe tomography (APT) demonstrated the potential of nanoscale geochronological evaluation of zircon (Valley et al. 2014, 2015). The APT investigations revealed ca. 10 nm-sized nano-clusters of radiogenic Pb, Y and REE located in disrupted zircon structure caused by α-recoil events (Valley et al. 2014). Mobilization of Pb and REE was interpreted to be caused by temperature driven diffusion during a re-heating event, in which Pb accumulated into nano-clusters positioned in preserved un-annealed damaged domains of zircon (Valley et al. 2014, 2015). These observations demonstrate important implications of a short range (few nanometres) Pb and REE diffusion in crystalline zircon, which is considered to have low diffusion rates in microscale (Cherniak et al. 2001; Cherniak 2010).

Metamictization and fluid-induced alteration can affect the structure of zircon significantly. Raman microspectroscopy serves as a profound tool to investigate distortion of the crystal structure, and was the focus of numerous studies of metamict and crystalline zircons (Nasdala et al. 1995, 2001, 2002, 2010; Geisler et al. 2001, 2007; Ende et al. 2021). The widths of Raman bands correlate with the crystallinity of zircon, whereas structural damage is represented by increase of FWHH (full width at half height) value of the $\nu_3(SiO_4)$ antisymmetric stretching vibration band and, thus, can be used to estimate the degree of metamictization in zircon (Nasdala et al. 1995, 1998, 2001). Raman contour maps of the linewidth of the $R(SiO_4)$ (Eg) mode of zircon near 356 cm^{-1} show a good correlation with U contents depicted by EPMA U Mα X-ray distribution maps (Geisler et al. 2007), and annealing experiments of natural and synthetic zircon support the relation of bandwidth with degree of structural damage related to the U content (Marsello and Garver 2010). Raman microspectroscopy of zircon emphasises the potential usability for other minerals, such as monazite and xenotime, that accumulate radiation damage over time, recrystallize during alteration or are important tools in U-(Th-)Pb geochronology.

2.2. Monazite

Monazite is a LREE phosphate and is an important accessory mineral used in investigations of igneous and metamorphic petrogenesis (Pyle et al. 2001; Pyle and Spear 2003; Williams et al. 2007). The usability of monazite in geochronology is related to its capacity to incorporate significant amounts of U and Th, negligible concentrations of common Pb (Parrish 1990; Williams and Jercinovic 2002; Williams et al. 2007), in combination with low diffusion rates of major and trace elements and a high closure temperature of Pb diffusion ($\geq$ 900 °C) that enable monazite to retain its geochemical information during most of the processes in the Earth’s crust (Cherniak et al. 2004; Cherniak 2010). In monazite, Th is favoured over U with a typical Th/U ratio exceeding 1 (Förster 1998; Williams et al. 2007). The incorporation of Th (and U) is related to substitution of the huttonite [$(Th,U)SiO_4$] and cheralite [$Ca(Th,U)(PO_4)_2$] components (Förster 1998; Förster and Harlov 1999; Spear and Pyle 2002; Linthout 2007). The cheralite substitution also enables integration of Ca in the monazite structure. Further substitution mechanisms in monazite may include wakefieldite-(Y) (YVO_4) and chernovite-(Y) ($YAsO_4$) with a close structural relation to xenotime. These enable minor substitutions of V and As in monazite (Jercinovic and Williams 2005; Ondrejka et al. 2007).

Application of monazite geothermometry is related to the temperature dependent element partitioning of HREE + Y in monazite, xenotime and garnet, which enables the potential to combine geochronological data with growth temperatures of monazite (Kingsbury et al. 1993; Gratz and Heinrich 1997; Heinrich et al. 1997; Andrehs and Heinrich 1998; Pyle et al. 2001). Such estimations are possible only because of equilibrium reactions during formation of co-existing monazite, xenotime and garnet, which lead to a temperature-dependent distribution of HREE + Y in both phases (Kingsbury et al. 1993; Gratz and Heinrich 1997; Heinrich et al. 1997; Pyle et al. 2001). An example for application of Y-in-monazite thermometry was presented in a petrochronological study of two ultrahigh temperature metamorphic events in polycyclic granulite facies rocks from Rogoland (South Norway) in which temperatures of 900–950 °C were estimated (Laurent et al. 2018). Another example is a study of granitic magmas from the Georgetown Inlier (North Queensland, Australia), which estimated ca. 730 °C temperature conditions for the formation of S-type granite based on saturation temperatures of zircon and monazite (Volante et al. 2020).

Monazite is stable at broad range of igneous and metamorphic conditions, whereas exact P-T conditions of monazite growth and/or breakdown depend on bulk rock composition and composition of fluid (Bingen et al. 1996; Broska and Siman 1998; Finger et al. 1998; Simpson et al. 2000; Harrison et al. 2002; Spear and Pyle 2002; Wing et al. 2003; Broska et al. 2005; Janots et al. 2006, 2008; Williams et al. 2007; Petrík et al. 2006; Ondrejka et al. 2012, 2016, 2022; Skrzypek et al. 2020). The stability of monazite also depends on the accompanying mineral assemblage, which can result in different reactions proceeding on a microscale distance (Budzyń et al. 2010). Moreover, monazite plays an important role in petrochronological studies of metasomatic events due to its records of fluid-mediated alteration (Williams et al. 2007, 2011; Villa and Williams 2013), which may lead to partial resetting of the U-(Th-)Pb age (Black et al. 1984; Seydoux-Guillaume et al. 2002c; Kelly et al. 2006; Harlov and Hetherington 2010; Harlov et al. 2011; Williams et al. 2011; Budzyń et al. 2015, 2017, 2021, 2022; Grand'Homme et al. 2016, 2018). Alteration of monazite commonly results in Pb-loss, but Th can be retained in the monazite structure, which emphasises the potential of monazite ceramics for isolation of nuclear waste material in contact with moderately saline fluids (Poitrasson et al. 2000).

Fluid-induced alteration of monazite commonly results in a replacement of monazite by apatite [$Ca_5(PO_4)_3(F,Cl,OH)$], allanite [$(Ce,Ca,Y)_2(Al,Fe^{3+})_3(SiO_4)_3(OH)$] and epidote [$Ca_2(Fe,Al)Al_2(SiO_4)(Si_2O_7)O(OH)$], which form corona textures (Broska and Siman 1998; Finger et al. 1998; Grapes et al. 2005; Budzyń et al. 2010; Ondrejka et al. 2012; Hentschel et al. 2020; Ji et al. 2021; Schulz 2021). This has been reported in S-type and K-rich I-type amphibolite facies metagranitoids from Alps, Carpathians and eastern Bohemian Massif, with reactions driven by a fluid supplying Ca, Fe, Si and Al (Finger et al. 1998). Broska and Siman (1998) suggested a reaction of monazite + annite + anorthite + quartz + fluids = apatite + allanite + muscovite during breakdown of monazite in metagranite (Western Carpathians). Prograde crystallization of monazite was documented in high-pressure metapelites at temperatures as low as 350 °C even with low bulk Ca composition, and retrograde crystallization of monazite was documented below 450 °C (Janots et al. 2006). The metamorphic sequence of monazite growth follows the relation of monazite → allanite → monazite in which allanite-xenotime associations formed in pelitic rocks above 450 °C together with rims of apatite, however, the exact stability is dependent on Ca content in the system, which was supplied by fluids derived from Ca-rich marbles and plagioclase (Janots et al. 2008). In the pelitic rocks, allanite breakdown and formation of monazite occur at minimum temperature 524 °C, but the exact temperature range in which allanite may be preserved depends on whole-rock composition, particularly the CaO/Na_2O ratio, i.e. allanite may be preserved up to 610 °C when CaO/Na_2O ratio > 0.93 (Janots et al. 2008). In granitic orthogneisses (Veľký Zelený Potok Valley, the Veporic Unit, Western Carpathians, central Slovakia), monazite breakdown resulted in REE mobilization and partial to complete replacement by apatite

+ $ThSiO_4$, and corona-textures of allanite and clinozoisite [$Ca_2Al_3(SiO_4)_3(OH)$] through reactions with Ca, Fe, Al, Si and F bearing post-magmatic hydrothermal fluids (Ondrejka et al. 2012, 2016). Similar corona-textures were found in metasedimentary rocks, granitoids, Variscan metagranitic rocks and Paleoproterozoic granite (Majka and Budzyń 2006; Budzyń et al. 2010; Lo Pò et al. 2016; Skrzypek et al. 2020; Ji et al. 2021; Ondrejka et al. 2022). In some cases, monazite breakdown enables mobilisation of LREE involving formation of secondary phases such as Th-rich silicate, Th–OH silicate, Th- and P-bearing crandallite–goyazite [solid solution of $(Ca,REE)Al_3(PO_4)_2(OH_5{\cdot}H_2O)$ and $(Sr,REE)Al_3(PO_4)_2(OH_5{\cdot}H_2O)$ endmembers] (Hecht and Cuney 2000; Papoulis et al. 2004).

Reactivity of monazite with alkali-bearing fluids was demonstrated in experimental studies at a broad range of P-T conditions (Harlov et al. 2007, 2011; Harlov and Hetherington 2010; Hetherington et al. 2010; Budzyń et al. 2011, 2015, 2017, 2021; Tropper et al. 2011; Williams et al. 2011; Betkowski et al. 2016; Grand'Homme et al. 2016, 2018). Experimental alteration of monazite resulted in a variety of textural changes, which range from dissolution pits at the rim and microporosity, to partial replacement of monazite by secondary phases. Formation of secondary phases depends on the starting materials and fluid composition involved in experiments. Experiments of monazite using various fluids (1M NaOH and $Na_2Si_2O_5$ + H_2O) resulted in partial replacement of monazite by Th-enriched monazite at the rim (Hetherington et al. 2010). Experiments involving an apatite-monazite assemblage resulted in replacement of monazite by vitusite [$Na_3(Ce,La,Nd)(PO_4)_2$], sazhinite {$Na_2Ce[Si_6O_{14}(OH)]{\cdot}n(H_2O)$} and britholite [$(REE,Ca,Na)_{10}(SiO_4,PO_4)_6(OH,F)_2$] (Betkowski et al. 2016). Experiments involving a complex mixture of starting materials, replicating composition of granitic to pelitic rocks, resulted in complex textures involving formation of various secondary phases (Budzyń et al. 2011, 2017; Williams et al. 2011). An assemblage of monazite, albite, K-feldspar, muscovite, biotite and CaF_2, together with a variety of alkali-rich fluids created a reactive Ca-rich environment at P-T conditions of 450–610 MPa and 450–500 °C (Budzyń et al. 2011). The experiments resulted in fluid-induced alteration of monazite and formation of allanite or fluorapatite with a britholite component depending on the alkali-rich fluid used in the experiment (Budzyń et al. 2011). Partial to complete resetting of the U-(Th-)Pb ages occurred at P-T conditions of 450 MPa and 450 °C due to fluid-induced removal of Pb in altered domains of monazite (Williams et al. 2011). A complex mineral mixture of monazite, labradorite, sanidine, biotite, muscovite, SiO_2 and CaF_2 was used in fluid-alteration experiments involving a high bulk CaO content at a wide range of P-T conditions (200–1000 MPa and 450–750 °C; Budzyń et al. 2017). The experiments resulted in complex textures of altered monazite and formation of fluorcalciobritholite $[(Ca,REE)_{10}(SiO_4,PO_4)_6F_2]$, REE-rich steacyite $[(K,\square)(Na,Ca)_2(Th,U)Si_8O_{20}]$ and REE-rich apatite (Budzyń et al. 2017). The alteration experiments using alkali fluids highlighted the reactivity of alkali-rich fluids in combination with a high CaO/Na_2O environment (Budzyń et al. 2011, 2017). The alteration by alkali-bearing fluids represents an important issue considering application of monazite thermometry and geochronology in petrological studies that require undisturbed monazite geochemistry, because element transport is greatly enhanced via fluid-induced coupled dissolution-reprecipitation processes (Williams et al. 2011; Didier et al. 2013; Budzyń et al. 2011, 2015, 2017, 2021; Grand’Homme et al. 2016, 2018).

Aside of fluid-mediated alteration, monazite also can be altered by radiation damage due to high contents of Th and U. Accumulation of radiation damage would lead to metamictization, however, structural recovery processes such as imminent defect-recovery by α-healing and thermal annealing at temperatures as low as 180 °C enables partial preservation of monazite structure over a long period of time (Seydoux-Guillaume et al. 2018; Nasdala et al. 2020). The process of α-healing is related to the energy loss of ejected α-particles by a decaying nucleus into the monazite structure, which releases enough energy to activate reconnection of the damaged structures independent from temperature (Seydoux-Guillaume et al. 2018).

Extensive investigation of monazite textures, structural properties and compositional variation related to alteration processes has been done at micro- to submicron scale (Black et al. 1984; Seydoux-Guillaume et al. 2002b, 2003, 2004, 2012, 2017, 2018; Grand’Homme et al. 2016, 2018; Fougerouse et al. 2018; Budzyń et al. 2021, 2022; Turuani et al. 2022, 2023). Transmission electron microscopy of monazite nanotexture from a Brazilian pegmatite have shown nano-patches of mottled radiation-damaged domains and well-crystallized domains, which form a mosaic structure of monazite (Seydoux-Guillaume et al. 2002b). An experimental study showed that the degree and abundance of such mottled nano-patches correlate with the α-dosage as a result of metamictization (Seydoux-Guillaume et al. 2004). Furthermore, TEM evaluation of experimentally altered monazite revealed replacement of primary monazite with well-crystallized secondary monazite and nanoporosity, which are well described features for fluid-induced coupled dissolution-reprecipitation processes (Harlov et al. 2011; Ruiz-Agudo et al. 2014; Grand’Homme et al. 2016, 2018; Budzyń et al. 2021, 2022). Fluid-mediated alteration commonly leads to formation of secondary inclusions in the mineral, pores or cracks. In monazite, Ca-, U-, Th-rich phases such as cheralite, uraninite and thorite are common inclusions, which are related to the release of Th and U from monazite and progressive mobilization by fluids (Seydoux-Guillaume et al. 2012, 2017; Grand’Homme et al. 2018; Budzyń et al. 2021, 2022). Recrystallization of monazite and formation of U- and Th-rich inclusions can strongly disturb the geochronological record and emphasize the need for nanoscale evaluation of monazite to correctly interpret U-Th-Pb ages. Furthermore, nanoscale investigations allow to differentiate geochemical signatures from secondary inclusions formed during alteration. Such differentiation was done by Seydoux-Guillaume et al. (2018), who reported nano-clusters of $CaSO_4$ embedded in the monazite lattice indicating $Ca^{2+} + S^{6+} = REE^{3+} + P^{5+}$ substitution during formation of monazite from an S-bearing melt (Rogoland, Norway). Fluid-induced alteration of monazite can result in a formation of sulphur inclusions during metasomatic events (Rasmussen et al. 2011; Seydoux-Guillaume et al. 2018). Experiments involving alkali-rich environment resulted in altered monazite with nanoinclusions of britholite as a result of the idealized reaction of $Na_2Si_2O_5 + H_2O + (LREE,Ca,Si)PO_4 = (Na,LREE,Ca)_5[(Si,P)O_4]_3OH$; a low abundance of these britholite inclusions was attributed to limited Ca supply with substituted Ca in monazite as the sole source (Harlov et al. 2011).

In monazite from granulite-facies rocks (Sandmata Complex, Rajasthan, India), Ca-rich nano-clusters (10 nm-sized) with a composition consistent with apatite were documented with TEM and Atom Probe Microscopy (APM) as a result of phase-exsolution shortly after monazite crystallization (Fougerouse et al. 2018). Partition of unsupported and radiogenic Pb from monazite into the apatite-clusters demonstrate the potential of age disturbance at nanoscale (Fougerouse et al. 2018).

2.3. Xenotime

Xenotime represents the fraction of the APO_4 series with predominantly Y and HREE occupation (Gd–Lu) on the A site and forms in a wide range of rocks ranging from low P-T conditions in diagenetic environments (Rasmussen 2005; Vallini et al. 2005; Rasmussen et al. 2010; McNaughton and Rasmussen 2018), during igneous processes, low- to high-grade metamorphism (Hawkins and Bowring 1999; Spear and Pyle 2002;

Broska et al. 2005; Hetherington et al. 2008; McNaughton and Rasmussen 2018; Budzyń et al. 2018, 2023a, b) and in hydrothermal veins in gold deposits (Vielreicher et al. 2003; Sarma et al. 2011; Fielding et al. 2017; Jian et al. 2023). The properties making xenotime a suitable mineral for U-Pb geochronology are similar to that of monazite, with a high resistance to alterations and the capability to incorporate U via coffinite ($USiO_4$) substitution (Smits 1989; Förster 2006) and Th via thorite ($ThSiO_4$) substitution (Förster 2006). Xenotime commonly contains more U than Th and the U/Th ratio may be used to differentiate its provenance, with U/Th > 10 in xenotime related to U-rich ore-formation, highly variable U/Th ratios in a diagenetic xenotime, and U/Th < 4 in hydrothermal xenotime (McNaughton and Rasmussen 2018). Negligible content of common Pb incorporated during xenotime crystallization leads to accumulation of solely radiogenic Pb (McNaughton et al. 1999; Fletcher et al. 2000; Rasmussen 2005). Diffusion of Pb in xenotime, in general, is slower than in monazite and zircon with a high closure temperature exceeding 900 °C, i.e. a grain of xenotime with an effective diameter of 10 µm would lose 1 % Pb due to diffusion in a time scale of ca. 5000 yrs at ca. 900 °C and would lose the same amount in ca. 10^9 yrs at ca. 600 °C (Cherniak 2006, 2010). Furthermore, a high resistance of xenotime to radiation damage has been evaluated by computer simulations, in which recovery of crystal distortion caused by radiation would begin shortly after at 0.89 ps (Urusov et al. 2012). Aside of its application as a geochronometer, xenotime is also used in the monazite-xenotime or garnet-xenotime thermometry (Heinrich et al. 1997; Pyle and Spear 2000). The temperature dependence of Y content in garnet was estimated empirically with a precision of ± 30 °C, but is only applicable if garnet-growth occurred in equilibrium with xenotime (Pyle and Spear 2000).

Xenotime is chemically more stable than monazite, nevertheless, it can be extensively altered during reactions induced by alkali-bearing fluid. Alteration of xenotime from granitic rocks from the Western Carpathians (Slovak Republic) lead to formation of corona-textures of apatite and Y-rich epidote in the presence of Ca-bearing fluids, whereas Y-rich epidote formed without apatite in rocks with a fluid composition of lower Ca/Al ratio (Broska et al. 2005). Complex alteration of magmatic xenotime involve recrystallization of secondary xenotime via coupled dissolution-reprecipitation with a melt-derived-fluid bearing F, Ca and other alkali-elements during hydrothermal stage of the pegmatite evolution (the case from Písek, Czech Republic; Švecová et al. 2016). In pegmatites, xenotime breakdown may also result in corona-textures with fluorapatite or hingganite-(Y) [$Y_2(\square)Be_2Si_2O_8(OH)_2$] caused by alteration in the presence of Ca-bearing fluids (Majka et al. 2011; Budzyń et al. 2018). Coupled dissolution-reprecipitation processes of xenotime alteration commonly result in the formation of uraninite and thorite inclusions (Hetherington and Harlov 2008; Ondrejka et al. 2016; Budzyń et al. 2018, 2023a, b).

The response of xenotime to prograde metamorphism was investigated in Alpine metapelites in terms of the allanite-monazite-xenotime phase relations, and in metasedimentary rocks from the Mount Barren Group, Western Australia (Janots et al. 2008; Rasmussen et al. 2011). In metapelites, xenotime breaks down before the growth of garnet, but forms again following garnet-growth from breakdown of allanite (ca. 556–580 °C) and from the breakdown of clinozoisite (ca. 560–610 °C) (Janots et al. 2008). These processes are controlled by the bulk CaO content and the CaO/Na_2O ratio indicating a coupled dependence of Ca and Na contents in the fluids (Janots et al. 2008). In metasedimentary rocks, breakdown of detrital xenotime releases Y, HREE and P for metamorphic growth of xenotime during greenschist- and amphibolite-facies via dissolution-reprecipitation reactions (Rasmussen et al. 2011). Xenotime breakdown during fluid-induced alteration may also result in similar corona-textures as in monazite, such as xenotime surrounded by apatite + (Y, HREE)-rich epidote in granitic rocks from Western Carpathians (Broska et al. 2005). Corona-textures may also include hellandite-(Y) [$(Ca,REE)_4Y_2Al\square_2(B_4Si_4O_{22})(OH)_2$] and/or hingganite-(Y) formed during xenotime breakdown driven by a fluid containing Y, B and Be (Ondrejka et al. 2022).

The reactivity of xenotime with alkaline- and alkali-bearing fluids was demonstrated in numerous experimental studies at a broad range of P-T conditions (Hetherington et al. 2010; Harlov and Wirth 2012; Budzyń and Kozub-Budzyń 2015; Budzyń et al. 2017, 2021; Budzyń and Sláma, 2019). In experiments with xenotime involving a set of different fluid compositions (2N NaOH, 2N KOH, $Na_2Si_2O_5$ + H_2O and NaF_2 + H_2O) along with the addition of SiO_2, Al_2O_3, ThO_2 and $ThSiO_4$, xenotime was reactive with all fluids, except for NaOH-bearing fluid, and resulted in formation of curvilinear intergrowths of Th- and Si-rich xenotime (Harlov and Wirth 2012). The high reactivity of xenotime with such fluids results in formation of a high variety of texturally complex secondary phases, when a more complex starting material was involved in experiments simulating granitic to pelitic rock composition (Budzyń and Kozub-Budzyń 2015; Budzyń et al. 2017). In these experiments, xenotime was highly reactive with Na-bearing fluid at low P-T conditions (200–400 MPa, 250–350 °C) and resulted in formation of (Y,REE)-rich silicate and (Y,REE)-rich fluorapatite, whereas xenotime did not react in experimental runs with Ca-bearing fluids until reaching 350 °C and 400 MPa (Budzyń and Kozub-Budzyń 2015). At higher P-T conditions (200–1000 MPa, 450–750 °C), a dependency of the xenotime reactivity with increasing temperature was suggested due to increased abundance of altered xenotime grains at higher temperatures, whereas formation of Y-rich fluorcalciobritholite either as individual crystals or as overgrowth on xenotime indicate elevated mobility of Y + HREE (Budzyń et al. 2017).

The important insights on the alteration processes were provided by the nanoscale investigations of experimentally altered xenotime (Harlov and Wirth 2012; Budzyń et al. 2021). Xenotime in nanoscale generally displays a high degree of crystallinity compared to monazite, characterized by a higher Th and U content, which shows mottled textures indicating various degrees of radiation damage (Harlov and Wirth 2012; Budzyń et al. 2021). The formation of Th- and Si-rich xenotime in experiments conducted by Harlov and Wirth (2012) revealed the exact position of the fluid reaction-front between altered and unaltered xenotime, and Th-enriched dislocations in the altered domains. The reaction front measures only few nanometres, but a band of several microns with Th- and Si-enriched xenotime follows the reaction-front (Harlov and Wirth 2012). Investigations of xenotime with transmission electron microscopy (TEM) have shown nucleation of Y-rich fluorcalciobritholite in amorphous layer between xenotime and crystalline Y-rich fluorcalciobritholite, demonstrating alteration at limited extent along the outermost boundary of the xenotime or in cracks and fissures (Budzyń et al. 2021).

Recent micro- to nanoscale investigations of ca. 979–988 Ma xenotime from pegmatite from Ås II feldspar quarry (Evje, S Norway) provided important insights into understanding of the alteration mechanisms (Budzyń et al. 2023a, b). The xenotime displayed radiation-damaged structure in primary, unaltered domains, and altered domains with microinclusions of (Th, U)-silicates, uraninite and minor galena. Sub-micron evaluation using TEM demonstrate how initial alteration processes took place at partially open grain boundaries and nano-fractures within primary xenotime domains, which resulted in U- and Th-depleted submicron domains and precipitation of submicron inclusions of (Th, U)-silicate, uraninite or coffinite (Budzyń et al. 2023b). The TEM investigations of unaltered xenotime domains showed for the first time evidence of U and Th segregation into the dislocations, which results in removal of fluid-mobile U^{4+} at the nanoscale and further implications on the disturbance of U-Pb age record (Budzyń et al. 2023a).

Nanoscale geochronological investigations of xenotime using atom probe tomography (APT) demonstrate possibility to estimate ages at analytical volume of 4 to 6 orders smaller than established methods and enables estimation of ages of secondary nanoinclusions, such as Pb-rich apatite in altered xenotime (Joseph et al. 2021, 2023). The xenotime from a pegmatite (ca. 1000 Ma, Grenville Province, Canada), commonly used as a reference material, contains spherical clusters of Pb-bearing apatite nanoinclusions and a dislocation filled with apatite, which formed after crystallization of xenotime (Joseph et al. 2023). The apatite inclusions dated using nanogeochronology were significantly younger (ca. 863 Ma) indicating fluid interaction with xenotime (Joseph et al. 2023). These nanoscale investigations demonstrate that even “unaltered” material (in terms of microscale observations) potentially recorded fluid-induced alteration, which can be dated using an analytical technique at nanoscale.

Alteration of zircon, monazite and xenotime unambiguously affect their geochemical characteristics and impact interpretation of petrogenetic data involving their provenance, geothermometry and petrochronology. The described natural and experimental cases of zircon, monazite and xenotime demonstrate the importance of further investigations in micro- to nanoscale to increase our understanding the alteration processes. A zircon-xenotime intergrowth from a pegmatite from the Piława Górna (the Góry Sowie Block, SW Poland) serves as an excellent example to investigate major and trace element mobilization, alteration processes and phase stabilities in relation to textural changes at micro- and nanoscale in the first part of this study (Chapter 3).

2.4. Raman microspectroscopy of monazite and xenotime

Monazite crystallizes with a monoclinic structure containing a $P2_1/n$ ($Z = 4$) symmetry (Beall et al. 1981; Ni et al. 1995; Mullica et al. 1996; Boatner 2002; Clavier et al. 2011; Huminicki and Hawthorne 2019; Lalla et al. 2021). The structure is arranged by polyhedra in a nine-fold oxygen coordination with the larger trivalent cation in the centre, which are connected at the edges to form a chain in b-direction; these chains are interconnected by PO_4 tetrahedra in c-direction (Fig. 1 a, b; Huminicki and Hawthorne 2019). Based on crystal symmetry, vibrational features of the monazite structure were defined by a factor group analysis with the equation $\Gamma_T = 18A_g + 17A_u + 18B_g + 16B_u$ (Begun et al. 1981).

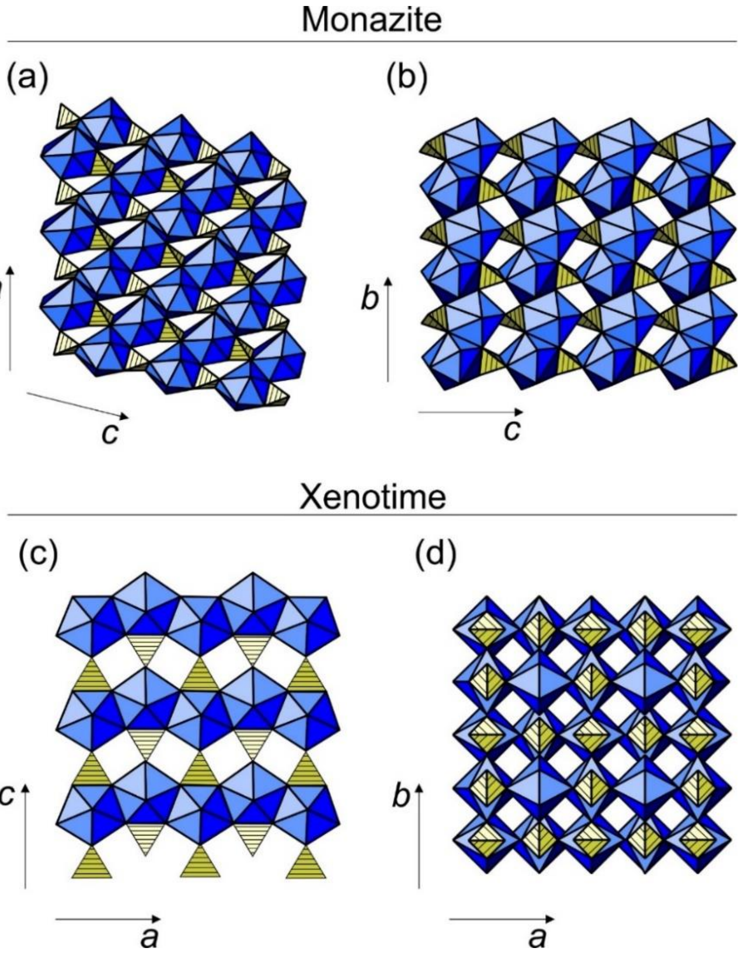

Fig. 1. Structural arrangement in monazite and xenotime (modified from Huminicki and Hawthorne 2019). (a) monazite projected onto (010) and (b) projected onto (100) plane. (c) xenotime projected onto the (010) and (d) projected onto (100) plane.

Thirty-six of these vibrational modes are Raman-active, i.e., $\Gamma_{int} = 9A_g + 9B_g$, $\Gamma_{ext} = 9\ A_g + 9B_g$ (Begun et al. 1981). Raman spectra of monazite typically result in lattice modes ranging from 100 to 350 cm^{-1}, internal PO_4 bending modes ranging from 500 to 700 cm^{-1}, and the most dominant symmetric stretching mode $v_1(PO_4)$ in the range of 960 to 990 cm^{-1} (Geisler et al. 2016). These represent the primary Raman features of the monazite spectrum.

Xenotime [$(Y,HREE)PO_4$] is a tetragonal mineral which forms isostructural to zircon in a space group of D_{4h}^{19} ($I4_1$/amd), Z = 2 (Fig. 1c, d; Wyckoff 1965; Begun et al. 1981; Ni et al. 1995; Mullica et al. 1996; Boatner 2002; Huminicki and Hawthorne 2019). The unit cell of xenotime structure contains two molecules, Y ions and $(PO_4)^{3-}$ occupy the D_{4h}^{19} site, whereas the oxygen atoms are located at sites with C_s symmetry (Begun et al. 1981). The oxygen atoms are coordinated in eight-fold dodecahedrons with the larger trivalent cation in the centre. These dodecahedrons are linked at their edges to form chains in b-direction. These chains are interconnected by PO_4 tetrahedra in c-direction to form a layer parallel to (100) and finally stack in a-direction (Fig. 1c, d; Ni et al. 1995; Huminickit and Hawthorne 2019). Factor group analysis of the xenotime structure results in twelve Raman active modes according to $\Gamma_{ext} = 2B_{1g} + 3E_g : \Gamma_{int} = 2A_{1g} + 2B_{1g} + B_{2g} + 2E_g$ (Begun et al. 1981). Raman spectra of xenotime can be divided like spectra of monazite, into the primary Raman features, that are lattice modes (100–300 cm^{-1}), internal (PO_4) bending modes (500–700 cm^{-1}) and internal (PO_4) stretching modes (900–1200 cm^{-1}).

Monazite and xenotime are orthophosphates with varying contents of REE. Because of the different ionic radii of the REE ions, different lattice parameters are preferred in the respective endmember $REEPO_4$. For example, $LaPO_4$ is reported to reach a = 6.8313 Å; b = 7.0705 Å; c = 6.5034 Å and b = 103.27° resulting in a unit cell volume of 305.73 Å^3, whereas $CePO_4$ is characterized by a = 6.7777 Å; b = 6.993 Å; c = 6.445 Å and b = 103.54° resulting in a unit cell volume of 296.98 Å^3 (Beall et al. 1981; Pepin and Vance 1981; Ni et al. 1995; Clavier et al. 2011). These examples demonstrate different unit cell parameters based on two close REE ions. Because of this fundamental characteristic each individual REE contributes differently to the gross structure of monazite and xenotime, and individual structural characteristics for each $REEPO_4$ need to be taken into account. Raman spectra of $REEPO_4$ from $LaPO_4$ to $LuPO_4$ demonstrate a direct correlation between position of Raman bands with the decreasing ionic radii from La to Lu (Begun et al. 1981). These "baseline spectra" for the lanthanide orthophosphates obtained by Begun et al. (1981) have been used as references until now (Silva et al. 2006; Ruschel et al. 2012; Heuser et al. 2014; Geisler et al. 2016; Clavier et al. 2018; Lalla et al. 2021). The influence of REE composition of synthetic orthophosphates $(La_{1-x}Eu_x)PO_4$ on spectral characteristics was demonstrated by the direct correlation of peak shift towards higher wavenumbers with increasing mol.% of Eu (Geisler et al. 2016).

Polarization Raman microspectroscopy applied to monazite-type orthophosphates ($LaPO_4$–$GdPO_4$) demonstrate how crystal orientation can result in significant changes of the Raman spectra (Silva et al. 2006). These include changes in intensities of Raman bands and appearance of fluorescence bands in the orientation of $y(xz)\bar{y}$ compared to $y(xx)\bar{y}$ at the example of spectra of $PrPO_4$ (Silva et al. 2006). These important observations demonstrate the relation of crystal orientation with Raman spectra and need to be considered when interpreting new features or vibrational changes in Raman spectra of minerals.

The Raman spectrum of monazite found versatile application in investigations of lattice distortion and distinction of the degree of radiation damage in monazite structure

(Seydoux-Guillaume et al. 2002b; Ruschel et al. 2012). The incorporation of the actinides (i.e. Th and U), but also Ca and Pb into the monazite structure causes distortion to neighbouring PO_4 groups due to the significant differences in ion radii and mass towards Ce. This has been demonstrated by a good correlation of FWHH values of $\nu_1(PO_4)$ symmetric stretching band of annealed monazite with the sum of U, Th, Ca and Pb (Ruschel et al. 2012). The empirical linear regression {FWHH [cm^{-1}] = 3.95 + 26.66 × (Th + U + Ca + Pb) [apfu]} resulted in a formula that enables calculation of band broadening caused by distortion of the structure by incorporating U, Th, Ca and Pb, and enable estimation of potentially radiation-damaged monazite structure when significantly higher FWHH values are measured compared to calculated values (Ruschel et al. 2012). As mentioned above, orientation of crystal to the excitation laser can result in significant changes of the Raman spectrum (Silva et al. 2006). However, it needs to be emphasised that the conclusions drawn from Ruschel et al. (2012) were derived from a large sample size of randomly oriented monazite grains, which demonstrate the use of comparing measured FWHH values with FWHH calculated based on composition.

Fluorescence is a common effect in Raman microspectroscopy and can be recognized by comparison of spectra using multiple laser wavelengths. If bands are shifting positions, disappear or new bands appear using different lasers, they are most likely caused by fluorescence. Fluorescence commonly appears as broad background bands that may superimpose the Raman signals and are caused by emission centres, which include activators such as lattice defects or minor elements, and the intensity of fluorescence depends on the presence of such activators and crystal orientation (Marfunin 1979; Belsky and Krupa 1999; Gaft et al. 2015). Fluorescence caused by REE^{3+} ions commonly appears as relatively sharp and characteristic bands. The reason for this lies within their unique electronic configuration of shielded $4f$ electronic transitions (*f*-*f* and f^{k-1}-*d*-configuration) of the REE^{3+} ions (Marfunin 1979; Lenz et al. 2013, 2015; Gaft et al. 2015). Because the fluorescence effects of REE^{3+}-bearing phases are characteristic for individual REE electronic transitions (Marfunin 1979; Lenz et al. 2015), Raman microspectroscopy may be used to identify spectral changes in unaltered and altered domains, which potentially underwent element transport, structural changes or developed pores filled with secondary phases.

Raman spectroscopic studies of monazite, xenotime and synthetic $REEPO_4$ endmembers aimed at specific regions of the Raman spectra, mostly in the range of ca. 0–1200 cm^{-1} where the primary Raman features are, with extended work focused on the $v_1(PO_4)$ symmetric stretching band (e.g. Begun et al. 1981; Seydoux-Guillaume et al. 2002b; Silva et al. 2006; Ruschel et al. 2012; Geisler et al. 2016; Nasdala et al. 2018; Budzyń et al. 2018, 2021, 2022, 2023b). The second part of this study (Chapter 4) focuses on Raman microspectroscopy of experimentally altered monazite and xenotime, altered monazite from Ankazobe district (Madagascar) and altered xenotime from pegmatite from Piława Górna using 488 nm, 532 nm, 633 nm and 780 nm lasers. This study investigates the broad spectral changes of primary Raman features and characteristic electronic transitions responsible for narrow and broad fluorescence effects in unaltered and altered domains of monazite and xenotime, which contributes to improvement of the Raman database and may serve as future reference.

3. Micro- to nanoscale investigation of a zircon-xenotime intergrowth from the pegmatite from Piława Górna (Góry Sowie Block, SW Poland)

3.1. Sample description

The sample of pegmatite with investigated zircon and xenotime comes from a quarry near Piława Górna in the Góry Sowie Block (Fig. 2). Several metres thick veins of pegmatite include textural zones of (i) a fine-grained outer border followed by (ii) a coarse-grained outer wall, (iii) an inner wall of intermediate zones (graphic zone and blocky microcline) and (iv) a quartz core (Pieczka et al. 2012, 2014; Szuszkiewicz et al. 2013). The pegmatite consists of large crystals of microcline, quartz, plagioclase and biotite, with accessory epidote, fluorapatite, Y-rich allanite-(Ce), xenotime, zircon and a vast number of other phases that include beryl, bismuth, cassiterite, chalcopyrite, galena, hematite and monazite-(Ce), representing only a few examples (Szuszkiewicz et al. 2013). Petrogenetic classification of the pegmatite may be considered to belong to the NYF + LCT [(Nb, Y, F) + (Li, Cs, Ta)] type (Černý and Ercit 2005; Pieczka et al. 2012, 2014; Szuszkiewicz et al. 2013).

The investigated intergrowth includes a ca. 2 mm-sized euhedral zircon and ca. 0.5 × 1 mm-sized xenotime (Fig. 3). The zircon demonstrates three distinct domains: (i) a patchy zoned core with microinclusions and submicron inclusions of uraninite and (U, Th)-rich phases; (ii) a patchy zoned rim with extensive microporosity and microinclusions of (U, Th)-rich phases; and (iii) a thin (several dozens of microns) crystalline outermost rim (Fig. 3). The entire xenotime is patchy zoned in high contrast back-scattered electron (BSE) imaging and has a domain of extensive microporosity in close proximity to the intergrown zircon, which is divided by a network of fractures and cracks from the xenotime domain with lesser microporosity.

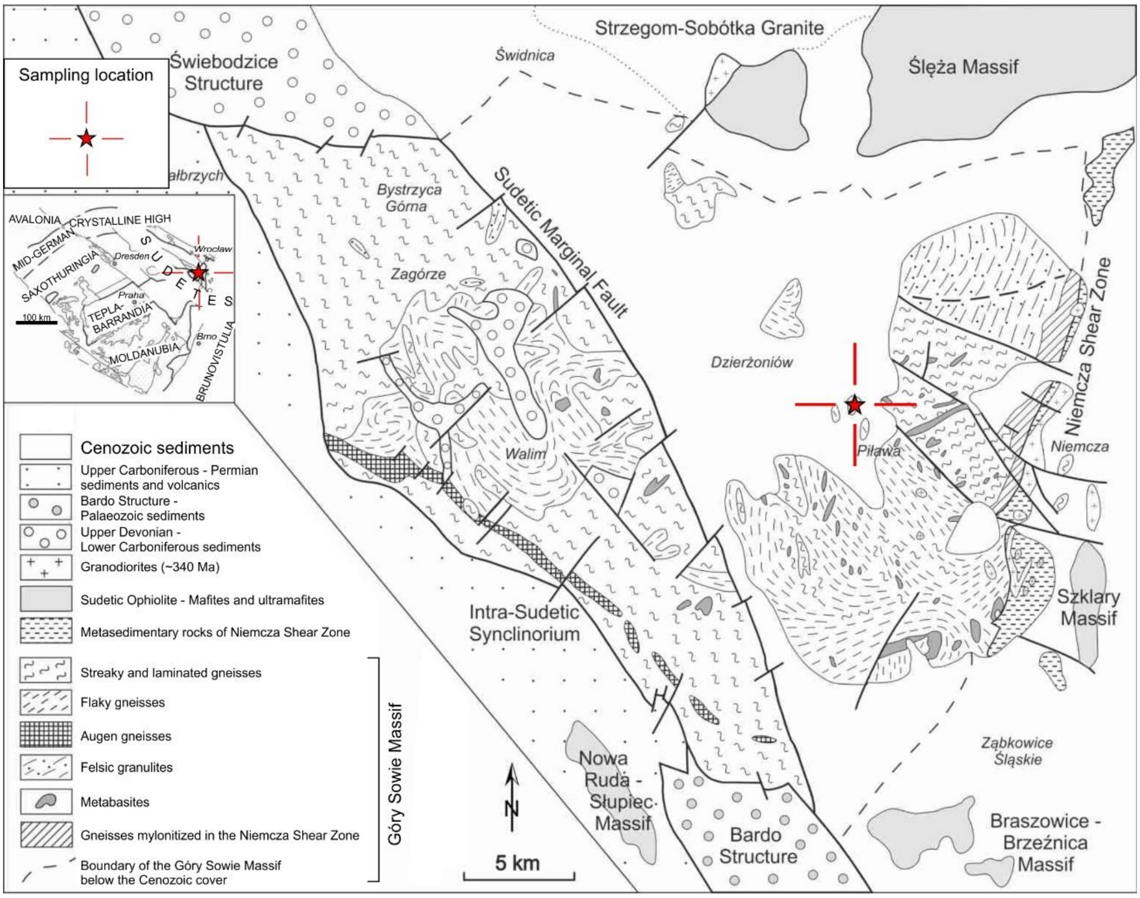

Fig. 2. Geological sketch with sampling location of the pegmatite in the quarry near Piława Górna; inset – position of the Góry Sowie Block in the Bohemian Massif (modified from Bröcker et al. 1998; Budzyń et al. 2018; Tramm et al. 2021).

The xenotime is partially replaced by two fluorapatite grains on both sides with an irregular boundary between xenotime and fluorapatite, which is related to proceeding replacement. The earlier study constrained that zircon-xenotime intergrowth originally formed in a Proterozoic pegmatite at ca. 2.09 Ga, followed by incorporation into the Late Devonian pegmatite as a restite at ca. 370 Ma when it underwent alteration induced by fluid or melt (Budzyń et al. 2018). Incorporation of the zircon into the Devonian pegmatite led to re-equilibration of the zircon core via diffusion-reaction processes and alteration of the zircon rim via coupled dissolution-reprecipitation processes (Budzyń et al. 2018). The xenotime was alterated via coupled dissolution-reprecipitation processes that resulted in formation of secondary fluorapatite at the edges of the phase boundary between xenotime and zircon, and growth of the REE-rich allanite at the rim of zircon

(Budzyń et al. 2018). The low-T fluid-induced alteration ended at ca. 280 Ma with formation of microinclusions of uraninite and U-rich phases in the structurally damaged intermediate zone between zircon core and rim (Budzyń et al. 2018).

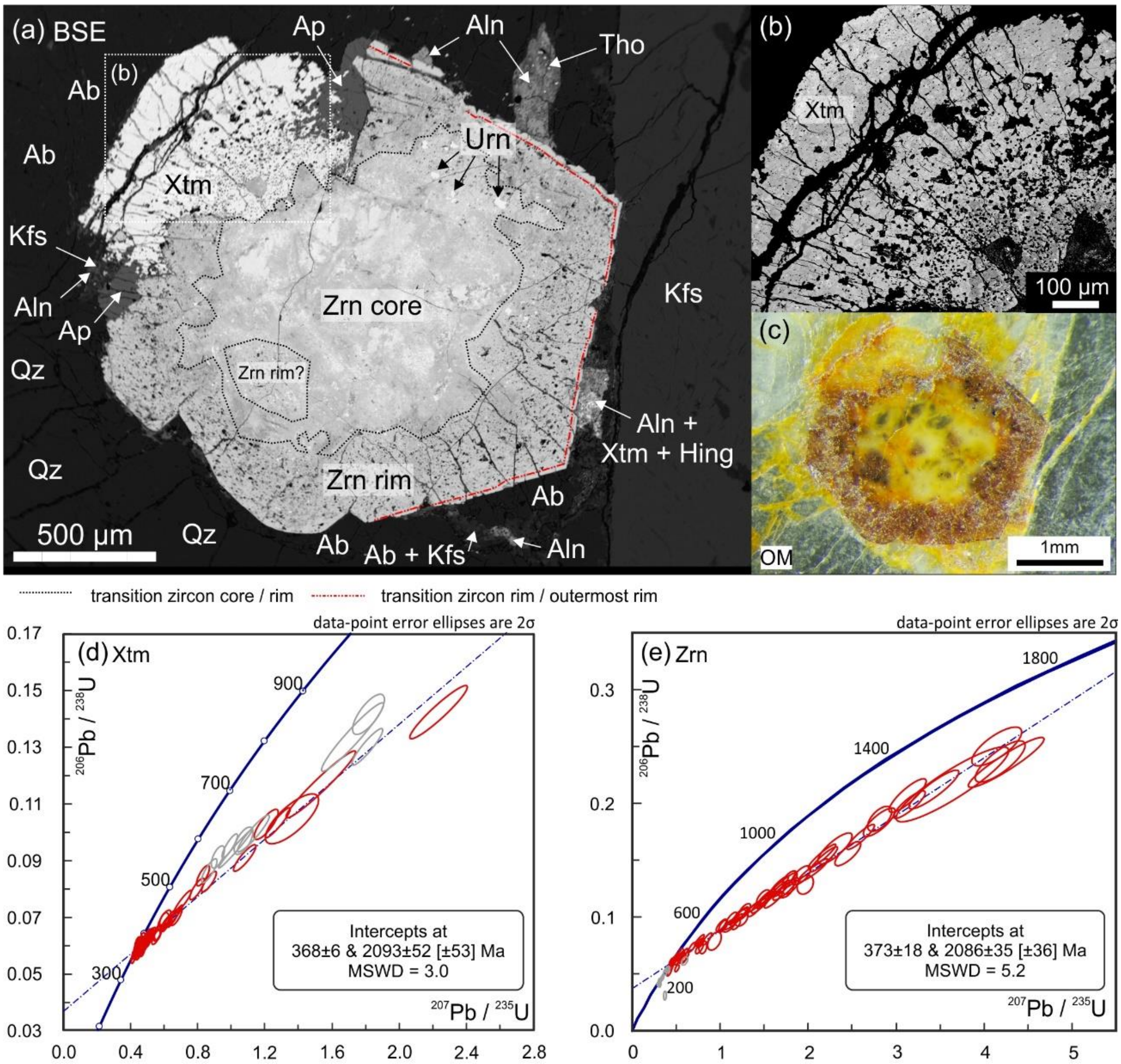

Fig. 3. Overview of the zircon-xenotime intergrowth (modified from Budzyń et al. 2018; Tramm et al. 2021): (a) BSE image representing the mineral assemblage surrounding the intergrowth; (b) high-contrast BSE image of the xenotime; (c) optical microscope (OM) image; (d, e) Concordia plots presenting results of LA-ICPMS U-Pb measurements of xenotime and zircon. Abbreviations: Ab – albite, Aln – Y-rich allanite-(Ce), Ap – fluorapatite, Hing – hingganite-(Y), Kfs – K-feldspar, Qz – quartz, Tho – thorianite, Xtm – xenotime, Zrn – zircon.

3.2. Analytical methods

Trace element measurements of zircon and xenotime were performed using a Thermo Scientific Element 2 high-resolution sector field ICP-MS coupled to a 193 nm ArF excimer laser (Teledyne Cetac Analyte Excite laser) at the Institute of Geology of the Czech Academy of Sciences (Prague, Czech Republic). Frequency of the used laser was set to 5 Hz and fluence of 3.5 J/cm^2 with a spot size of 16 µm. The flow rate of the carrier gas (He) was 0.9 L/min, the carrier gas was flushed through the two-volume ablation cell. Before introduction into the ICP, the carrier gas was mixed with Ar- and N-gas flushed at a rate of 0.7 L/min Ar and 0.005 L/min N_2 using an in-house glass signal homogenizer (design of Tunheng and Hirata 2004) in order to produce a smooth, spike-free signal. The oxide level was kept low (< 0.1 %), whereas the signal was tuned for maximum sensitivity. The typical acquisition time consisted of 15 seconds for a blank measurement, and 25 seconds for trace element measurements containing the signals from the ablated materials. In-between analysis, the ICP was washed for 30 seconds. Data collection was divided into two resolution modes, (i) first ablation and data collection at low-mass resolution ($m/\Delta m = 300$: ^{89}Y, ^{91}Zr, ^{93}Nb, ^{139}La, ^{140}Ce, ^{141}Pr, ^{146}Nd, ^{147}Sm, ^{153}Eu, ^{157}Gd, ^{159}Tb, ^{163}Dy, ^{165}Ho, ^{166}Er, ^{169}Tm, ^{172}Yb, ^{175}Lu, ^{178}Hf, ^{181}Ta, ^{232}Th and ^{238}U; plus ^{208}Pb in xenotime and fluorapatite, and ^{204}Pb, ^{206}Pb, ^{207}Pb and ^{208}Pb in zircon) and (ii) second ablation at a spot close to first ablation for collection of data at medium-mass resolution mode ($m/\Delta m = 4000$: ^{23}Na, ^{27}Al, ^{31}P, ^{44}Ca, ^{45}Sc, ^{56}Fe, ^{89}Y and ^{90}Zr; plus ^{47}Ti in xenotime and fluorapatite, and ^{49}Ti in zircon). Sequence of the measurements was arranged to repeated blocks of 2 analyses of NIST SRM612, one analysis of the BCR-2 standard, one analysis of 91500 zircon reference material (Wiedenbeck et al. 1995) and 10 unknowns.

For calibration of trace element data, the NIST SRM612 glass was used with Zr as an internal standard for zircon analyses and Y as an internal standard for xenotime analyses. The calibration was supported by concentrations of Zr and Y from data of the investigated zircon and xenotime obtained with EPMA. The background noise of each element was multiplied by 3.25 to estimate the individual detection limits. The time-resolved signals were processed using Glitter software (van Achterbergh et al. 2001). Precision of the analyses (1 RSD) ranges from 5 to 15% for most elements. A homogenized basalt reference material BCR-2 (USGS) and zircon 91500 (Wiedenbeck et al. 1995) were used to monitor the accuracy during measurements.

Transmission electron microscopy (TEM) investigations were performed at the German Research Centre of Geoscience (GeoForschungsZentrum GFZ, Potsdam, Germany) in 11 foils, which were cut using focused ion beam (FIB) milling. The areas to cut FIB-foils were chosen at locations of characteristic domains of zircon and xenotime to evaluate the nano-texture potentially related to various alteration processes. The process of cutting the FIB-foils followed several steps, (i) selection of 20 × 2 µm areas, which then (ii) were protected with a 1.5 µm layer of Pt as protection against FIB sputtering with the Ga-ion beam, (iii) for the raw FIB-foils, an acceleration voltage of 30 kV and beam current of 45 nA were set for the lateral sputtering. Afterwards, the raw foils were placed on a Cu grid (half-moon) and thinned out to ca. 150 nm thickness. For this purpose, acceleration voltage of 30 kV was set and beam current from 0.79 nA to 80 pA in order to secure no damage to the final product. For the last polishing steps, the acceleration voltage was reduced to 5 kV and beam current set to 41 pA, such that the final size and thickness of the FIB-foils was 20 × 10 × 0.15 µm. For detailed information on the sample preparation procedure see Wirth (2004, 2009).

TEM observations were conducted using a FEI Tecnai G2 X-Twin TEM, equipped with a Fishione high-angle annular dark-field (HAADF) detector, a Gatan electron energy-loss spectrometer (EELS) and an EDAX X-ray analyser. For the electron source, a Schottky field emitter was used. High-resolution electron microscopy images (HREM) were used to calculate diffraction patterns as Fast Fourier Transforms (FFT) with which crystallographic parameters, such as Miller indices (hkl), angles between adjacent planes and the dhkl spacing, were obtained for phase identification. In order to identify phases unambiguously, angles have to be accurate within an error of ≤1°. The FFT measurements enabled identification of angles with an error of <0.5°, thus suitable for phase identification. The HAADF images were acquired as Z-contrast images with a camera length of 75 mm; the resulting images show bright objects with a higher density or a chemical composition dominated by high atomic numbers (e.g. U or Th). Bright field (BF) images were also obtained during TEM observations. In BF mode, the contrast is reversed compared to HAADF images, which means that phases with chemical composition dominated by high atomic numbers appear dark, because the electrons are strongly absorbed by phases with high atomic numbers, higher density or higher crystallinity.

3.3. Geological background

The Góry Sowie Block is located in the central part of the Sudety Mts. (NE Bohemian Massif, SW Poland) and is divided by the Sudetic Marginal Fault into the eastern Fore-Sudetic Block and the western, mountainous part – the Góry Sowie Mts. (Fig. 2). The Góry Sowie Block consists of a complex mosaic including migmatitic para- and orthogneisses, amphibolites, minor granulites, garnet peridotites, pegmatites and calc-silicate rocks (Kryza 1981; Żelaźniewicz 1990). Geochronological investigations of the basement complex constrained record of two major events prior to the maximum of

Variscan orogenesis, (i) ca. 500 Ma granitic intrusion and (ii) Caledonian tectonics (480–440 Ma), which are related to closure of the Iapetus/Tornquist ocean (Kröner and Hegner 1998; Turniak et al. 2000; Schneider et al. 2006). This was then followed by reworking of the material during closure of Rheic ocean (400–360 Ma) and Variscian orogenesis (340–330 Ma) (Turniak et al. 2000; Gordon et al. 2005; Schneider et al. 2006).

The Góry Sowie Block recorded several (up to five) tectonic and metamorphic episodes during reworking of the crustal material (Żelaźniewicz 1990), which include a HP-HT event at ca. 400–393 Ma (O'Brien et al. 1997; Gordon et al. 2005; Kryza and Fanning 2007; Tabaud et al. 2021; Budzyń et al. 2022); amphibolite-facies migmatization at ca. 385–380 Ma (Gordon et al. 2005; Kryza and Fanning 2007; Budzyń et al. 2018, 2022; Tabaud et al. 2021; Jastrzębski et al. 2021); and rapid cooling at ca. 370–360 Ma (Bröcker et al. 1998; Marheine et al. 2002; Schneider et al. 2006). Geochronological investigations of the Góry Sowie Block, Variscan massifs and Orlica-Śnieżnik Complex emphasised the complex nature of the central Sudetes, consisting of peri-Gondwanan crustal fragments and arc terranes, welded together by closed basins and seaways as a result of mutual collision and collision with Baltica, by demonstrating high variability of age constraints between adjoining terranes (Matte et al. 1990; Schneider et al. 2006). The ages of hornblende and micas from the amphibolite-facies gneisses and amphibolites of the western mountainous part of the Góry Sowie Block are constrained to be between 382 ± 1 Ma and 373 ± 0.5 Ma by Ar-Ar dating, whereas the eastern part of the Block bear younger Ar-Ar cooling ages of 337 ± 0.8 Ma and 274.3 ± 1.7 Ma (Schneider et al. 2006). The latter corresponds to the sampling location of the zircon-xenotime intergrowth from pegmatite, in which termination of low temperature alteration were constrained to ca. 280 Ma (Budzyń et al. 2018).

The injections of pegmatites occurred relatively late in tectonometamorphic history of the Góry Sowie Block, probably during the fourth tectonic stage (Żelaźniewicz 1990). Xenotime from pegmatite vein from Zagórze Śląskie (the western part of the Góry Sowie Block) yielded TIMS ^{207}Pb/^{206}Pb ages from 383 ± 5 Ma to 370 ± 5 Ma (Timmermann et al. 2000). In the eastern part of the Góry Sowie Block, monazite and uraninite from pegmatite from Piława Górna yielded ages of 377.6 ±1.3 Ma (SHRIMP) and 380.7 ± 2.4 Ma (EPMA), respectively (Turniak et al. 2015). Later study constrained LA-ICPMS U-Pb ages (lower intercepts in Concordia diagrams) of zircon and xenotime from pegmatite from Piława Górna to 373 ± 18 Ma and 368 ± 6 Ma, respectively, which provide record of the re-equilibration during the pegmatite formation, followed by ca. 280 Ma (EPMA Th-U-total Pb age) crystallization of the uraninite inclusions in zircon, which records termination of the fluid-mediated, low-temperature alteration of zircon (Budzyń et al. 2018).

3.4. Results

3.4.1. Geochemical characteristics of xenotime

Chondrite-normalized xenotime data show typical LREE << HREE patterns with an increasing convex slope from La to Sm, a negative Eu anomaly and a nearly flat plateau from Gd to Lu (Fig. 4a). The data demonstrate homogeneous HREE contents, but highly variable LREE concentrations. Geochemically closely related elements Ta vs. Nb and Zr vs. Hf display a strong positive linear correlation (Fig. 4b, c). Data of Zr vs. LREE display a correlation for La and Ce with Zr (Fig. 4d). Element distribution of (Th + U) vs. (Ca + Si) shows a cluster of data at ca. 8000 ppm Th + U and ca. 1800–3100 ppm Ca + Si (Fig. 4e). Few data points align with (Th + U)/(Ca + Si) = 1, which suggests partial substitution of huttonite and cheralite components (Förster 1998; Spear and Pyle

2002). Data of Si vs. Zr scatter below 1500 ppm Zr and 3000 ppm Si, whereas some data align with Zr/Si = 1 (Fig. 4f), which may indicate partial substitution of the zircon component (Spear and Pyle 2002). Plots of nonformula elements Fe vs. Al roughly suggest exponential correlation, whereas data of Fe vs. Ti display no correlation (Fig. 4g).

3.4.2 Geochemical characteristics of zircon

The chondrite-normalized REE patterns generally display an increasing slope from Gd to Lu in all zircon data, but differ in LREE distribution between the zircon core, rim and outermost rim (Fig. 5). Zircon core data show elevated LREE, a negative Eu anomaly and a slightly increasing slope from Gd to Lu (Fig. 5a). The elevated LREE values are not typical for igneous zircon, which usually shows an increasing slope from La to Sm with a strong positive Ce anomaly (Speer 1980; Hoskin 2000; Hoskin and Schaltegger 2003), and resemble closer LREE-enriched patterns of hydrothermal type-II zircon (Hoskin 2005; Cavosie et al. 2006). Zircon rim data display even higher LREE values above 1000× than the core data, whereas the outermost rim data display significantly lower concentrations of REE than in the core and rim (Fig. 5b, c). The REE concentrations of the investigated zircon reflect overall exceptionally high contents compared to wide range of compositions reported for zircon (e.g. El-Bialy and Ali 2013; Nardi et al. 2013; Bell et al. 2016, 2019), which emphasises its rare and exotic characteristics.

Zircon core data cluster at exceptionally high U contents of ca. 19000–106000 ppm), whereas zircon rim data scatter at ca. 2500–26600 ppm U, and the outermost rim data display low U contents below 3500 ppm (Fig. 6a). The P vs. (HREE + Y) plots of zircon core and rim data scatter at elevated contents of ca. 9300–34500 ppm and 5800–48300 ppm (HREE + Y) over a wide range of P concentration, whereas outermost rim data concentrate at ca. 1000 ppm P and 2000–4100 ppm (HREE + Y)

(Fig. 6b). The relation of (Nb + Ta) vs. Y shows positive trends in zircon core and rim data, which are nearly parallel to the Y/(Nb + Ta) = 100 line in the core and Y/(Nb + Ta) = 10 in the rim (Fig. 6c). The outermost rim data display lower concentrations, but follow the trend of Y/(Nb + Ta) = 10.

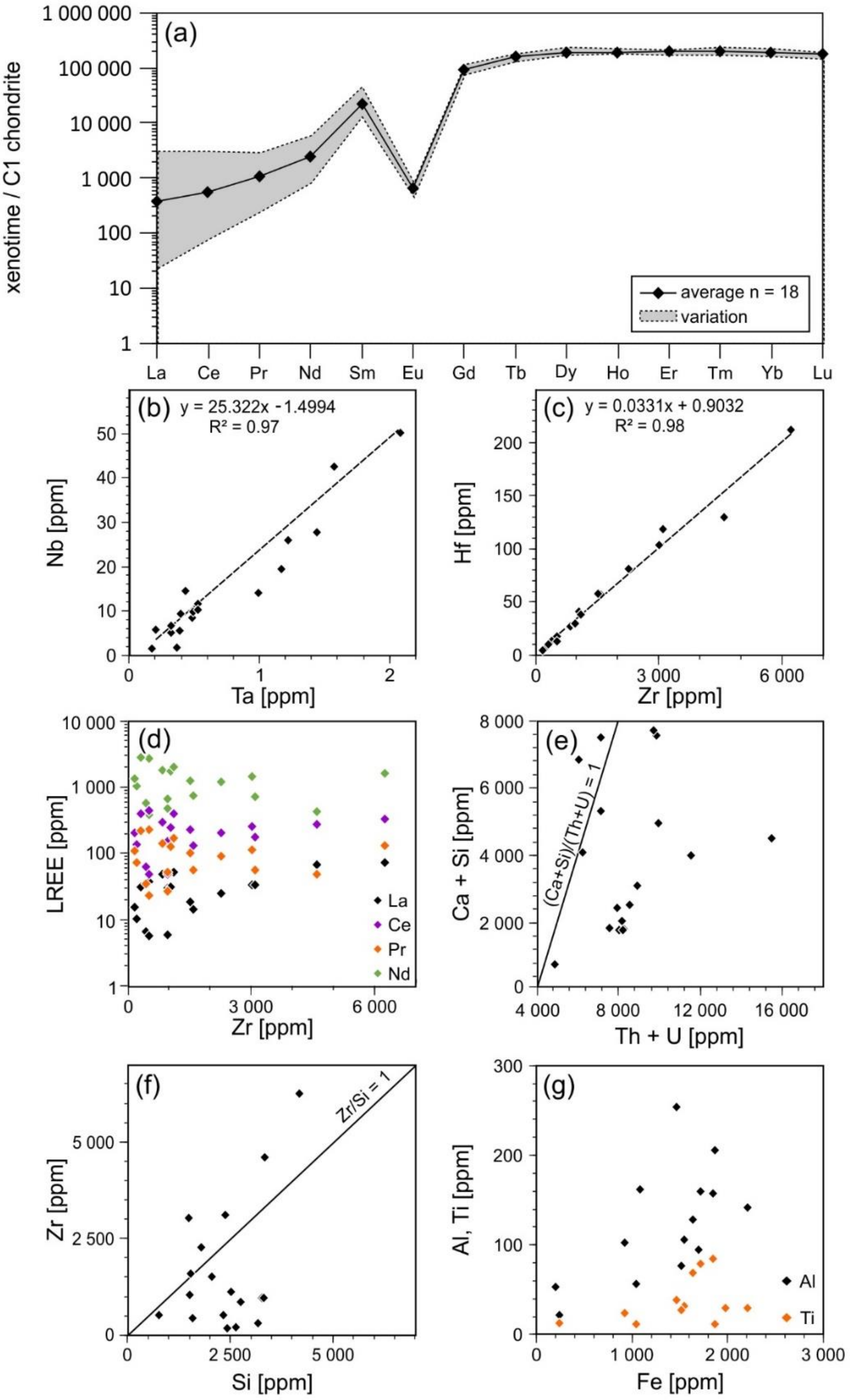

Fig. 4. Summary of LA-ICPMS trace element data of xenotime. C1 chondrite composition from McDonough and Sun (1995). Modified from Tramm et al. (2021).

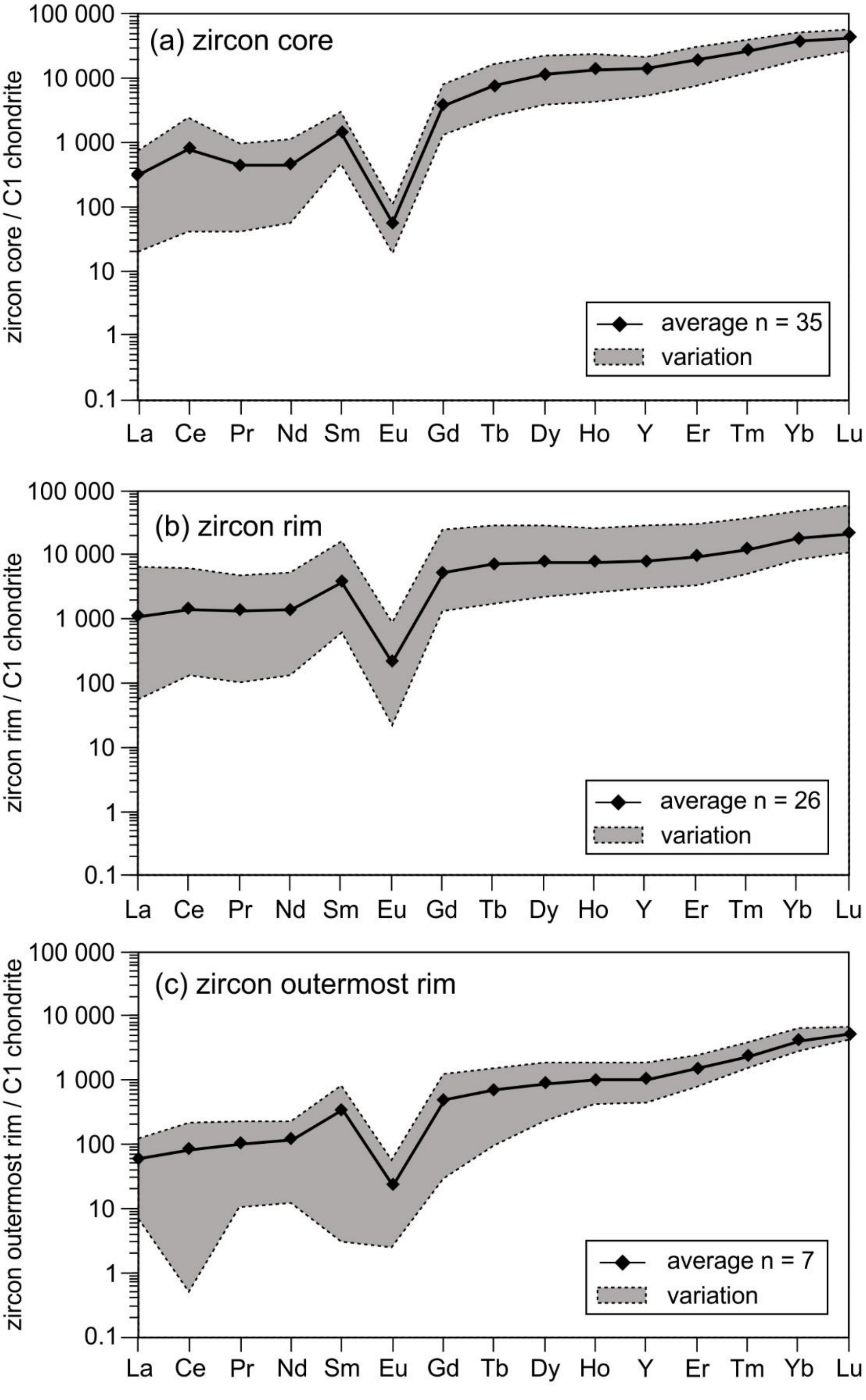

Fig. 5. Chondrite-normalized trace element patterns in (a) the zircon core, (b) the zircon rim and (c) the zircon outermost rim. C1 chondrite composition after McDonough and Sun (1995). Modified from Tramm et al. (2021)

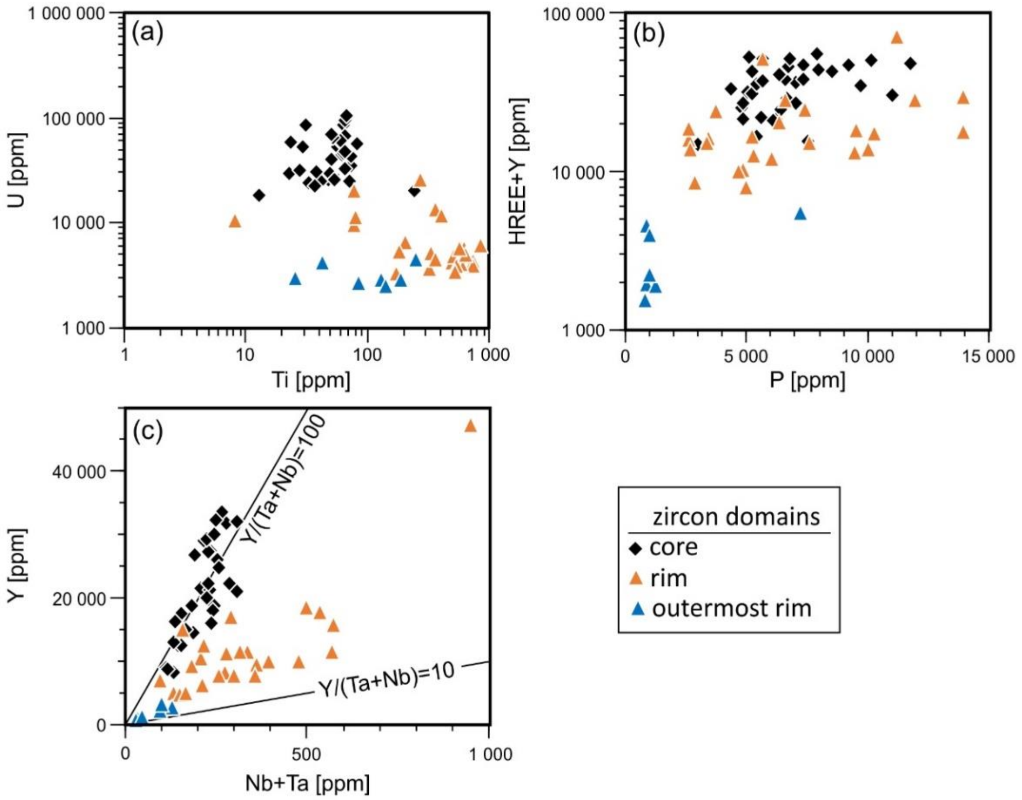

Fig. 6. Summary of LA-ICPMS trace element data for the zircon. Modified from Tramm et al. (2021).

Chondrite normalized $\mathrm{La_N}$ and $\mathrm{Ce_N}$ show elevated concentrations in most zircon core and rim data (Fig. 7a, b), which are magnitudes higher than the Hf vs. $\mathrm{La_N}$ and $\mathrm{Ce_N}$ fields of typical igneous zircons (Hoskin and Schaltegger 2003). Similarly, zircon core data scatter magnitudes higher than the Hf vs. U field from Hoskin and Schaltegger (2003), whereas rim and outermost rim data partially plot in the igneous zircon field (Fig. 7c). Most core data of Hf vs. U/Th scatter at U/Th ≈ 0.04–0.3, whereas rim and outermost rim data scatter at a broad range of U/Th ≈ 0.02–2.0 in the rim and U/Th ≈ 0.02–1.0 in the outermost rim (Fig. 7d).

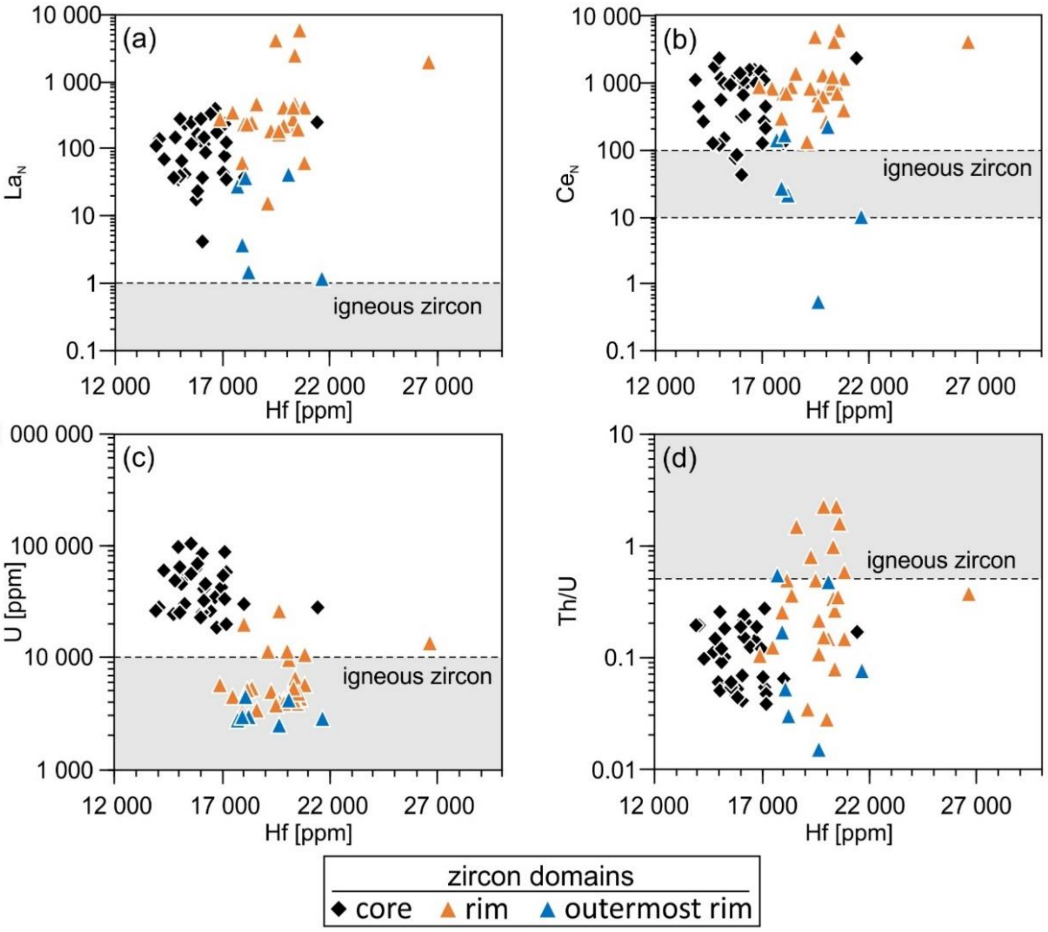

Fig. 7. Constraints on the provenance of the investigated zircon based on trace element data. Fields of igneous zircon after Hoskin and Schaltegger (2003). Modified from Tramm et al. (2021).

3.4.3. TEM structural observations and analyses of Xenotime

Nanoscale investigation of xenotime and zircon were conducted with TEM in a total of 11 FIB-foils cut from distinct textural domains (Fig. 8). Patchy zoned micro-domains of xenotime display a network of dislocations in nanoscale and microporosity (Fig. 9a), whereas the smooth contrast in HAADF image of xenotime of FIB-foil F02 demonstrates high crystallinity of xenotime (Fig. 9b). The dislocations are occasionally pinned by nanopores (Fig. 9d, e). Several micropores and nanopores are filled with secondary Fe-silicates, solid solution of coffinite-thorite or Th-bearing uraninite (Fig. 9c, l). The U-rich phases contain C, which suggests partial substitution of blatonite

[$(UO_2)CO_3 \times H_2O$] (Fig. 9r, s). The material that surrounds the pore filled with coffinite-thorite solid solution and uraninite is composed of (i) an inner wall, which contains a matrix of poorly crystalline Y-phosphate (potentially radiation-damaged xenotime) and small nanocrystals of xenotime, and (ii) an outer diffuse rim (ca. 50 nm thick) of radiation-damaged primary xenotime (Fig. 9m–p). This demonstrates the potential of locally high degree of radiation damage in xenotime due to a high dosage of α-radiation. In rare cases, nanopores contain a hexagonal Pb-phosphate [$Pb_3(PO_4)_2$] that was identified based on crystallographic parameters (Fig. 9h–k, q).

3.4.4. TEM structural observations and analyses of the zircon core

The patchy-zoned zircon core can be subdivided into three sub-domains: (i) bright patchy domains (FIB-foil F05), (ii) dark patchy domains (FIB-foil F06) and (iii) domains that contain clusters of microinclusions (henceforth inclusion-rich domain, FIB-foil F07; Fig. 8). The bright patchy domains show submicron patchy zoning of bright and dark zircon patches at nanoscale in HAADF image (Fig. 10a). A region of coarser patchy zoning is divided by an array of micropores from a region of finer patchy zoning. The micropores are partially filled with nanoinclusions of Th- and U-rich oxides (most likely thorianite and uraninite) and embedded in a Ca- and F-rich phosphate (most probably fluorapatite) located at the wall of the pores.

A single grain of galena formed in a matrix of fluorapatite in a nanopore (Fig. 10b–f). The HREM images of the fluorapatite show an amorphous structure close to the galena inclusion, whereas its crystallinity increases with distance to the contact zone (Fig. 10f, g). Despite the rare abundance of galena inclusions in the investigated zircon, its presence displays significance for potential Pb mobilization and retention of unsupported Pb in zircon.

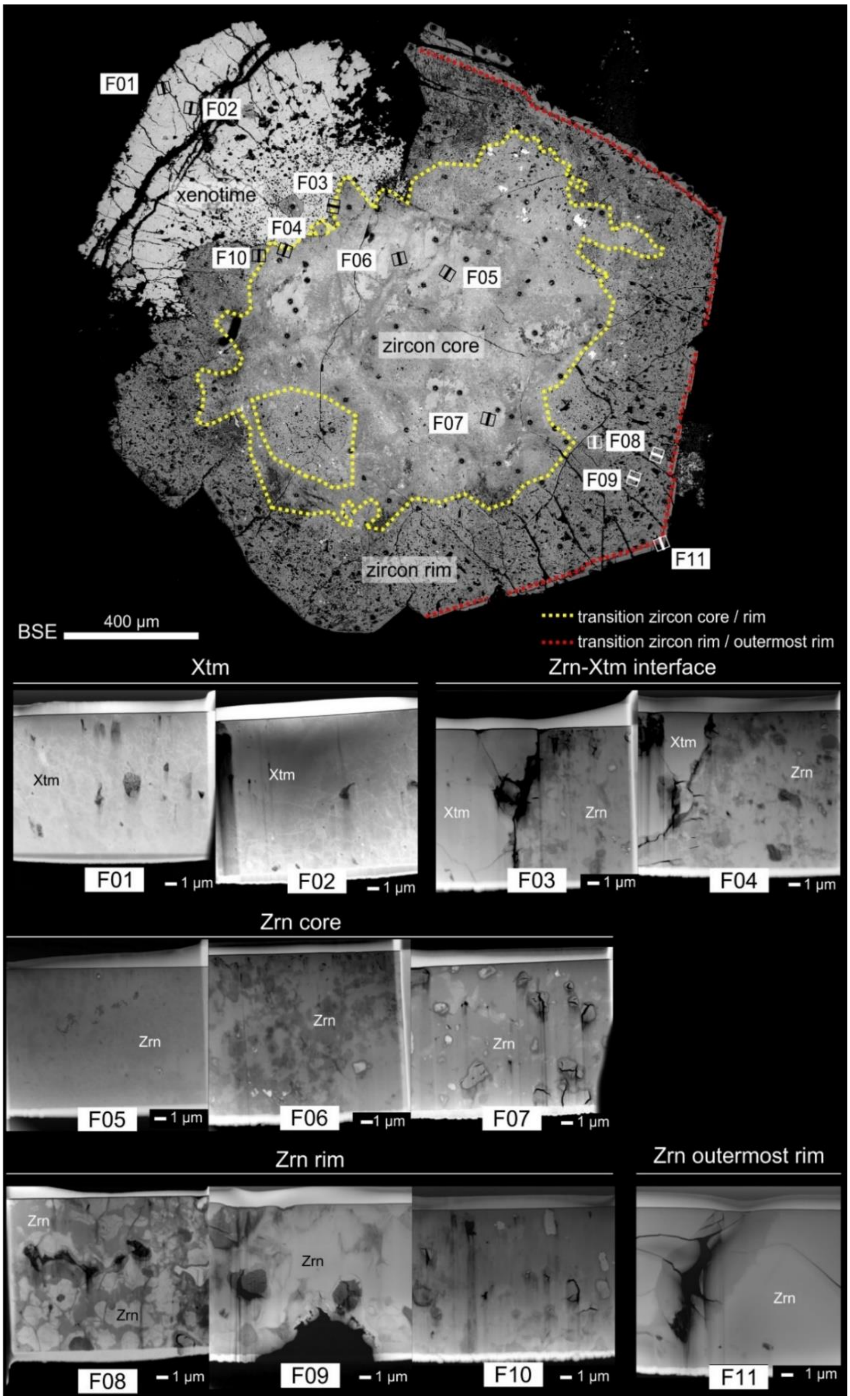

Fig. 8. Overview of FIB-foils cut from xenotime and zircon. Modified from Tramm et al. (2021).

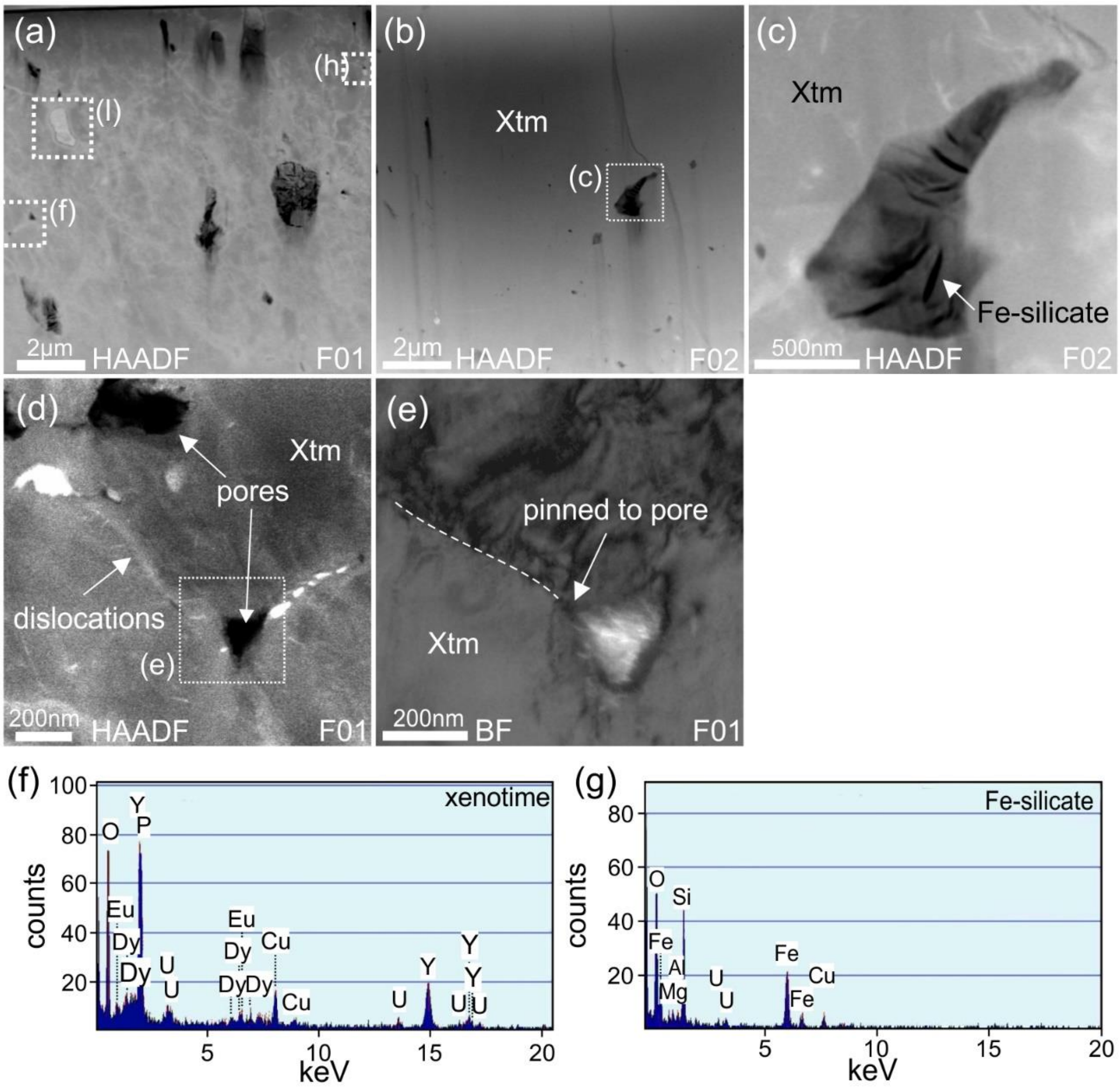

Fig. 9. TEM results for the xenotime (modified from Tramm et al. 2021). (a, b) Overview image of FIB-foils F01 and F02. (c) HAADF image demonstrating micropore filled with Fe-silicate. (d) Dislocation veins occasionally pinned to nanopores. (e) A shifted crystal lattice along dislocations (dotted line) resulting in a shift of diffraction contrast. (f, g) EDX spectra of xenotime and Fe-silicate. (h) Nanopore enclosing $Pb_3(PO_4)_2$. (i–k) BF, HREM and FFT images show unicrystallinity of $Pb_3(PO_4)_2$. (l) Inclusions of coffinite-thorite solid solution and uraninite in a nanopore. (m) The rim of the nanopore with nanocrystals of xenotime. (n) Xenotime nanocrystals (dashed line) in the poorly crystalline xenotime matrix. (o, p) HREM and FFT images of the primary xenotime with a highly damaged crystal structure surrounding the pore. (q–s) EDX spectra of $Pb_3(PO_4)_2$ with crystallographic parameters, coffinite-thorite solid solution and uraninite. Abbreviations: Cof-Thr – coffinite-thorite solid solution, Urn – uraninite, Xtm – xenotime.

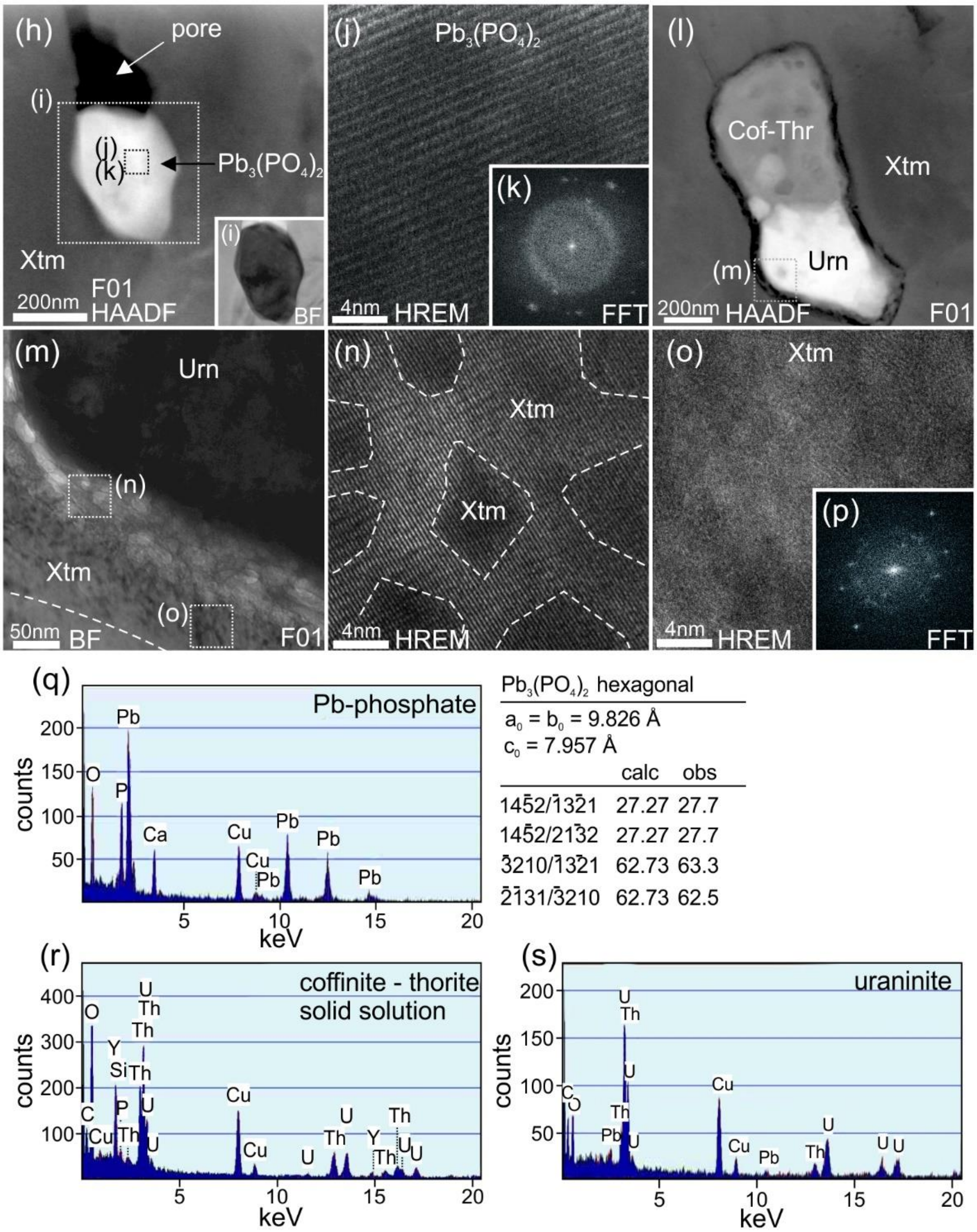

$Pb_3(PO_4)_2$ hexagonal

$a_0 = b_0 = 9.826$ Å

$c_0 = 7.957$ Å

	calc	obs
$14\bar{5}2/\bar{1}3\bar{2}1$	27.27	27.7
$14\bar{5}2/21\bar{3}2$	27.27	27.7
$\bar{3}210/\bar{1}3\bar{2}1$	62.73	63.3
$\bar{2}\bar{1}31/\bar{3}210$	62.73	62.5

Fig. 9. (continued)

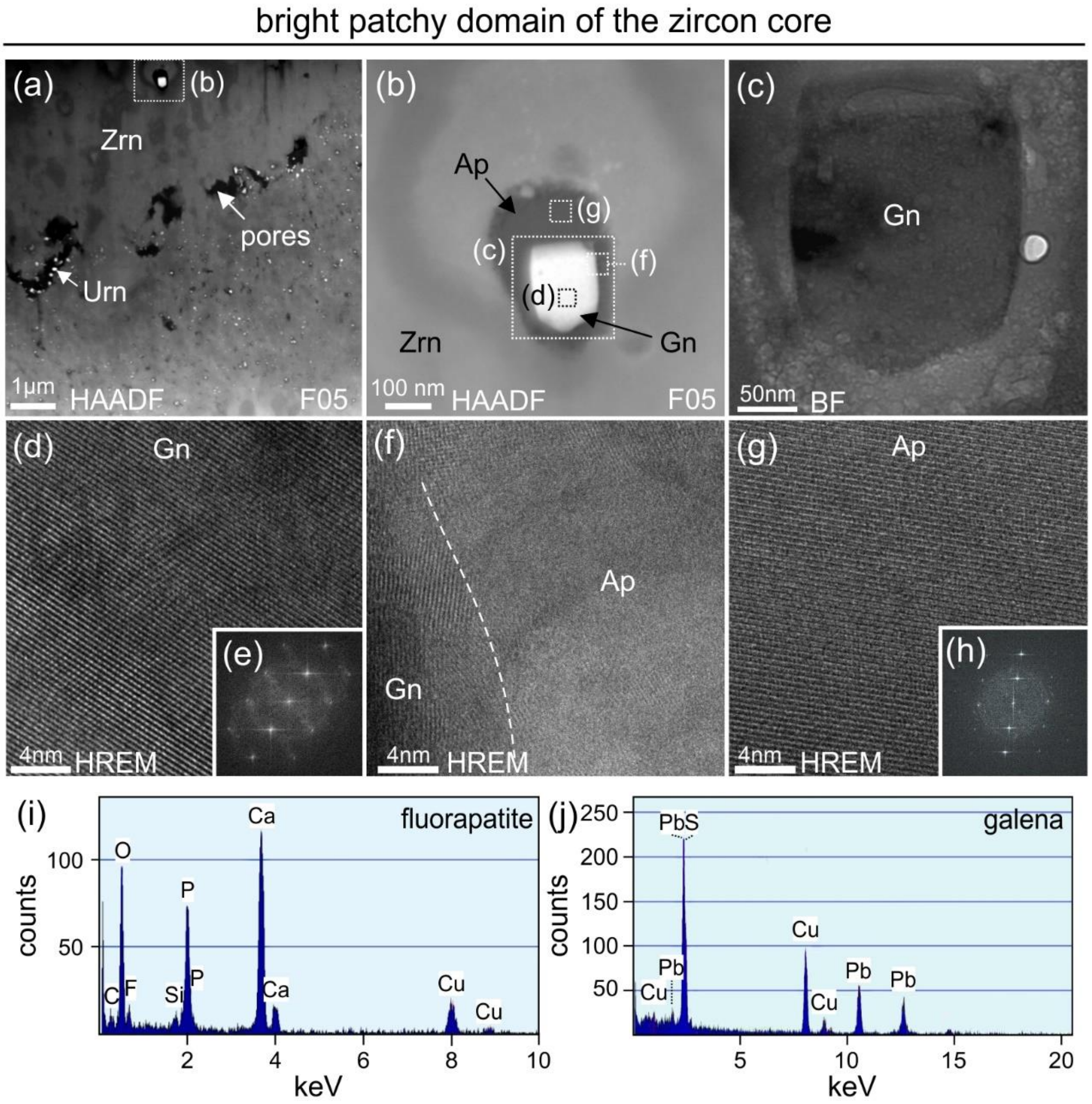

Fig. 10. TEM results for the metamict core of the zircon, which consists of three domains (modified from Tramm et al. 2021). The bright patchy domain: (a) overview of the FIB-foil revealing two areas of patchy zoning divided by a group of micropores. (b–e) Inclusion of galena surrounded by secondary fluorapatite. (f) HREM image of the transition between galena and amorphous fluorapatite. (g) HREM and (h) FFT image of the crystalline fluorapatite ca. 10 nm from the transition with the galena inclusion. (i–j) EDX spectra of fluorapatite and galena inclusions.

The dark patchy domains in the zircon core are dominated by coarser patchy zoning compared to patchy zoning of the bright domains (Figs. 10a, 11a). In both domains, the dark patches of zircon contain higher U and Th concentrations compared to bright patches, which is indicated by better defined peaks of U and Th in EDX spectra of the dark patches compared to bright patches (Fig. 11h, i). The brightness of HAADF images is controlled by concentration of elements with high atomic numbers, the density of material and crystallinity, thus, it may be expected that higher contents of U and Th create a brighter image in HAADF. However, due to their radioactivity they also destroy the crystal integrity of zircon by radiation damage, which results in lower density of material. Therefore, the bright nanopatches of zircon (in HAADF mode), which contain lower U and Th contents, retain their crystal integrity more and contain a higher density than darker patches. This conclusion is confirmed by BF imaging, which displays a reversed contrast compared to HAADF, because bright cloudy areas indicate a lower degree of crystallinity and a lower density of material, whereas darker contrast results from more electron adsorption due to a higher crystallinity and/or density of material (Fig. 11b). Furthermore, the bright and dark patches (in HAADF) show diffuse diffraction rings indicating different degrees of a metamict state (Fig. 11c, d).

Inclusions present in the dark domains of the zircon core are predominantly composed of Th- and U-oxides, i.e. most probably thorianite and uraninite, however, their small size and interfering signals from the surrounding material prevented unambiguous identification. A “large” uraninite inclusion (ca. 500 × 900 nm) is surrounded by a dark rim of amorphous zircon (Fig. 11e, f). The BF image of the uraninite indicates a single crystal (Fig. 11f), however, broad diffuse scattering in the diffraction patterns indicates presence of an amorphous phase (Fig. 11g). This contradiction may be caused by high density of U atoms hindering electron transparency. The uraninite contains C, which suggests substitution of blatonite (Fig. 11j).

The inclusion-rich domain contains a higher abundance of micro- and nanopores compared to other domains of the zircon core (Fig. 12). The micropores are filled with U-rich zircon, which is interpreted as a secondary zircon (Zrn2) based on comparison with EDX spectra of the primary zircon (Figs. 11h, i, 12e). The inclusions of secondary zircon have a crystalline structure and are cut by veins of lesser crystalline coffinite (Fig. 12a, b). A dark rim of amorphous primary zircon is surrounding the inclusions. Nanopores are filled with clusters of small uraninite-flakes or uraninite-cubes, which are embedded in a coffinite matrix (Fig. 12c, d). Coffinite shows a minor C content in EDX spectrum, which suggests substitution of a blatonite component (Fig. 12f).

3.4.5. TEM structural observations and analyses of the zircon rim

The zircon rim displays extensive microporosity with a broad range of different phases that form inclusions (FIB-foils F08–F10; Fig. 8). Compared to the core, the rim has irregular patchy zoning with several micron-sized patches, which show sharp boundaries in HAADF imaging (Fig. 13a). Secondary phases include Fe-silicates accompanied by monazite to Pb-bearing Fe-oxides (Fig. 13b–d), and uraninite and uraninite-thorianite solid solution accompanied by xenotime (Fig. 13i, o). Inclusions of Fe-rich phases either display a lamellar texture of Fe-silicates or folded plates of Fe-oxides embedded in a matrix of Fe-silicate (Fig. 13b–d). In one nanopore containing Fe-silicate and monazite, a vein of mottled zircon is connected to the pore (dashed line in Fig. 13b). In the nanopore which contain Fe-oxides and Fe-silicate, cloudy patches of zircon are disconnected from the pore-wall (Fig. 13c).

Aside of Fe-rich phases, uraninite represents another dominant phase that formed inclusions in micropores. An example is shown in a micropore filled with polycrystalline uraninite surrounded by an irregular rim of amorphous zircon (Fig. 13i, j). The crystallinity of zircon increases with distance to the uraninite inclusion as shown in HREM images and sharper diffraction patterns with lower diffuse scattering intensity in the crystalline material (Fig. 13k–n). The outermost rim of zircon is homogeneous in nanoscale (FIB-foil F11; Fig. 8).

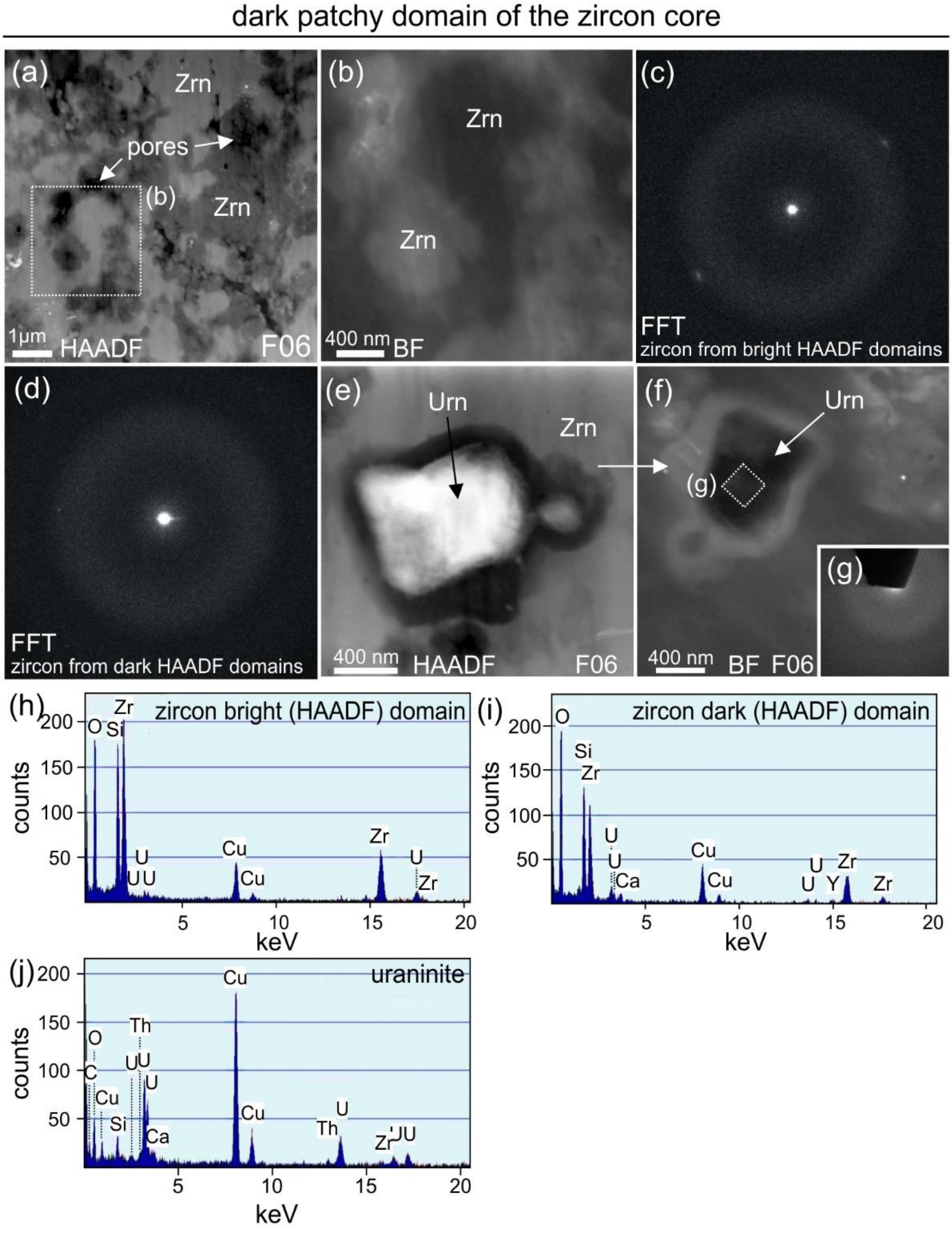

Fig. 11. The dark patchy domain (modified from Tramm et al. 2021): (a) Overview of a coarse patchy zoning displaying bright and dark domains. (b) BF image showing differences in crystallinity and density of the patchy zones; here, the contrast is inverted compared with HAADF. (c, d) Diffraction patterns of the patchy domains of zircon. (e) Nanoinclusion of uraninite, which is common in the dark patchy domain. (f) BF image of the uraninite that indicates unicrystallinity, yet (g) diffuse diffraction rings indicate a low degree of crystallinity. (h–j) EDX spectra of the bright and dark zircon patches, and the uraninite inclusion. Abbreviations: Urn – uraninite; Zrn – zircon.

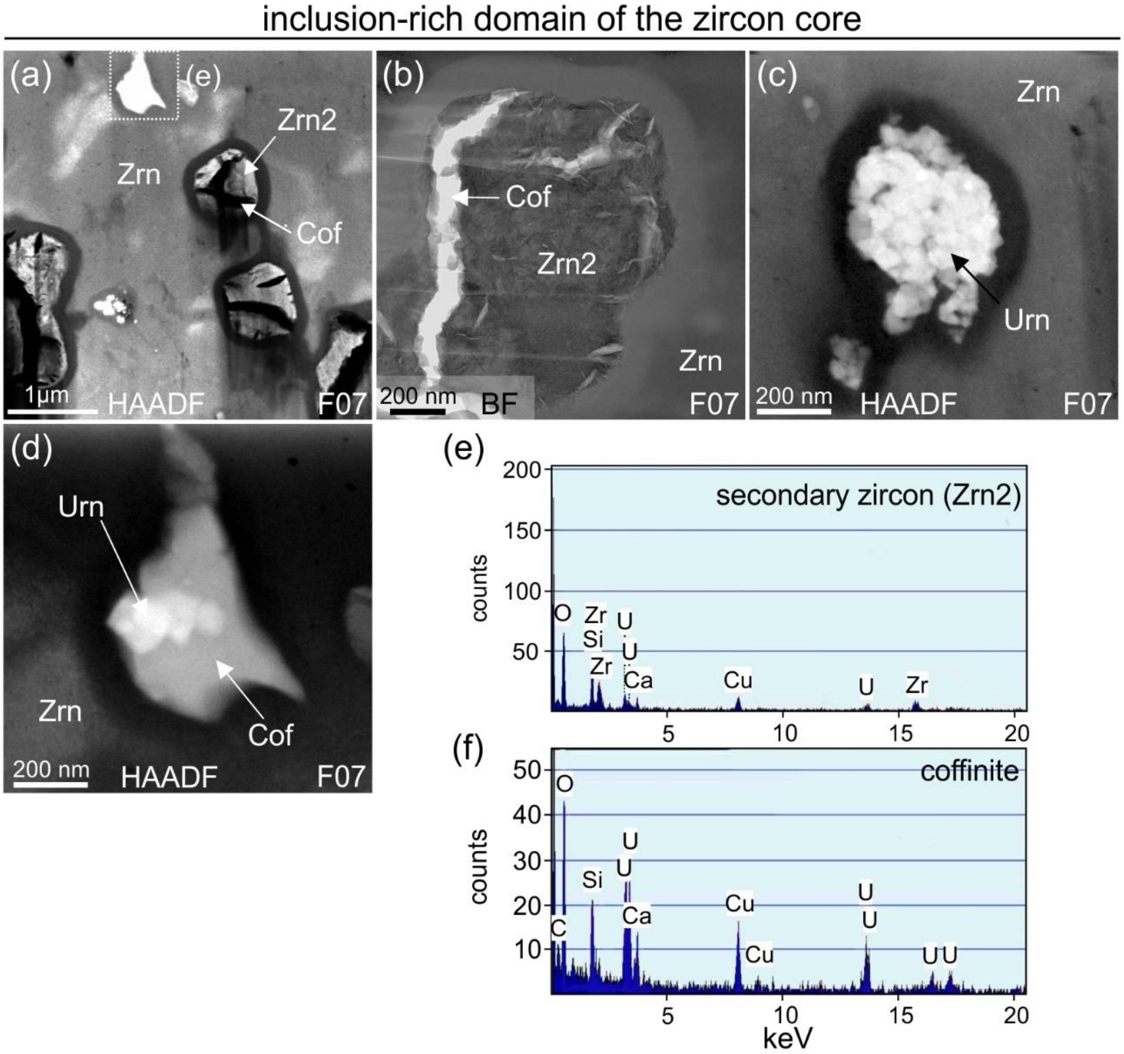

Fig. 12. The inclusion-rich domain (modified from Tramm et al. 2021): (a) HAADF overview of the inclusion-rich domain. (b) BF image U-rich zircon inclusion (Zrn2) cut by veins of coffinite. (c) Aggregate of flakes of Pb-bearing uraninite. (d) Cubic inclusions of uraninite embedded in coffinite. (e, f) EDX spectra of secondary zircon (Zrn2) and coffinite. Abbreviations: Cof – coffinite, Gn – galena, Urn – uraninite, Zrn – zircon.

3.4.6. TEM structural observations and analyses of the zircon-xenotime interface region

The contact between the crystalline xenotime and the metamict, patchy zoned zircon is a sharp and distinct phase boundary (Figs. 14, 15). Microporosity is present in xenotime, but significantly more abundant in zircon. In the region of the contact between xenotime and zircon, small spheres of uraninite form nanoinclusions in xenotime (Fig. 14c), whereas cubic crystals embedded in a matrix of Y-rich Ca-phosphate (possibly Y-bearing fluorapatite) are present in the zircon (Fig. 14d). The sharp boundary is reflected by HAADF (Fig. 14e) and BF imaging (Fig. 14f), which also reveals a fine rim (ca. 100 nm) of a matrix of radiation-damaged xenotime. An EDX-line scan over 400 nm across the phase boundary of xenotime and zircon reveals a distinct and sharp compositional transition of only few nanometres directly at the phase boundary (Fig. 14e, g–l). The transition from xenotime to zircon is represented by a sharp decrease of Y and a significant increase of Si, Zr, Ca and Th (Fig. 14g, i–l).

The FIB-foil F04 (Fig. 8) cut from the zircon-xenotime transition shows a micropore in the primary xenotime, a few microns from the zircon-xenotime phase boundary (Fig. 15). At the wall of the pore, a sphere of fibrous Fe-oxides surrounded by oscillatory zoned Pb-bearing Fe-silicates embedded in secondary zircon. The fibrous core of the inclusion bears nanocrystals of Pb-bearing Fe-oxides embedded in a matrix of Fe-silicates (Fig. 15b, c). A line-measurement from the xenotime into the aggregate shows a distinct and sharp compositional transition at the phase boundaries corresponding to typical composition of Y-rich xenotime, Zr-, Si- and Th-rich zircon and Fe-oxides (Fig. 15c, f–m).

To summarize, all investigated domains of xenotime and zircon display distinct characteristics in regards to textures in micro- and nanoscale and presence of nanoinclusions. A summary presenting textural features and secondary phases in zircon and xenotime is given in Table 1.

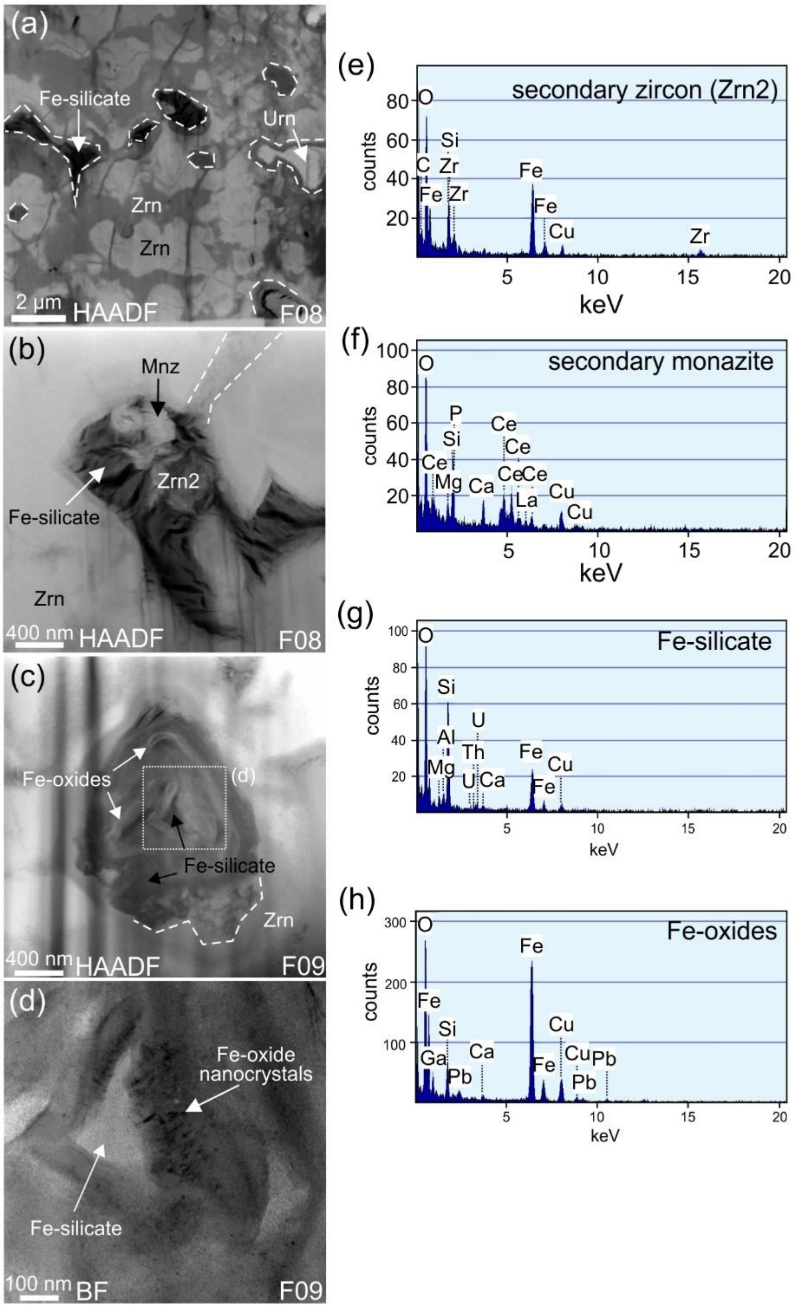

Fig. 13. TEM results from the rim of the zircon (modified from Tramm et al. 2021). (a) HAADF overview shows patchy zoned zircon with high microporosity filled by Fe-silicate or uraninite. (b) Micropore enclosing Fe-silicate and monazite attached to a channel of patchy zoned zircon (dashed lines). (c) Fe-oxides formed folded layers in a nanopore embedded in Fe-silicate. (d) Nanocrystals of Fe-oxides in the core of folded material. (e–h) EDX spectra of secondary zircon (Zrn2), monazite, Fe-oxide and Fe-silicate. (i) An uraninite inclusion in a micropore. (j) Amorphous zircon surrounding the nanopore with the uraninite. (k–n) HREM images of zircon show increasing crystallinity subsequently with increasing distance from the uraninite inclusion. (o) A rare case of a micropore containing inclusions of xenotime and uraninite-thorianite solid solution from FIB-foil F10 located at transition between core and rim of zircon in close proximity to the intergrown xenotime. Galena also formed in a nanopore close to the xenotime inclusion. (p) HREM image of the uraninite-thorite solid solution oxide reveals clouds of shifted crystal orientation indicating polycrystallinity. Abbreviations: Gn – galena, Mnz – monazite, Urn – uraninite, Urn-Tho – uraninite-thorianite solid solution, Xtm – xenotime, Zrn – zircon.

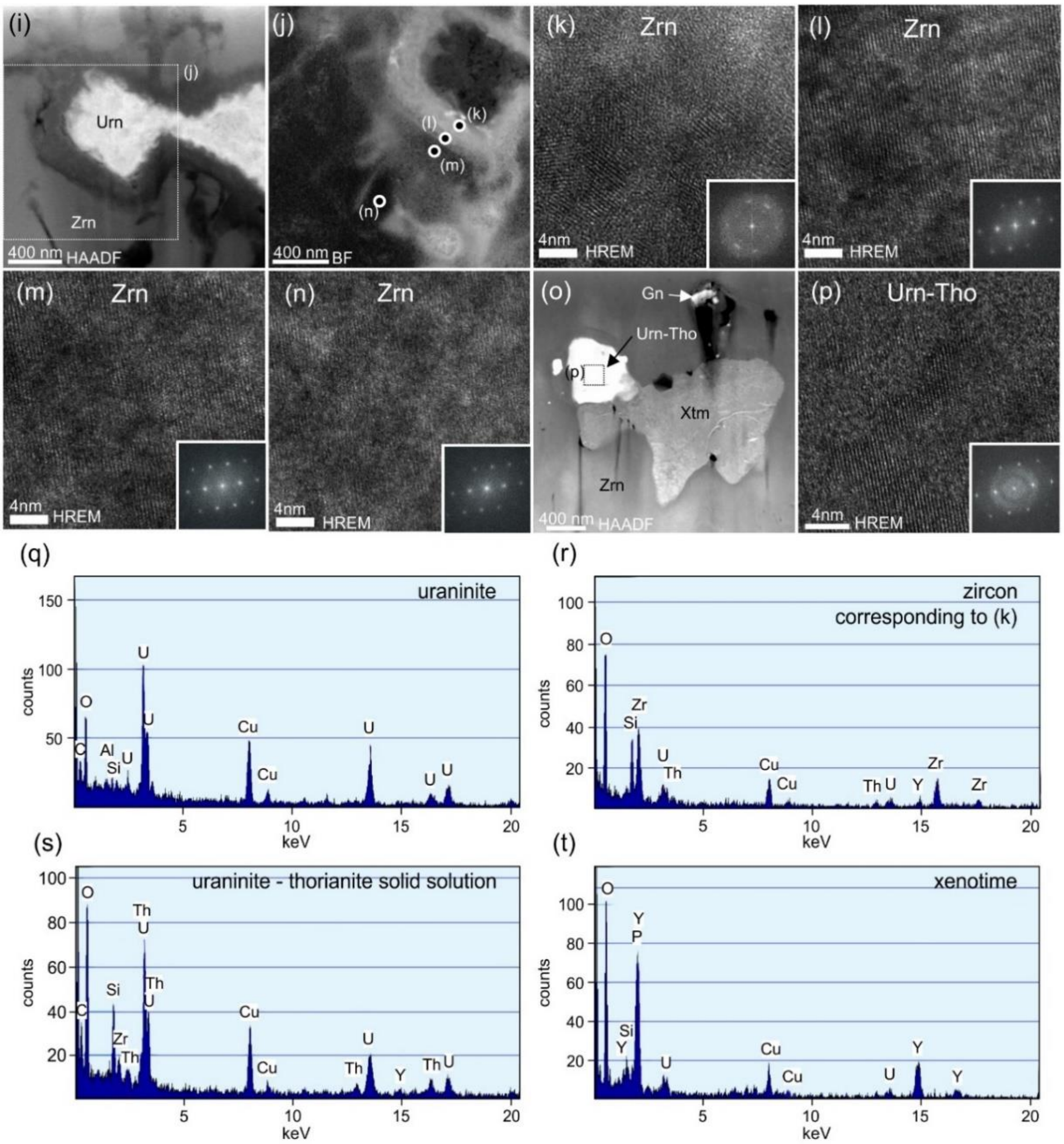

Fig. 13. (continued)

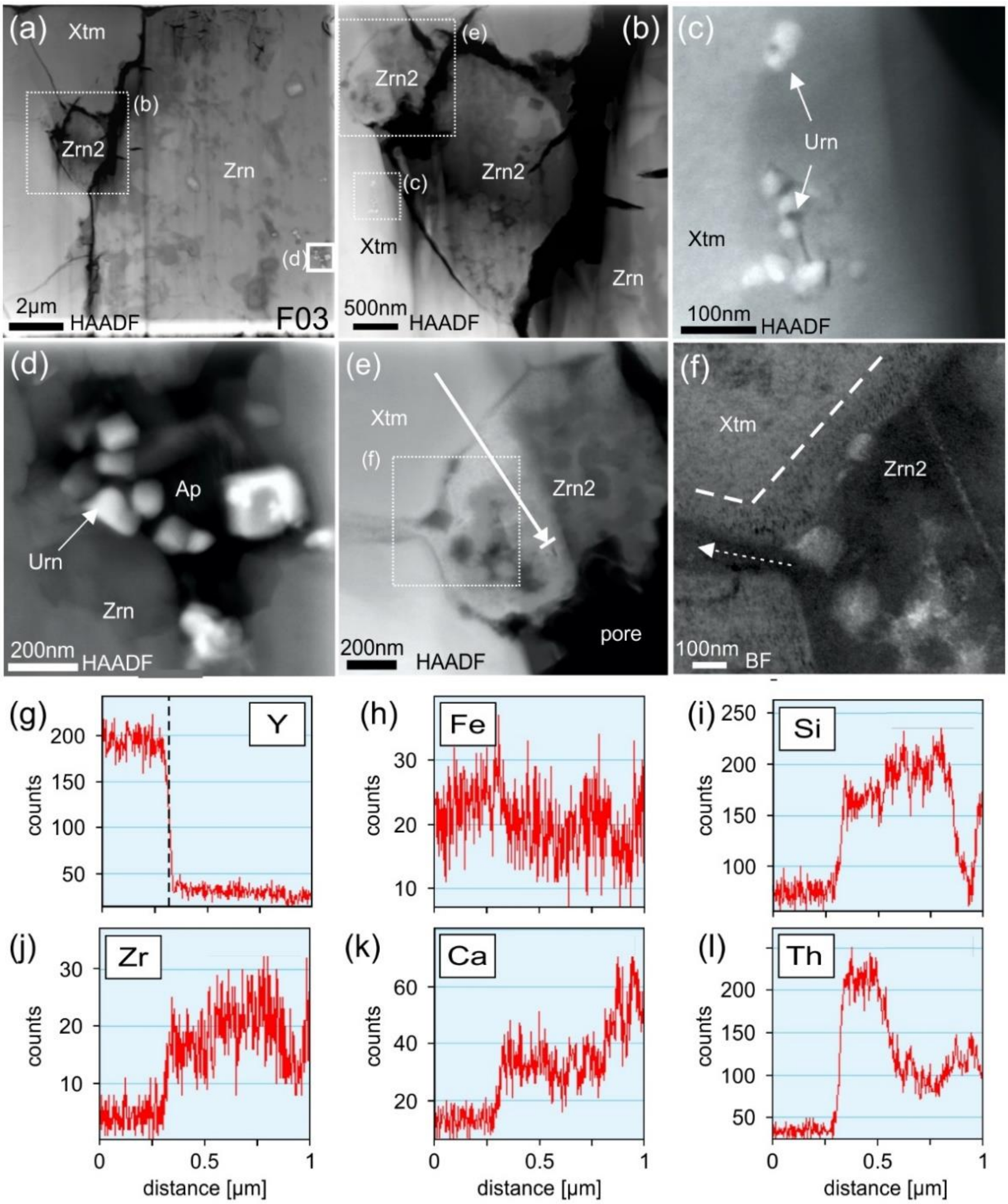

Fig. 14. TEM results for the zircon-xenotime interface (modified from Tramm et al. 2021). (a) HAADF overview of the sharp phase-boundary between xenotime and patchy zoned zircon (F03). (b) A domain located at the phase boundary with alteration pits in the primary xenotime, partially filled with secondary zircon (Zrn2). (c) Nanocrystals of uraninite in xenotime close to the phase-boundary and (d) nanocrystals of uraninite embedded in fluorapatite in zircon. (e) The alteration pit shows the reaction front with secondary zircon adjacent to primary xenotime. The white arrow represents the EDX line measurement in (g–l). (f) BF image showing a ca. 100 nm thick rim of altered xenotime containing fine nanocrystals (dark areas). The inclusions in the secondary zircon (Zrn2) form a pathway penetrating into the primary xenotime (white dotted arrow).

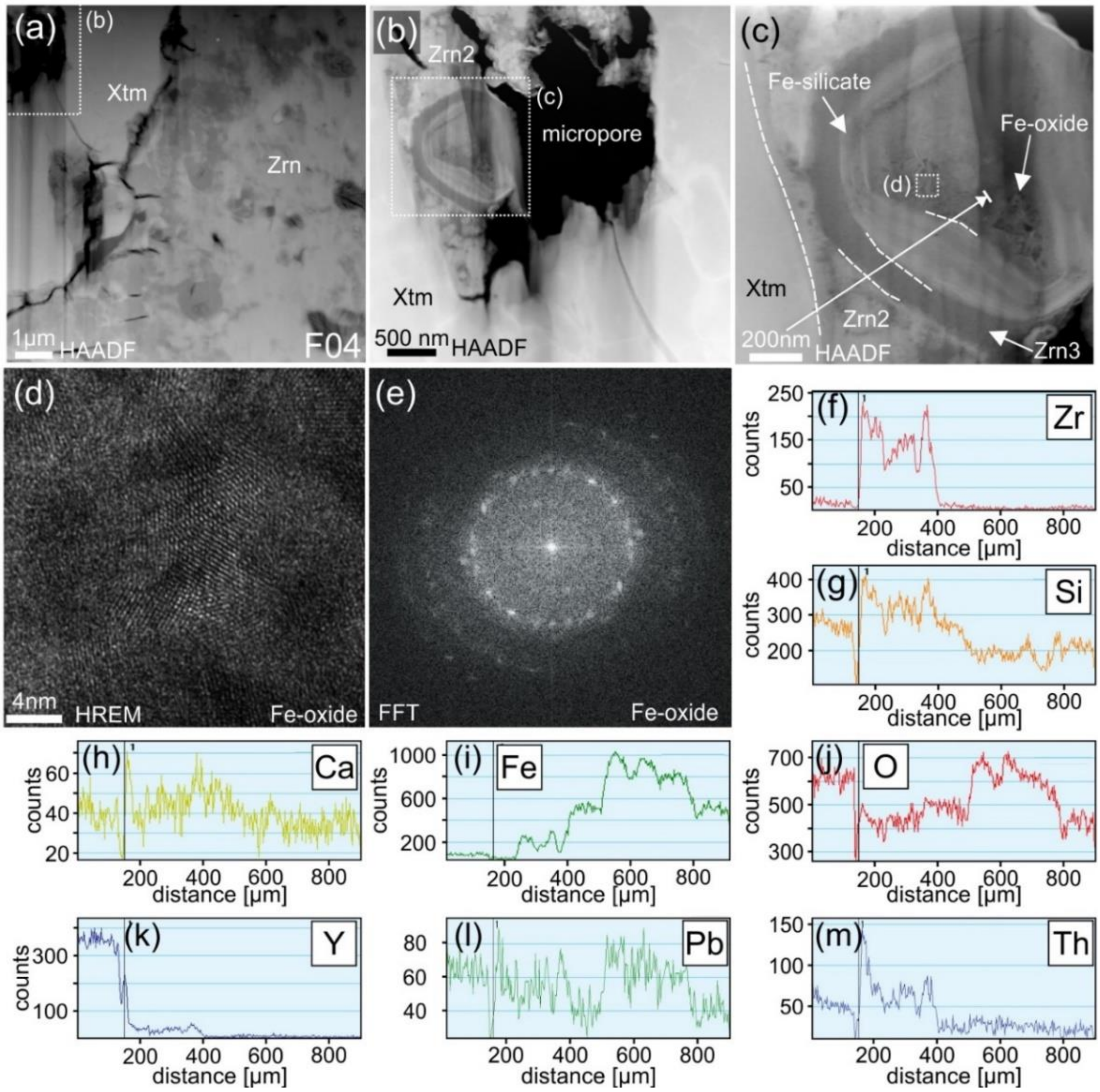

Fig. 15. TEM results for the zircon-xenotime interface (modified from Tramm et al. 2021). (a) Overview of the zircon-xenotime phase boundary (F04) with a micropore in xenotime close to the phase-boundary. (b) HAADF image showing the micropore enclosing secondary zircon (Zrn2) and an aggregate containing a fibrous core of Fe-oxides surrounded by an oscillatory zoned rim with varying contents of a Pb-bearing Fe-silicate. (c) The aggregate is embedded in secondary zircon (Zrn3) forming a ca. 70 nm thick amorphous rim. The white arrow represents the EDX line measurement presented in (f–m). (d) HREM image of the fibrous Fe-oxide revealing randomly oriented islands of crystal patterns indicating polycrystallinity. (e) The diffraction pattern shows multiple diffraction centres typical for a polycrystalline mineral surface.

Table 1. Summary of micro- and nano-textures observed with EPMA and TEM in the investigated zircon and xenotime.

Phase / Domain	**Texture**		**Porosity**		**Secondary phases**		
	micro texture	nano-texture	micro-pores	nano-pores	inclusions	major	minor
xenotime							
	patchy zoning	homogeneous + fine network of dislocations	x		Fe-silicates	x	
				x	uraninite	x	
				x	coffinite-thorite	x	
				x	$Pb_3(PO_4)_2$		x
zircon core							
bright patchy domain	patchy zoning	patchy zoning dominated by bright domains	x	x	fluorapatite		x
				x	galena		x
				x			
				x			
dark patchy domain		patchy zoning dominated by dark domains		x	uraninite	x	
Inclusion-rich domain		patchy zoning + high porosity	x		secondary zircon	x	
			x		coffinite (as veins)	x	
				x	uraninite		x
				x	coffinite (grains)		x
zircon rim							
	patchy zoning	patchy zoning + high porosity	x		Fe-silicates	x	
			x		secondary zircon	x	
			x		uraninite	x	
			x		Fe-oxides		x
				x	xenotime		x
				x	uraninite-thorianite		x
				x	galena		x
zircon crystalline rim							
	homogeneous crystalline	homogeneous crystalline					
zircon-xenotime interface							
on the xenotime side	patchy zoning	homogeneous + dissolution pits at phase boundary	x		secondary zircon	one inclusion	
			x		(Fe, Pb)-silicates		
			x		Fe-oxides		
				x	uraninite		x
on the zircon side	patchy zoning	patchy zoning		x	uraninite		x
				x	fluorapatite		x

3.5. Discussion

3.5.1. LA-ICPMS trace element characteristics of xenotime and zircon

The small variations in chondrite-normalized HREE patterns indicate that xenotime remained stable during alterations, which occurred during formation of the Late Devonian pegmatite, with respect to the major element composition (Fig. 4a). Variations of nonformula and trace elements can provide information on mineral composition during formation, fluid-mediated alteration and the fluid composition. Substitution mechanisms in xenotime include components of zircon due to the isostructural nature of xenotime and zircon (Spear and Pyle 2002). This is partially reflected by a weak correlation of Zr and Si (Fig. 4f). However, the Si content in xenotime is also related to substitutions of coffinite and thorite components (Förster 1998, 2006; Spear and Pyle 2002), and may also be reflected in part by the presence of Fe-silicate submicron inclusions (Figs. 4e, 9b, c). Correlation of Fe vs. Al can be related to (i) the transport of Al into the xenotime structure via fluid-supported diffusion followed by homogenization or (ii) incorporation during the formation of the xenotime (Fig. 4g). A dominant group of inclusions includes Fe-rich phases, thus, Fe may serve as a key indicator for the presence of fluids, because Fe is generally not present in xenotime. Furthermore, pegmatites form in an environment which is strongly influenced by hydrous melts containing significant amounts of fluids that enable temperature-related diffusion (Simmons and Webber 2008; London and Morgan 2012; London 2021).

In case of zircon, several substitution mechanisms have to be taken into account considering the exchange of Zr. Simple substitution of tetravalent elements (e.g. U^{4+}, Th^{4+}, Ti^{4+} and Sn^{4+}) can directly substitute Zr^{4+} (Hoskin and Schaltegger 2003). Here, the exceptionally high content of U (up to ca. 10 wt.%) in the investigated zircon reflects the most dominant substituent for Zr^{4+}. A common mechanism in zircon involves substitution of the xenotime component $(Y, REE)^{3+} + P^{5+} = Zr^{4+} + Si^{4+}$ (Speer 1980). However, due to lack of clear correlation of (HREE + Y) and P data, the xenotime substitution has been obstructed by other P occupations (Fig. 6b). This is confirmed by the presence of fluorapatite inclusions (Fig. 10b). Partial substitution via coupled $Y^{3+} + (Nb, Ta)^{5+} = 2\ Zr^{4+}$ (Es'kova 1959) may be considered due to positive parallel trends of Y/(Nb + Ta) = 100 in the zircon core and Y/(Nb + Ta) = 10 in the zircon rim (Fig. 6c). In summary, presence of secondary inclusions can interfere with the interpretation of the true geochemical signatures of zircon and xenotime. Formation of micro- to nanoporosity and precipitation of secondary inclusions commonly result from fluid-mediated alteration processes, however, it cannot be excluded that some inclusions were incorporated into the xenotime or zircon prior to alteration during growth of their host mineral.

3.5.2. Alteration processes at a submicron scale

There are two well-described alteration mechanisms that can result in formation of complex textures in the primary mineral, its replacement by secondary minerals and formation of porosity, (i) diffusion-reaction and (ii) coupled dissolution-reprecipitation processes, which proceed under a broad range of temperature conditions (Geisler et al. 2002, 2003a, 2007; Putnis 2002, 2009; Putnis et al. 2005; Putnis and Putnis 2007; Hetherington et al. 2010; Nasdala et al. 2010; Putnis and Austrheim 2010, 2013; Soman et al. 2010; Harlov et al. 2011; Seydoux-Guillaume et al. 2012, 2015; Ruiz-Agudo et al. 2014; Budzyń et al. 2017, 2018, 2021, 2022, 2023a, b; Villa and Hanchar 2017; Zamyatin et al. 2017). The results of both alteration processes display similar features and characteristics in regards to formation of porosity and precipitation of secondary inclusions, however, their mechanisms differ significantly. The diffusion-reaction process is temperature-driven and mediated by a hydrous medium (most likely H^+), resulting in nanoporosity that enhances a fast exchange between the reaction-front and the fluid and supports gradual structural ordering in the primary mineral towards the reaction-front (Geisler et al. 2003a, c, 2004, 2007). These characteristics are reflected in a metamict zircon, which displays a gradual recovery of the damaged structure (Geisler et al. 2007). During diffusion-reaction processes incompatible elements enter the solution and may precipitate as phase inclusions (Geisler et al. 2007).

Fluid-mediated coupled dissolution-reprecipitation reactions, on the other hand, result in a replacement of the primary material by secondary phases in a solid-state (Putnis 2002, 2009; Putnis et al. 2005; Geisler et al. 2007; Putnis and Putnis 2007; Putnis and Austrheim 2010, 2013; Harlov et al. 2011; Seydoux-Guillaume et al. 2012; Ruiz-Agudo et al. 2014; Villa and Hanchar 2017; Budzyń et al. 2018, 2021, 2022, 2023a, b). A characteristic feature is a sharp compositional boundary between primary and secondary phases, which is the result of the dissolution of bonds and coupled formation of new bonds at the reaction-front progressively moving through the mineral (Putnis 2002, 2009; Geisler et al. 2007; Putnis and Austrheim 2013). Typical results of coupled dissolution-reprecipitation processes include nano- and microporosity due to the loss of volume of the altered mineral (Geisler et al. 2007; Putnis and Austrheim 2013). In the investigated xenotime, coupled dissolution-precipitation processes resulted in significant alteration. This is reflected by developed patchy zoning and formation of nano- and micropores filled with secondary inclusions, which include Fe-oxides, Fe-silicates, Pb-phosphate, uraninite and coffinite-thorite solid solution (Fig. 9). Xenotime remained crystalline, even though it underwent high dosage of α-radiation. This is related to imminent annealing of the damaged structure (Rafiuddin et al. 2020). The effect preventing amorphization of xenotime due to α-radiation may be similar to annealing of monazite (Seydoux-Guillaume et al. 2002, 2018; Nasdala et al. 2020). Indeed, computer simulations predict imminent reparation (0.82 ps) of damaged structures after occurrence of a decay event (Urusov et al. 2012). Because of its resistance towards structural damage from α-radiation, the strongly damaged crystal structure of xenotime close to uraninite and coffinite-thorite inclusions was unexpected (Fig. 9l–o). Local radiation damage of xenotime structure revealed by HREM and FFT images is probably related to the exceptional high dosage of α-radiation, which caused more damage to the structure than could be repaired by annealing (Fig. 9o, p).

The metamict zircon core has been affected by diffusion-reaction processes, which supported partial annealing of the crystal structure (cf. Budzyń et al. 2018). This is confirmed by HAADF imaging that shows a fine matrix of patchy zoning with bright and dark nanopatches, which may be the result of partial annealing induced by diffusion-reaction processes (Figs. 10, 11). The varying contrast of the nanopatches reflects variations in U and Th contents that are higher in dark patches, which results in a more damaged crystal structure and lower density of material. Zircon starts to anneal at temperatures as low as ca. 200 °C (Geisler et al. 2007; Nasdala et al. 2010). Thus, it is possible that hot fluids locally supported annealing, which gradually reconnected crystalline islands and repaired the primary zircon structure. During this process, elements mobilized by the fluid accumulated in the matrix of the metamict zircon to form secondary zircon, which is highly enriched in U. The patchy zoning of the zircon, present at micro- and nanoscale, is interpreted as the result of combined metamictization and annealing effects, which were predominantly supported by temperature-driven diffusion-reaction processes.

TEM observations demonstrate that the resolution of commonly used microanalytical techniques are not sufficient to determine the detailed characteristics of small patches in zircon, shown in BSE image with respect to their complex texture and composition (Figs. 3a, 8). The formation of nanoinclusions of galena embedded in fluorapatite suggest release of Pb from zircon, whereas F, S, Ca and P must have been transported into the system by a fluid (Fig. 10b). The presence of these inclusions is probably related to coupled dissolution-reprecipitation processes rather than diffusion-reaction alone.

Amorphous zircon, which is surrounding inclusions of uraninite in nanopores of the dark patchy domain, demonstrates enhanced radiation damage by the high dosage of α-radiation from the uraninite inclusions (Fig. 11e). The secondary aggregates of U-rich zircons, formed as bright microinclusions visible in BSE imaging in the inclusion-rich domain of the zircon core are accompanied by submicron scale coffinite or uraninite veins (Fig. 12a, b). The close relation of the secondary U-rich zircon and the coffinite and uraninite may reflect limited diffusion of these components when they were released from the altered zircon during alteration.

The zircon rim contains a network of micropores, which are predominantly filled by Fe-silicate or uraninite (Fig. 13b, i). The high abundance of secondary Fe-bearing phases indicate significant amounts of Fe brought into the system by fluids. Occasionally, micropores are adjacent to veins of cloudy textured zircon (Fig. 13b). The texture is probably related to variations in density, composition or crystallinity, and potentially represent a preferred pathway for fluids. These fluid-pathways may have enabled a rapid chemical exchange between zircon and the fluids typical for coupled dissolution-reprecipitation processes. Furthermore, in some nanopores containing Fe-oxides, cloudy zircon is dispatched from the wall of the pore, which may indicate the progressive dissolution of zircon during expansion of the pore (Fig. 13c).

Nanoscale observations of the outermost-rim of zircon reveal a homogeneous crystalline structure (FIB-foil 11, Fig. 8). The outermost rim is generally depleted in nonformula elements compared to the zircon core and porous rim that are enriched in nonformula elements (Figs. 5–7). Coupled dissolution-reprecipitation processes may result in partial to complete replacement of primary phases by secondary phases, which can remain the same structure but possess a different composition, particularly in case of nonformula and trace elements (Putnis 2002, 2009; Putnis et al. 2005; Putnis and Putnis 2007; Geisler et al. 2007; Putnis and Austrheim 2010, 2013; Ruiz-Agudo et al. 2014; Villa and Hanchar 2017). Furthermore, the zircon outermost rim follows the euhedral prismatic shape of the original zircon. These characteristics may suggest that the origin of the outermost rim is the result of partial replacement due to coupled dissolution-reprecipitation processes rather than overgrowth.

The zircon-xenotime phase boundary highlights related alteration processes. Alteration at the phase-transition is demonstrated by a concave pit at the border of xenotime, in which secondary zircon has formed (Figs. 14, 16). The secondary nature of the zircon is indicated by a diffuse matrix accompanied by nanopatches of dark contrasting crystal islands in BF imaging and the presence of small cubic flakes of unknown material (Fig. 14f). The secondary zircon displays a heterogeneous texture compared to the smooth patchy zoned texture of primary zircon in the core (Figs. 10a, 11a, 14e). Furthermore, the concave pit, in which the secondary zircon is embedded, shows a narrow pathway of zircon penetrating into the xenotime (Fig. 14e, f). This channel may have served as a fluid-pathway into the xenotime, which imply precipitation of secondary zircon after dissolution of primary xenotime.

A micropore in xenotime contains an aggregate of Fe-rich silicate and Fe-oxides, which are embedded in a matrix of secondary zircon (Fig. 15b, c). The zircon shows two distinct textures, (i) a matrix of cloudy textured zircon (Zrn2) and (ii) a smooth rim of zircon (Zrn3) with a dark contrast around the aggregate of Fe-rich silicates and Fe-oxide. Material of the micropore was partially lost during preparation of the FIB-foil. The Fe-rich material consists of a wall of alternating layers of Pb-bearing Fe-silicate and a core of Pb-bearing needles of Fe-oxides (Fig. 15c). The core of the aggregate probably formed due to precipitation of Pb-bearing Fe-oxide, which was later enclosed by layered Pb-bearing Fe-silicate. The sharp transition from Fe-oxides to layered Fe-silicates indicate a change in fluid composition.

3.5.3. Constraints on the magmatic or hydrothermal origin of zircon in pegmatite

Formation of pegmatites is related to complex processes involving hydrous melts, for which several theories have been formulated but no unified consensus has yet been reached (e.g. Jahns and Burnhan 1963; London and Morgan 2012; Thomas and Davidson 2013, 2015; London 2014, 2015, 2021). The recent models suggest granitic melts with typical fluid content as a source of pegmatites. These melts enrich during refining processes with a flux layer enriched in fluids which (i) float buoyantly on the melt or (ii) in a network of diffusion emphasizing elements, such as cations of rare alkalis, B, H, K and REE, or F and P (Simmons and Webber 2008; London and Morgan 2012; London 2021). Because of the high contents of fluids during pegmatite formation, distinct geochemical characteristics between typical igneous or hydrothermal zircons may be not present in zircons formed in pegmatites and rather reflect a unique geochemical fingerprint.

Geochemical characteristics of zircon can provide information regarding its igneous or hydrothermal origin and geological setting under which it has formed. The element distribution of Y vs. U/Yb and Hf vs. U/Yb are commonly used to differentiate between continental and oceanic provenances (Grimes et al. 2007, 2015; El-Bialy and Ali

2013). Data of the investigated zircon fall into the continental field, which is in agreement with the formation of pegmatites from granitic melts (Fig. 16a, b). Differentiation of magmatic and hydrothermal zircon, or its alteration, may provide useful information to decipher the complex history of the zircon in this study (Hoskin and Schaltegger 2003; El-Bialy and Ali 2013; Bell et al. 2019). In igneous systems, Hf is an important indicator for magmatic evolution of zircons (Hoskin and Schaltegger 2003; Claiborne et al. 2006). This is due to formation of solid solutions of $HfSiO_4$ and $ZrSiO_4$ related to the close cation radii of Hf^{4+} = 0.83 Å and Zr^{4+} = 0.84 Å (Shannon 1976). The investigated zircon shows overabundance of normalized La (La_N) and Ce (Ce_N) in relation to Hf contents compared to typical magmatic zircons (Fig. 7a, b). The exceptionally high contents of U (up to ca. 10 wt.%) interfere with application of the Th/U ratio, however, zircon rim data plot partially into the magmatic fields (Fig. 7c, d). On the other hand, fields of zircon origin suggest a geochemical fingerprint closer to hydrothermal origin based on element relations La vs. $(Sm/La)_N$ and $(Sm/La)_N$ vs. Ce /Ce*, whereas the U vs. Ca plot implies alteration of the investigated zircon (Fig. 16c–e). Furthermore, the relation of La_N and Pr_N indicate hydrothermal zircon, thus, the commonly used geochemical indices rather imply a hydrothermal origin of the investigated zircon (Fig. 16f).

In more recent studies a different approach was proposed to differentiate between magmatic and hydrothermal zircons (Bell et al. 2016, 2019). The light rare earth element index (LREE-I = Dy/Nd + Dy/Sm) was used to classify magmatic (LREE-I > 60) or hydrothermal / altered (LREE-I < 10) zircons (Bell et al. 2016). Using the LREE-I shows that only a fraction of data from the zircon core falls into the field of magmatic zircon (Fig. 17). Indeed, combined BSE and TEM observations reveal alteration of the zircon core in micro- and nanoscale (Figs. 3a, 8, 10, 11). However, the geochemical distribution of the core data follows a consistent trend, which may suggest igneous origin followed by alteration.

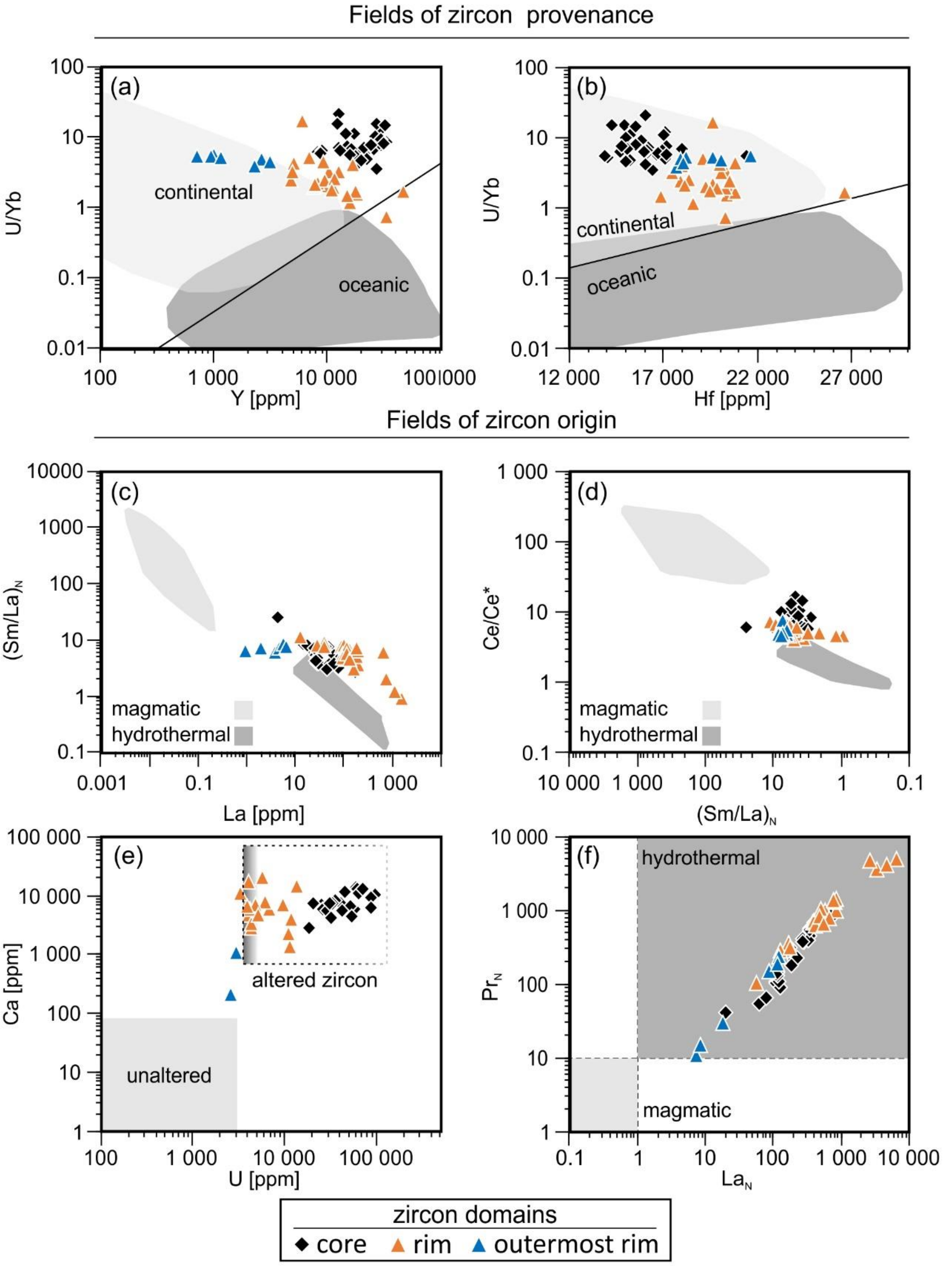

Fig. 16. Geochemical data of the zircon distributed in (a, b) discrimination fields of provenance (Grimes et al. 2007). (c, d, f) Distinction into zircons of magmatic or hydrothermal origin compared with zircons from the Boggy Plain Zoned Pluton (Hoskin 2005). (e) Discrimination of magmatic and altered zircons (after Bouvier et al. 2012). Modified from Tramm et al. (2021).

The zircon rim data scatter mostly below LREE-I = 10 and suggest extensive alteration (Fig. 17). Overall, the geochemical data of the zircon core and rim show two distinct trends and indicate different alteration processes, which are consistent with TEM observations. Thus, the zircon core was altered predominantly via the diffusion-reaction processes, whereas coupled dissolution-reprecipitation processes dominated in the alteration of the rim. The LREE-I demonstrated not only its usability to recognize origin of zircon, but also bears the potential to distinguish between different alteration mechanisms, if combined with textural observations of EPMA and TEM. The combined conclusions further emphasise how different alteration processes possess the capability to partially or completely overwrite the original geochemical fingerprint of the primary zircon.

3.5.4. Element transport and composition of the fluids in the zircon-xenotime intergrowth

The composition of the reactive fluid is the dominant factor that controls stability of phases penetrated by fluids, including (i) formation of porosity when primary material is dissolved, (ii) precipitation of secondary inclusions when element concentration reach saturation in solution and (iii) formation of secondary phases with the same structure as the original phase, but different composition (e.g. dissolution of U, Th, Pb-rich primary zircon coupled with precipitation of secondary U, Th, Pb-poor zircon).

The following conclusions about the fluid-mediated transport of elements between the xenotime, the zircon and the environment can be drawn from the comprehensive information provided by the discussed geochemistry of xenotime and zircon, and TEM observations of secondary phases and inclusions in the pores (Fig. 18):

(i) The metamict core of zircon underwent only minor element transport mediated by a hydrous fluid introducing Ca and Na. Porosity was generally limited to nanoscale (Figs. 10a, 11a), which served as traps for P, Pb, U and Th, as a result of diffusion-reaction processes. Local interconnected microporosity in inclusion-rich domains of the zircon core may indicate coupled dissolution-reprecipitation processes, which served as fluid-pathways further penetrating the zircon core. The zircon core may have incorporated Fe during formation, which is reflected in elevated Fe contents. However, despite no secondary Fe-rich phases are documented in the core, a fluid-mediated supply of Fe to the core cannot be excluded.

(ii) The zircon rim was penetrated by Ca- and Fe-bearing fluids, which resulted in microporosity formed due to coupled dissolution-reprecipitation reactions. Concentration of Fe is more than one magnitude higher in the zircon rim compared to the elevated contents in the core (Fig. 17d). Thus, most of the Fe was supplied by the fluid and captured in pores of the rim.

(iii) The zircon-xenotime phase boundary enabled major element transport via fluids, which was effectively supported by coupled dissolution-reprecipitation processes. This is reflected in formation of most exotic inclusions (e.g. Fe-silicate) and formation of secondary zircon in dissolution pits of primary xenotime directly at the phase boundary (Figs. 14, 15). The fluid was most likely also enriched in F. This is indicated by formation of two fluorapatite grains replacing the xenotime at the edges of the zircon-xenotime interface. The fluorapatite shows a sharp boundary with the xenotime, whereas a diffuse textural zone is present between fluorapatite and zircon (Fig. 3a). The fluorapatite served as a sink for Ca and F supplied by the fluid. Penetration of a F-rich fluid is further supported by the documentation of fluorapatite inclusions in zircon-xenotime interface (Fig. 14d), and transport of F deeper into the zircon may be indicated by fluorapatite inclusions in the zircon core (Fig. 10b).

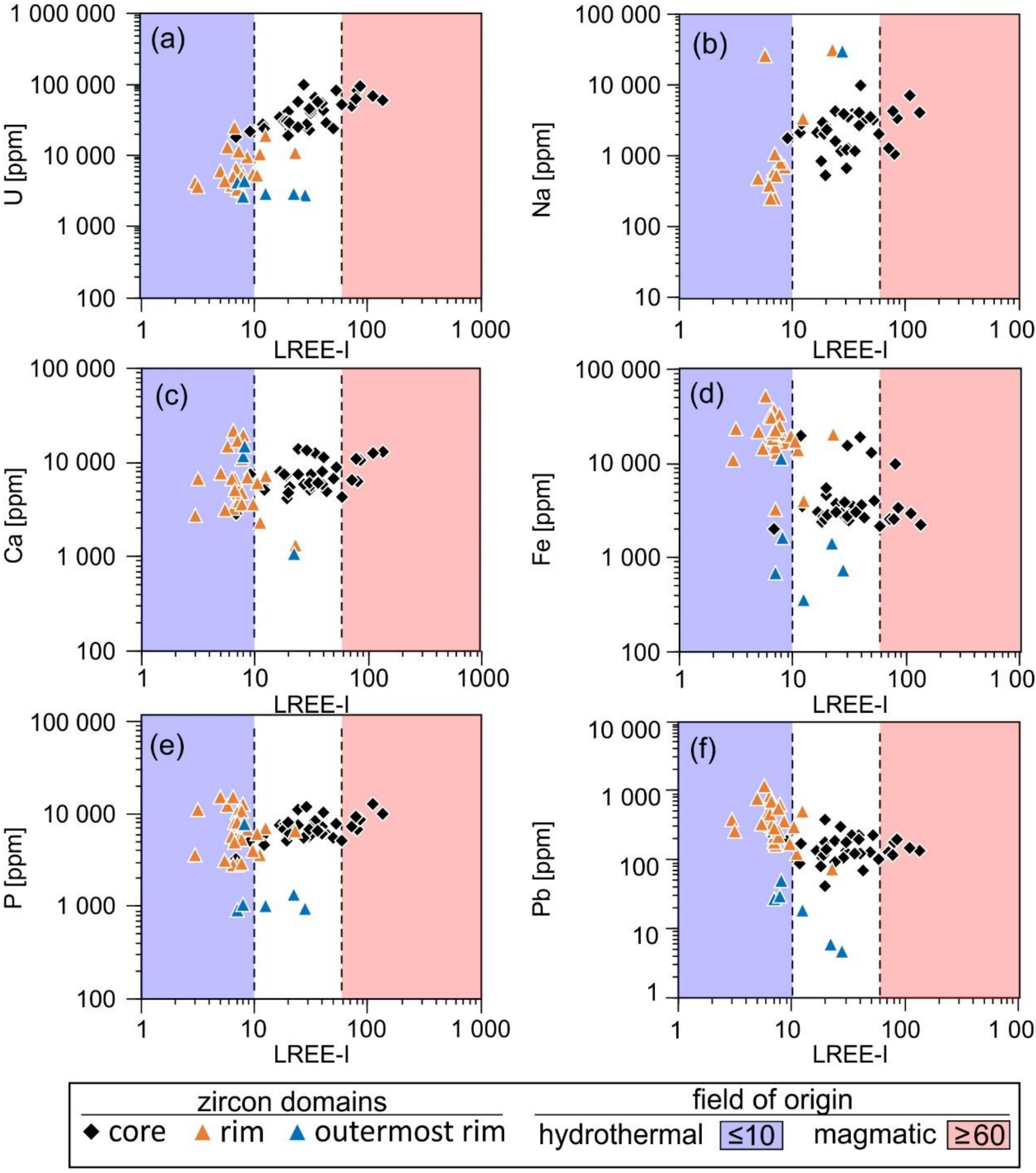

Fig. 17. Geochemical zircon data (modified from Tramm et al. 2021) using the LREE index (LREE-I = Dy/Nd + Dy/Sm; after Bell et al. 2016). Classification into hydrothermally altered zircons (LREE-I < 10, blue) and magmatic zircons (LREE-I > 60, red) according to Bell et al. (2016).

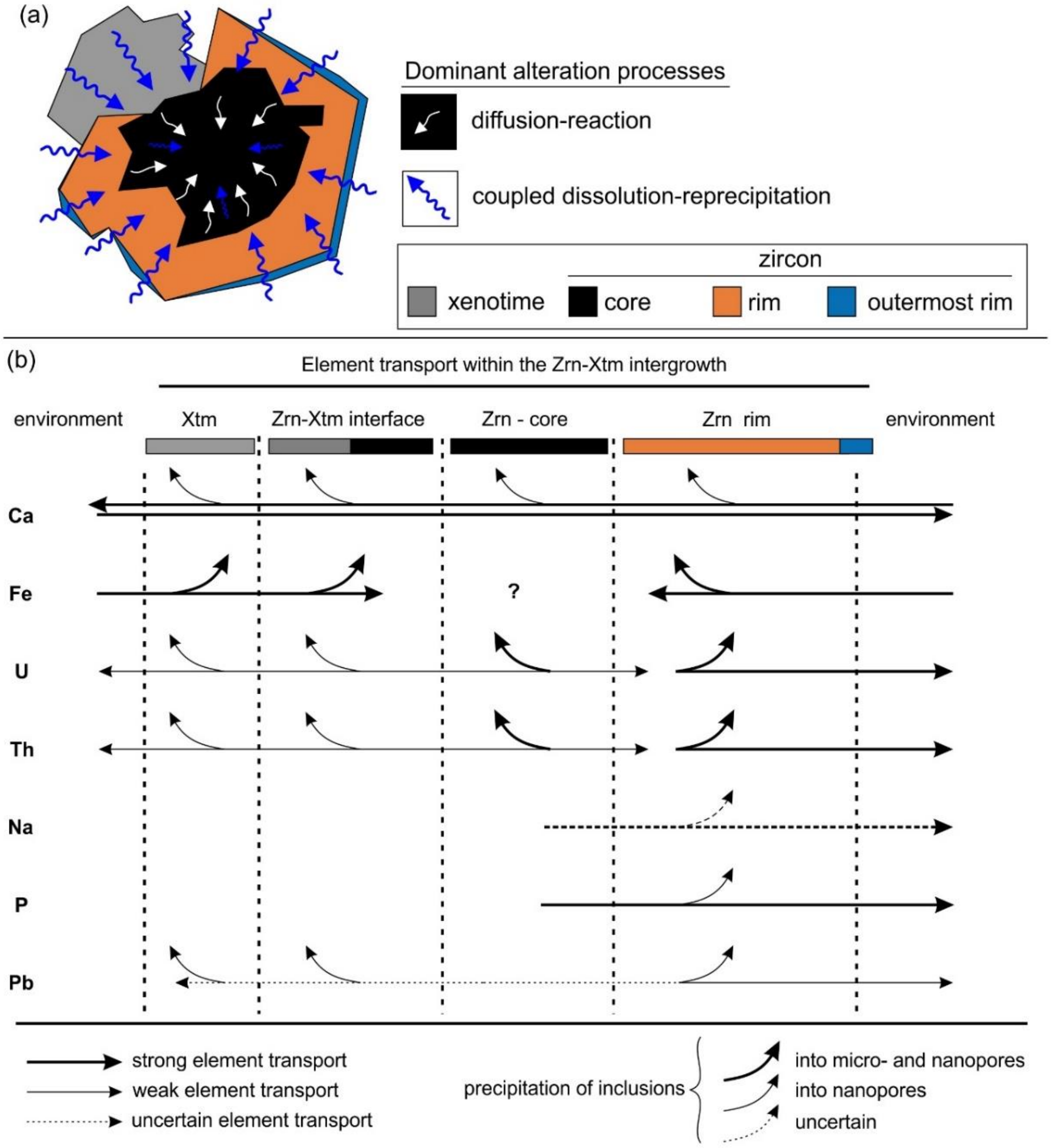

Fig. 18. Sketch of the investigated zircon-xenotime intergrowth with a summary of the element transport during fluid-mediated alteration processes. Modified from Tramm et al. (2021).

3.5.5. Geochronological implications

Interpretation of isotopic U-Th-Pb data have to consider substitution mechanisms in the mineral structure, which can result in compositional variations. Accumulation of nanoinclusions containing U, Th and Pb may interfere with the original geochronological record of the host mineral. Microinclusions can be recognized during measurements with microanalytical methods, such as SEM, EPMA or LA-ICPMS. During LA-ICPMS analysis microinclusions are recognized by changes in the isotopic signal, whereas nanoinclusions may be below the signal resolution and thus remain undetected. Furthermore, clusters of nanoinclusions can influence the average signal of the measurement. This can have significant impact on the interpretation of isotopic data, which may not reflect the true geochronological record. In this study, such nanoinclusions that would significantly affect U-Th-Pb ages include galena, uraninite and thorite.

Nanoscale observations of the patchy domains of the zircon core (Figs. 10a, 11a) reveal various degrees of a radiation damage (Figs. 10a, 11a–d). This is demonstrated by patchy zoning with bright and dark nanopatches of different degrees of crystallinity. Moreover, these patches are relatively scarce of nanoinclusions, which concentrate in the connected pore-systems (Figs. 10a, 11a). Therefore, nanoscale heterogeneity of U and Th contents and variations in crystallinity are the predominant factors that potentially result in discordant U-(Th-)Pb age data in these domains. The inclusion-rich domain is dominated by accumulation of secondary inclusions including U-rich zircon, coffinite and uraninite (Fig. 12). The high abundance of nano- to microinclusions in this domain may significantly disturb the geochronological record, because unambiguous differentiation of inclusions in zircon is challenging using microanalytical methods.

The zircon rim displays well-developed microporosity containing inclusions of Pb-bearing Fe-oxides, Pb-bearing Fe-silicates and uraninite. The presence of these inclusions indicates substantial element transport of U, Th and Pb. Because nanoinclusions that accumulate these elements are not detectable at the microscale, interpreting the ages recorded in highly heterogeneous domains with a high abundance of nanoinclusions has to be treated with caution. Based on the information presented in this study, it is recommended to implement nanoscale observations into the procedure of geochronological evaluation to assess the potential interference from nanoinclusions, particularly in case of highly altered or complexly textured minerals used in geochronology.

The altered, patchy-zoned xenotime shows an extensive microporosity close to the zircon (Fig. 3). Nanoscale observations revealed crystalline xenotime, which contains a network of dislocations in FIB-foils cut from domains of lower porosity (FIB-foils F01, F02; Fig. 8). Microinclusions can be easily detected using microanalytical methods, whereas nanoinclusions of Pb-phosphate, uraninite and thorite may not be recognized and possess the potential to contribute to the U, Th and Pb data obtained from domains with high abundance of nanoinclusions. Such alteration processes can result in disturbance of the U-(Th)-Pb age record (cf. Williams et al. 2011; Budzyń et al. 2015, 2021; Grand'Homme et al. 2016, 2018). In summary, reconstructions of the history recorded in rocks should start from nanoscale, particularly considering nanoscale alteration, which allows us to understand the broader context of the environment from which the studied minerals originate.

4. Raman microspectroscopy of unaltered and altered monazite and xenotime

4.1. Materials

Alteration of monazite and xenotime can affect their structural and compositional properties, which may lead to recrystallization, element mobilization or disturbance of recorded age. Evaluation of these effects with Raman microspectroscopy is the focus of this chapter. Variably altered monazite and xenotime with different concentrations of REE, U, Th and different age were investigated in (i) products of experiments focused on the stability of monazite and xenotime, (ii) altered monazite from Ankazobe (Madagascar), (iii) altered xenotime from Piława Górna (Góry Sowie Block, SW Poland). Synthetic REE-phosphates ($LaPO_4$–$LuPO_4$ and YPO_4) have been also selected for this study. High concentrations of Th and U potentially induced radiation damage in the structure, which may potentially enhance alteration processes at microscale to submicron scale (e.g. Ruschel et al. 2012; Seydoux-Guillaume et al. 2012; Grand'Homme et al. 2018; Budzyń et al. 2021, 2022).

The monazite and xenotime from experiments were selected from the products of runs at P-T conditions of 200 MPa / 350 °C, 400 MPa / 450 °C, 600 MPa / 550 °C, 800 MPa / 650 °C, and 1000 MPa / 750 °C (Tables 2, 3). The experiments were performed using cold-seal autoclaves on a hydrothermal line and piston-cylinder apparatus at the Deutsche GeoForschungsZentrum (GFZ), Potsdam, Germany (Budzyń and Kozub-Budzyń 2015; Budzyń et al. 2015, 2017). Starting materials for experiments with monazite included natural monazite of a pegmatite from Burnet County, Texas, USA (LA-ICPMS Concordia age 1100.5 ± 11.6 Ma; Budzyń et al. 2021), albite, sanidine, biotite, muscovite, SiO_2, CaF_2, $Na_2Si_2O_5$ and doubly distilled H_2O. Starting materials in the experiments with xenotime included xenotime from the North-West Frontier Province (NWFP) in Pakistan (LA-ICPMS Concordia age 38.4 ± 0.6 Ma; Budzyń and Sláma 2019), albite, labradorite, sanidine, biotite, muscovite, garnet, SiO_2, CaF_2, $Na_2Si_2O_5$, and doubly distilled H_2O. Initial Burnet monazite and NWFP xenotime used in experiments were also selected for analysis. For more details on experimental procedure see Budzyń et al. (2017).

An approximately 0.7 × 1.1 cm-sized chunk of ca. 278 g crystal of altered monazite from Ankazobe, Madagascar (henceforth, Ankazobe monazite) was selected for Raman microspectroscopy and EPMA investigations. The age of the Ankazobe monazite has been constrained to ca. 515.4 ± 4.8 Ma (2s, MSWD = 0.90, LA-ICPMS U-Pb analysis; Budzyń and Sláma, personal communication). The Ankazobe monazite was supplied by a mineral dealer, but the exact location remains uncertain.

Raman microspectroscopy investigations were also performed on the altered xenotime from the pegmatite from Piława Górna, which has been investigated in chapter 3 (Fig. 3). The xenotime displays patchy zoning in high contrast BSE imaging and has a domain with extensive microporosity in close proximity to the zircon. The domains of interest are the patchy zoned xenotime core and “outer” rim (i.e. not intergrown with zircon), and the patchy zoned domains dominated by microporosity, located close to the zircon.

Table 2. Summary of experimental conditions and notes on the products (modified from Budzyń et al. 2015, 2017), from which monazite was selected for Raman microspectroscopy investigations in this study.

Experiment label	T (°C)	P (MPa)	Duration (days)	Notes
Exp1	350	200	40	Monazite grains display dissolution pits and porosity at the rim. REE-rich steacyite formed at the surface of monazite.
Exp2	450	400	18	Monazite grains are partially replaced by REE-rich steacyite and show dissolution pits along the rim. REE-rich steacyite formed accumulations of crystals at the rim of monazite and fills cracks in monazite. Occasionally, small crystals of fluorcalciobritholite formed close to steacyite.
Exp3	550	600	8	Monazite grains display porosity. One grain displays patchy zoning. At the rim of altered monazite, REE-rich fluorcalciobritholite formed small crystals. Occasionally, fine crystals of cheralite formed between fluorcalciobritholite and monazite.
Exp4	650	800	6	Monazite grains display porosity and dissolution pits at the rim, where fluorcalciobritholite formed. Occasionally fine crystals of cheralite formed in between fluorcalciobritholite and monazite.
Exp5	750	1000	4	Monazite grains are surrounded by a fine rim of fluorcalciobritholite. A cluster of monazite grains is embedded in melt and partially replaced by fluorcalciobritholite.

Table 3. Summary of experimental conditions and notes on the products (modified from Budzyń and Kozub-Budzyń 2015, Budzyń et al. 2017), from which xenotime was selected for Raman microspectroscopy investigations in this study.

Experiment	T (°C)	P (MPa)	Duration (days)	Notes
Exp1	350	200	40	Xenotime grains investigated in this study are unaltered and there are no secondary phases on their surface. Minor amounts of tiny crystals of Y-rich silicate, Y-rich apatite and amphibole formed in this run.
Exp2	450	400	18	Xenotime grains appear unaltered without the presence of secondary phases on its surface. Secondary phases formed delicate crystals composed of Y-rich silicate, Y-rich apatite and amphibole.
Exp3	550	600	8	Xenotime grains appear unaltered without the presence of secondary phases on its surface. Secondary phases formed delicate crystals composed of Y-rich silicate, Y-rich apatite and amphibole.
Exp4	650	800	6	Xenotime grains display dissolution pits on the surface. Y-rich fluorcalciobritholite partially replaced xenotime or formed on the surface of xenotime.
Exp5	750	1000	4	Xenotime grains display dissolution pits on the surface. Y-rich fluorcalciobritholite partially replaced xenotime or formed on the surface of xenotime. A cluster of xenotime grains is embedded in melt and partially replaced by Y-rich fluorcalciobritholite.

4.2. Analytical methods

The experimental products, which included monazite and xenotime, were mounted in 1" rounded epoxy resin. The grain mounts were polished with fine sandpaper (1200 / 2000 / 5000) followed by a final polishing with a STRUERS LaboPol–5 diamond paste.

Initial evaluation of the monazite and xenotime from experimental products was performed on the polished 1" grain mounts without carbon coating. The BSE imaging and EDS analyses were performed using a field emission scanning electron microscope FEI Quanta 200 at a low-vacuum at the Faculty of Geology, Geophysics and Environmental Protection, AGH University of Science and Technology (Kraków, Poland).

Raman microspectroscopy measurements of monazite and xenotime from experimental products, the Ankazobe monazite (in a polished 1" grain mount) and the xenotime from Piława Górna (in a thin section of the pegmatite) were conducted using a Thermo Scientific DXR Raman Microscope (henceforth, instrument A) with a 532 nm laser at the Faculty of Geology, Geophysics and Environmental Protection, AGH University of Science and Technology (Kraków, Poland). The measurements were performed at a room temperature using an apparatus of a 25 µm pinhole, a 900 lines / mm grating, a CCD detector, and an air Olympus (100× / 0.80NA) objective. Single spot measurements were conducted using a 532 nm diode laser at a power of 10 mW, an exposure time of 3 s, and 100 accumulations. Spectra were processed using Thermo Scientific OMNIC software. Post-processing of the spectra was done using fluorescence corrections and automatic baseline correction. Deconvolution was done using the Gaussian-Lorentzian band shape after Ruschel et al. (2012). Obtained FWHH (full width at half height) values of the $\nu_1(PO_4)$ symmetric stretching band were corrected according to the instrumental broadening (Nasdala et al. 2001).

Synthetic REE phosphates ($LaPO_4$–$LuPO_4$ and YPO_4 in a polished 1" grain mount) were measured using 532 nm and 780 nm lasers to compare their Raman features with monazite and xenotime, and to differentiate between Raman bands and potential fluorescence effects present in the spectrum. The 780 nm laser measurements were carried out using instrument A with a 15 mW power and a grating of 400 lines / mm. All displayed Raman spectra obtained with instrument A range from 150 to 3500 cm^{-1} due to artefacts below 150 cm^{-1}.

Monazite and xenotime grains from two experiments (200 MPa / 350 °C and 1000 MPa / 750 °C representing the lowest and highest P-T conditions of chosen experiments) were selected for Raman microspectroscopy measurements conducted with a WITec confocal CRM alpha 300 Raman microscope (WITec GMBH, Ulm, Germany; henceforth instrument B). Measurements were performed at room temperature at the Raman Imaging Group of Jagiellonian University (Kraków, Poland). The spectrometer was equipped with air-cooled solid-state lasers operating at 488 nm, 532 nm and 633 nm, and a CCD detector cooled to -60 °C. The lasers were coupled to the microscope via optical fibre with a diameter of 50 µm (488 nm and 532 nm excitation wavelengths) or 100 µm (633 nm excitation wavelength). An air Olympus MPLAN (100× / 0.90NA) objective was used. The spectral resolution was equal to 3 cm^{-1}. The monochromator of the spectrometer was calibrated using a radiation spectrum from a calibrated xenon lamp (WITec UV light source). In addition, the standard alignment procedure (single-point calibration) was performed before measurement with the use of the Raman scattering line produced by a silicon plate (520.5 cm^{-1}). Integration time for a single spectrum was 1 s, and the number of accumulations per collected spectrum was equal to 100 (acquisition time per single spectrum 100 s). In case of Raman mapping, spectra were gathered with a 0.5 s integration time and the measurement step of 1 µm. The Raman measurements and data analysis were performed using WITec software (WITec Project Plus 5.1).

After the Raman microspectroscopy measurements, the mounts were carbon-coated for compositional analysis and backscattered electrons (BSE) imaging using a JEOL SuperProbe JXA-8230 electron microprobe equipped with five wavelength dispersive spectrometers (WDS) at the Laboratory of Critical Elements AGH – KGHM at AGH University of Science and Technology (Kraków, Poland). Electron-probe microanalysis (EPMA) was conducted using a 15 kV acceleration voltage, a 100 nA probe current, and a 3 µm spot size. Each EPMA spot was close to the earlier Raman microspectroscopy spot. Data were corrected using an in-house ZAF procedure. See Supplementary Table B1 for more analytical details.

Additional major and trace element analyses of monazite and xenotime were conducted using a Thermo Scientific Element 2 high-resolution sector field ICP-MS coupled to a 193 nm ArF excimer laser (Teledyne Cetac Analyte Excite laser) at the Institute of Geology of the Czech Academy of Sciences (Prague, Czech Republic). The time-resolved signal data were processed using Glitter software (Van Achterbergh et al. 2001). The precision of the analyses (1 RSD) ranges between 5 and 15% for most elements. The accuracy was monitored by using a homogenized basalt reference material BCR-2 (USGS). See Supplementary Table B2 for more analytical details.

4.3. Results of Raman microspectroscopy of monazite

4.3.1. Compositional and textural characteristics of monazite

The Burnet monazite grains display are homogenous in BSE images. Composition of the Burnet monazite includes 27.95–32.71 wt.% Ce_2O_3, 9.48–11.85 wt.% ThO_2, 0.28–0.34 wt.% UO_2 and 0.48–0.60 wt.% PbO (Supplementary Table B3). Chondrite-normalized data of the Burnet monazite demonstrate typical LREE >> HREE patterns with a slight increase from La to Ce, a decreasing slope from Sm to Lu, and negative anomalies of Eu and Y (Fig. 20a).

Monazite from experiments at low to moderate P-T conditions (200 MPa / 350 °C, 400 MPa / 450 °C, 600 MPa / 550 °C) are extensively altered, which is demonstrated by developed porosity and faint patchy-zoning that are typical results of fluid-mediated coupled dissolution-reprecipitation processes (Fig. 19a–c). Unaltered domains are compositionally similar to the Burnet monazite, whereas altered domains are characterized by depletion of Th, U and Pb (Supplementary Table B3). One exception is presented by one grain of monazite from Exp3, which shows patchy zoning (Fig. 19l). Chondrite-normalized data of unaltered monazite domains from Exp1–Exp3 are similar to the patterns of Burnet monazite, whereas altered domains demonstrate significant depletion of the HREE (Fig. 20b–d).

Alteration of monazite from experimental products at high P-T conditions of 800 / 650 °C and 1000 MPa / 750 °C (Exp4 and Exp5, respectively) include dissolution on the surface and developed porosity. Composition of the monazite from Exp4 and Exp5 is similar to that of the Burnet monazite (Supplementary Table B3).

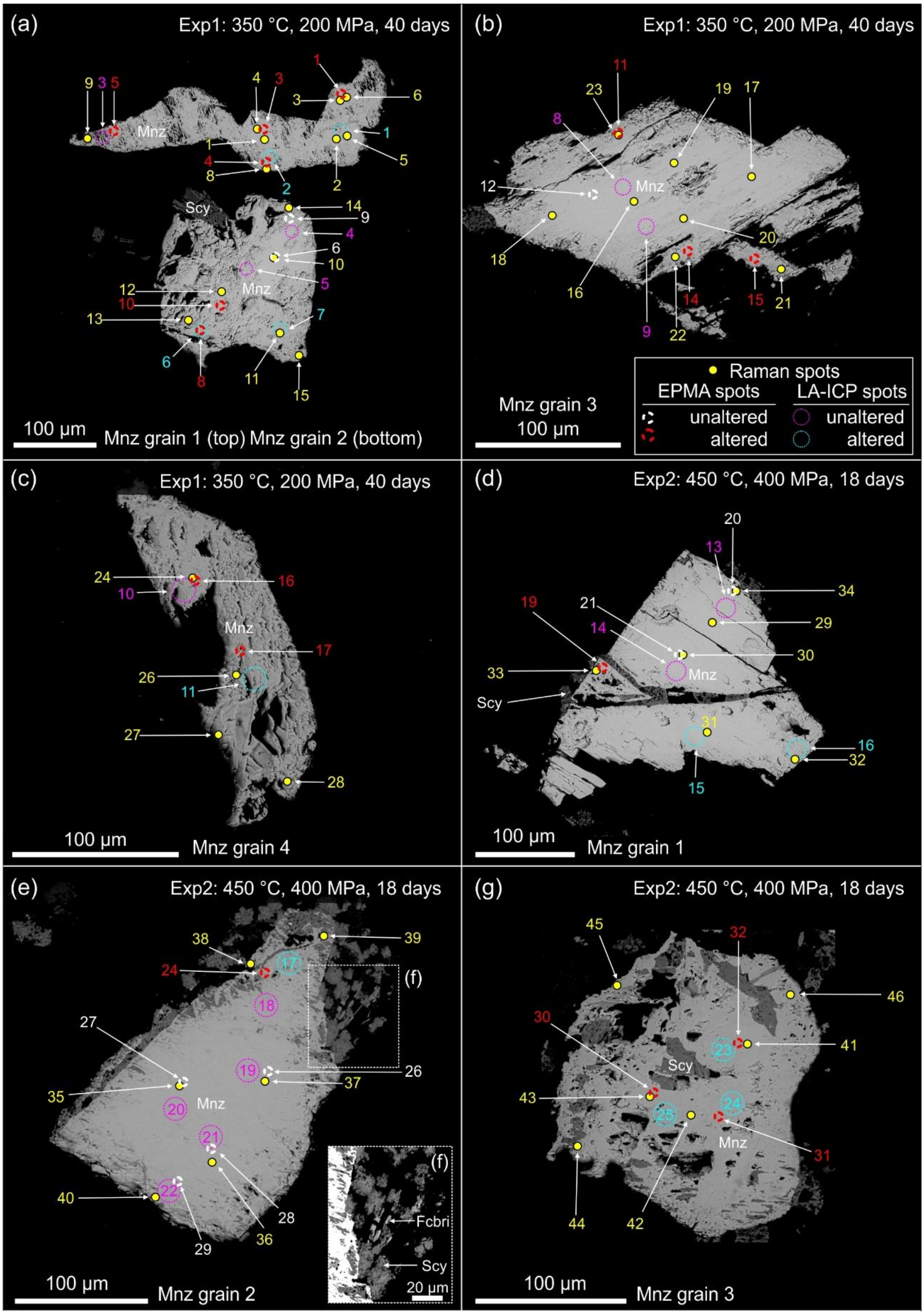

Fig. 19. Back-scattered electron (BSE) images of monazite grains from the experimental products. A low current used to avoid damaging of the sample surface prevented observing high-contrast patchy zoning in most monazite grains. Mineral abbreviations: Cher – cheralite, Fcbri – fluorcalciobritholite, Mnz – monazite and Scy – REE-rich steacyite

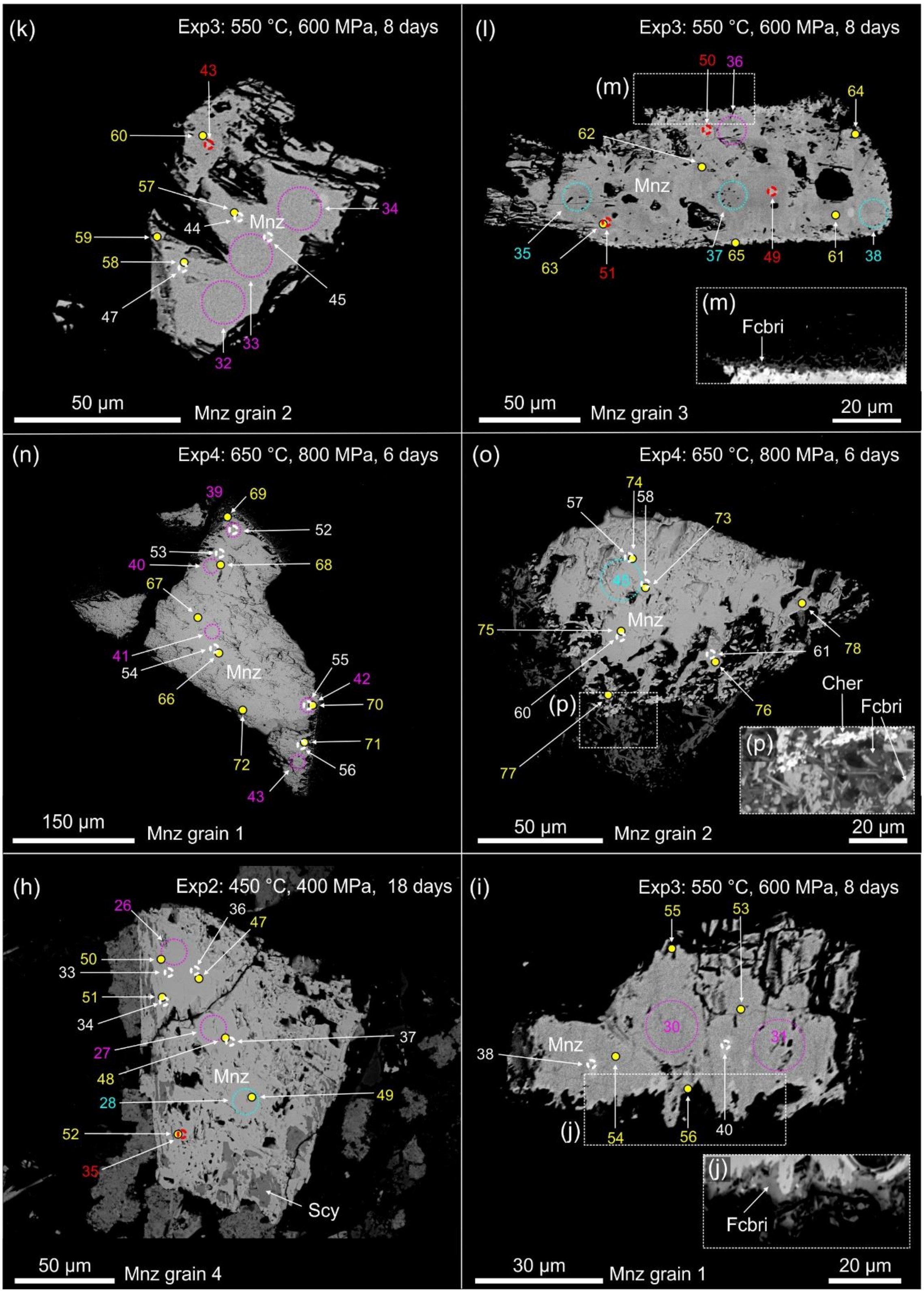

Fig. 19. (continued)

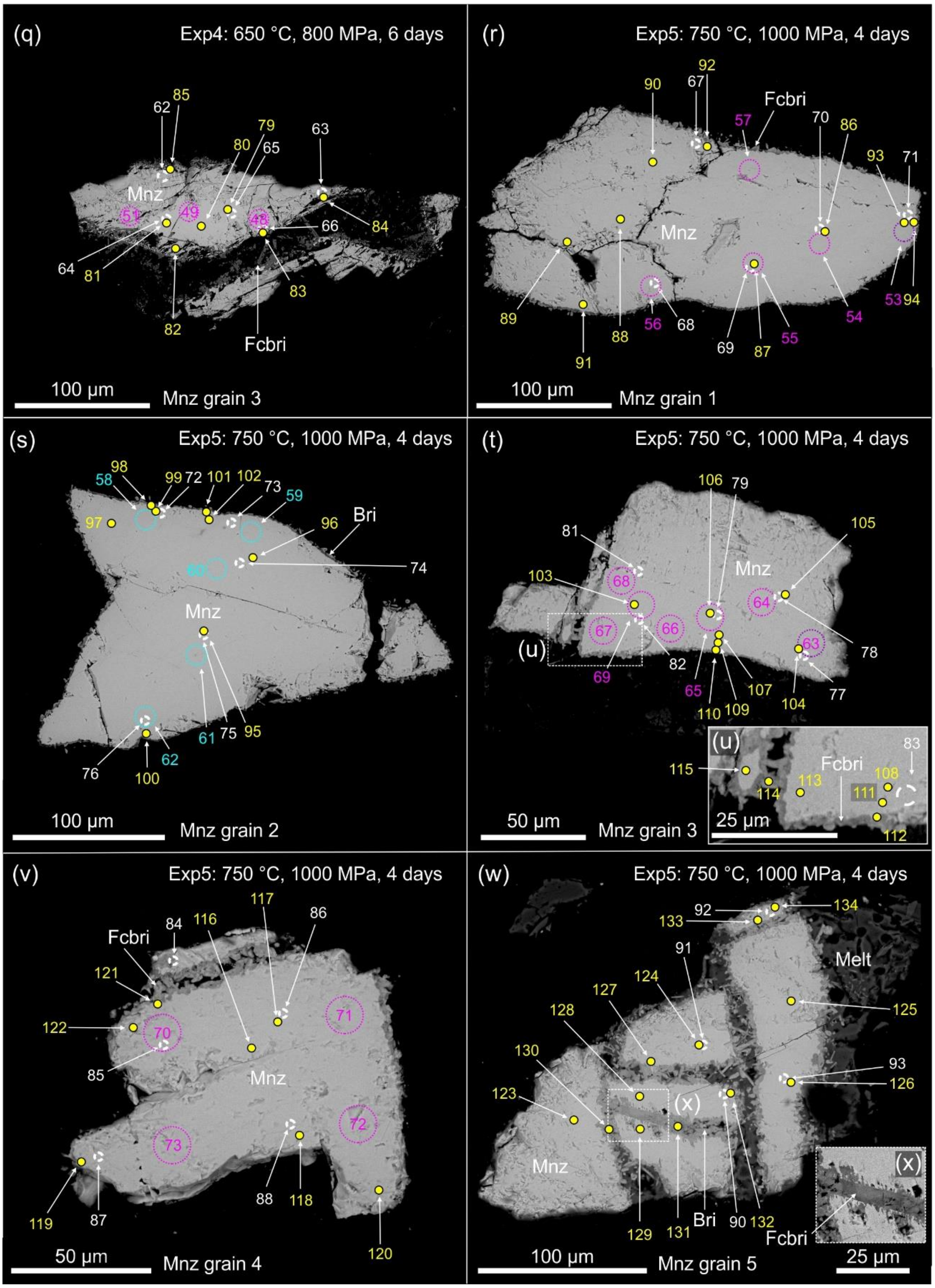

Fig. 19. (continued)

Chondrite-normalized data show similar patterns to those of the Burnet monazite (Fig. 20e, f), except occasionally less pronounced negative anomalies of Eu and Y. The latter may suggest incorporation of Eu released from feldspars during partial melting in the experiments via fluid-induced coupled dissolution-reprecipitation processes at submicron scale (cf. Budzyń et al. 2021).

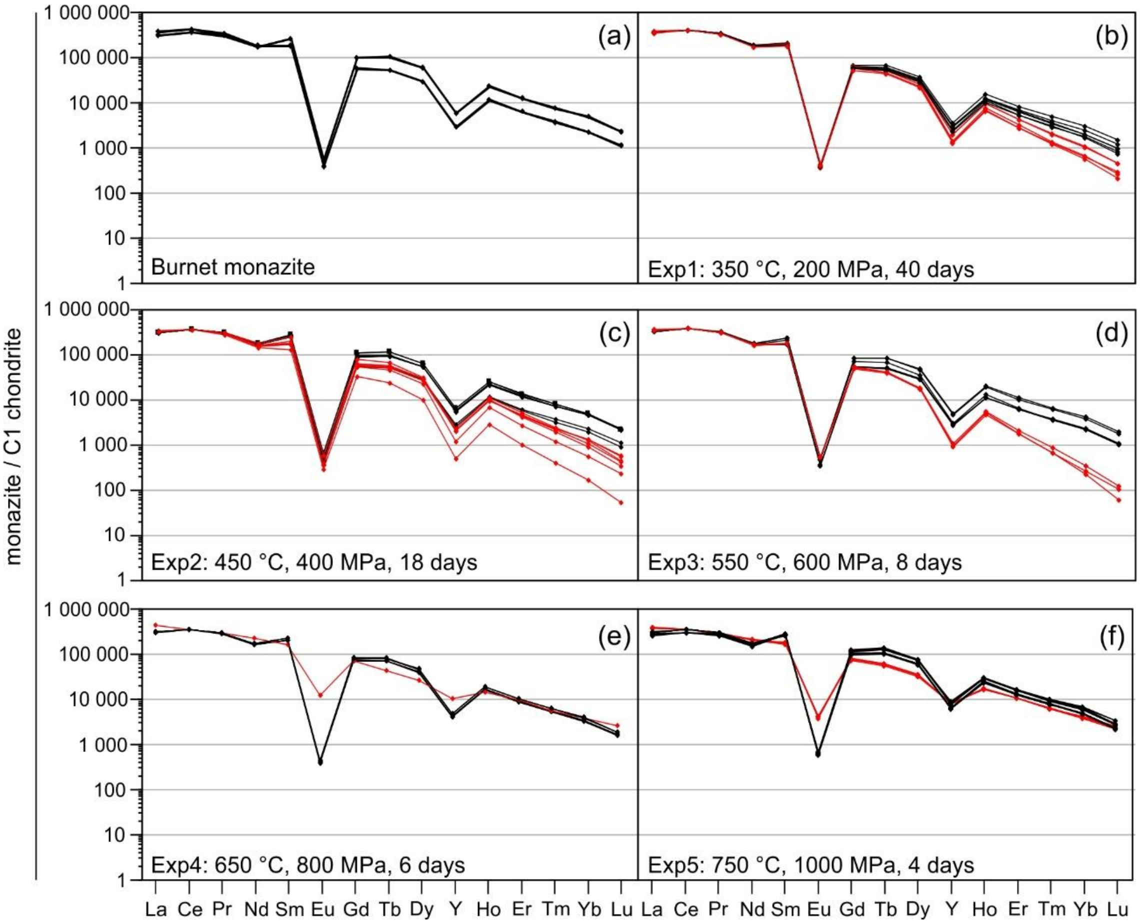

Fig. 20. Chondrite-normalized REE distribution patterns of Burnet monazite and monazite from experimental products. Composition of C1 chondrite after McDonough and Sun (1995). Black line – unaltered monazite, red line – altered monazite.

The Ankazobe monazite contains unaltered domains in the core, which are mostly homogeneous in BSE images, and an extensively altered rim containing porosity and numerous inclusions of thorite, xenotime, and mica with a composition similar to phengite (Fig. 21). The composition of the unaltered domains in Ankazobe monazite is typical for common monazite. This includes 25.83–26.41 wt.% Ce_2O_3, 7.19–7.58 wt.%

ThO_2, 0.33–0.38 wt.% UO_2 and 0.17–0.19 wt.% PbO (Supplementary Table B3). The altered domains contain 26.33–32.81 wt.% Ce_2O_3 and are depleted in Th, U and Pb (5.00–7.18 wt.% ThO_2, 0.07–0.17 wt.% UO_2 and 0.11–0.16 wt.% PbO; Supplementary Table B3).

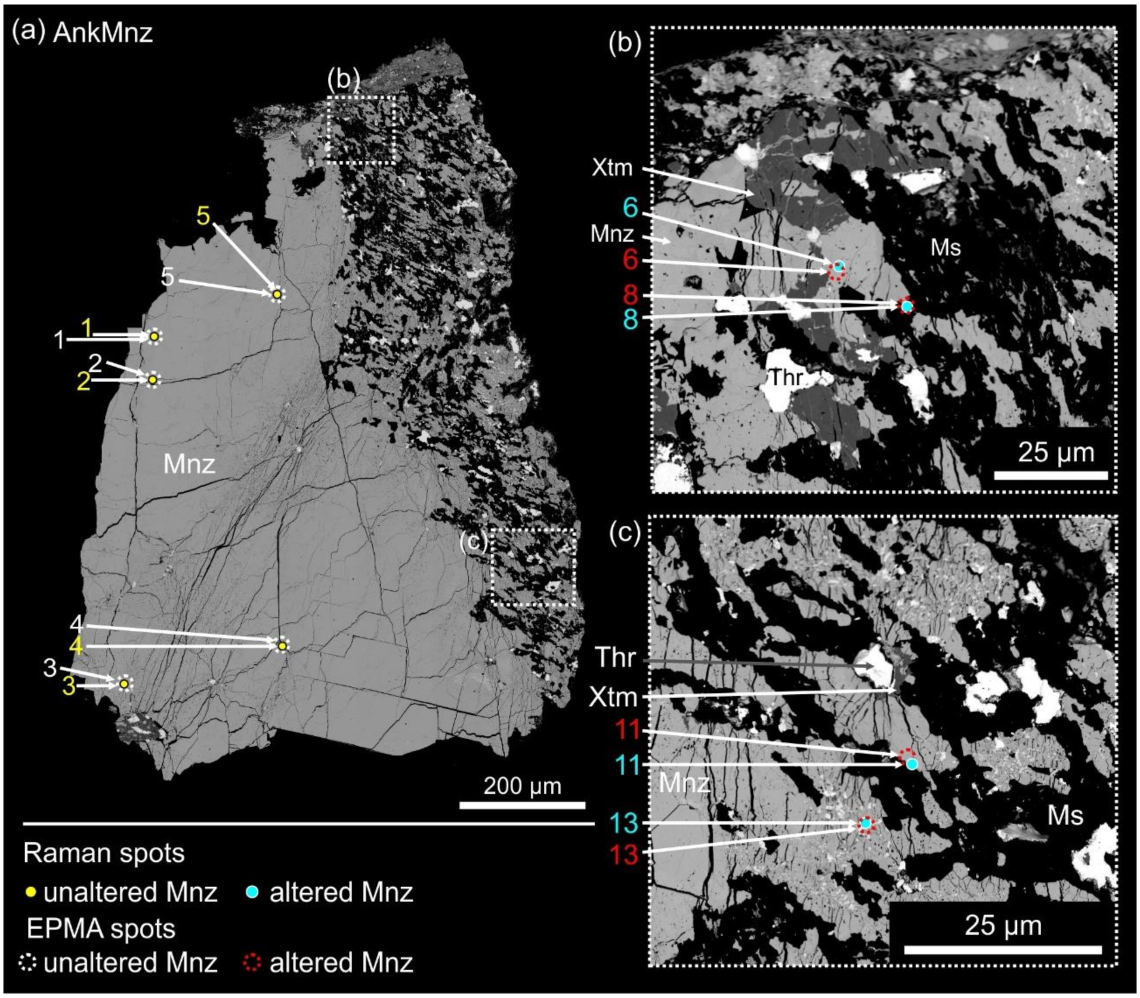

Fig. 21. BSE images of monazite from Ankazobe (Madagascar). (b, c) Altered domains of monazite contain inclusions of thorite, xenotime, and mica with a composition similar to phengite. Mineral abbreviations: Ms – muscovite (phengite), Mnz – monazite, Thr – thorite and Xtm – xenotime.

4.3.2. Raman microspectroscopy of the Burnet monazite and $LaPO_4$–$GdPO_4$ – instrument A (532 nm and 780 nm lasers)

Raman spectra of the Burnet monazite from instrument A (532 nm) include primary Raman features of (i) lattice modes (150–300 cm^{-1}), (ii) internal bending modes (500–700 cm^{-1}) with a dominant symmetric bending band $\nu_2(PO_4)$ at 464 cm^{-1} and (iii) the predominant $v_1(PO_4)$ symmetric stretching band at 973 cm^{-1}, (iv) followed by the antisymmetric stretching band $v_3(PO_4)$ at 1067 cm^{-1} (Fig. 22a; Table 4). Furthermore, fluorescence effects caused by electronic transitions of REE^{3+} ions are present at mid-range 1500–2500 cm^{-1} and at high-range 3000–3500 cm^{-1}.

At mid-range, fluorescence effects include two broad shoulders and a dominant peak at 2029 cm^{-1}. For comparison, the $NdPO_4$, $SmPO_4$, $EuPO_4$ and, to a lesser extent, $GdPO_4$ also show fluorescence effects at mid-range (Fig. 22b). The $SmPO_4$ spectrum shows weak fluorescence effects also in high-range. The $EuPO_4$ spectrum is dominated by fluorescence effects and primary Raman features are completely superimposed, however, these strong effects are not present in the Burnet monazite spectrum due to negligible Eu_2O_3 contents.

4.3.3. Raman microspectroscopy of monazite from experiments – instrument A (532 nm)

The Raman spectra (instrument A, 532 nm) of monazite from experiments are generally similar to the Burnet monazite spectrum with only minor variations, which include small variations of intensities in the range of lattice modes, symmetric bending mode $v_2(PO_4)$ and fluorescence effects at mid- and high-range (Figs. 22a, 23). Peak positions of the $v_1(PO_4)$ symmetric stretching band of monazite spectra from experiments range from 969–982 cm^{-1} compared to that of the Burnet monazite at 973 cm^{-1} (Tables 4, 5). Raman spectra of monazite from Exp3 and Exp4 (600 MPa / 550 °C and 800 MPa / 650 °C) show overall increased background fluorescence effects at 800–1200 cm^{-1} (spectra 7, 8; Fig. 23c), and elevated fluorescence effects at mid-range (spectra 8–11; Fig. 23c, d).

Aside of Raman spectra similar to those of the Burnet monazite, some spectra collected closely to secondary phases show significant differences (Figs. 22a, 24). The spectrum of monazite from Exp2 (400 MPa / 450 °C), in which REE-rich steacyite has formed as microinclusions in monazite, shows a new distinct peak at 1129 cm^{-1} and increased intensity and broadening of mid-range and high-range fluorescence effects (Raman spots 50–52; spectrum 15; Figs. 19h, 24a). The shape of fluorescence effects at mid-range differs significantly compared to the fluorescence effects of the Burnet monazite with an asymmetric peak at 2027 cm^{-1} and a distinct broad peak at 2271 cm^{-1}.

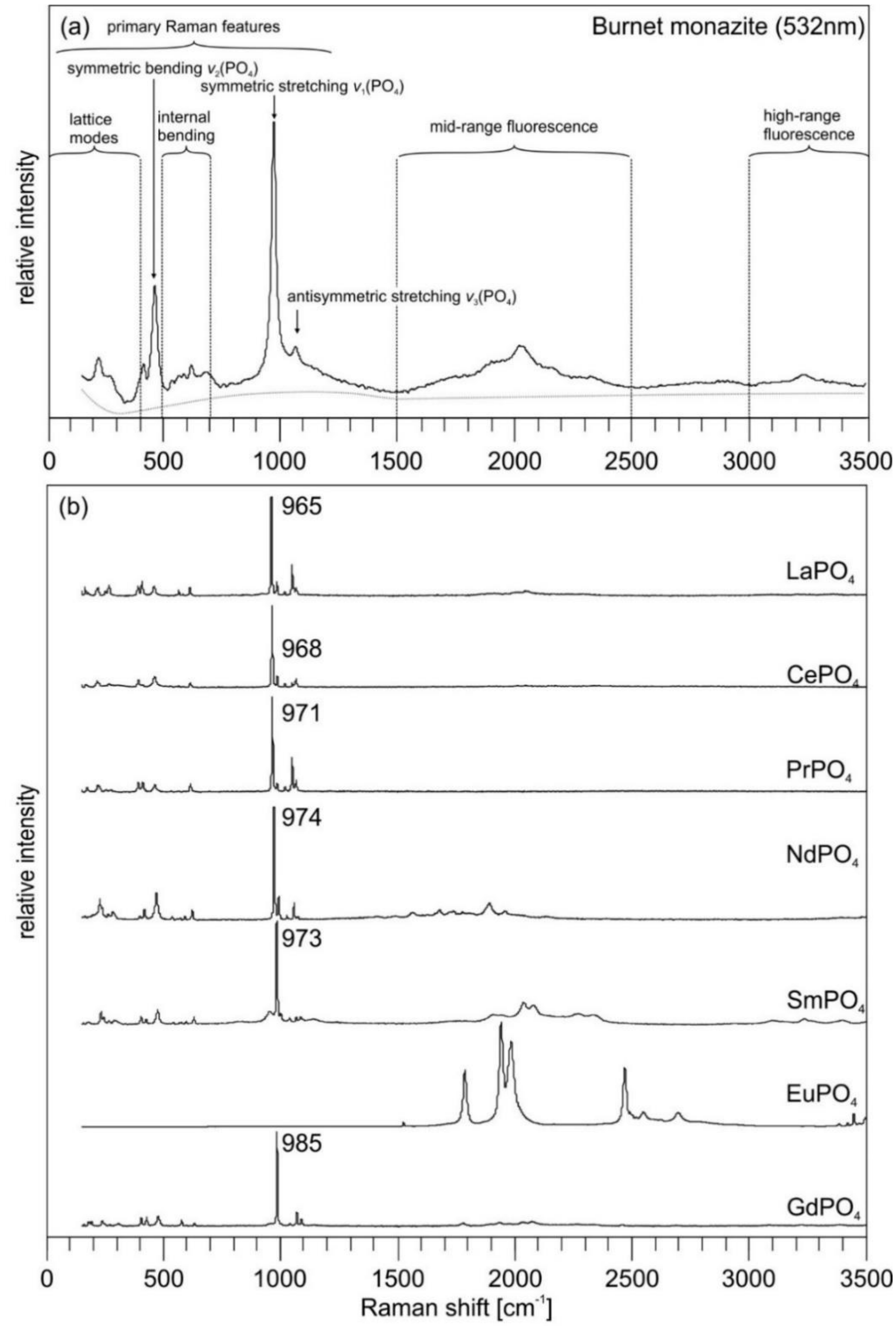

Fig. 22. Raman spectra of (a) the Burnet monazite and (b) synthetic REE phosphates ($LaPO_4$–$GdPO_4$) obtained with instrument A (532 nm). The Raman spectrum of monazite can be divided into primary Raman features (0–1200 cm^{-1}) and fluorescence effects (mid-range 1500–2500 cm^{-1} and high-range 3000–3500 cm^{-1}).

Table 4. Raman data of Burnet monazite (BrtMnz) obtained with 532 nm laser and Raman data of synthetic $LaPO_4$–$GdPO_4$ obtained with 532 nm and 780 nm lasers.

532 nm								**780 nm**							**Assigned bands(1)**	
BrtMnz	$LaPO_4$	$CePO_4$	$PrPO_4$	$NdPO_4$	$SmPO_4$	$EuPO_4$(2)	$GdPO_4$	$LaPO_4$(2)	$CePO_4$(2)	$PrPO_4$	$NdPO_4$(2)	$SmPO_4$	$EuPO_4$	$GdPO_4$	symmetry	modes
-	(w) 167	-	(w) 176	-	-	-	-	-	-	-	-	-	(w) 174	-	Bg	lattice
-	(w) 216	(w) 217	-	-	-	-	-	-	-	-	-	-	-	-	Ag,Bg	lattice
-	(w) 223	(w) 225	(w) 221	-	(w) 228	-	(w) 235	-	-	-	-	-	-	-	Ag,Bg	lattice
(w) 225	-	-	(w) 230	(w) 224	(w) 240	-	-	-	-	(w) 224	-	(m) 230	(w) 234	(w) 235	Ag,Bg	lattice
-	(w) 270	-	-	(w) 234	-	-	-	-	-	(w) 233	-	-	(s) 244	(w) 247	Ag,Bg	lattice
-	-	-	-	*(w) 281*	-	-	-		-	-	-	-	-	-	-	-
-	-	-	-	-	-	-	-	-	-	-	-	-	-	(w) 392	-	-
-	(w) 393	(w) 395	(w) 395	-	-	-	(w) 402	-	-	(w) 398	-	-	(w) 403	(w) 403	Ag,Bg	lattice
(w) 418	(w) 411	-	(w) 414	(w) 416	(w) 400	-	(w) 425	-	-	(w) 417	-	-	(w) 425	-	Ag,Bg	lattice
(m) 464	(w) 463	(w) 465	(w) 466	(m) 468	(w) 470	-	(w) 475	-	-	(w) 469	-	(m) 472	-	(m) 476	Ag,Bg	$v_2(PO_4)$
	(w) 569	-	-	-		-	(w) 575	-	-	-	-	-	-	-	-	-
(w) 621	(w) 616	(w) 618	(w) 619	(w) 621	(w) 625	-	-	-	-	-	-	(w) 627	(w) 630	(w) 632	Ag,Bg	$v_4(PO_4)$
sh(w) 961	-	-	-	-	(w) 949	-	-	-	-	-	-	-	-	-	-	-
(s) 973	**(s) 965**	**(s) 968**	**(s) 971**	**(s) 974**	**(s) 979**	-	**(s) 985**	-	-	**(s) 974**	-	**(s) 981**	**(s) 989**	**(s) 987**	Ag,Bg	$\boldsymbol{v_1(PO_4)}$
sh(w) 994	(w) 989	(w) 990	(w) 991	(w) 994	(w) 996	-	-	-	-	(w) 994	-	(w) 999	-	-	-	-
(w) 1067	(m) 1054	-	(m) 1056	(w) 1059	-	-	(m) 1070	-	-	(m) 1058	-	-	(m) 1069	-	-	$v_3(PO_4)$
-	(w) 1062	-	-	-	-	-	-	-	-	-	-	-	-	-	-	-
-	(w) 1072	(w) 1071	(w) 1073	-	-	-	(w) 1090	-	-	(w) 1076	-	-	(w) 1093	-	-	-

Notes:

(1) – assigned bands according to Begun et al. (1981) and Silva et al. (2006)

(2) – overwhelming fluorescence effects prevented unambiguous data deconvolution

sh – shoulder, *Italic – fluorescence bands*

Intensities of presented data are normalized to $v_1(PO_4)$ band (**bold**) equal to 1.0: weak (w) 0.05–0.2, medium (m) 0.2–0.5, strong (s) 0.5–1.0

Only significant signals above background are presented.

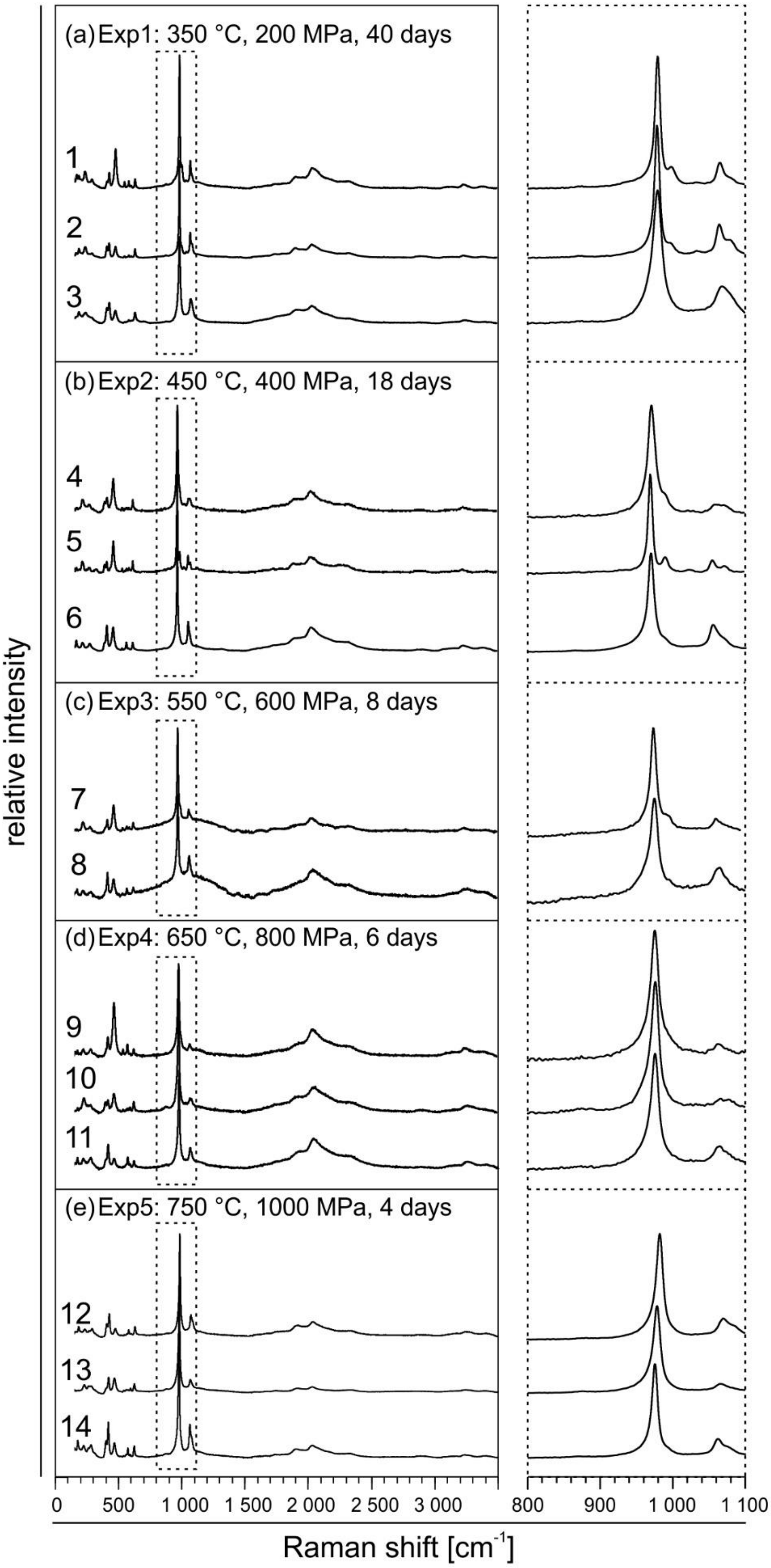

Fig. 23. Raman spectra of monazite from experimental products obtained with instrument A (532 nm). Left side – wide spectra (150–3500 cm^{-1}) show similar features as the Burnet monazite spectrum. Right side – zoomed-in spectra corresponding to dotted rectangles in range of 800–1100 cm^{-1}.

Table 5. Raman data of monazite from experiments obtained with 532 nm laser.

Raman spectra and corresponding Raman spots of monazite(1)							
Exp1			Exp2			Exp3	
spectrum 1 (n=8) spots: 1–6, 8, 9	spectrum 2 (n=13) spots: 11–15, 21–28	spectrum 3 (n=6) spots: 10, 26–20	spectrum 4 (n=11) spots: 29–32, 35–37, 40–43	spectrum 5 (n=6) spots: 33, 34, 38, 39, 44, 45	spectrum 6 (n=3) spots: 47–49	spectrum 7 (n=7) spots: 56–61, 65	spectrum 8 (n=4) spots: 53–55, 64
(w) 163	-	-	-	-	-	-	-
-	(w) 180	(w) 179	-	-	(w) 171	-	-
-	-	-	-	(w) 216	(w) 217	-	-
(w) 230	(w) 231	(w) 232	(w) 220	(w) 226	-	(w) 224	-
-	-	-	-	-	-	-	-
-	-	-	-	-	(w) 276	(w) 280	-
-	(w) 402	(m) 402	(w) 394	(w) 394	-	-	-
(w) 421	(w) 421	(m) 422	(w) 413	(w) 411	(m) 412	(w) 416	(m) 418
(w) 472	(w) 471	(w) 470	(m) 462	(m) 463	(m) 462	(m) 466	(m) 466
-	-	-	-	-	(w) 567	-	(w) 571
(w) 626	(w) 626	(w) 626	(w) 617	(w) 617	(w) 617	(w) 621	(w) 622
sh(w) 972	*sh*(w) 973	sh(w) 971	sh(w) 962	sh(w) 960	sh(w) 961	sh(w) 963	sh(m) 968
(s) 978	**(s) 978**	**(s) 979**	**(s) 970**	**(s) 969**	**(s) 970**	**(s) 973**	**(s) 974**
(w) 996	(w) 997	sh(w) 992	sh(w) 989	(w) 989	sh(w) 980	sh(w) 991	-
-	-	(w) 1040	-	(w) 1054	(m) 1055	-	-
(m) 1063	(m) 1063	(m) 1066	(w) 1065	-	(w) 1067	-	(m) 1063
sh(w) 1078	sh(w) 1080	sh(w) 1079	-	(w) 1070	-	-	-
mid-range fluorescence effects							
-	-	*sh(w) 1819*	-	-	*sh(w) 1767*	-	-
(w) 1903	*(w) 1897*	*(w) 1917*	-	-	*(w) 1910*	-	-
(w) 2036	*(w) 2031*	*(w) 2029*	*(w) 2024*	*(w) 2022*	*(w) 2029*	*(w) 2034*	*(m) 2055*
sh(w) 2135	*sh(w) 2116*	*sh(w) 2127*	-	-	*sh(w) 2101*	-	-
-	-	-	-	-	*sh(w) 2307*	-	-

Notes:

(1) – Raman spectra from Fig. 23 and corresponding Raman spots from Fig. 19

(2) – band assignment after data of $LaPO_4$ – $GdPO_4$ end-members (Table 4) and according to previous studies (Begun et al. 1981; Silva et al. 2006)

sh – shoulders; *italic – fluorescence bands*

Intensities of presented data are normalized to $v_1(PO_4)$ band (**bold**) equal to 1.0: weak (w) 0.05–0.2, medium (m) 0.2–0.5, strong (s) 0.5–1.0, very strong (vs) >1.0

Only significant signals above background are presented.

Table 5. (Continued).

Raman spectra and corresponding Raman spots of monazite$^{(1)}$						**assigned bands**$^{(2)}$	
Exp4			Exp5				
spectrum 9 (n=4) spots: 66–68, 72	spectrum 10 (n=8) spots: 71, 73–78, 83	spectrum 11 (n=5) spots: 79–81, 84, 85	spectrum 12 (n=17) spots: 86–93, 95–97, 100, 102, 116–118, 120	spectrum 13 (n=7) spots: 103–108, 113	spectrum 14 (n=7) spots: 123–126, 128, 129	symmetry	modes
-	-	-	-	-	-	Bg	lattice
-	-	-	(w) 184	-	(w) 176	Bg	lattice
-	-	-	-	-	-	Ag,Bg	lattice
-	(w) 227	-	(w) 233	(w) 227	(w) 222	Ag,Bg	lattice
-	-	-	-	-	-	Ag,Bg	lattice
-	-	-	(w) 289	-	(w) 281	Ag	lattice
-	-	-	(w) 405	-	(w) 397	Ag,Bg	lattice
(m) 417	-	(m) 418	(m) 425	(w) 420	(m) 417	Ag,Bg	lattice
(s) 465	(m) 464	-	(w) 473	(w) 466	(w) 467	Ag,Bg	$v_2(PO_4)$
-	-	-	(w) 579	-	(w) 572	-	-
-	-	-	(w) 629	(w) 623	(w) 621	Ag,Bg	$v_4(PO_4)$
sh(m) 968	sh(m) 970	sh(m) 969	sh(m) 976	sh(m) 971	sh(w) 967	-	-
(s) 975	**(s) 976**	**(s) 975**	**(s) 982**	**(s) 978**	**(s) 975**	Ag,Bg	**$v_1(PO_4)$**
-	-	-	-	-	sh(w) 987	-	-
-	-	-	-	-	-	-	-
-	-	(w) 1066	(w) 1069	(w) 1065	(w) 1061	Ag,Bg	$v_3(PO_4)$
-	-	-	sh(w) 1084	-	sh(w) 1076	-	-
mid-range fluorescence effects							
-	-	-	-	-	-	-	-
-	-	-	*(w) 1917*	-	-	-	-
(m) 2033	*(m) 2052*	*(m) 2032*	*(w) 2031*	-	*(w) 2028*	-	-
-	-	*sh(m) 2097*	*sh(w) 2125*	-	-	-	-
-	-	-	-	-	-	-	-

Some Raman spectra of monazite from Exp3–Exp5, obtained closely to secondary fluorcalciobritholite, show significant changes compared to those of the Burnet monazite. These include (i) the presence of a peak at ca. 869 cm^{-1}, (ii) increased background fluorescence effects at 800–1200 cm^{-1} and (iii) a significant increase of intensity and broadening of fluorescence effects at mid-range and high-range (Fig. 24b–d; Table 6). Positions of the $v_1(PO_4)$ symmetric stretching band range from 969 cm^{-1} to 983 cm^{-1}, whereas some spectra present (i) a shift towards lower wavenumbers (962–963 cm^{-1}; spectra 17, 18; Fig. 24b, c), or (ii) a shoulder developed at that location (spectra 19, 20; Fig. 24d; Table 6).

Two spectra show splitting into two peaks at ca. 965 cm^{-1} and 975 cm^{-1} (spectra 21, 22; Fig. 24d). The shape of mid-range fluorescence effects partially resembles that of the Burnet monazite and it includes one dominant peak and two asymmetric shoulders (spectra 17, 18, 21, 22; Fig. 24c, d). The dominant fluorescence-peak is shifted to a higher wavelength (2081–2099 cm^{-1}) compared to 2028 cm^{-1} in the Burnet monazite, and a more pronounced shoulder is present at ca. 2260 cm^{-1}. Two other spectra show a lesser pronounced fluorescence-peak with two shoulders (spectra 19, 20; Fig. 24d). One spectrum from a compositionally altered domain of the patchy-zoned monazite (Fig. 19l, m) shows a broad increase in background fluorescence (300–1500 cm^{-1}), without the presence of mid- to high-range fluorescence effects (spectrum 16; Fig. 24b).

Spectra of fluorcalciobritholite show similarities to the spectra of monazite from Exp3–Exp5, which demonstrate significant spectral differences compared to Burnet monazite (Fig. 24e). These include (i) a more distinct peak at 861–863 cm^{-1}, (ii) an increased background fluorescence (800–1200 cm^{-1}) and (iii) a similar shape of fluorescence effects at mid-range and high-range.

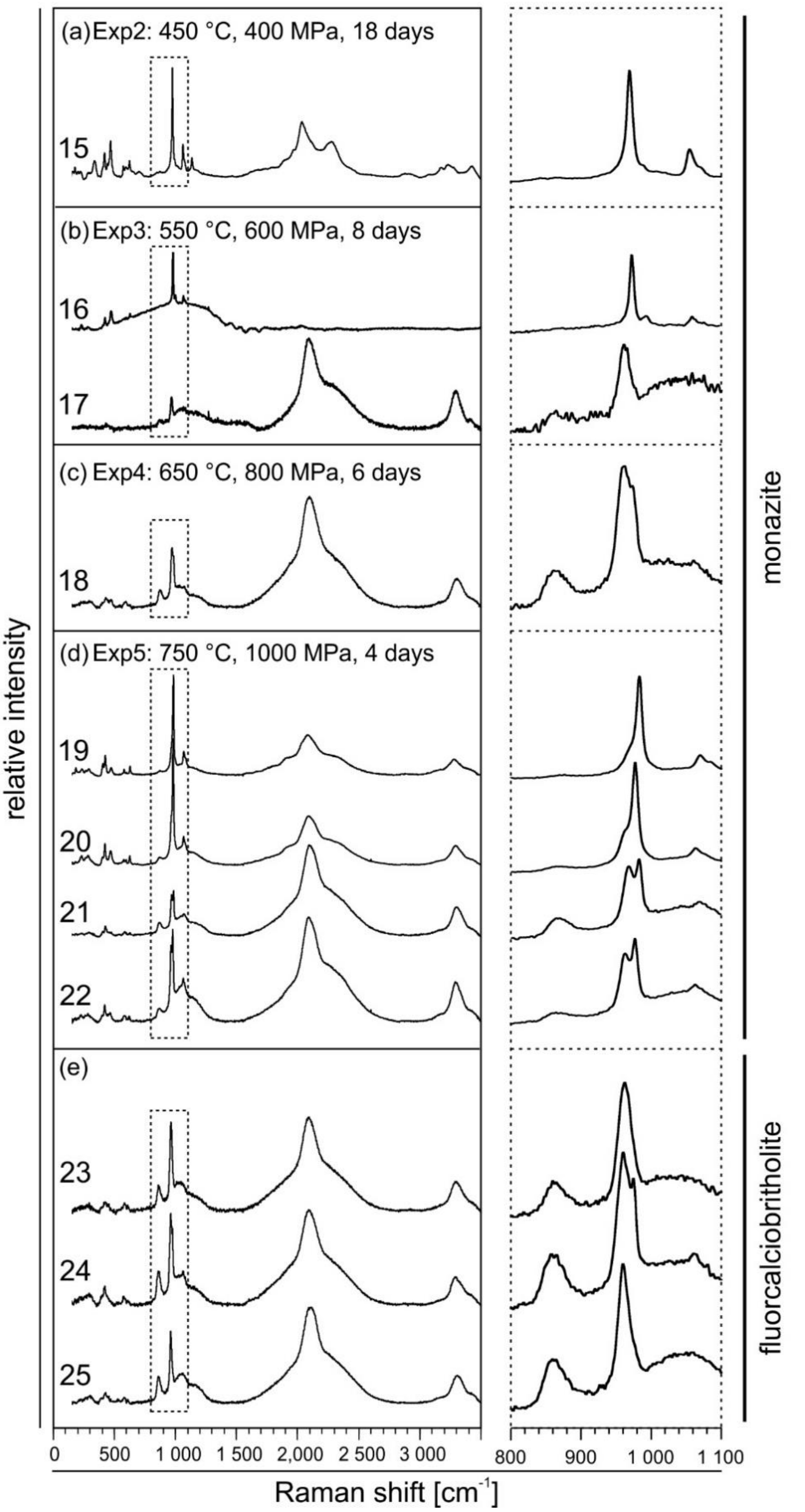

Fig. 24. Raman spectra that demonstrate major differences compared to that of Burnet monazite. (a–d) Monazite spectra and (e) fluorcalciobritholite spectra from experimental products of Exp2–Exp5 were obtained with 532 nm laser (instrument A). The spectral changes compared to Burnet monazite spectrum include peak shift of the v_1PO_4 symmetric stretching band, development of shoulders or distinct new peaks, increased intensity and broadening of fluorescence effects at mid-range and high-range (see text for details). Right side – zoomed-in spectra corresponding to dotted rectangles.

The dominant Raman band of fluorcalciobritholite is located at lower wavenumbers (960–962 cm^{-1}) compared to the $v_1(PO_4)$ band of monazite (969–983 cm^{-1}). One fluorcalciobritholite spectrum displays splitting into two bands, a prominent band at 960 cm^{-1} and a band of slightly lesser intensity at 975 cm^{-1} (spectrum 24; Fig. 24e).

Comparison of FWHH values of the $v_1(PO_4)$ symmetric stretching band vs. calculated FWHH values based on EPMA data of the Th, U, Ca and Pb content provide valuable information about the monazite structure, particularly because monazite can develop a significant structural disorder due to accumulation of self-radiation damage over time (Ruschel et al. 2012). Measured FWHH values of the Burnet monazite are significantly higher than calculated values (12.21–15.85 cm^{-1} vs. 7.23–8.67 cm^{-1}, respectively; Fig. 25a).

Raman data of monazite from Exp1–Exp3 follow a similar trend in unaltered domains, which generally yield higher values of measured FWHH than calculated values (7.93–15.23 cm^{-1} vs. 7.31–9.16 cm^{-1}, respectively). On the other hand, measured FWHH of altered domains demonstrate lower values than calculated ones (1.72–6.38 cm^{-1} vs. 5.78–8.83 cm^{-1}, respectively; Fig. 25b–d).

Measured FWHH values of monazite from Exp4 and Exp5 belong solely to compositionally unaltered domains and measured FWHH are generally lower than calculated values (3.02–12.75 cm^{-1} vs. 7.58–10.21 cm^{-1}, respectively; Fig. 25e, f). The combined Raman data of compositionally unaltered monazite domains from experiments (Exp1–Exp5) demonstrate a general trend of decreasing FWHH values with increasing temperature conditions.

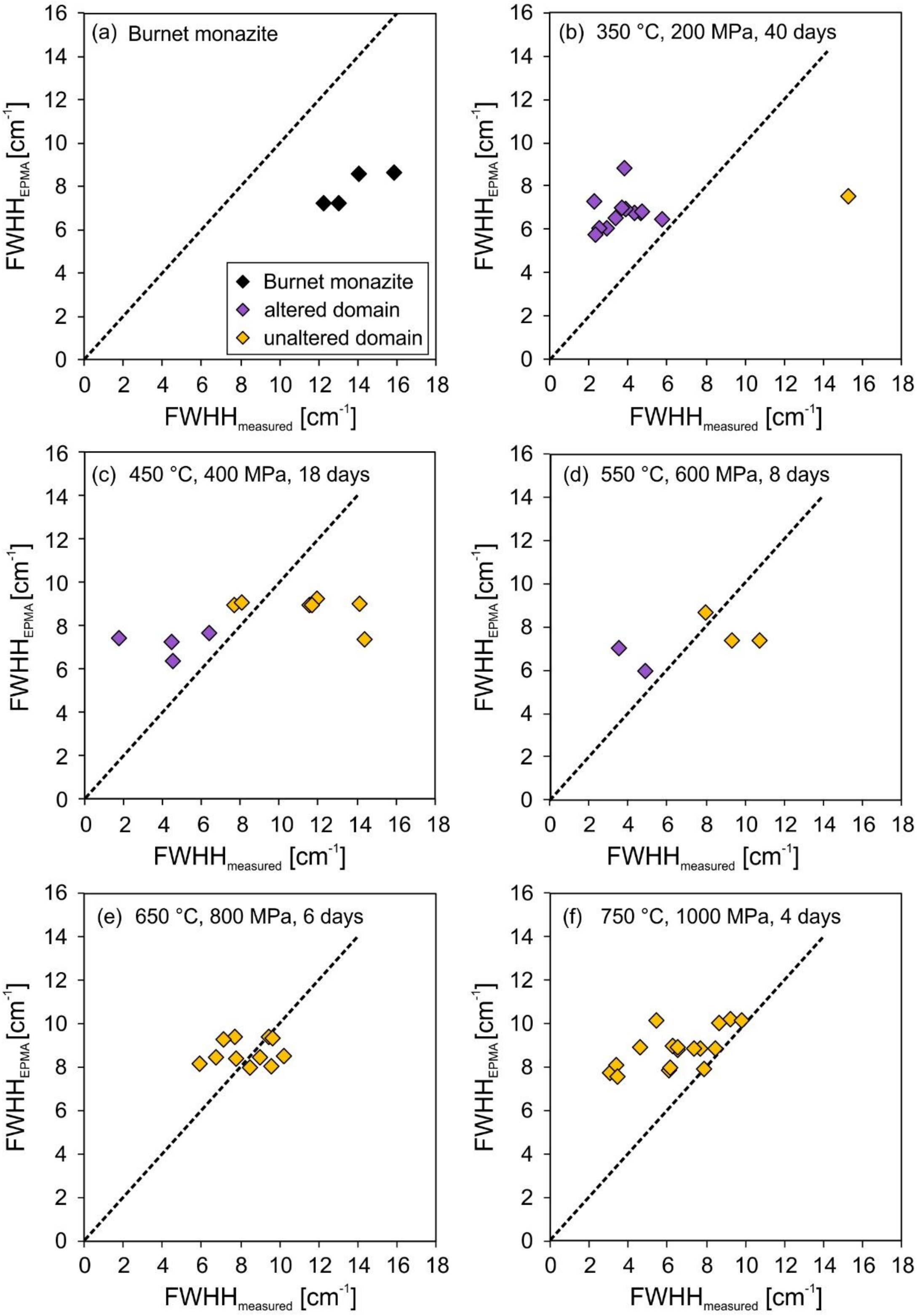

Fig. 25. Measured FWHH values vs. calculated FWHH of $v_1(PO_4)$ symmetric stretching band of Burnet monazite and monazite from experimental products. Calculated FWHH values based on the compositional EPMA data using the formula FWHH [cm^{-1}] = 3.95 + 26.66 × (Th + U + Ca + Pb) [apfu] after Ruschel et al. (2012).

Table 6. Raman data of monazite and fluorcalciobritholite from experiments (532 nm and 633 nm).

Raman spectra and corresponding Raman spots of monazite and fluorcalciobritholite							
Exp2 (monazite)(2)	Exp3 (monazite)(2)		Exp4 (monazite)(2)	Exp5 (monazite)(2)			
spectrum 15 (*n* = 3)	spectrum 16 (*n* = 1)	spectrum 17 (*n* = 1)	spectrum 18 (*n* = 3)	spectrum 19 (*n* = 4)	spectrum 20 (*n* = 6)	spectrum 21 (*n* = 2)	Spectrum 22 (*n* = 2)
spot: 50-52	spot: 62	spot: 56	spot: 69, 70, 82	spot: 94, 98, 99, 119	spot: 110–112, 115, 127, 134	spot: 101, 121	spot: 109, 133
(w) 171	-	-	-	-	-	-	-
-	(w) 224	-	-	-	(w) 227	-	-
-	-	-	-	-	(w) 282	-	-
(w) 331	-	-	-	-	-	-	-
-	-	-	-	-	(w) 398	-	-
(m) 412	(w) 416	-	-	(w) 405	(w) 419	-	-
-	-	-	-	(m) 425	-	(m) 425	(m) 420
(m) 461	(m) 466	-	-	(w) 473	(w) 466	-	(w) 459
(w) 567	-	-	-	-	-	-	-
(w) 617	-	-	-	(w) 628	(w) 622	-	-
-	-	-	-	-	-	(m) 869	(w) 868
-	-	**(s) 962**	**(s) 963**	-	sh(m) 963	-	(s) 962
sh(w) 957	-	-	-	sh(m) 976	-	-	-
(s) 969	**(s) 973**	-	-	**(s) 983**	**(s) 977**	**(s) 967**	**(s) 977**
sh(w) 984	sh(w) 993	-	*(m) 1024*	-	sh(w) 990	(s) 982	-
(m) 1054	(w) 1059	-	-	-	-	*(s) 1040*	(m) 1032
sh(w) 1067	-	-	-	-	(w) 1063	-	(w) 1065
-	-	(vs) 1086	-	(w) 1070	sh(w) 1078	-	(m) 1159
(w) 1129	-	-	*(s) 1182*	-	-	-	-
mid-range fluorescence effects							
sh(w) 1896	-	-	-	*sh(w) 1809*	*sh(w) 1811*	-	*sh(m) 1833*
(m) 2027	-	-	*sh(s) 1927*	*(w) 1919*	*sh(w) 1927*	*sh(s) 1949*	*sh(w) 1935*
sh(m) 2085	-	*(vs) 2087*	*(vs) 2085*	*sh(m) 2081*	*(m) 2084*	*(vs) 2099*	*(vs) 2088*
(m) 2271	-	*sh(vs) 2261*	*sh(vs) 2230*	*sh(m) 2291*	*sh(m) 2260*	*sh(vs) 2247*	*sh(s) 2245*
high-range fluorescence effects							
-	-	-	-	-	-	-	*sh(w) 3167*
(w) 3235	-	*(vs) 3291*	*(s) 3292*	*(m) 3289*	*(w) 3293*	*(s) 3299*	*(s) 3293*
(w) 3419	-	-	-	-	-	-	*sh(w) 3404*
-	-	-	-	-	-	-	-

Notes:

(1) – band assignment to monazite after data of $LaPO_4$ – $GdPO_4$ end-members (Table 4) and according to previous studies (Begun et al. 1981; Silva et al. 2006)

(2) – data collected with instrument A (532 nm) corresponding to spectra in Fig. 24 and Raman spots in Fig. 19

(3) – data collected with instrument B (633 nm) corresponding to spectra 1 (Mnz) and 5 (Fcbri) in Fig. 26f and Raman spots in Fig. 26j

sh – shoulders, *italic – fluorescence bands*

Intensities of presented data are normalized to most dominant Raman band (**bold**) equal to 1.0: weak (w) 0.05–0.2, medium (m) 0.2–0.5, strong (s) 0.5–1.0, very strong (vs) >1.0; *sh* – shoulders; * – fluorescence

Only significant signals above background are presented.

Table 6. (Continued).

Raman spectra and corresponding Raman spots of monazite and fluorcalciobritholite					**assigned band(1)**	
Exp4–Exp5 (fluorcalciobritholite)(2)			Exp5 (monazite)(3)	Exp5 (fluorcalciobritholite)(3)		
spectrum23 (n = 1)	spectrum24 (n = 1)	spectrum25 (n = 1)	spectrum1 (n = 1)	spectrum5 (n = 1)	symmetry	modes
spot: 131	spot: 130	spot: 114	spot: 1	spot: 5		
-	-	-	(w) 179	-	Bg	lattice
-	-	-	-	-	Ag,Bg	lattice
-	(w) 297	-	(w) 286	-	Ag	lattice
-	-	-	-	-	-	-
-	-	-	(m) 400	-	Ag,Bg	lattice
-	-	-	-	-	Ag,Bg	lattice
-	(m) 419	-	(m) 420	(m) 424	Ag,Bg	lattice
-	-	-	(w) 467	-	Ab,Bg	v$_2$(PO$_4$)
-	-	-	(w) 574	-	-	-
-	-	-	(w) 624	-	Ag,Bg	v$_4$(PO$_4$)
(m) 863	(m) 861	(m) 862	-	(s) 868	-	-
(s) 962	**(s) 960**	**(s) 960**	sh(m) 961	(s) 962	-	-
-	(s) 975	-	**(s) 976**	-	Ag,Bg	v$_1$(PO$_4$)
-	-	-	-	-	-	-
(m) 1025	*(m) 1014*	-	-	-	-	-
-	-	*(s) 1046*	-	-	-	-
-	(w) 1062	-	(m) 1064	-	Ag,Bg	v_3(PO$_4$)
-	-	-	(w) 1079	-	-	-
-	-	*sh(w) 1181*	-	-	-	-
mid-range fluorescence effects						
-	-	-	-	-	-	-
sh(m) 1895	*sh(m) 1936*	*sh(m) 1962*	-	-	-	-
(s) 2089	*(s) 2092*	*(s) 2101*	-	-	-	-
sh(s) 2212	*sh(s) 2234*	*sh(s) 2253*	-	-	-	-
high-range fluorescence effects						
-	-	-	-	-	-	-
(m) 3294	*(m) 3285*	*sh(w) 3202*	-	-	-	-
-	*sh(w) 3376*	*(m) 3309*	-	-	-	-
-	-	*sh(w) 3423*	-	-	-	-

4.3.4. Comparison of Raman spectra of monazite from Exp1 and Exp5 – instruments A (780 nm) and B (488 nm, 532 nm and 633 nm)

Two grains of monazite from Exp1 and a cluster of monazite-chunks from Exp5, which are embedded in melt, were selected for analyses with instrument B using 488 nm, 532 nm and 633 nm lasers (Fig. 26). Spectra of monazite (488 nm, Instrument B) show significant fluorescence effects that superimpose the primary Raman features (Fig. 26a, b). The symmetric stretching band $v_1(PO_4)$ in the monazite grains from Exp1 and from the core of monazite from Exp5 (spectra 1 and 2) is located at 981 cm^{-1} (Fig. 26a, b). The $v_1(PO_4)$ band of monazite spectra from the rim closely to fluorcalciobritholite is shifted to 965–966 cm^{-1}, which corresponds well to the dominant band at 965 cm^{-1} in the fluorcalciobritholite spectrum (spectra 3–5; Fig. 26b).

The monazite spectra (instrument B; 532 nm) generally show the same features as spectra measured with instrument A (Figs. 23, 26c, d). However, the spectra from Exp1 show additional fluorescence effects at 2900–3000 cm^{-1}, which are not documented in any Raman spectrum from instrument A. One monazite spectrum from Exp5 collected close to fluorcalciobritholite shows splitting of the $v_1(PO_4)$ band into two peaks: (i) a peak at 965 cm^{-1} similar to peak position of REE-rich fluorcalciobritholite (965–966 cm^{-1}) and (ii) a peak at 979 cm^{-1}, consistent with the peak position of 979–980 cm^{-1} in monazite (spectrum 3; Fig. 26d).

Spectra recorded with the 633 nm laser (instrument B), display the least interference of fluorescence effects in the range of 100–2600 cm^{-1} compared to spectra of 488 nm and 532 nm lasers (Fig. 26e, f). Fluorescence effects, however, is present as a broad background (750–1000 cm^{-1}) in monazite from experiment Exp5 (Fig. 26f). All peak positions obtained with 633 nm laser are slightly shifted towards lower wavenumbers compared to spectra obtained with 488 nm and 532 nm lasers. Positions of the $\nu_1(PO_4)$ band of monazite are located at 974–976 cm^{-1}, whereas the peak position from REE-rich fluorcalciobritholite is positioned at 961 cm^{-1}.

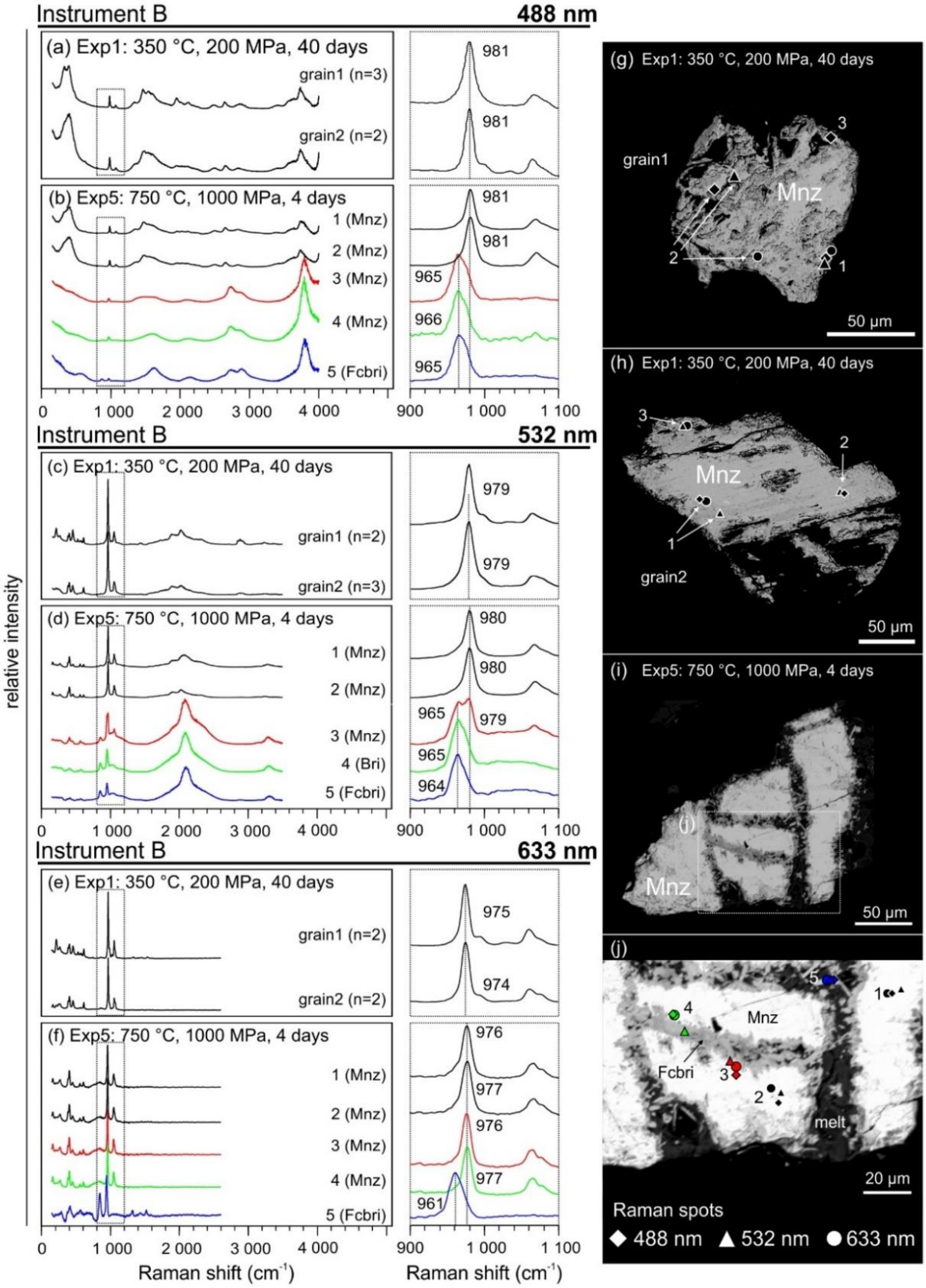

Fig. 26. Raman spectra of selected monazite grains from Exp1 and Exp5 obtained with 480 nm, 532 nm, 633 nm lasers measured at similar positions (instrument B; 488 nm, 532 nm and 633 nm). Diamond – Raman spot with 488 nm laser, triangle – Raman spot with 532 nm laser, circles – Raman spot with 633 nm laser. Right side – zoomed-in spectra corresponding to dotted rectangles in range of 900–1100 cm^{-1}. (g–j) BSE images of monazite with marked Raman spots. Mineral abbreviations: Fcbri – fluorcalciobritholite, Mnz – monazite.

A monazite spectrum (instrument A; 780 nm) from Exp1 shows fluorescence effects, which completely superimpose the primary Raman features (Fig. 27a). Fluorescence is possibly caused by combined contribution of La^{3+}, Ce^{3+} and potentially Gd^{3+}, which is reflected in reference spectra of $LaPO_4$, $CePO_4$ and $GdPO_4$ (Fig. 27b). Therefore, the 780 nm laser is suggested here as not useful for Raman characterization of natural monazite-(Ce).

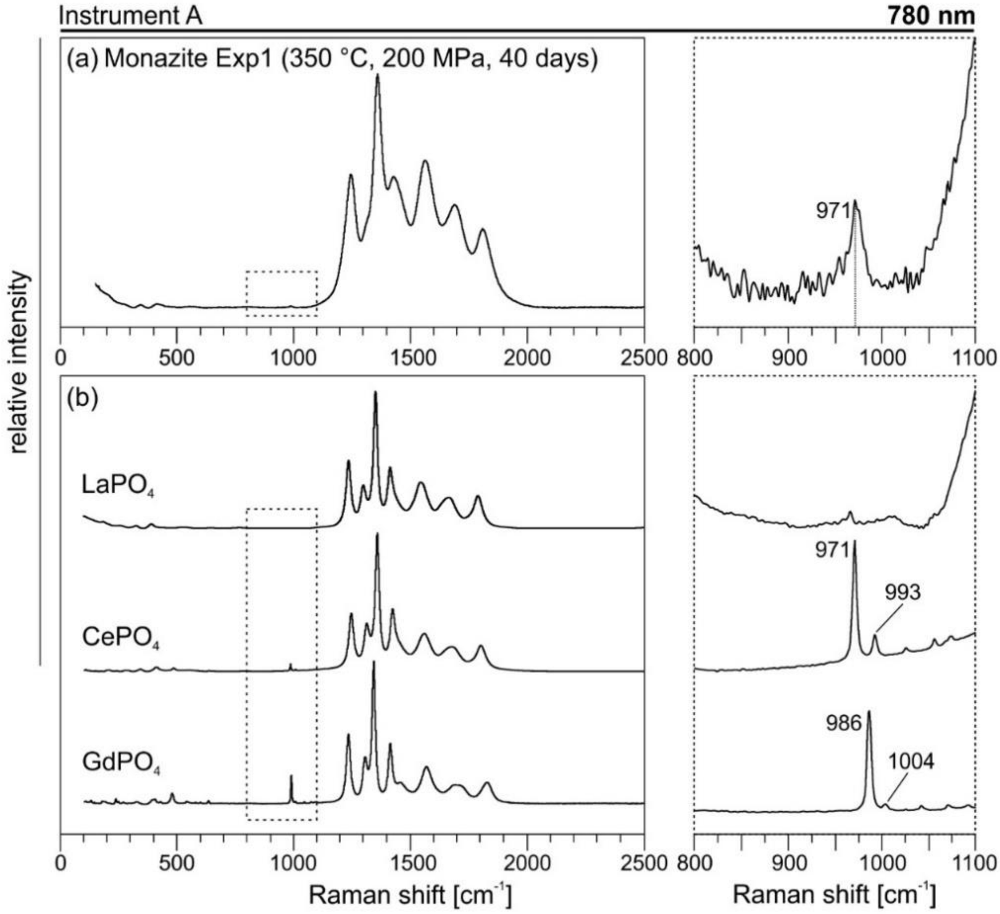

Fig. 27. Raman spectra (instrument A; 780 nm) of (a) monazite from Exp1 and (b) synthetic $LaPO_4$, $CePO_4$ and $GdPO_4$. The spectra are dominated by fluorescence effects. Right side – zoomed-in spectra corresponding to dotted rectangles.

4.3.5. Raman microspectroscopy of the Ankazobe monazite – instrument A (532 nm)

Raman spectra of compositionally unaltered domains of the Ankazobe monazite are similar to Raman spectra of the Burnet monazite. Similarities include (i) lattice modes, (ii) pronounced internal bending modes (500–700 cm^{-1}) with a lesser symmetric bending $\nu_2(PO_4)$ mode at 466 cm^{-1}, (iii) the dominant $\nu_1(PO_4)$ symmetric stretching band at 976 cm^{-1} and (iv) a similar fluorescence effects at mid- and high-range (Fig. 28a). Raman spectra of altered domains show increased background-fluorescence (800–1500 cm^{-1}) and either a new broad peak at ca. 1325 cm^{-1} (spectrum 27) or a low intensity spectrum with negligible mid-range fluorescence effects, and no fluorescence effects at high-range (spectrum 28). Measured FWHH values of $v_1(PO_4)$ symmetric stretching band are higher than calculated FWHH in both, unaltered domains (10.52–13.22 cm^{-1} vs. 6.46–6.60 cm^{-1}, respectively) and altered domains (6.32–10.15 cm^{-1} vs. 4.26–6.34 cm^{-1}, respectively; Fig. 28b).

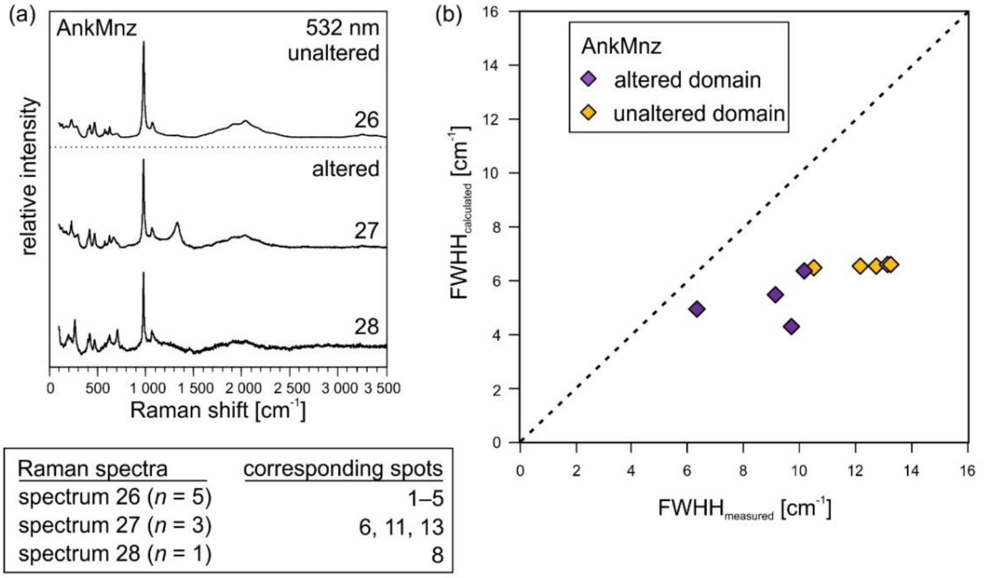

Raman spectra	corresponding spots
spectrum 26 (*n* = 5)	1–5
spectrum 27 (*n* = 3)	6, 11, 13
spectrum 28 (*n* = 1)	8

Fig. 28. Raman data (instrument A) of Ankazobe monazite (AnkMnz). (a) Raman spectra of unaltered Ankazobe monazite are similar to those of the Burnet monazite, whereas spectral variation is present in altered domains. Raman spots corresponding to spectra are shown in Fig. 21. (b) Calculated FWHH values based on the compositional EPMA data using the formula FWHH [cm^{-1}] = 3.95 + 26.66 × (Th + U + Ca + Pb) [apfu] (after Ruschel et al. 2012).

4.3.6. Hyperspectral mapping and EPMA-WDS compositional X-ray mapping of monazite – instrument B (532 nm and 633 nm)

Hyperspectral maps (instrument B) were conducted on selected areas of monazite grains from Exp5 (1000 MPa, 750 °C) using 532 nm and 633 nm lasers (Fig. 29). The maps were collected using a 1 µm step size. A combined image from characteristic spectra were achieved using true compound analysis (TCA) based on a selection of characteristic Raman spectra of the various phases.

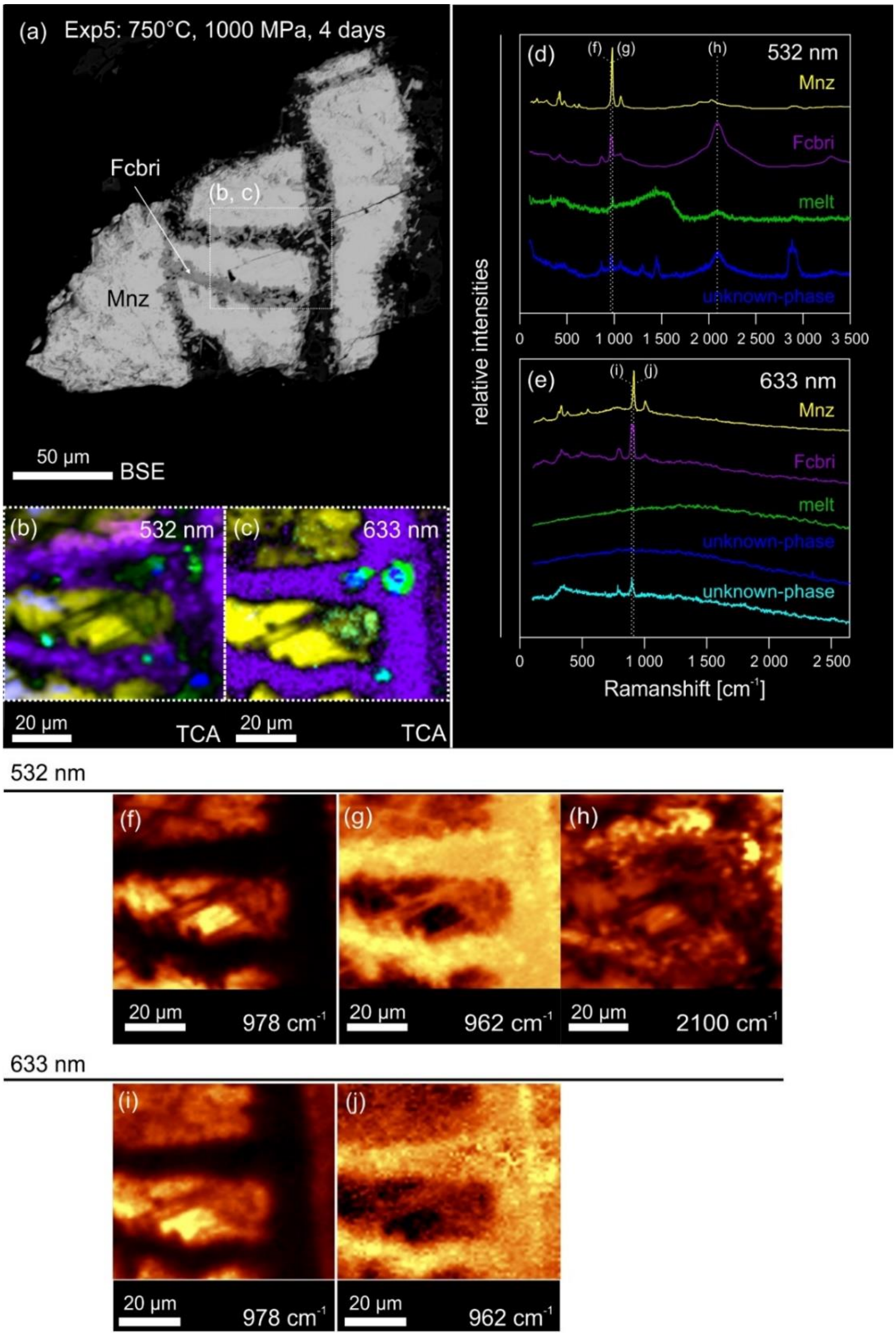

Fig. 29. Hyperspectral mapping (instrument B) of a selected area of monazite from Exp5 (1000 MPa / 750 °C / 4 days). (a, b) BSE image of overview and selected area. (c, d) TCA map of Raman spectra (532 nm) of individual phases. (e–g) Intensity maps of selected distinct bands: 978 cm^{-1} $v_1(PO_4)$ symmetric stretching band of monazite, 962 cm^{-1} dominant Raman band of REE-rich fluorcalciobritholite, 2100 cm^{-1} fluorescence effects at mid-range. (h, i) TCA map of Raman spectra (633 nm) of individual phases. (j, k) Intensity maps of selected bands. Abbreviations: Fcbri – fluorcalciobritholite, Mnz – monazite.

The monazite grains are embedded in melt and secondary REE-rich fluorcalciobritholite crystals formed in the gaps between monazite grains and at dissolution pits. The resulting spectral image correlates well with the BSE image (TCA; Fig. 29a–c). Intensity maps of the $v_1(PO_4)$ symmetric stretching band obtained with 532 nm and 633 nm lasers, reveal two domains in monazite: (i) a domain with peak position at 978 cm^{-1}, which fits to the general Raman data of the monazite, and (ii) a domain with a significant shift towards 962 cm^{-1} (Fig. 29f–j).

Additional EPMA-WDS compositional X-ray mapping demonstrates small compositional variations in the same area of hyperspectral mapping (Fig. 30). The monazite is homogeneous, whereas Th-rich microinclusions are present at the rim of monazite (Fig. 30b).

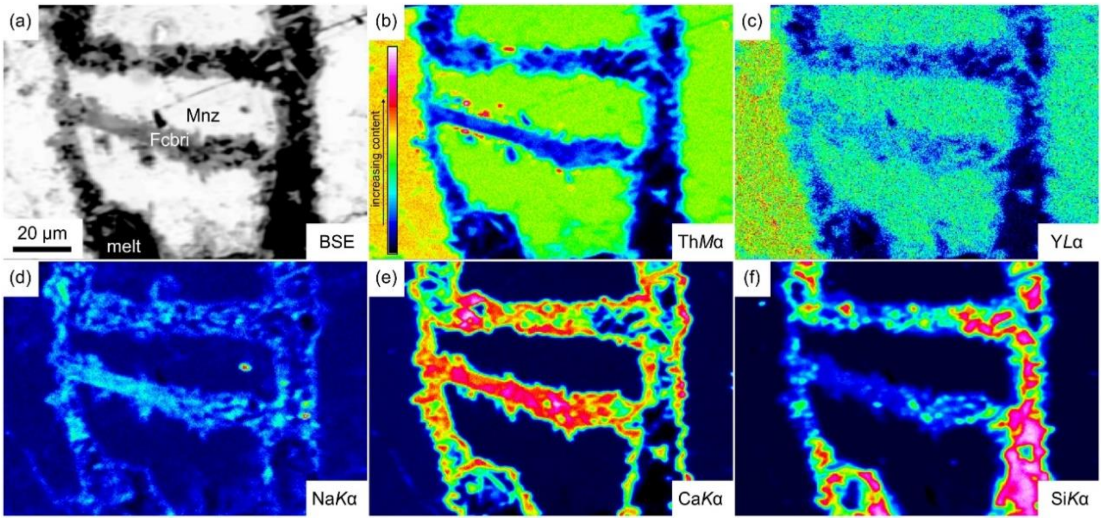

Fig. 30. EPMA-WDS compositional X-ray maps of a selected area of monazite from Exp5 (1000 MPa / 750 °C), which correspond to the area of hyperspectral mapping. Mineral abbreviations: Fcbri – fluorcalciobritholite, Mnz – monazite.

4.4. Results of Raman microspectroscopy of xenotime

4.4.1. Textural and compositional characteristics of xenotime

The NWFP xenotime displays a homogenous contrast in BSE image. The compositional details of NWFP xenotime are presented in Supplementary Table B6. Chondrite-normalized data of NWFP xenotime follow the LREE << HREE patterns typical for xenotime and demonstrate a steep increasing slope from La to Tb, followed by a gentle nearly flat decreasing slope from Tb to Lu (Fig. 32).

Xenotime grains from experiments at P-T conditions of 200 MPa / 350 °C, 400 MPa / 450 °C and 600 MPa / 550 °C (Exp1–Exp3) are homogeneous in BSE imaging without textural evidence of alteration (Fig. 31a–h). Xenotime grains from experiments at high P-T conditions of 800 MPa / 650 °C and 1000 MPa / 750°C (Exp4 and Exp5) display alteration at their rims in the form of partial dissolution and formation of Y-rich fluorcalciobritholite (Fig. 31i–l). The composition of xenotime from all experiments (200 MPa / 350 °C, 400 MPa / 450 °C, 600 MPa / 550 °C, 800 MPa / 650 °C, 1000 MPa / 750 °C) is similar to the composition of NWFP xenotime (Supplementary Table B6). Chondrite normalized patterns of xenotime from experiments are similar to those of NWFP xenotime (Fig. 32). These include variations from La to Nd and small variations from Tm to Lu in xenotime grains from lower P-T conditions (200 MPa / 350 °C, 400 MPa / 450 °C; Fig. 32b, c), whereas xenotime grains from moderate to high P-T conditions (600 MPa / 550 °C, 800 MPa / 650 °C, 1000 MPa / 750 °C) display homogenous REE distribution from La to Lu (Fig. 32d–f).

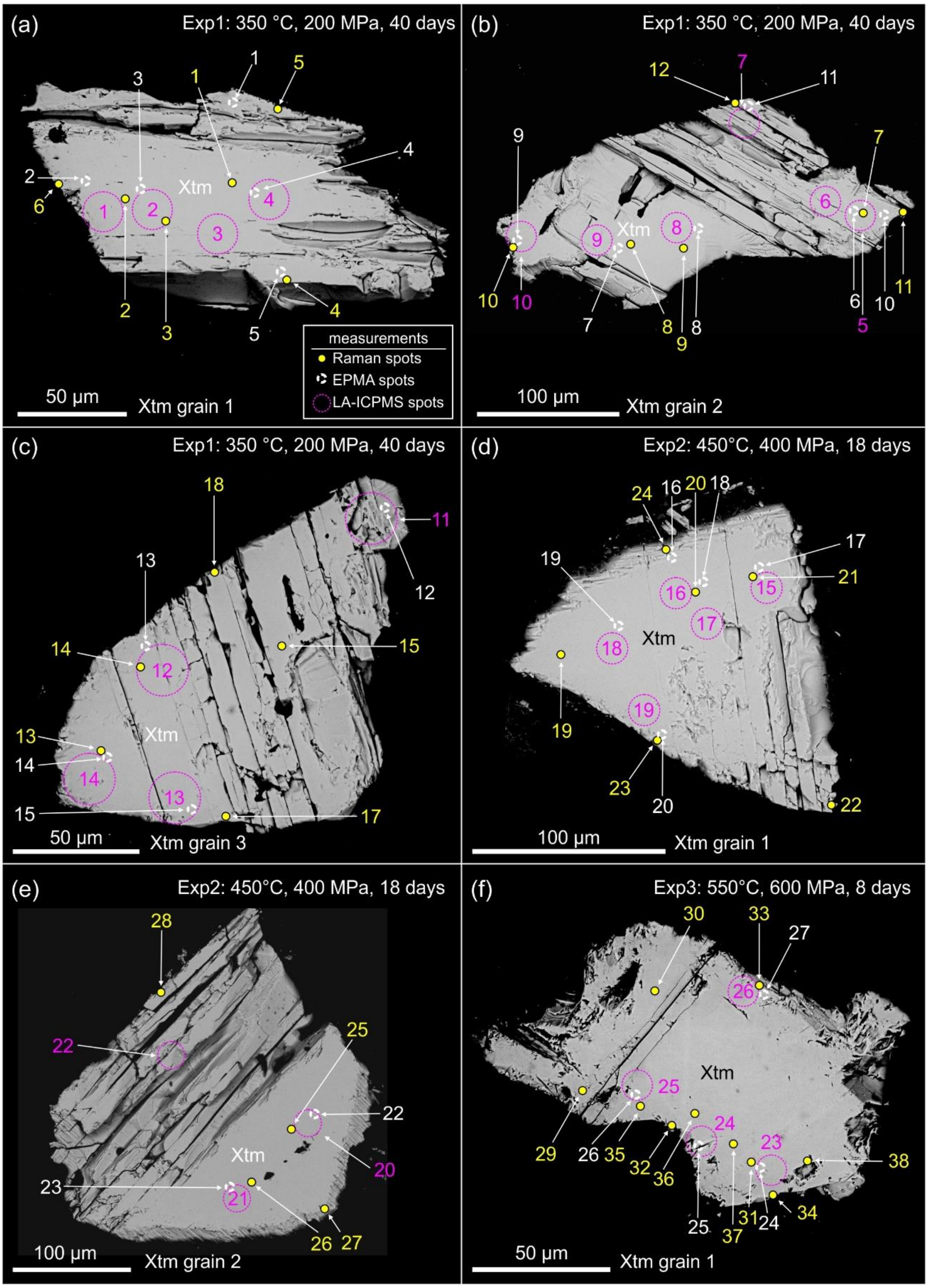

Fig. 31. BSE images of xenotime from the experimental products (Exp1–Exp5) with marked Raman, EPMA and LA-ICPMS spots. Mineral names abbreviations: Xtm – xenotime, YFcbri – Y-rich fluorcalciobritholite.

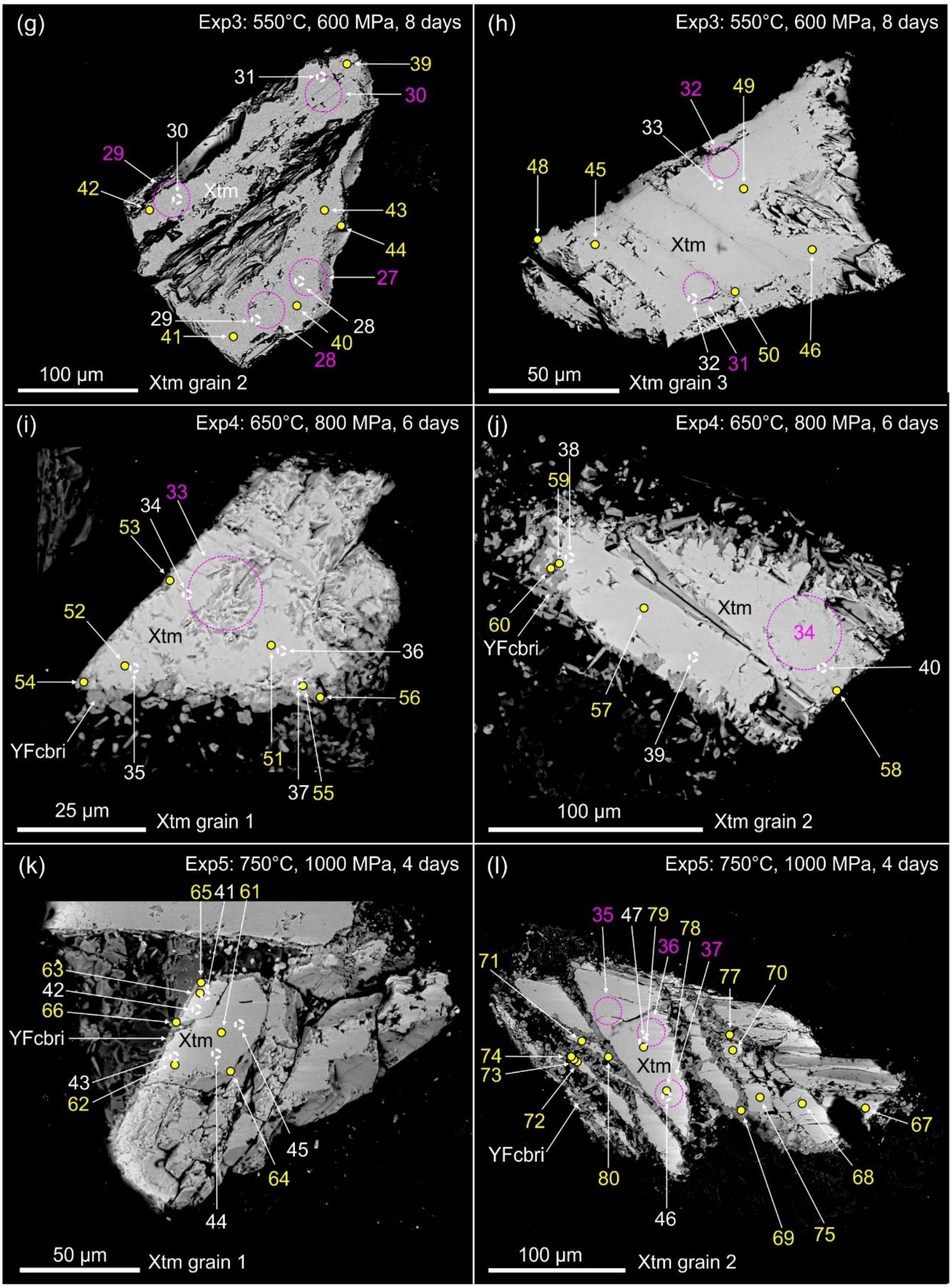

Fig. 31. (continued)

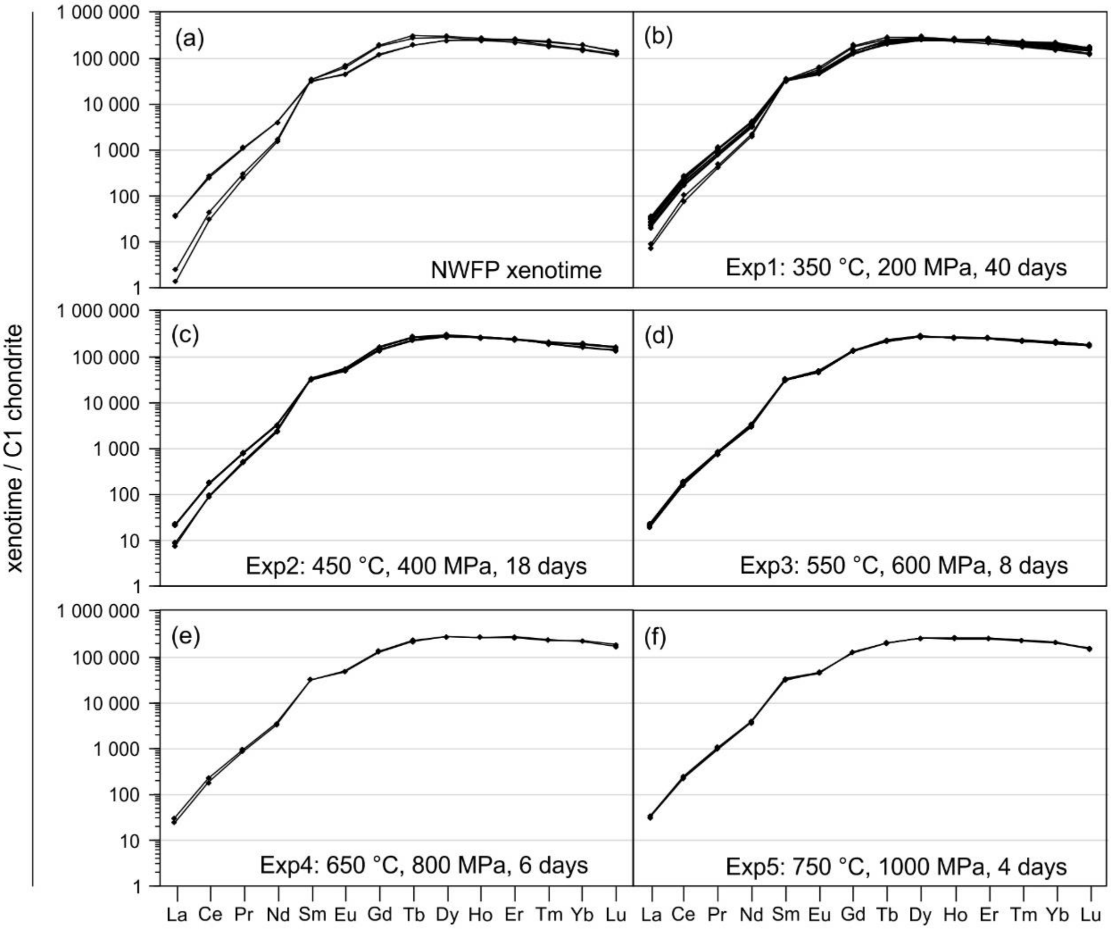

Fig. 32. Chondrite-normalized REE patterns of NWFP xenotime and xenotime from experimental products. C1 chondrite composition from McDonough and Sun (1995).

4.4.2. Raman microspectroscopy of NWFP xenotime, $TbPO_4$–$LuPO_4$ and YPO_4 – instrument A (532 nm and 780 nm)

The Raman spectrum of the NWFP xenotime includes primary Raman features of $v_1(PO_4)$ symmetric stretching band and $v_2(PO_4)$ antisymmetric stretching band, whereas lattice modes and internal bending modes are superimposed by fluorescence effects at low-range (100–800 cm^{-1}; Fig. 33a; Table 7). The fluorescence effects of the REE phosphates $HoPO_4$, $ErPO_4$ (Fig. 33b), and $SmPO_4$ (Fig. 22b) are consistent to previous works, thus, attribution of characteristic electronic transitions responsible for fluorescence were done in accordance to Lenz et al. (2015). Low-range fluorescence effects contribute to electronic transitions of Ho^{3+} ($^5S_2 \rightarrow {}^5I_8$) and Er^{3+} ($^4S_{3/2} \rightarrow {}^4I_{15/2}$), which are also present in Raman spectra of synthetic $HoPO_4$ and $ErPO_4$ (Fig. 33b; Table 7). The NWFP xenotime shows weak to moderate fluorescence signals at mid-range (1500–3000 cm^{-1}), which are caused by Eu^{3+} ($^5D_0 \rightarrow {}^7F_2$), Sm^{3+} ($^4G_{5/2} \rightarrow {}^6H_{9/2}$) and Eu^{3+} ($^5D_0 \rightarrow {}^7F_3$) ions. Finally, the spectrum of NWFP xenotime shows moderate to strong fluorescence effects at high-range (3000–3500 cm^{-1}) contributed by Sm^{3+} ($^4G_{5/2} \rightarrow {}^6H_{9/2}$) and Ho^{3+} ($^5F_5 \rightarrow {}^5I_8$) ions.

4.4.3 Raman microspectroscopy of xenotime from experiments – instrument A (532 nm)

The majority of xenotime spectra from experimental products are very similar, which is related to the chemical stability of xenotime (spectra 1–4, 7; Fig. 34a–e; Table 8). However, some spectra of xenotime from experiments Exp4 and Exp5 (800 MPa / 650 °C, 1000 MPa / 750 °C) show significant spectral variation (spectra 5, 6, 8, 9; Fig. 34d, e; Table 8). These include (i) increase of background fluorescence at low-range and broadening of Ho^{3+} and Er^{3+} fluorescence-bands, (ii) development of a shoulder at ca. 800 cm^{-1}, (iii) broadening of mid-range fluorescence effects, and (iv) significant broadening and increased intensity of Eu^{3+} ($^5D_0 \rightarrow {}^7F_3$) fluorescence effects at ca. 2650 cm^{-1} (spectra 6, 9; Fig. 34d, e). The $\nu_1(PO_4)$ symmetric stretching band of xenotime is stable at positions of ca. 1000–1001 cm^{-1}, however, a subtle band occasionally appears at ca. 967 cm^{-1} (spectra 5, 6, 8, 9; Fig. 34d, e; Table 8). Comparing Raman spectra of Y-rich fluorcalciobritholite with those of xenotime, fluorescence effects generally show higher intensity and broadening, and the Er^{3+} ($^5D_0 \rightarrow {}^7F_3$) fluorescence band is the most prominent band at ca. 2641–2647 cm^{-1} (Fig. 34d, e).

Fluorescence effects at high-range (induced by Sm^{3+} and Ho^{3+}) are not present in the spectra of Y-rich fluorcalciobritholite. Weak bands at 966–970 cm^{-1} are interpreted as the primary Raman band of the Y-rich fluorcalciobritholite. These are at higher Raman shift than Raman bands of fluorcalciobritholite from experiments with monazite located at 960–962 cm^{-1} (Figs. 24f, 34f). The additional band at ca. 860 cm^{-1} observed in REE-rich fluorcalciobritholite spectra is not present, however, in Raman spectra of Y-rich fluorcalciobritholite.

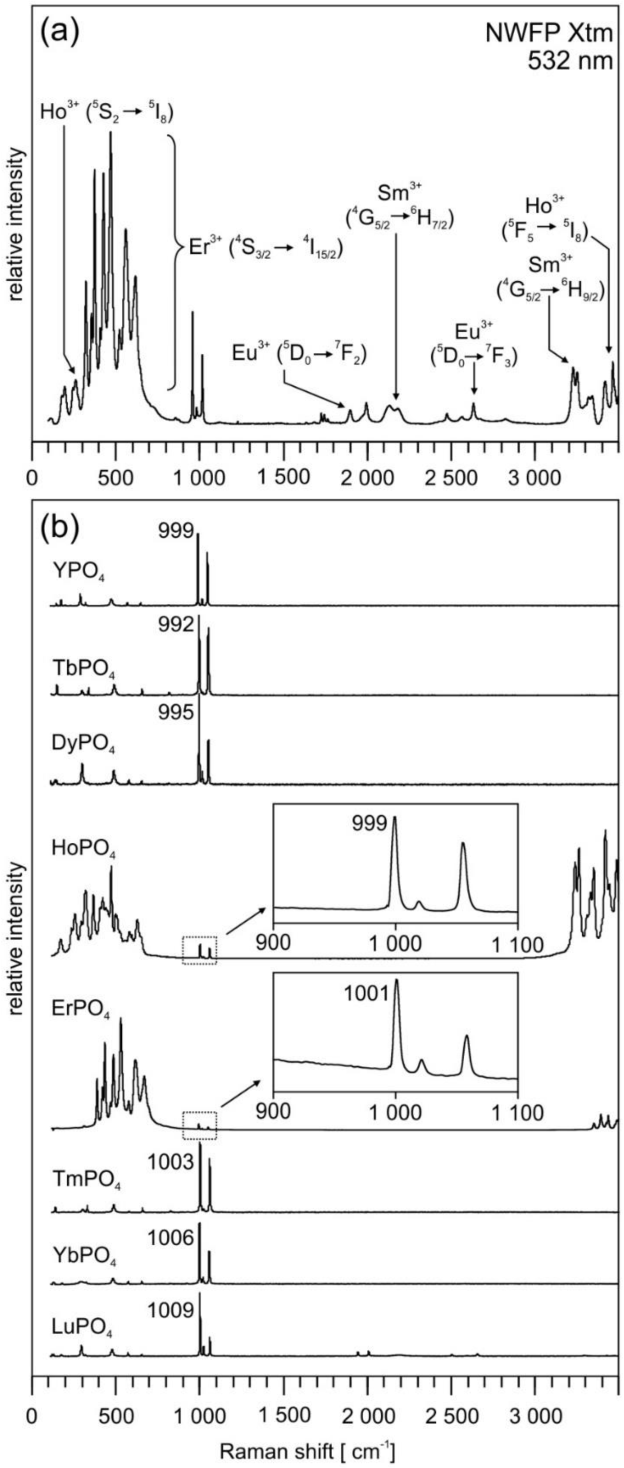

Fig. 33. Raman spectra of NWFP xenotime, and synthetic $TbPO_4$–$LuPO_4$ and YPO_4. Electronic transitions attributed to fluorescence after Lenz et al. (2015).

Table 7. Raman data of NWFP xenotime (532 nm laser), and synthetic $TbPO_4$–$LuPO_4$ and YPO_4 (532 nm and 780 nm lasers).

532 nm	**532 nm**							
NWFP Xtm	YPO_4	$TbPO_4$	$DyPO_4$	$HoPO_4$	$ErPO_4$	$TmPO_4$	$YbPO_4$	$LuPO_4$
-	-	-	(w) 128	-	-	-	-	-
-	-	(w) 138	(w) 138	-	-	(w) 136	-	-
-	-	-	-	*(vs) 167*	-	-	-	-
-	(w) 182	-	-	-	-	-	-	-
(m) 231	-	-	-	*(vs) 232*	-	-	-	-
(m) 250	-	-	-	*(vs) 252*	-	-	-	-
(w) 295	(w) 296	(w) 289	(m) 293	*(vs) 290*	-	(w) 301	-	(w) 303
(m) 314	(w) 329	(w) 329	-	*(vs) 316*	-	(w) 327	-	-
(vs) 373	-	-	-	*(vs) 362*	*(vs)377*	-	-	-
(s) 406	-	-	-	*(vs) 404*	*(vs)410*	-	-	-
(vs) 425	-	-	-	*(vs) 418*	*(vs)424*	-	-	-
-	-	-	-	*(vs) 436*	-	-	-	-
(m) 456	-	-	-	*sh(vs) 445*	*(vs)458*	-	-	-
-	-	-	-	*(vs) 468*	-	-	-	-
(vs) 477	(w) 481	(w) 482	(w) 483	*(vs) 494*	*(vs)477*	(w) 486	(w) 487	(w) 486
(vs) 519	-	-	-	*(vs) 503*	-	-	-	-
-	-	-	-	*(vs) 521*	*(vs)523*	-	-	-
-	-	-	-	*(vs) 554*	-	-	-	-
(m) 570	-	-	(w) 574	*(vs) 577*	*(vs)571*	-	-	(w) 581
(vs) 609	-	-	-	*(vs) 593*	-	-	-	-
-	-	-	-	*(vs) 624*	*(vs)611*	-	-	-
(vs) 662	-	(w) 649	(w) 651	*(vs) 645*	*(vs)666*	(w) 658	(w) 660	-
(w) 695	-	-	-	-	-	-	-	-
-	-	(w) 813	-	-	-	-	-	-
(s) 999	**(s) 999**	**(s) 993**	**(s) 995**	**(s) 999**	**(s)1001**	**(s) 1003**	**(s) 1006**	**(s) 1009**
-	-	-	-	-	-	sh(w) 1008	-	-
(w) 1023	(w) 1024	-	(w) 1016	(w) 1019	(w)1021		(w) 1027	(w) 1030
(s) 1056	(s) 1056	(s) 1048	(m) 1052	(s) 1055	(m)1058	(s) 1061	(s) 1065	(m) 1067
mid-range fluorescence effects								-
(w) 1755	-	-	-	-	-	-	-	-
(w) 1773	-	-	-	-	-	-	-	-
(w) 1924	-	-	-	-	-	-	-	*(w) 1948*
(m) 2019	-	-	-	-	-	-	-	*(w) 2013*
(w) 2155	-	-	-	-	-	-	-	-
(w) 2204	-	-	-	-	-	-	-	-
(w) 2492	-	-	-	-	-	-	-	-
(w) 2578	-	-	-	-	-	-	-	-
(m) 2649	-	-	-	-	-	-	-	-
high-range fluorescence effects								
(s) 3232	-	-	-	*(vs) 3234*	-	-	-	-
(s) 3256	-	-	-	*(vs) 3257*	-	-	-	-
(m) 3323	-	-	-	*(vs) 3306*	-	-	-	-
(m) 3345	-	-	-	*(vs) 3327*	-	-	-	-
(m) 3423	-	-	-	*(vs) 3345*	-	-	-	-
(s) 3465	-	-	-	*(vs) 3414*	*(vs) 3425*	-	-	-
-	-	-	-	*(vs) 3438*	*(vs) 3467*	-	-	-
-	-	-	-	*(vs) 3482*	-	-	-	-

Notes:

(1) – assigned bands according to Begun et al. (1981)

sh – shoulder; *italic – fluorescence bands*

Intensities of presented data are normalized to $v_1(PO_4)$ band (**bold**) equal to 1.0: weak (w) 0.05–0.2, medium (m) 0.2–0.5, strong (s) 0.5–1.0, very strong (vs) > 1.0

Only significant signals above background are presented.

Table 7. (Continued).

780 nm								**Assigned bands**(1)	
YPO_4	$TbPO_4$	$DyPO_4$	$HoPO_4$	$ErPO_4$	$TmPO_4$	$YbPO_4$	$LuPO_4$	symmetry	#
-	-	(w) 131	(w) 131	(w) 131	-	-	-	Bg	22B
-	(w) 140	-	(w) 139	(w) 139	-	-	(w) 139	Eg	21B
(w) 156	-	-	-	-	*(vs) 149*	-	-	-	-
(w) 185	-	-	-	-	*(vs) 182*	*(w) 182*	(w) 185	Bg	18B
-	-	-	-	-	-	-	-	-	-
-	-	-	-	-	*(vs) 263*	*(m) 263*	(w) 267	Eg	15B
(m) 299	(w) 291	(m) 294	(m) 297	(m) 299	*(vs) 309*	*(w) 303*	(m) 304	Eg	14B
(w) 331	(w) 331	-	(w) 329	(w) 321	*(vs) 343*	*(w) 345*	-	Bg	13B
-	-	-	-	(w) 384	*(vs) 388*	-	-	-	-
-	-	-	-	-	-	(w) 406		-	-
-	-	-	-	-	-	-	-	-	-
-	-	-	-	-	-	-	-	-	-
-	-	-	-	(w) 440	*(vs) 456*	-	-	-	-
-	-	-	-	-	-	-	-	-	-
(w) 484	(w) 484	(w) 485	(w) 485	(w) 486	-	(w) 489	(w) 488	Ag	10B
-	-	sh(w) 507	-	-	-	-	-	-	-
-	-	-	-	-	-	-	-	-	-
-	-	-	-	-	*(vs) 531*	-	-	-	-
(w) 581	-	(w) 576	(w) 577	(w) 579	*(vs) 576*	(w) 581	(w) 581	Eg	8B
-	-	-	-	-	-	-	-	-	-
-	-	-	-	-	-	-	-	-	-
(w) 659	(w) 650	(w) 652	-	(w) 657	-	-	(w) 664	Bg	6B
-	-	-	-	(w) 679	-	-	-	-	-
-	-	-	-	-	-	-	-	-	-
(s) 1001	**(s) 994**	**(s) 997**	**(s) 1000**	**(s) 1002**	**(s) 1005**	**(s) 1007**	**(s) 1010**	**Ag**	**1B**
-	-	-	-	-	-	-	-	-	-
(w) 1026		(w) 1017	(w) 1020	(w) 1023	(w) 1026	(w) 1028	(w) 1031	Eg	2B
(s) 1058	(s) 1049	(s) 1053	(s) 1056	(s) 1059	(s) 1063	(s) 1066	(s) 1068	Bg	3B
mid-range fluorescence effects									
-	-	-	-	-	-	-	-	-	-
-	-	-	-	-	-	-	-	-	-
-	-	-	-	-	-	-	-	-	-
-	-	-	-	-	-	-	-	-	-
-	-	-	-	-	-	-	-	-	-
-	-	-	-	-	-	-	-	-	-
-	-	-	-	-	-	-	-	-	-
-	-	-	-	-	-	-	-	-	-
-	-	-	-	-	-	-	-	-	-
high-range fluorescence effects									
-	-	-	-	-	-	-	-	-	-
-	-	-	-	-	-	-	-	-	-
-	-	-	-	-	-	-	-	-	-
-	-	-	-	-	-	-	-	-	-
-	-	-	-	-	-	-	-	-	-
-	-	-	-	-	-	-	-	-	-
-	-	-	-	-	-	-	-	-	-
-	-	-	-	-	-	-	-	-	-

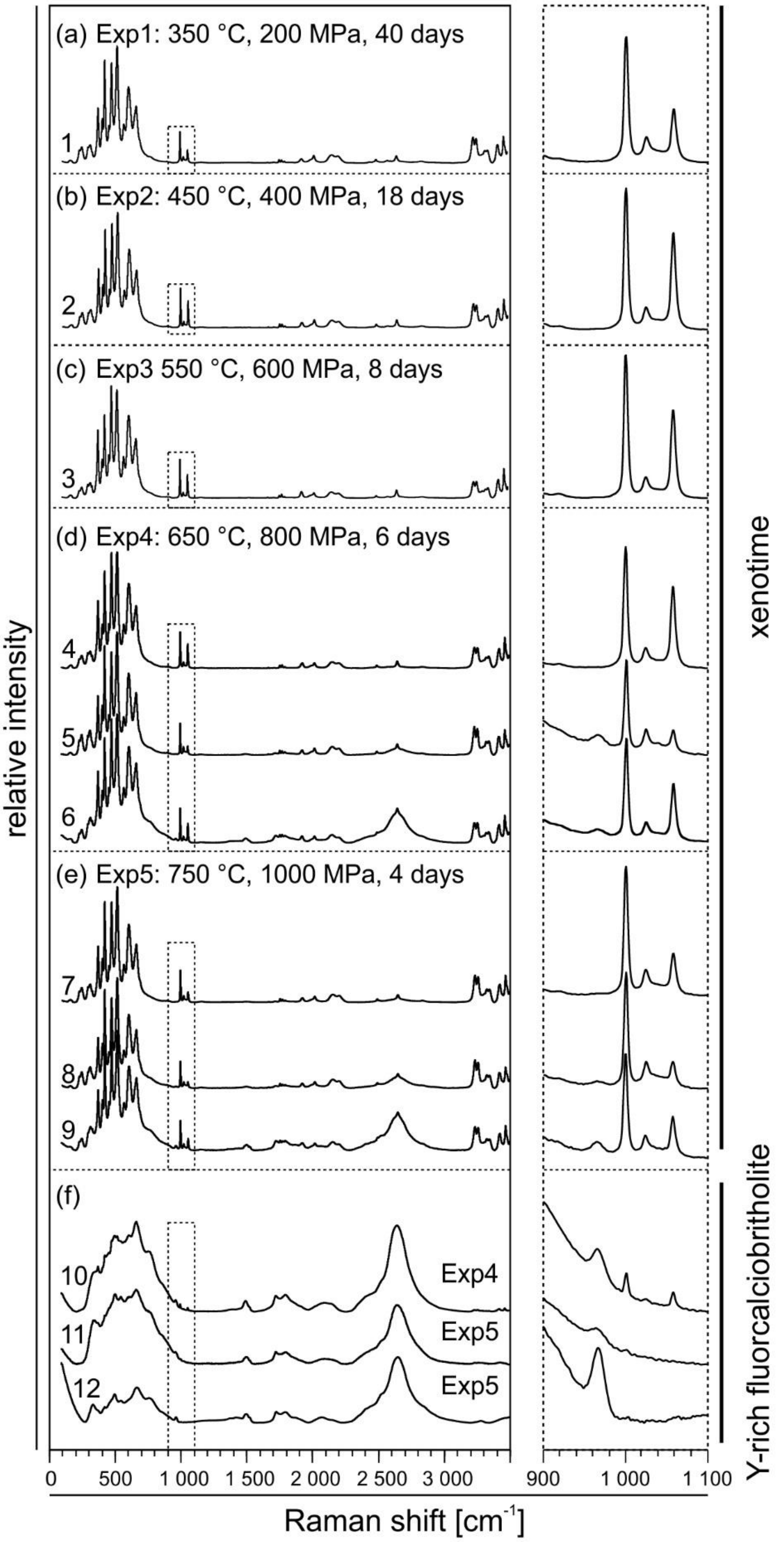

Fig. 34. Raman spectra of (a–e) xenotime from Exp1–Exp5 and (f) Y-rich fluorcalciobritholite from Exp4 and Exp5. Right side – zoomed-in spectra corresponding to dotted rectangles in range of 900–1100 cm^{-1}.

Table 8. Raman data of xenotime and Y-rich fluorcalciobritholite from experiments (532 nm laser).

Raman spectra and corresponding Raman spots of xenotime(1)											
Exp1 (xenotime)	Exp2 (xenotime)	Exp3 (xenotime)	Exp4 (xenotime)			Exp5 (xenotime)			Exp4, Exp5 (Y-rich fluorcalciobritholite)		
spectrum1 (n = 17) spots: 1-18	spectrum 2 (n = 10) spots: 19-28	spectrum 3 (n = 21) spots: 29-46, 48-50	spectrum 4 (n = 4) spots: 51-53, 58	spectrum 5 (n = 1) spot: 59	spectrum 6 (n = 3) spots: 54, 55, 59	spectrum 7 (n = 9) spots: 61, 62, 64, 67, 68, 71, 78-80	spectrum 8 (n = 2) spots: 70, 75	spectrum 9 (n = 2) spots: 63, 72	spectrum 10 (n = 2) spots: 56, 60	spectrum 11 (n = 2) spots: 74, 77	spectrum 12 (n = 4) spots: 65, 66, 69, 73
(m) 233	*(m) 233*	*(w) 233*	*(m) 234*	*(m) 235*	*(m) 235*	*(m) 234*	*(m) 234*	-	-	-	-
(s) 250	*(m) 251*	*(m) 252*	*(m) 251*	*(s) 252*	*(m) 252*	*(m) 251*	*(s) 251*	*(m) 252*	-	-	-
(s) 298	*(m) 298*	*(m) 297*	*(m) 298*	-	-	*(s) 298*	*(s) 299*	-	-	-	-
(s) 315	*(m) 315*	*(m) 316*	*(m) 316*	*(vs) 317*	*(s) 317*	*(s) 315*	*(s) 315*	*(s) 317*	-	-	-
-	*(m) 330*	*(m) 331*	*(m) 330*	-	*(s) 331*	*(m) 330*	-	*(s) 331*	-	*(s) 340*	*(m) 334*
(vs) 375	*(vs) 375*	*(vs) 375*	*(vs) 375*	*(vs) 376*	*(vs) 376*	*(vs) 375*	*(vs) 375*	*(vs) 375*	*(s) 352*	-	-
(vs) 407	*(vs) 407*	*(s) 407*	*(vs) 408*	*(vs) 408*	*(vs) 408*	*(vs) 408*	*(vs) 408*	*(vs) 408*	*(w) 376*	-	*sh(m) 376*
(vs) 426	*(vs) 426*	*(vs) 426*	*(vs) 426*	*(vs) 426*	*(vs) 426*	*(vs) 426*	*(vs) 426*	*(vs) 426*	*(m) 428*	-	*(m) 421*
(vs) 458	*(s) 458*	*(vs) 458*	*(vs) 458*	*(vs) 458*	*(vs) 458*	*(vs) 458*	*(vs) 458*	*(vs) 459*	-	*sh(vs) 443*	*sh(m) 466*
(vs) 478	*(vs) 478*	*(vs) 477*	*(vs) 478*	*(vs) 478*	*(vs) 478*	*(vs) 478*	*(vs) 478*	*(vs) 478*	-	*(s) 506*	*(m) 501*
(vs) 520	*(vs) 520*	*(vs) 520*	*(vs) 520*	*(vs) 520*	*(vs) 520*	*(vs) 520*	*(vs) 520*	*(vs) 520*	*(vs) 503*	*(s) 550*	*(m) 546*
(vs) 572	*(s) 572*	*(vs) 571*	*(vs) 572*	*(vs) 571*	*(vs) 572*	*(vs) 572*	*(vs) 572*	*(vs) 572*	-	*(s) 595*	*sh(m) 595*
(vs) 607	*(vs) 608*	*(vs) 609*	*(vs) 609*	*(vs) 608*	*(vs) 610*	*(vs) 608*	*(vs) 608*	*(vs) 609*	*(s) 600*	*(vs) 666*	*(s) 668*
(vs) 666	*(vs) 666*	*(vs) 665*	*(vs) 665*	*(vs) 666*	*(vs) 666*	*(vs) 666*	*(vs) 666*	*(vs) 666*	*(vs) 670*	-	-
-	-	-	-	-	-	-	-	-	*(vs) 769*	*sh(vs) 769*	*(s) 772*
-	-	-	-	-	-	-	-	-	*(m) 875*	*(m) 878*	*sh(m) 874*
-	-	-	-	(w)967	-	-	-	(w) 966	**(w) 970**	**(w) 966**	**(w) 967**
(s) 1000	**(s) 1000**	**(s) 1000**	**(s) 1000**	**(s) 1001**	**(s) 1001**	**(s) 1000**	**(s) 1000**	**(s) 1001**	(w) 1000	-	-
(w) 1025	(w) 1025	(w) 1024	(w) 1025	(w) 1025	(w) 1025	(w) 1025	(w) 1025	(w) 1025	-	-	-
(m) 1058	(s) 1058	(s) 1058	(s) 1058	(m) 1058	(s) 1058	(m) 1058	(w) 1057	(m) 1058	(w) 1058	-	-

Notes:

(1) – Raman spectra from Fig. 34 and corresponding Raman spots from Fig. 31

sh – shoulders, *italic – fluorescence bands*

Xenotime-spectra: intensities of presented data are normalized to v_1(PO_4) band (**bold**) equal to 1.0: weak (w) 0.05–0.2, medium (m) 0.2–0.5, strong (s) 0.5–1.0, very strong (vs) >1.0

Y-rich fluorcalciobritholite-spectra: intensities of presented data are normalized to characteristic Raman band (966–970 cm^{-1}; **bold**) equal to 1.0: weak (w) 0.5–1.0, medium (m) 1.0–5.0, strong (s) 5.0–10.0, very strong (vs) >10.0

Only significant signals above background are presented.

Table 8. (Continued).

Raman spectra and corresponding Raman spots of xenotime$^{(1)}$											
Exp1 (xenotime)	Exp2 (xenotime)	Exp3 (xenotime)	Exp4 (xenotime)			Exp5 (xenotime)			Exp4, Exp5 (Y-rich fluorcalciobritholite)		
spectrum1	spectrum 2	spectrum 3	spectrum 4	spectrum 5	spectrum 6	spectrum 7	spectrum 8	spectrum 9	spectrum 10	spectrum 11	spectrum 12
(n = 17)	(n = 10)	(n = 21)	(n = 4)	(n = 1)	(n = 3)	(n = 9)	(n = 2)	(n = 2)	(n = 2)	(n = 2)	(n = 4)
spots: 1-18	spots: 19-28	spots: 29-46, 48-50	spots: 51-53, 58	spot: 59	spots: 54, 55, 59	spots: 61, 62, 64, 67, 68, 71, 78-80	spots: 70, 75	spots: 63, 72	spots: 56, 60	spots: 74, 77	spots: 65, 66, 69, 73
mid-range fluorescence effects											
-	-	-	-	*(m) 1495*	*(w) 1496*	-	-	*(m) 1502*	*(m) 1495*	*(m) 1501*	*(m) 1496*
-	-	-	-	*(m) 1727*	*(m) 1726*	-	-	*(m) 1724*	*(m) 1726*	*(m) 1723*	*(m) 1728*
(w) 1755	*(w) 1755*	*(w) 1756*	*(w) 1756*	*(m) 1756*	*(m) 1756*	*(w) 1756*	*(m) 1756*	*(m) 1755*	*(m) 1802*	*(m) 1803*	*(m) 1792*
(w) 1774	*(w) 1774*	*(w) 1774*	*(w) 1774*	*(m) 1774*	*(m) 1774*	*(w) 1774*	*(w) 1774*	*(m) 1774*	*(m) 2093*	-	-
(w) 1794	-	-	-	*(m)1795*	*(m) 1795*	*(w) 1795*	*(w) 1795*	*(m) 1795*	-	-	-
(w) 1926	*(w) 1927*	*(w) 1926*	*(w) 1929*	*(m) 1926*	*(w) 1924*	*(w) 1925*	*(m) 1924*	*(m) 1923*	-	-	-
(m) 2020	*(w) 2020*	*(w) 2020*	*(w) 2019*	*(m) 2020*	*(m) 2020*	*(m) 2019*	*(m) 2021*	*(m) 2021*	-	-	-
(m) 2156	*(w) 2156*	*(w) 2154*	-	-	-	-	*(m) 2158*	*(m) 2156*	-	-	*(m) 2070*
(m) 2203	*(w) 2203*	*(w) 2204*	*(w) 2202*	*(m) 2156*	*(m) 2156*	*(m) 2157*	-	-	-	-	-
-	-	-	-	*sh(m) 2426*	*sh(w) 2427*	*(m) 2203*	*(m) 2202*	-	-	-	-
(w) 2493	*(w) 2493*	*(w) 2493*	*(w) 2494*	*(w) 2493*	*(w) 2494*	*(w) 2493*	*(m) 2493*	*sh(w) 2419*	-	*sh(m) 2440*	*(m) 2437*
-	-	-	-	*sh(m) 2513*	*sh(s) 2513*	-	-	*sh(m) 2509*	-	*sh(m) 2520*	*(m) 2519*
(m) 2650	*(w) 2649*	*(w) 2649*	*(m) 2649*	*(vs) 2650*	*(vs) 2650*	*(m) 2650*	*(s) 2650*	*(vs) 2649*	*(vs) 2647*	*(vs) 2641*	*(vs) 2644*
-	-	-	-	*(m) 2791*	*sh(w) 2790*	*(w) 2837*	-	*sh(w) 2808*	-	*sh(s) 2751*	*(m) 2805*
high-range fluorescence effects											
(s) 3234	*(s) 3233*	*(m) 3234*	*(s) 3234*	*(s) 3235*	*(s) 3234*	*(s) 3234*	*(vs) 3234*	*(s) 3234*	*(w) 3232*	-	-
(s) 3257	*(s) 3257*	*(m) 3257*	*(s) 3258*	*(s) 3258*	*(s) 3258*	*(s) 3257*	*(vs) 3258*	*(s) 3258*	*(w) 3259*	-	-
-	-	*(m) 3303*	-	-	-	-	-	-	-	-	-
-	*(m) 3323*	*(m) 3325*	*(m) 3325*	*(m) 3324*	*(m) 3324*	*(m) 3323*	*(s) 3323*	*(m) 3323*	-	-	-
(s) 3344	*(m) 3345*	*(m) 3345*	*(m) 3344*	*(s) 3344*	*(m) 3344*	*(m) 3345*	*(s) 3346*	*(m) 3344*	-	-	-
(s) 3422	*(m) 3422*	*(s) 3423*	*(s) 3423*	*(s) 3423*	*(s) 3423*	*(s) 3423*	*(s) 3419*	*(s) 3424*	*(w) 3424*	-	-
(s) 3466	*(s) 3466*	*(m) 3466*	*(s) 3466*	*(vs) 3466*	*(s) 3466*	*(s) 3466*	*(s) 3466*	*(s) 3466*	*(w) 3465*	-	-

4.4.4. Comparison of Raman spectra of xenotime from Exp1 and Exp5 – instrument A and B (488 nm, 532 nm, 633 nm and 780 nm)

Raman spectra of xenotime from Exp1 and Exp5 obtained with 488 nm laser are dominated by fluorescence effects, which superimpose the primary Raman features except for the distinct peaks of the $v_1(PO_4)$ symmetric stretching band at ca. 1006–1007 cm^{-1}, and the $v_3(PO_4)$ antisymmetric stretching bands B2 – 1031 cm^{-1} and B3 – 1064 cm^{-1} (Fig. 35a, b). The fluorescence effects of these spectra is composed of (i) weak signals at low-range (ca. 100–300 cm^{-1}), (ii) moderate fluorescence effects at mid-range (1200–1750 cm^{-1}) followed by a group of dominant peaks (1800–2500 cm^{-1}), and (iii) weak signals at high-range (3000–4000 cm^{-1}) with one moderate peak at ca. 3500 cm^{-1}. A distinct dominant Raman band is present at 974 cm^{-1} in the Y-rich fluorcalciobritholite spectrum (Fig. 35a, b).

Raman spectra of xenotime obtained with 532 nm laser resulted in similar spectra compared to Raman spectra obtained with instrument A (Figs. 34, 35c, d). Comparison of Y-rich fluorcalciobritholite spectra obtained with instrument A with those obtained with instrument B show extensively broader fluorescence bands at low-range in spectra from instrument B (combined Ho^{3+}: $^5S_2 \rightarrow {}^5I_8$ and Er^{3+}: $^4S_{3/2} \rightarrow {}^4I_{15/2}$), which completely superimpose all Raman signals (Figs. 34f, 35d). Fluorescence effects at mid-range, however, are less pronounced in spectra obtained with instrument B compared to those from instrument A.

Raman spectra of xenotime obtained with 633 nm laser show strong fluorescence effects at low-range (100–900 cm^{-1}) and weak fluorescence effects at mid-range (ca. 1300–1700 cm^{-1}), primary $v_1(PO_4)$ symmetric stretching bands are located at 1001–1002 cm^{-1} and antisymmetric stretching bands at ca. 1026 cm^{-1} and ca. 1060 cm^{-1} (Fig. 35e, f). The low-range fluorescence effects are caused by contributions of electronic transitions of Ho^{3+} ($^5F_5 \rightarrow {}^5I_8$) and Er^{3+} ($^4F_{9/2} \rightarrow {}^4I_{15/2}$) according to Lenz et al. (2015). Raman spectra of Y-rich fluorcalciobritholite show fluorescence at low-range composed of a broad background, whereas the distinct primary band is shifted towards 969 cm^{-1} compared to 974 cm^{-1} in spectra obtained with 488 nm (Figs. 32f, 33b).

A Raman spectrum of xenotime from Exp1 obtained with the 780 nm laser shows strong fluorescence at low-range (100–700 cm^{-1}), which can be attributed to contribution of Tm^{3+} ions as it is reflected in the $TmPO_4$ spectrum compared to a fluorescence free spectrum of YPO_4 (Fig. 36). Primary Raman features in xenotime spectrum are still visible in the range of 900–1100 cm^{-1}, while fluorescence effects superimpose the region of lattice modes and internal bending modes (100–700 cm^{-1}). Furthermore, fluorescence effects are present at mid-range in the spectrum of xenotime from Exp1, whereas spectrum of $TmPO_4$ does not show fluorescence effects at higher wavenumber (> 700 cm^{-1}). These effects do resemble fluorescence effects of $LaPO_4$, $CePO_4$ and $GdPO_4$ at the range of 1400–1800 cm^{-1}, whereas two fluorescence bands present in the spectra of the synthetic phosphates are missing in the spectrum of xenotime at ca. 1200–1300 cm^{-1} (Figs. 27b, 34a).

4.4.5. Raman microspectroscopy of xenotime from pegmatite from Piława Górna – instrument A (532 nm laser)

The xenotime from the pegmatite from Piława Górna is intergrown with zircon and displays patchy zoning in high contrast BSE image (Figs. 3, 37). The xenotime contains a domain with extensive microporosity in close proximity to the phase boundary with zircon. Raman spectra of the xenotime core and "outer" rim (i.e. not intergrown with the zircon), predominantly show similar spectra to those of the NWFP xenotime and xenotime from experiments (Figs. 33, 34, 38).

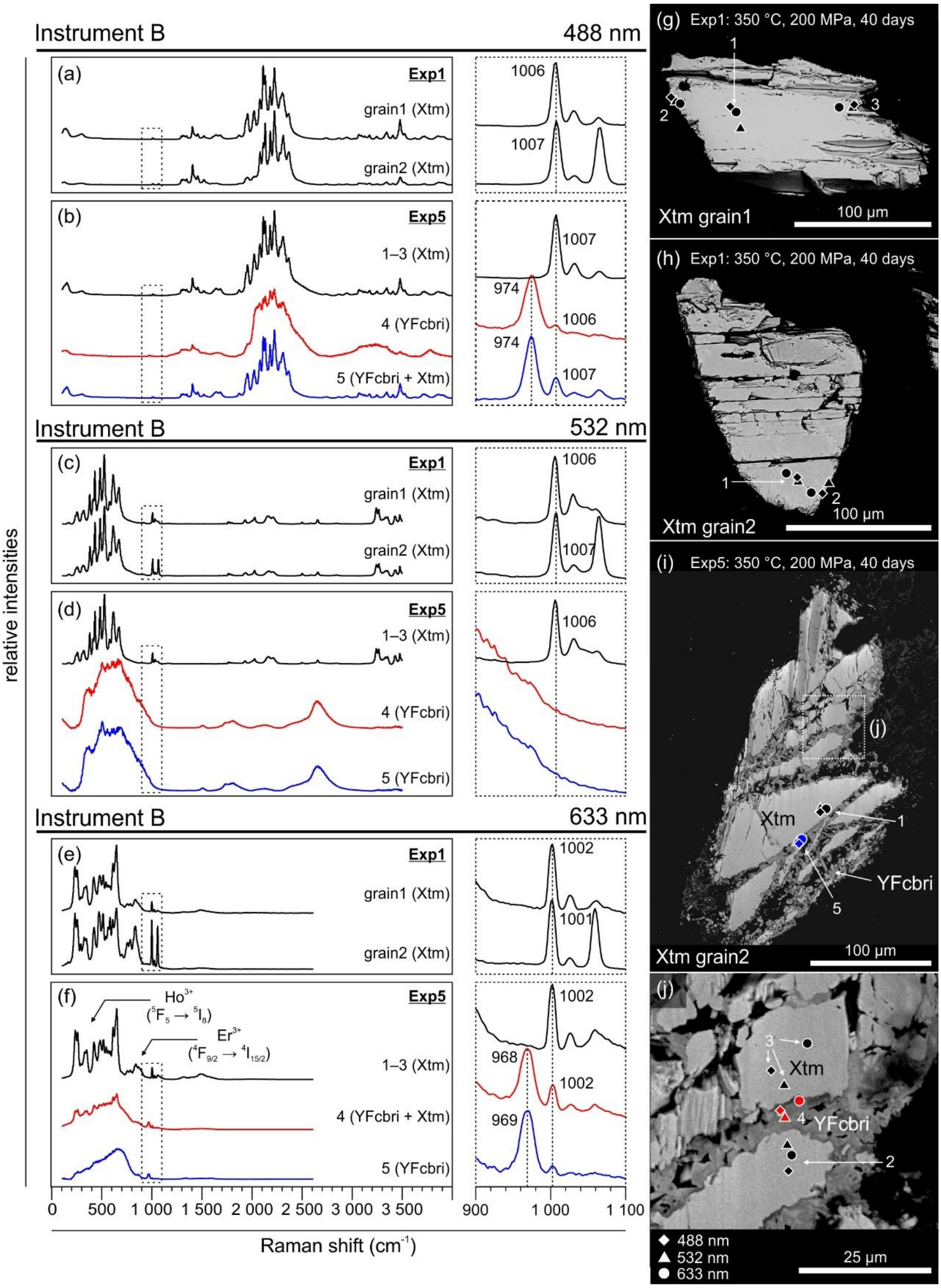

Fig. 35. Raman spectra of selected xenotime from Exp1 and Exp5 obtained with (a, b) 488 nm, (d, e) 532 nm and (e, f) 633 nm lasers. Right side – zoomed-in spectra in range of 900–1100 cm^{-1} (dashed boxes). (g–j) BSE images of the selected grains with locations of measurements. Diamond – Raman spot obtained with 488 nm laser, triangle – Raman spot obtained with 532 nm laser, circle – Raman spot obtained with 633 nm laser. Electronic transitions attributed to fluorescence effects of spectra obtained with 633 nm laser taken from Lenz et al. (2015). Mineral abbreviations: YFcbri – Y-rich fluorcalciobritholite, Xtm – xenotime.

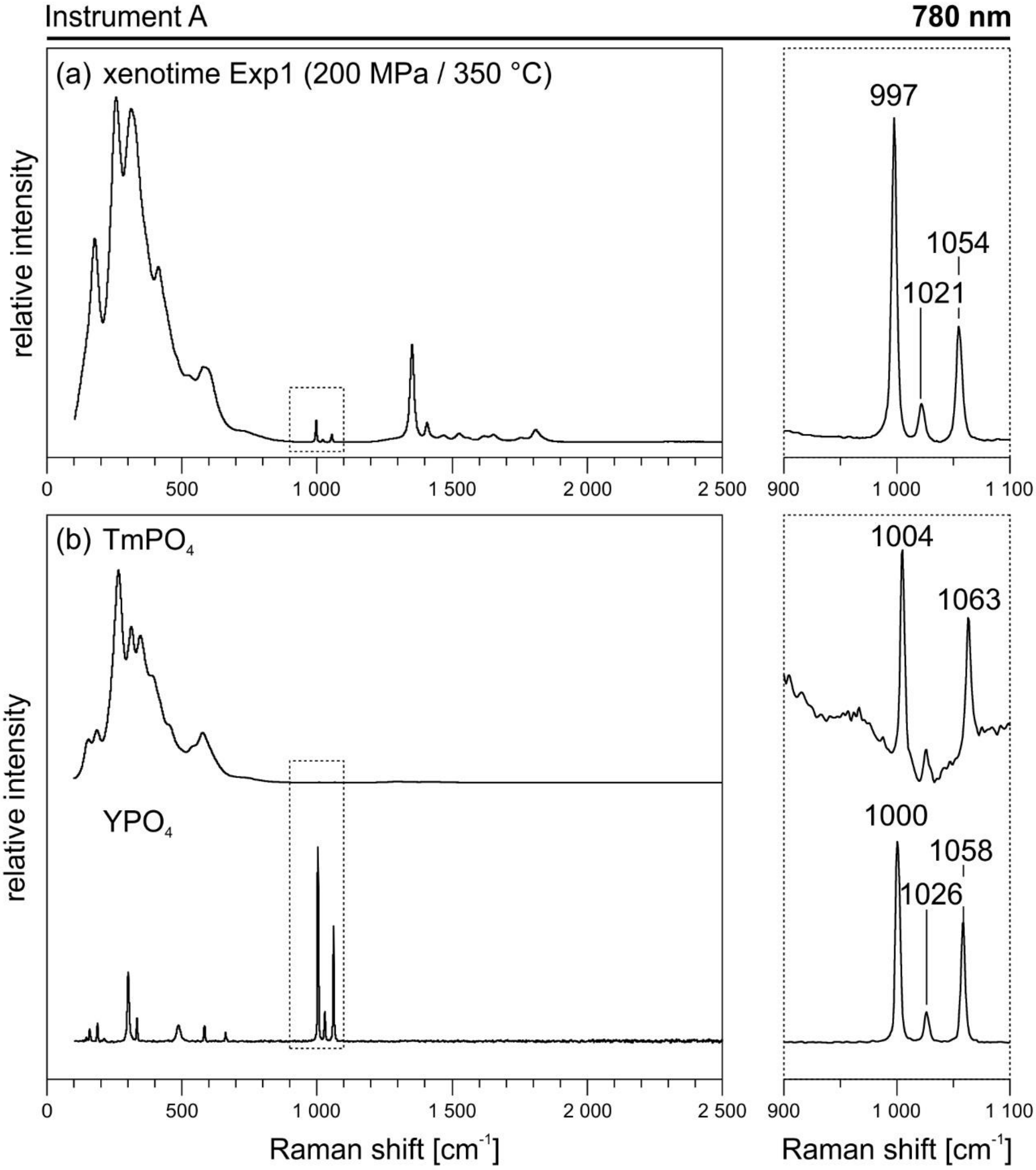

Fig. 36. Raman spectra (instrument A; 780 nm) of (a) xenotime from Exp1 and (b) synthetic $TmPO_4$ and YPO_4. The spectra of xenotime and $TmPO_4$ are overwhelmed by fluorescence effects, whereas YPO_4 shows a fluorescence-free spectrum. Right side – zoomed-in spectra corresponding to dotted rectangles.

The similarities include strong fluorescence effects at low range caused by Ho^{3+} and Er^{3+} ($^5S_2 \rightarrow {}^5I_8$ and $^4S_{5/2} \rightarrow {}^4I_{15/2}$), weak fluorescence effects at mid-range caused by Sm^{3+} ($^4G_{5/2} \rightarrow {}^6H_{7/2}$), weak fluorescence effects at high-range caused by Sm^{3+} ($^4G_{5/2} \rightarrow {}^6H_{9/2}$) and moderate fluorescence effects at high-range caused by Ho^{3+} ($^5F_5 \rightarrow {}^5I_8$).

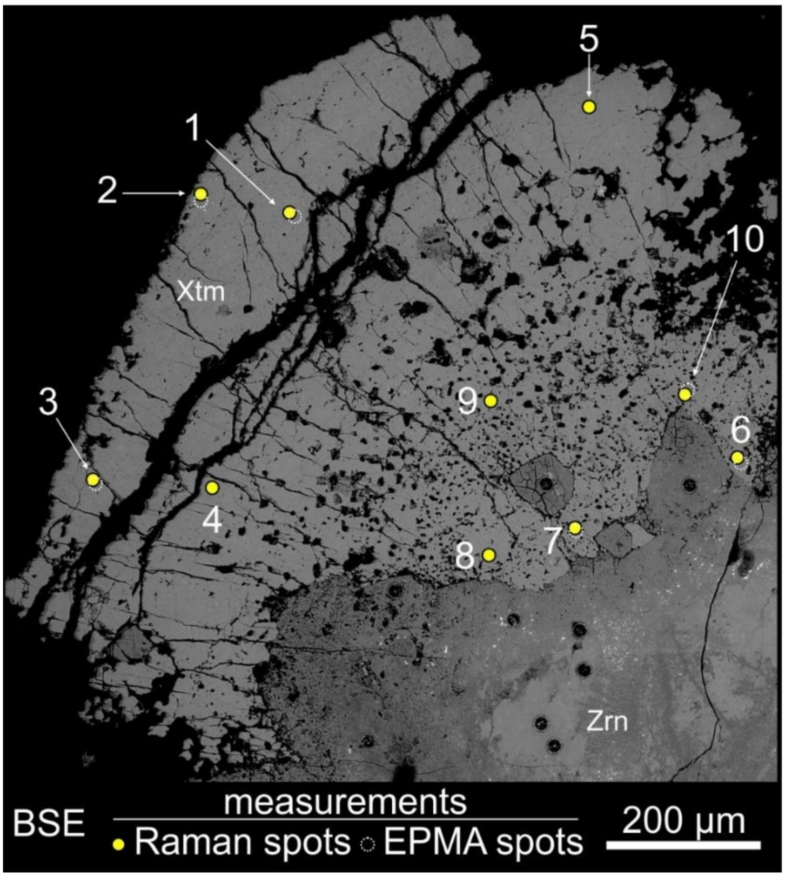

Fig. 37. BSE image of the xenotime intergrown with zircon in pegmatite from Piława Górna (NE Bohemian Massif, SW Poland) with marked locations of Raman and EPMA measurements.

Fluorescence effects caused by Eu^{3+} ($^5D_0 \rightarrow {}^7F_2$) at the range of 1800–2000 cm^{-1}, which is present in spectra of NWFP xenotime, however, is missing in spectra of the xenotime from the pegmatite. One spectrum of xenotime from the “outer” rim shows broad fluorescence effects in the range of 1200–1700 cm^{-1} (spectrum 2; Fig. 38a). Spectra of xenotime from the domain with extensive microporosity are similar to other spectra of xenotime, but the increase of background fluorescence at 1200–1700 cm^{-1} is more prominent (spectra 3, 4; Fig. 38a). FWHH values of the $v_1(PO_4)$ symmetric stretching band of xenotime from the xenotime core and “outer” rim (7.31–8.54 cm^{-1}) and from the microporous domain (8.50–9.03 cm^{-1}) are significantly higher than FWHH values of xenotime from experiments (4.58–6.25 cm^{-1}), whereas peak positions (998–1000 cm^{-1}) are within spectral resolution of 3 cm^{-1} (Fig. 38b). Furthermore, FWHH values of the inner domains are slightly higher compared to FWHH’s of the outer rim domains.

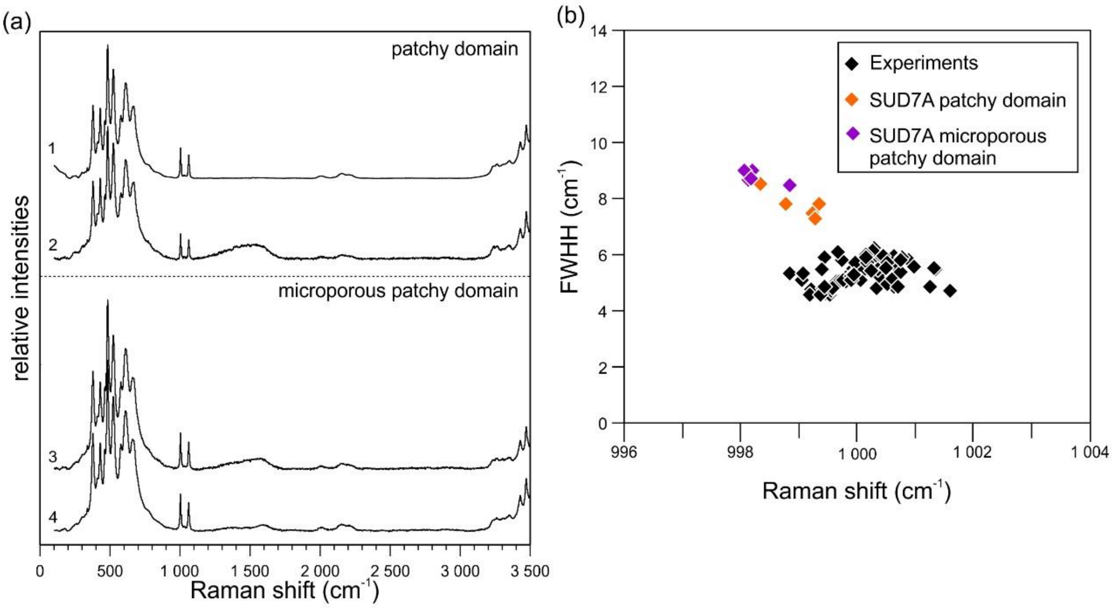

Raman spectra and corresponding Raman spots

patchy domain		microporous patchy domain	
spectrum 1 (*n* = 4)	1,2,4,5	spectrum 3 (*n* = 2)	6,8
spectrum 2 (*n* = 1)	3	spectrum 4 (*n* = 3)	7,9,10

Fig. 38. (a) Raman spectra of xenotime, which is intergrown with zircon in pegmatite from the Piława Górna (SUD7A). Raman spectra correspond to Raman spots in Fig. 37. (b) Raman shift of $\nu_1(PO_4)$ symmetric stretching band of the xenotime SUD7A and xenotime from experiments vs. FWHH values of the $\nu_1(PO_4)$ symmetric stretching band.

4.4.6. Hyperspectral mapping and EPMA-WDS compositional X-ray mapping of xenotime – instrument B (532 nm and 633 nm)

The hyperspectral maps of xenotime demonstrate correlation with the BSE image, however, not as good as the maps of monazite. This is probably related to similarity of xenotime spectra and Y-rich fluorcalciobritholite spectra, which hindered a clear picture. Regardless, the TCA image of xenotime demonstrates characteristic spectral features of Y-rich fluorcalciobritholite in maps obtained with 532 nm and 633 nm lasers (Fig. 39c, d). The TCA image collected with the 633 nm laser shows a gradual shift from xenotime to Y-rich fluorcalciobritholite, whereas only sharp and distinct boundaries between xenotime and Y-rich fluorcalciobritholite are present in the BSE image (Fig. 39d). Intensities of distinct fluorescence effects in the range of 3250 cm^{-1} are representative for xenotime (Fig. 39h), whereas fluorescence effects at 1500 cm^{-1} and 2650 cm^{-1} correspond to the presence of Y-rich fluorcalciobritholite (Fig. 39f, g), which roughly reflects the dominant centres of both phases and fit to the TCA map and BSE image.

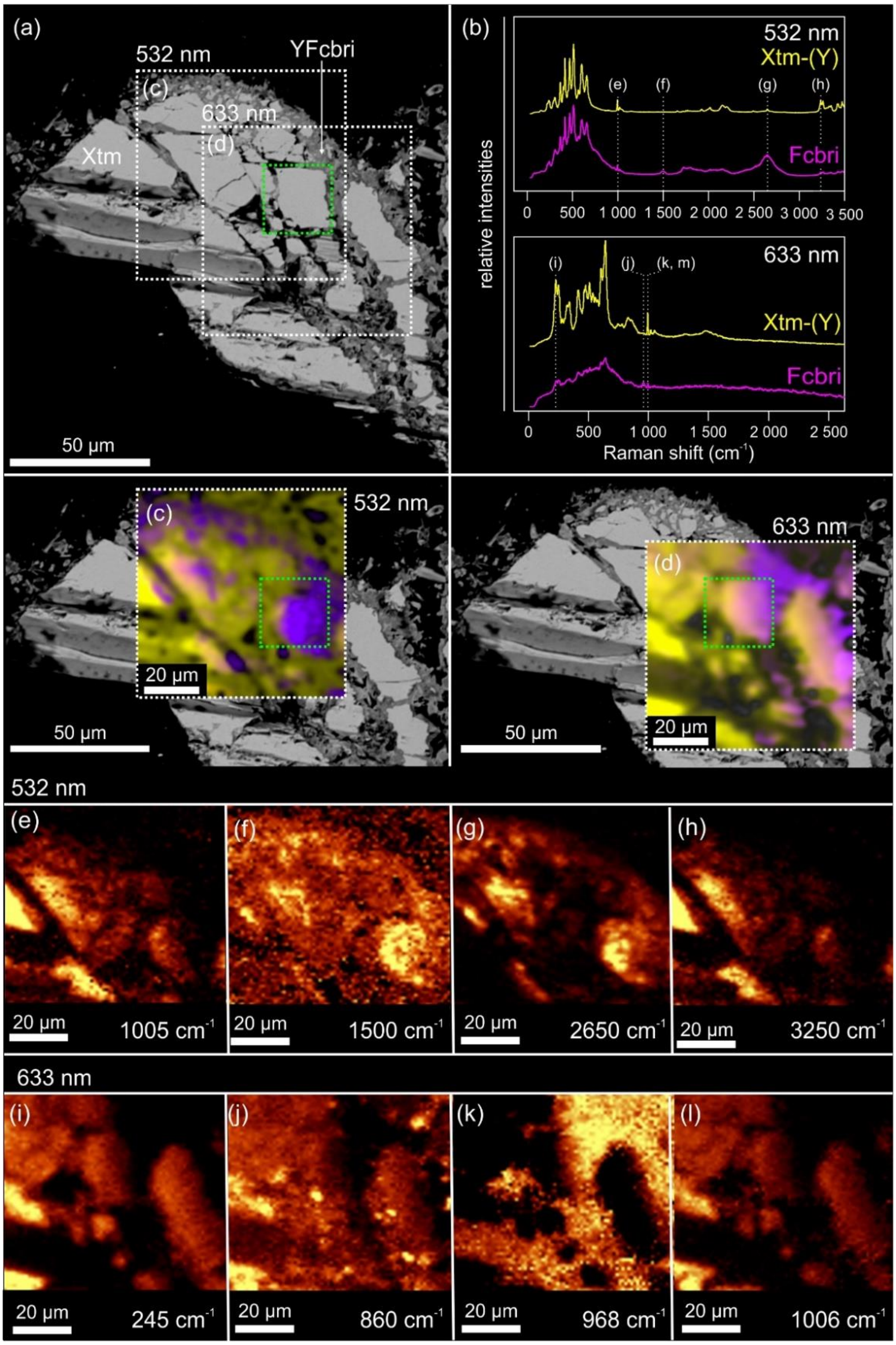

Fig. 39. Figure caption on next page.

Fig. 39. Hyperspectral mapping (instrument B) of selected areas of xenotime from Exp5 (1000 MPa, 750 °C, 4 days). (a) EPMA BSE image of the altered monazite with the selected area for mapping. (b) Raman spectra of xenotime and Y-rich fluorcalciobritholite obtained with 532 nm and 633 nm lasers. (c, d) TCA maps displaying xenotime in yellow and Y-rich fluorcalciobritholite in pink. (e–h) Intensity maps of selected distinct bands (532 nm). (i–l) Intensity maps of selected distinct bands (633 nm). (a, c, d) Green dashed square – highlighted area corresponding to the same position in BSE image and hyperspectral maps obtained with 532 nm and 633 nm lasers. Abbreviations: YFcbri – Y-rich fluorcalciobritholite, Xtm – xenotime.

Both hyperspectral maps indicate underlying signals of Y-rich fluorcalciobritholite, which overlap with signals of xenotime, at the same position were BSE imaging shows a homogeneous surface of xenotime (green dashed squares in Fig. 39). Furthermore, EPMA-WDS compositional maps collected from the same area as the hyperspectral map do not indicate presence of fluorcalciobritholite underlying xenotime, whereas the hyperspectral map does (Fig. 40).

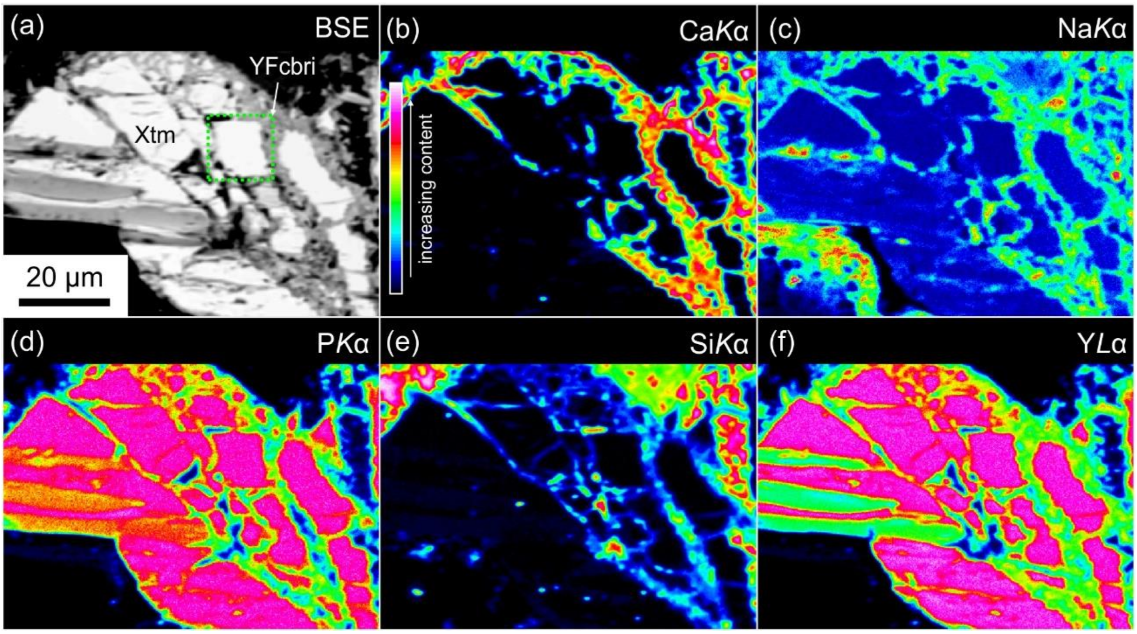

Fig. 40. EPMA-WDS compositional X-ray mapping of a selected area of xenotime from Exp5 (1000 MPa / 750 °C). Green dashed square – location of interest from hyperspectral map (green dashed square in Fig. 39). Mineral abbreviations: YFcbri – Y-rich fluorcalciobritholite, Xtm – xenotime

4.5. Discussion

4.5.1. Characteristics of Raman spectra of synthetic $LaPO_4$–$GdPO_4$ and the Burnet monazite

In the Raman spectra of monazite up to 36 vibrational active modes (Ag + Bg) can be present. However, due to a broad set of REE in monazite composition, attribution of specific Raman bands to vibrational modes of individual symmetry is still controversial even for pure REE phosphates and would require *ab initio* quantum calculations (Ruschel et al. 2012). In this study, unambiguous identification of Raman bands for natural monazite remains challenging and is based on new Raman data of synthetic REE phosphates (Table 4) and data from previous studies (Begun et al. 1981; Silva et al. 2006). Certain characteristic Raman bands of the Burnet monazite [$v_1(PO_4)$, $v_2(PO_4)$, $v_3(PO_4)$ and $v_4(PO_4)$] display divergence compared to what would be predicted from the compositional data (Supplementary Table B3). The Burnet monazite mainly contains Ce (0.412–0.483 apfu), thus, the Raman data would be expected to mainly reflect spectral data similar to that of $CePO_4$. However, amongst the normal modes, only the symmetric bending mode $v_2(PO_4)$ at 464 cm^{-1} fits best with the peak position from $CePO_4$ (465 cm^{-1}; Table 4). The other modes of the Burnet monazite are shifted towards higher values, and best fit $NdPO_4$ [$v_1(PO_4)$ at 974 cm^{-1} and $v_4(PO_4)$ at 625 cm^{-1}] and $GdPO_4$ [$v_3(PO_4)$ at 1070 cm^{-1}]. These shifts are caused by the cumulated contribution of different REE into the structure of monazite, because the ionic radii of the PO_4^{3-} bonds of REE phosphates correlate inversely with the peak position of the vibrational modes (Begun et al. 1981; Silva et al. 2006). Such a correlation was shown in synthetic $REEPO_4$ of mixed compositions, such as $Ce_{0.5}Sm_{0.5}PO_4$ or $La_{1-x}Eu_xPO_4$, in which the peak positions shifted according to the proportion of element occupancy (Ruschel et al. 2012; Geisler et al. 2016). Therefore, contribution of different REE in the Burnet monazite produces a shift of vibrational modes towards higher wavenumbers. This cumulated contribution may also explain appearance of shoulder bands at ca. 961 cm^{-1}, which could be related to the predominant LREE content in the Burnet monazite fitting to the bonding length of the $LaPO_4$ [$\nu_1(PO_4)$ at 965 cm^{-1}] and $CePO_4$ [$\nu_1(PO_4)$ at 968 cm^{-1}] endmember structures (Table 4).

The phosphates $NdPO_4$, $SmPO_4$ and $EuPO_4$ display distinct fluorescence effects (Fig. 22b). Recalculation of Raman shift into wavenumbers enables comparison with calculated energy-levels of electronic transitions which are responsible for fluorescence (Dieke and Crosswhite 1963; Marfunin 1979; Gaft et al. 2015). Fluorescence of $NdPO_4$ was studied previously, and is caused by the $^4F_{3/2} \rightarrow {}^4I_{9/2}$ electronic transition at wavenumbers in the range of 10600–11800 cm^{-1} (Lenz et al. 2013). The fluorescence effects observed in Raman spectra of the $NdPO_4$ in this study, however, occur at much higher range of ca. 16500–17500 cm^{-1} wavenumber (Fig. 41). This indicates excitation of the $^4I_{9/2}$ electron to much higher energetic levels. Indeed, unidentified electronic transitions occur at energy-levels close to the observed spectral range in Dieke diagrams (Fig. 41). In the case of $SmPO_4$ spectrum, fluorescence peaks occur as a broad background peak in the range of ca. 18000 cm^{-1} wavenumber and in two groups of fluorescence peaks, (i) in the range of ca. 16400–17200 cm^{-1} and (ii) ca. 15200–16000 cm^{-1} wavenumber (Fig. 41). The $^4G_{5/2} \rightarrow {}^6H_{5/2}$ electronic transition corresponds well to the background peak at ca. 18000 cm^{-1} wavenumbers, whereas the group of fluorescence peaks fall in-between possible electronic transitions of $^4G_{5/2} \rightarrow {}^6H_{5/2}$ and $^6F_{11/2} \rightarrow {}^6H_{5/2}$ described in Dieke diagrams (Dieke and Crosswhite 1963; Gaft et al. 2015). The Raman spectrum of $EuPO_4$ is superimposed by fluorescence effects within the range of ca. 15400–17000 cm^{-1} wavenumbers in which the three most dominant fluorescence peaks are located at wavenumbers of ca. 16815 cm^{-1}, 16857 cm^{-1} and 17012 cm^{-1} corresponding to the $^5D_0 \rightarrow$

$^7F_0$–$^7F_5$ electronic transitions (Gaft et al. 2015). Unambiguous attribution of electronic transitions to the observed fluorescence peaks is difficult with Raman data alone, because they are based on quantum calculations of a simplified theory and consideration of over 3000 wave functions regarding REE (Gaft et al. 2015). Therefore, attribution of electronic transitions remains ambiguous and would require detailed calculation, which would exceed the scope of this study.

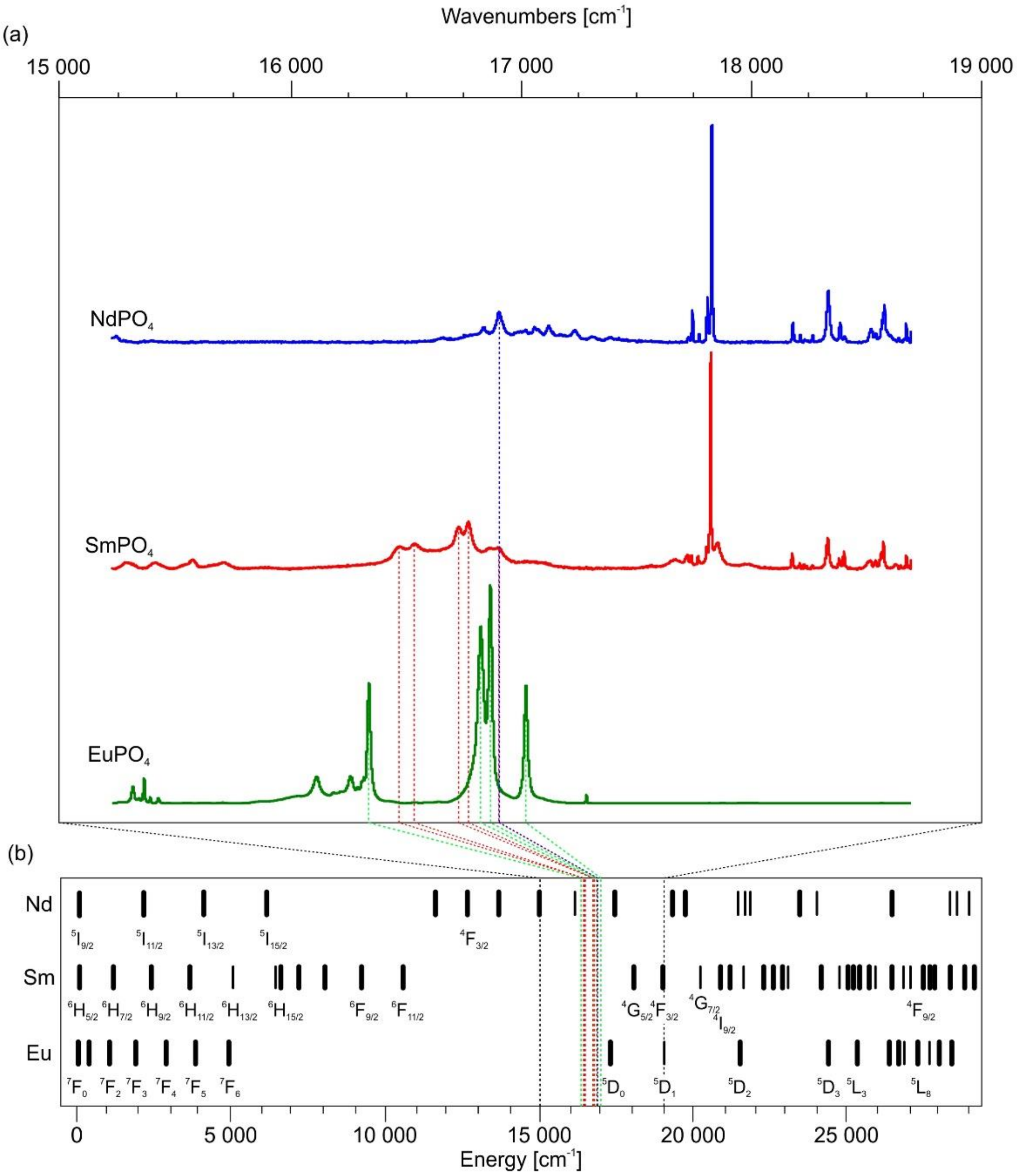

Fig. 41. Raman spectra of synthetic REEPO$_4$. (a) Spectra of NdPO$_4$, SmPO$_4$ and EuPO$_4$ recalculated to wavenumbers. (b) Energy-levels of electronic transitions taken from Dieke diagrams (Dieke and Crosswhite 1963; Gaft et al. 2015).

4.5.2. Characteristics of Raman spectra of synthetic $TbPO_4$–$LuPO_4$, YPO_4 and the NWFP xenotime

The xenotime structure [D4h19 (I41/amd), Z=2] has a higher symmetry than monazite (P21/n, Z=4), which results in 12 Raman active modes instead of 36 likewise in monazite (Begun et al. 1981; Mullican et al. 1996; Clavier et al. 2018). Declination of Raman bands of synthetic $TbPO_4$–$LuPO_4$ and YPO_4 (Table 7) and the NWFP xenotime are based on previous work (Begun et al. 1981). The small variation of ca. 4 cm^{-1} of data of $TbPO_4$–$LuPO_4$ and YPO_4 obtained with 532 nm and 780 nm compared to data from Begun et al. (1981) easily enable identification of fluorescence bands. Xenotime incorporates predominantly Y in its structure, but also substantial portion of HREE (Gd–Lu) and traces of remaining REE. Therefore, spectral data of NWFP xenotime is expected to primarily reflect that of YPO_4. Indeed, there are Raman bands which are located at the expected positions, such are 1B = 999cm^{-1} of the $v_1(PO_4)$ symmetric stretching band, 2B = 1024 cm^{-1} and 3B = 1057 cm^{-1} of the $v_3(PO_4)$ antisymmetric stretching bands (Table 7). It has been shown in Raman spectra of a xenotime from Novo Horizonte (Baha, Brazil), that fluorescence effects caused by the Ho^{3+} ($^5S_2 \rightarrow {}^5I_8$) and Er^{3+} ($^4S_{3/2} \rightarrow {}^4I_{15/2}$) superimpose the lattice and internal bending modes of xenotime using the 532 nm laser (Lenz et al. 2015). The Raman spectra of NWFP xenotime in this work also show these fluorescence effects, thus, electronic transitions of the responsible REE are attributed according to Lenz et al. (2015). Deconvolution of the fluorescence bands reveal, that the position of some fluorescence-bands fit those of potential lattice modes present in REE phosphates. This demonstrates the potential of misinterpreting the relatively narrow fluorescence-bands as lattice modes at plausible positions, if they are not detected by comparison with spectra of $HoPO_4$ and $ErPO_4$. Only the weak band at 295 cm^{-1} (Table 7) could possibly be attributed to the 14B mode of the YPO_4 (296 cm^{-1})

described by Begun et al. (1981). However, identifications of Raman bands should always be done with caution in the presence of fluorescence effects, therefore, the band at 295 cm^{-1} is inconclusive and should be attributed to fluorescence effects caused by Ho^{3+} electronic transition rather than a lattice mode.

4.5.3. Raman microspectroscopy of monazite from experiments

Despite resistance towards radiation damage caused by the radioactive decay of U, Th and daughter isotopes due to low temperature annealing effects (Seydoux-Guillaume et al. 2002c, 2018; Nasdala et al. 2020), it has been shown that monazite can accumulate significant amounts of radiation damage leading to distortion of its structure reflected in a band broadening of the $v_1(PO_4)$ symmetric stretching band (Seydoux-Guillaume et al. 2002b; Ruschel et al. 2012; Grand'Homme et al. 2018; Budzyń et al. 2021, 2022). The Burnet monazite displays high values of measured FWHH compared to calculated FWHH values based on EPMA data of U, Th, Pb and Ca contents (12.21–15.85 cm^{-1} vs. 7.23–8.67 cm^{-1}, respectively; Fig. 25), which indicates moderate structural disorder of the monazite caused by radiation damage.

Monazite grains from experimental products at low to moderate P-T conditions (200 MPa / 350 °C, 400 MPa / 450 °C, 600 MPa / 550 °C) contain altered domains, which are depleted in U, Th and Pb (Supplementary Table B3). These altered domains are also depleted in HREE, from Gd to Lu, at the chondrite-normalized patterns (Figs. 18, 19). The low FWHH values of $v_1(PO_4)$ bands in altered domains of monazite reflect recrystallization due to coupled dissolution-reprecipitation processes induced by alkaline fluids, which mobilized U, Th, Pb and Gd–Lu (Fig. 25b–d; cf. Budzyń et al. 2021). On the other hand, unaltered domains of monazite predominantly show higher measured FWHH values compared to calculated ones (7.93–15.23 cm^{-1} vs. 7.31–9.16 cm^{-1}; Fig. 25b–d). The higher measured FWHH values indicate that monazite retained the moderate disorder of the structure, whereas the spread of data towards lower measured FWHH values indicate partial structural recovery via thermal annealing (cf. Ruschel et al. 2012; Seydoux-Guillaume et al. 2012, 2018; Nasdala et al. 2020; Budzyń et al. 2021, 2022). The gradual shift of measured FWHH values from the unaltered domains of monazite towards lower values with increasing temperature conditions (Exp1–Exp5) support the interpretation of increasing contribution of thermal annealing with increasing temperature (Fig. 25b–d).

The Raman data of compositionally unaltered monazite from Exp2 (400 MPa / 450 °C) show significant changes compared to those of the Burnet monazite at two locations in close proximity to REE-rich steacyite (spots 50, 51; Fig. 19h; spectrum 15; Fig. 24a). These spectral changes include appearance of a new distinct peak at 1128 cm^{-1} and increase of mid-range fluorescence effects. The close proximity of measurements to the secondary REE-rich steacyite suggests potential contribution of this phase in the Raman spectra of monazite. Raman spectra of synthetic minerals similar to that of steacyite [$(K,\square)(Na,Ca)_2(Th,U)Si_8O_{20}$], i.e. $(Ca_{0.5}Na_{0.5})_2NaUSi_8O_{20}$ and $(Ca_{0.5}Na_{0.5})_2NaThSi_8O_{20}$, have been studied by Jin and Soderholm (2015). Raman spectra of these minerals include a band at a similar position as in the spectra of REE-rich steacyite, at positions 1144 cm^{-1} and 1139 cm^{-1} in $(Ca_{0.5}Na_{0.5})_2NaUSi_8O_{20}$ and $(Ca_{0.5}Na_{0.5})_2NaThSi_8O_{20}$, respectively. These bands were attributed to the antisymmetric stretching of the Si-O-Si bond (Jin and Soderholm 2015). Steacyite crystallizes in a tetragonal structure (Perrault and Szymanski 1982) with a similar stoichiometry to the minerals studied by Jin and Soderholm (2015). Identification of phases should not be done based only on one Raman band and a lack of reference spectra, however, the additional peak at 1128 cm^{-1} in the monazite spectra may suggest contribution of the antisymmetric stretching of the Si-O-Si bond related to the presence of REE-rich steacyite or possibly a similar phase, which is too small for identification with used methods (spectrum 15; Fig. 24a).

Some Raman spectra obtained from compositionally unaltered monazite domains from Exp5 (1000 MPa / 750 °C) in close proximity to secondary fluorcalciobritholite, display significant spectral changes compared to that of the Burnet monazite (Raman spots 99, 111, 134; EPMA spots 72, 83, 92; Fig. 19s, u, w). The spectral characteristics include a new peak at 860 cm^{-1}, increase of fluorescence effects at mid-range and at high-range (spectra 19, 20; Fig. 24d), which are similar to spectra of fluorcalciobritholite (spectra 23–25; Fig. 24e). Submicron alteration such as formation of submicron inclusions of fluorcalciobritholite may contribute to the Raman spectra of monazite, but this would require confirmation using nanoscale investigations. A recent TEM study of monazite revealed formation of nanoporosity across monazite rims and cores with numerous nanoinclusions of cheralite, which formed at 1000 MPa / 650 °C and 200 MPa / 750 °C (Budzyń et al. 2021). Fine grains of cheralite were also observed in this study at the phase boundary of monazite and fluorcalciobritholite from Exp4 (Fig. 19p), however, the features of a synthetic cheralite [$CaTh(PO_4)_2$] spectrum described by Raison et al. (2008) are not present in the fluorcalciobritholite spectra observed in this study. The Raman data do not confirm the presence of cheralite. Nanoinclusions of britholite have been documented with TEM in altered monazite at P-T conditions of 1000 MPa and 900 °C in earlier experimental study (Harlov et al. 2011), thus, the presence of nanoinclusions of fluorcalciobritholite in monazite investigated here is possible.

Signals of fluorcalciobritholite in Raman spectra of monazite may be used to identify its presence based on the distinct Raman features, which include a shifted $\nu_1(PO_4)$ band towards lower wavenumbers (ca. 960–965 cm^{-1}), the appearance of a new band at ca. 860 cm^{-1} and increased fluorescence effects at mid- and high-range in accordance to fluorcalciobritholite reference spectra. Two Raman spectra, in which signals of fluorcalciobritholite dominate over signals of monazite spectra, were obtained very close to micropores filled with fluorcalciobritholite (spectra 17, 18; Fig. 24c, e). This most probably indicates the presence of fluorcalciobritholite below the surface of the measured monazite, which possibly resulted from the submicron fluid-mediated alteration (Raman spots 56, 69, 70, 82; Fig. 19i, n, q).

4.5.4. Raman microspectroscopy of xenotime from experiments

The similarity of most Raman spectra of xenotime from all experiments demonstrates its chemical stability (spectra 1–4, 7; Fig. 34a–e). Textural evidence of alteration of xenotime from Exp4 and Exp5 (800–1000 MPa, 650–750 °C), however, are present as (i) dissolution pits at the rim of xenotime, (ii) formation of secondary Y-rich fluorcalciobritholite as overgrowth, and (iii) partial replacement of xenotime by Y-rich fluorcalciobritholite (Fig. 29i–l). Indeed, some Raman spectra show changes of fluorescence effects at the very rim of xenotime from Exp4 and Exp5 close to Y-rich fluorcalciobritholite (spectra 6, 8, 9; Fig. 34d, e). Comparison of these changes with representative spectra of the Y-rich fluorcalciobritholite emphasize resemblance (Fig. 34f). This is particularly true for the dominant Eu^{3+} ($^5D_0 \rightarrow {}^7F_3$) fluorescence band at ca. 2650 cm^{-1}, whereas other electronic transitions from the Eu^{3+} ($^5D_0 \rightarrow {}^7F_2$) fluorescence bands at ca. 1900 and 2000 cm^{-1}, do not increase in intensity in spectra of xenotime nor Y-rich fluorcalciobritholite.

4.5.5. Hyperspectral mapping of monazite and xenotime

The hyperspectral maps of monazite fit well with EPMA-WDS compositional X-ray maps and BSE images, and provided new information on the structural variations in monazite by revealing domains with a shift in peak position from 978 cm^{-1} to 962 cm^{-1} (Figs. 29, 30). These characteristics were obtained with both excitation lasers

(532 nm and 633 nm), which confirm structural changes in the crystal lattice of monazite. This example demonstrates the high potential of combining Raman hyperspectral mapping and EPMA compositional X-ray mapping to provide broader information in terms of identification of phases, their composition and structural characteristics.

In the case of xenotime, hyperspectral mapping resulted in a more ambiguous TCA images, which are partially contradicting BSE images and EPMA-WDS compositional X-ray maps (Figs. 39, 40). Raman signals attributed to the presence of Y-rich fluorcalciobritholite are present in domains, where only xenotime is observed with BSE images and compositional X-ray maps (green square, Figs. 39, 40). When interpreting hyperspectral maps, vertical resolution together with lateral resolution of the image should be considered (Tabaksblat et al. 1992; Everall 2010). The vertical resolution of the hyperspectral maps can be estimated with the formula $\Delta z = \lambda \times NA^{-2}$ (with NA = 0.45) and results in ca. 2.6 µm depth with 532 nm and ca. 3.1 µm depth with 633 nm laser. A focused electron beam when using EPMA possesses a resolution as low as 6 μm^3 when applied on xenotime (Hetherington et al. 2008). Interpretation of the hyperspectral maps of xenotime in combination with EPMA-WDS compositional X-ray maps lead to the conclusion that the spectral signals belong to Y-rich fluorcalciobritholite, which is located below the xenotime (green square Figs. 39, 40). The EPMA electron beam during compositional mapping of xenotime probably did not excite electrons deep enough into the sample in order to reveal chemical variation. In terms of EPMA measurements, this particular domain of xenotime may be suitable for chemical evaluation. However, the Raman data from hyperspectral mapping suggest caution if trace element analysis or geochronological evaluation of this domain is considered using microscopic methods such as LA-ICPMS or SIMS (Secondary Ion Mass Spectrometry).

In summary, hyperspectral mapping demonstrates the usage of Raman microspectroscopy to evaluate suitable areas for further measurements with microanalytical methods, because commonly used BSE images, which are commonly used for textural evaluation, only reflect the imminent surface of the sample. The 532 nm laser proofed to be useful for hyperspectral mapping of monazite, and was partially useful for xenotime, therefore the 532 nm laser may be considered in future studies of monazite and xenotime. In addition to the fluorescence-rich 488 nm and 780 nm lasers, other excitation lasers should also be investigated for the potential use of monazite and xenotime Raman microspectroscopy in future studies.

4.5.6. Application of Raman microspectroscopy to monazite and xenotime

Raman microspectroscopy of unaltered and compositionally altered domains of monazite provide useful information regarding identification of structural recovery based on band narrowing (decrease of FWHH values), that can be induced by recrystallization via fluid-induced coupled dissolution-reprecipitation processes (Putnis 2002, 2009; Harlov et al. 2011; Seydoux-Guillaume et al. 2012) or thermal annealing of damaged crystal structure (Meldrum and Boatner 1997; Ruschel et al. 2012; Seydoux-Guillaume et al. 2012, 2018; Nasdala et al. 2020). This correlation has been documented for a large variety of crystallographically randomly oriented samples, and distinguishes between band broadening caused by incorporation of the nonformula elements U, Th, Ca and Pb and band broadening caused by radiation damage (Ruschel et al. 2012). Indeed, Raman data of monazite from experiments in this study show a weak correlation with the contents of U, Th, Ca and Pb roughly following the trend calculated for annealed natural monazite (Ruschel et al. 2012).

In the case of the Ankazobe monazite, unaltered domains display significant band broadening of the $\nu_1(PO_4)$ symmetric stretching band in the range of 10.52–13.22 cm^{-1}

FWHH at relatively constant composition of U, Th, Ca and Pb (Fig. 42a). The variation of high FWHH values of the Ankazobe monazite reflects different degrees of irradiation damage in the crystal structure due to U and Th decay. In comparison, the Burnet monazite shows band broadening in range of 12.21–15.85 cm^{-1} FWHH (Fig. 25a). Radiation damage induced to the monazite structure accumulates over time, thus, the older Burnet monazite (LA-ICPMS U-Pb Concordia age 1100.5 ± 11.6 Ma; Budzyń et al. 2021) with higher Th and U contents could accumulate more radiation damage than the younger Ankazobe monazite (LA-ICPMS U-Pb Concordia age 515.4 ± 4.8 Ma; Budzyń, Sláma, personal communication). Altered domains of the Ankazobe monazite show significant band narrowing (6.32–10.15 cm^{-1}; Fig. 42a) and depletion of Th, U and Pb, which indicate lower degree of radiation damage due to recrystallization via fluid-aided coupled dissolution-reprecipitation processes. These observations are consistent with earlier studies (Ruschel et al. 2012; Seydoux-Guillaume et al. 2012, 2018; Nasdala et al. 2020; Budzyń et al. 2021, 2022), and demonstrate the value of Raman microspectroscopy in the selection of unaltered monazite domains for geochronological measurements.

An attempt to evaluate a potentially similar relation of U, Th, Ca and Pb contents in xenotime structure, as has been demonstrated for monazite, was not satisfactory. No correlation of FWHH values with U, Th, Ca and Pb contents could be documented in this study based on data of xenotime from experiments or data of the naturally altered xenotime from the Piława Górna pegmatite (Fig. 42b). The reason for lack of such correlation is related to the generally low contents of U, Th, Ca and Pb in the investigated xenotimes. Consequently, these nonformula elements do not distort the xenotime structure in the same way as they affect the structure of monazite. Indeed, the NWFP xenotime is very young (38.4 ± 0.6 Ma, Budzyń et al. 2019) and has low U and Th concentrations. Therefore, radiation damage may have not accumulated sufficiently in the

NWFP xenotime to reflect band broadening in Raman data in this study. The xenotime from pegmatite from Piława Górna, on the other hand, went through the high-temperature alterations at ca. 370 Ma (Budzyń et al. 2018). The timescale of 370 Ma was long enough to accumulate radiation damage in the xenotime structure after alteration ended. This is demonstrated by higher FWHH values of xenotime from the pegmatite from Piława Górna (7.31–9.03 cm^{-1} FWHH) compared to those of xenotime from experimental products (4.58–6.25 cm^{-1} FWHH; Fig. 42b). This implies a certain degree of radiation damage accumulated in the xenotime from the pegmatite from Piława Górna compared to the highly crystalline xenotime from experimental products.

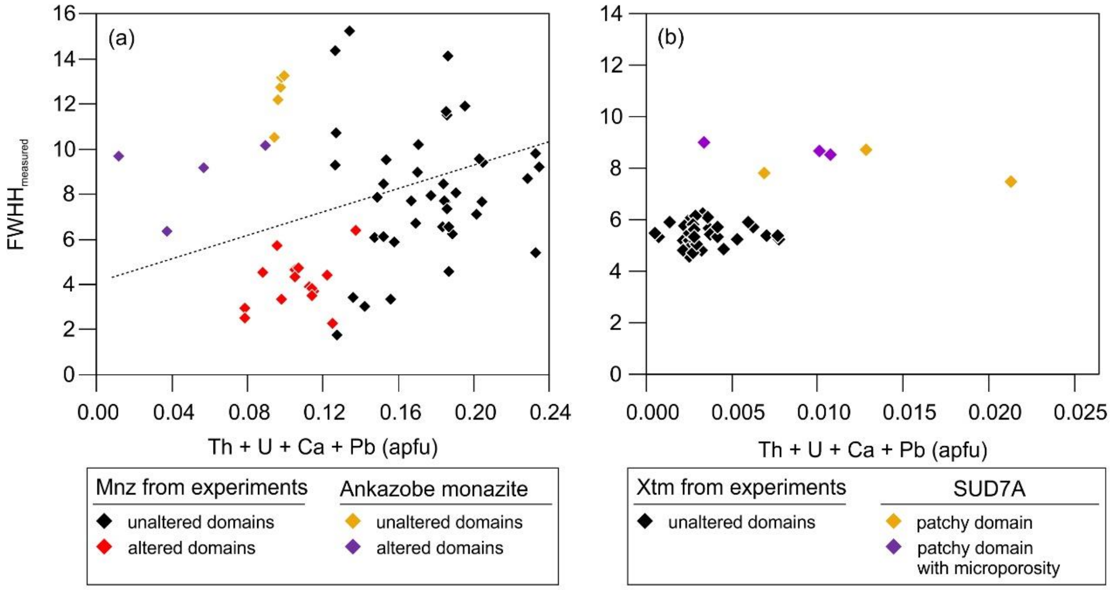

Fig. 42. Sum of Th, U, Ca and Pb (apfu) vs. measured FWHH values of the symmetric stretching band v_1(PO$_4$) of (a) monazite from experiments and Ankazobe monazite, and (b) xenotime from experiments and xenotime from pegmatite from Piława Górna (SUD7A). Dashed line indicates correlation of sum of Th, U, Ca and Pb with FWHH values of annealed natural monazite based on a formula FWHH = 3.95 + 26.66 × (Th + U + Ca + Pb) [apfu] (Ruschel et al. 2012).

For comparison, moderate degree of radiation damage was demonstrated in a micro- to nanoscale study of the xenotime from the pegmatite (Evje, S Norway), including Raman microspectroscopy and TEM, in which the primary xenotime (ca. 980 Ma) yielded high FWHH values (13.28–15.56 cm^{-1}; Budzyń et al. 2023b). Altered domains of the xenotime demonstrated a crystalline structure with low FWHH values beginning at 1.07 up to moderated values of 9.76 cm^{-1} (Budzyń et al. 2023b), which fall within the range of FWHH values measured of xenotime from Piława Górna. Furthermore, TEM evaluation of the xenotime from Evje demonstrated how fluid-mediated mobilization of U, Th and Si lead to segregation of these elements into a network of dislocations of the xenotime accompanied by radiation-damaged material surrounding those dislocations (Budzyń et al. 2023a).

The Raman data of xenotime from pegmatite from Piława Górna, and data of the xenotime from pegmatite from Evje, demonstrate two cases in which Raman microspectroscopy served as a good tool to investigate and identify radiation-damaged domains in xenotime. The extent of band broadening may also enable an assessment of the degree of radiation damage in comparison with the highly crystalline, low Th and U xenotime from experiments, which is significant because xenotime is considered to be highly resistant to radiation damage. On the contrary, it has been demonstrated in both cases that xenotime can accumulate low to moderate degrees of radiation damage.

To summarize, the Raman microspectroscopy data presented in this study provide information about presence of foreign phases underlying the surface of monazite and xenotime, radiation damage to the structure and recrystallization via fluid-induced alteration based on spectral changes such as appearance of new peaks, narrowing of band widths of the $v_1(PO_4)$ symmetric stretching band and significant increase and broadening of fluorescence effects. Application of hyperspectral mapping, in particular, provide additional important information of the structural properties of monazite and xenotime that complement commonly used EPMA-WDS compositional X-ray mapping. The chosen excitation lasers 532 nm and 633 nm are complementary to other microscopic methods such as LA-ICPMS and EPMA, whereas Raman spectra of the other used lasers (488 nm and 780 nm) were obstructed by broad fluorescence effects and, thus, are less suited for broad evaluation of monazite and xenotime. The spectra obtained with 488 nm and 780 nm lasers, however, may bear potential for specific studies of characteristics of fluorescence effects, e.g. in photoluminescence spectroscopy. Further evaluation with more suitable laser lines in order to achieve more characteristic spectral data of monazite, xenotime and fluorcalciobritholite without (or to a lesser extent) the interference of fluorescence effects, especially in the range of lattice and internal bending modes (100–700 cm^{-1}), are necessary to improve our knowledge and to assess future potential of Raman microspectroscopy in petrochronological studies.

5. Conclusions

The results of this study constrain various alteration processes that occur at submicron-scale and progress into microscale, leaving distinct textural features in the altered mineral, its composition and structural arrangement. The investigated zircon from a pegmatite from Piława Górna demonstrated records of multiple alteration, including alkaline fluid-induced diffusion-reaction processes the core, and coupled dissolution-reprecipitation processes fluid in the rim, leading to formation of interconnected microporosity and secondary micro- to nanoinclusions of Fe-rich phases, uraninite, coffinite and thorite in the presence of an Fe- and alkaline-rich fluid. The Fe-rich fluids also altered the intergrown xenotime via coupled dissolution-reprecipitation processes, which demonstrate patchy zoning, microporosity and inclusions of Fe-silicate, coffinite-thorite solid solution and uraninite. Accumulation of U and Th-rich inclusions in zircon and xenotime lead to a locally high dosage of alpha irradiation, which lead to amorphization of zircon and even xenotime. Differentiation of alteration processes were accomplished due to the combination of LA-ICPMS trace element analysis and TEM investigations, which allowed us to estimate the geochemical characteristics and textural evaluation at nanoscale, emphasizing the importance of combining micro- and nanoscale methods. The combined study of LA-ICPMS and TEM micro- to nanoscale evaluation of a natural case of pegmatite containing altered xenotime and zircon, and Raman microspectroscopy evaluation of monazite and xenotime, known orthophosphates typical for pegmatitic environments, provide valuable information of alteration mechanisms and how submicron alteration can affect microscopic textures.

The Raman data for monazite and xenotime from the laboratory experiments demonstrate how structural changes, due to alteration processes, are reflected in distinct spectral characteristics. These include shift of peak positions, band broadening and narrowing, and changes in intensity and broadening of REE-characteristic fluorescence effects. The FWHH value of the $v_1(PO_4)$ symmetric stretching band of monazite provides valuable information about the structural properties of monazite. Band broadening of the $v_1(PO_4)$ band are the result of various degrees of radiation damage to the crystal structure due to decay of U and Th. Significant band narrowing on the other hand, in combination with U, Th and Pb depletion and enrichement of Ca, indicate recrystallized domains as a result of fluid-induced coupled dissolution-reprecipitation processes. Whereas, progressive band narrowing at elevated temperatures, in chemically unaffected domains, indicate thermal annealing processes. Comparison of Raman spectra obtained with various lasers has shown that the (i) 532 nm laser is well suited to identify the characteristic Raman features and fluorescence effects in monazite, and (ii) the 633 nm laser provided the most fluorescence-free monazite spectra. The xenotime spectra demonstrate fluorescence effects in the range of primary Raman features (ca. 100–800 cm^{-1}) collected with both, 532 nm and 633 nm lasers. The Raman spectra of monazite and xenotime collected with the 488 nm and 780 nm lasers are not recommended due to extensive fluorescence effects present in the spectra of monazite and xenotime. The collective Raman data of this study demonstrate the importance and applicability of Raman microspectroscopy to petrochronological studies of monazite and xenotime, particularly in regards to selection of suitable analyses, identification of secondary phases, underlying phase transitions and structural changes caused by alteration. This is particularly emphazised by hyperspectral maps which provide additional structural information to monazite and xenotime (and other phases), which are generally complementing compositional evaluation with EPMA-WDS mapping. In the case of xenotime, hyperspectral mapping demonstrates the potential to identify and reveal signals of underlying secondary phases or phase transitions, which are missed by surface near analytical methods such as EPMA-WDS maps, and proves to be very useful in understanding potentially underlying interferences when microscopic analysises are applied. The Raman data enables differentiation of alteration mechanisms such as structural damage due to self-irradiation, recrystallization due to coupled dissolution-reprecipitation or thermal annealing effects if combined with compositional data. On the other hand, it also became clear, that this field bears the potential to extent the data and our understanding much further. Therefore, future works of Raman microspectroscopic investigation of monazite and xenotime could improve distinct characteristic changes in the spectra collected with other not yet evaluated excitation lasers.

Fluid-induced alteration processes change the geochemistry and structure of the minerals, which often hinders estimation of their original geochemical fingerprint, disturbs or resets their ages or lead to transformation into new phases. Understanding the effects of alteration bears the potential to estimate P-T conditions and age of metasomatic or hydrothermal events, which is important to reconstruct the history of the rocks and, in a broader scale, orogens. This study demonstrates the importance of understanding sub-micron alteration processes and how micro-textures of monazite, xenotime and zircon can be affected by them proving potential danger of misinterpretation if disregarded. The detailed characterisation of Raman data of monazite and xenotime from experimental products and naturally altered cases, in combination with EPMA and LA-ICPMS analysises, expand our understanding of alteration processes recorded by monazite and xenotime. The expanded Raman database of LREE to HREE bearing orthophosphates monazite and xenotime may serve as reference in future spectroscopic, geochemical and petrochronological investiagations of complexly altered monazite and xenotime.

6. References

Anderson J.A., Hanchar J.M., Hodges K.V., van Soest M.C. (2020) Mapping radiation damage zoning in zircon using Raman spectroscopy: Implications for zircon chronology. Chemical Geology 538, 119494.

Andrehs G., Heinrich W. (1998) Experimental determination of REE distributions between monazite and xenotime: Potential for temperature-calibrated geochronology. Chemical Geology 149, 83–96.

Austrheim H., Putnis C.V., Engvik A.K., Putnis A. (2008) Zircon coronas around Fe–Ti oxides: a physical reference frame for metamorphic and metasomatic reactions. Contributions of Mineralogy and Petrology 156, 517–527.

Beall G.W., Boatner L.A., Mullica D.F., Milligan W.O. (1981) The structure of cerium orthophosphate, a synthetic analog of monazite. Journal of Inorganic and Nuclear Chemistry 43, 101–105.

Begun G.M., Beall G.W., Boatner L.A., Gregor W.J. (1981) Raman Spectra of the Rare Earth Orthophosphates. Journal of Raman Spectroscopy 11, 273–278.

Bell E.A., Boehnke P., Harrison T.M. (2016) Recovering the primary geochemistry of Jack Hills zircons through quantitative estimates of chemical alteration. Geochimica et Cosmochimica Acta 191, 187–202.

Bell E.A., Boehnke P., Barboni M., Harrison T.M. (2019) Tracking chemical alteration in magmatic zircon using rare earth element abundances. Chemical Geology 510, 56–71.

Belousova E.A., Griffin W.L., O’Reilly S.Y., Fisher N.I. (2002) Igneous zircon: trace element composition as an indicator of source rock type. Contributions to Mineralogy and Petrology 143, 602–622.

Belsky A.N., Krupa J.C. (1999) Luminescence excitation mechanisms of rare earth doped phosphors in the VUV range. Display 19, 185–196.

Betkowski W.B., Harlov D.E., Rakovan J.F. (2016) Hydrothermal mineral replacement reactions for an apatite-monazite assemblage in alkali-rich fluids at 300-600 °C and 100 MPa. American Mineralogist 101, 2620–2637.

Bingen B., Demaiffe D., Hertogen J. (1996) Redistribution of rare earth elements, thorium, and uranium over accessory minerals in the course of amphibolite to granulite facies metamorphism: The role of apatite and monazite in orthogneisses from southwestern Norway. Geochimica et Cosmochimica Acta 60, 1341–1354.

Black L.P., Fitzgerald S.H., Harley S.L. (1984) Pb isotopic composition, colour, and microstructure of monazites from a polymetamorphic rock in Antarctica. Contributions to Mineralogy and Petrology 85, 141–148.

Boatner L.A. (2002) Synthesis, Structure, and Properties of Monazite, Pretulite, and Xenotime. Reviews in Mineralogy and Geochemistry 48, 87–121.

Bouvier A.S., Ushikubo T., Kita N.T., Cavosie A.J., Kozdon R., Valley J.W. (2012) Li isotopes and trace elements as a petrogenetic tracer in zircon: insights from Archean TTGs and sanukitoids. Contributions to Mineralogy and Petrology 163, 745–768.

Broska I., Siman P. (1998) The breakdown of monazite in the West-Carpathian Veporic orthogneisses and Tatric granites. Geologica Carpathica 49, 161–167.

Broska I., Williams C.T., Janák M., Nagy G. (2005) Alteration and breakdown of xenotime-(Y) and monazite-(Ce) in granitic rocks of the Western Carpathians, Slovakia. Lithos 82, 71–83.

Bröcker M., Żelaźniewicz A., Enders M. (1998) Rb-Sr and U-Pb geochronology of migmatitic gneisses from the Góry Sowie (West Sudetes, Poland): the importance of Mid-Late Devonian metamorphism. Journal of the Geological Society, London 155, 1025–1036.

Budzyń B., Kozub-Budzyń G.A. (2015) The stability of xenotime in high Ca and Ca-Na systems, under experimental conditions of 250–350°C and 200–400 MPa: the implications for fluid-mediated low-temperature processes in granitic rocks. Geological Quarterly 59, 316–324.

Budzyń B., Sláma J. (2019) Partial resetting of U–Pb ages during experimental fluid-induced re-equilibration of xenotime. Lithos 346–347, 105163.

Budzyń B., Hetherington C.J., Williams M.L., Michalik M. (2010) Fluid–mineral interactions and constraints on monazite alteration during metamorphism. Mineralogical Magazine 74, 659–681.

Budzyń B., Harlov D.E., Williams M.L., Jercinovic M.J. (2011) Experimental determination of stability relations between monazite, fluorapatite, allanite, and REE-epidote as a function of pressure, temperature, and fluid composition. American Mineralogist 96, 1547–1567.

Budzyń B., Konečný P., Kozub-Budzyń G.A. (2015) Stability of monazite and disturbance of the Th-U-Pb system under experimental conditions of 250–350 °C and 200–400 MPa. Annales Societatis Geologorum Poloniae 85, 405–424.

Budzyń B., Harlov D., Kozub-Budzyń G.A., Majka J. (2017) Experimental constraints on the relative stabilities of the two systems monazite-(Ce) – allanite-(Ce) – fluorapatite and xenotime-(Y) – (Y,HREE)-rich epidote – (Y,HREE)-rich fluorapatite, in high Ca and Na-Ca environments under P-T conditions of 200–1000 MPa and 450–750 °C. Mineralogy and Petrology 111, 183–217.

Budzyń B., Sláma J., Kozub-Budzyń G.A., Konečný P., Holický I., Rzepa G., Jastrzębski M. (2018) Constraints on the timing of multiple thermal events and re-equilibration recorded by high-U zircon and xenotime: Case study of pegmatite from Piława Górna (Góry Sowie Block, SW Poland) Lithos 310–311, 65–85.

Budzyń B., Wirth R., Sláma J., Birski Ł., Tramm F., Kozub-Budzyń G.A., Rzepa G., Schreiber A. (2021) LA-ICPMS, TEM and Raman study of radiation damage, fluid-induced alteration and disturbance of U-Pb and Th-Pb ages in experimentally metasomatised monazite. Chemical Geology 583, 120464.

Budzyń B., Wirth R., Sláma J., Kozub-Budzyń G., Rzepa G., Schreiber A. (2022) A detailed and comprehensive TEM, EPMA and Raman characterization of high-metamorphic grade monazites and their U-Th-Pb systematics (the Góry Sowie Block, SW Poland). Chemical Geology 607, 121015.

Budzyń, B., Wirth, R., Sláma, J., Kozub-Budzyń, G.A., Schreiber, A. (2023a) Atomic-scale Th and U segregation into dislocation cores and U-Pb age discordance in xenotime. Lithos 444–445, 107105.

Budzyń B., Wirth R., Sláma J., Kozub-Budzyń G.A., Konečný P., Rzepa G., Schreiber A. (2023b) Micro- to nanoscale constraints on metasomatic alterations of xenotime, inclusions of Th-, U- and Pb-phases and their geochronological implications (Ås pegmatite, Evje and Hornnes, S Norway). Chemical Geology 632, 121538.

Caruba R., Iacconi P. (1983) Les zircons des pegmatites de Narssârssuk (Groëland)—l’eau et les groupments OH dans les zircons meamictes. Chemical Geology 38, 75–92.

Cavosie A.J., Valley J.W., Wilde S.A. (2006) Correlated microanalysis of zircon: Trace element, δ^{18}O, and U–Th–Pb isotopic constraints on the igneous origin of complex >3900 Ma detrital grains. Geochimica et Cosmochimica Acta 70, 5601–5616.

Chen C.-H., Lee C.-Y., Lin J.-W., Chu M.-F. (2019) Provenance of sediments in western Foothills and Hsuehshan Range (Taiwan): A new view based on the EMP monazite versus LA-ICPMS zircon geochronology of detrital grains. Earth-Science Reviews 190, 224–246.

Cherniak D.J. (2006) Pb and rare earth element diffusion in xenotime. Lithos 88, 1–14.

Cherniak D.J. (2010) Diffusion in accessory minerals: zircon, titanite, apatite, monazite and xenotime. In: Zhang Y., Cherniak D.J. (Eds.) Diffusion in Minerals and Melts. Reviews in Mineralogy and Geochemistry 72, 827–869.

Cherniak D.J., Watson E.B. (2001) Pb diffusion in zircon. Chemical Geology 172, 5–24.

Cherniak D.J., Watson E.B., Grove M., Harrison T.M. (2004) Pb diffusion in monazite: A combined RBS/SIMS study. Geochemica et Cosmochimica Acta 68, 829–840.

Claiborne L.L., Miller C.F., Walker B.A., Wooden J.L., Mazdab F.K., Bea F. (2006) Tracking magmatic processes through Zr/Hf ratios in rocks and Hf and Ti zoning in zircons: an example from the Spirit Mountain batholith, Nevada. Mineralogical Magazine 70, 517–543.

Clavier N., Podor R., Dacheux N. (2011) Crystal chemistry of the monazite structure. Journal of the European Ceramic Society 31, 941–976.

Clavier N., Mesbah A., Szenknect S., Dchauex N. (2018) Monazite, rabdophane, xenotime & churchite: Vibrational spectroscopy of gadolinium phosphate polymorphs. Spectrochimica Acta Part A: Molecular and Biomolecular Spectroscopy 205, 85–94.

Corfu F., Hanchar J.M., Hoskin P.W.O., Kinny P. (2003) Atlas of Zircon Textures. Reviews in Mineralogy and Geochemistry 53, 469–500.

Černý P., Ercit T.S. (2005) The classification of granitic pegmatites revisited. Canadian Mineralogist 43, 2005–2026.

Dawood Y.H., Abd El-Naby H.H. (2007) Mineral chemistry of monazite from the black sand deposits, northern Sinai, Egypt: a provenance perspective. Mineralogical Magazine 71, 389–406.

Didier A., Bosse V., Boulvais P., Bouloton J., Paquette J.L., Montel J.M., Devidal J.L. (2013) Disturbance versus preservation of U–Th–Pb ages in monazite during fluid–rock interaction: textural, chemical and isotopic in situ study in microgranites (Velay Dome, France). Contributions to Mineralogy and Petrology 165, 1051–1072.

Dieke G.H., Crosswhite H.M. (1963) Emission Spectra of the Doubly and Triply Ionized Rare Earths. Journal of the Optical Society of America 51, 675–686.

Dröllner M., Barham M., Kirkland C.L., Roberts M.P. (2023) Older than they look: Cryptic recycled xenotime on detrital zircon. Geology 51, 768–772.

El-Bialy M.Z., Ali K.A. (2013) Zircon trace element geochemical constraints on the evolution of the Ediacaran (600–614 Ma) post-collisional Dokhan Volcanics and Younger Granites of SE Sinai, NE Arabian–Nubian Shield. Chemical Geology 360, 54–73.

Ende M., Chanmuang N.C., Reiners P.W., Zamyatin D.A., Gain S.E.M., Wirth R., Nasdala L. (2021) Dry annealing of radiation-damaged zircon: Single-crystal X-ray and Raman spectroscopy study. Lithos 406–407, 106523.

Es’kova E.M. (1959) Geochemistry of Nb and Ta in the nepheline syenite massifs of the Vishnevyie Mountains. Geokhimiya 2, 130–139 (in Russian).

Everall N.J. (2010) Confocal Raman microscopy: common errors and artefacts. Analyst 135, 2512–2522.

Ewing R.C. (1999) Nuclear waste form for actinides. Proceedings of the National Academy of Sciences of the United States of America 96, 3432–3439.

Ewing R.C. (2001) The design and evaluation of nuclear-waste forms: clues from mineralogy. Canadian Mineralogist 39, 697–715.

Ewing R. C., Lutze W. (1991) High-level nuclear waste immobilization with ceramics. Ceramics International 17, 287–293.

Ewing R.C., Meldrum A., Wang L., Weber W.J., Corrales L.R. (2003) Radiation effects in zircon. In: Hanchar J.M., Hoskin P.W.O. (Eds.) Zircon. Reviews in Mineralogy and Geochemistry 53, 387–425.

Ferry J. M., Watson E.B. (2007) New thermodynamic models and revised calibrations for the Ti-in-zircon and Zr-in-rutile thermometers. Contributions to Mineralogy and Petrology 154, 429–437.

Fielding I.O.H., Johnson S.P., Zi J.W., Rasmussen B., Dunkley D.J., Sheppard S., Wingate M.T.D., Rogers J.R. (2017) Using In Situ SHRIMP U-Pb Monazite and Xenotime Geochronology to Determine the Age of Orogenic Gold Mineralization: An Example from the Paulsens Mine, Southern Pilbara Craton. Economic Geology 112, 1205–1230.

Finger F., Broska I., Roberts M.P., Schermaier A. (1998) Replacement of primary monazite by apatite-allanite-epidote coronas in an amphibolite facies granite gneiss from the eastern Alps. American Mineralogist 83, 248–258.

Fletcher I.R., Rasmussen B., McNaughton N.J. (2000) SHRIMP U–Pb geochronology of authigenic xenotime and its potential for dating sedimentary basins. Australian Journal of Earth Sciences 47, 845–859.

Fougerouse D., Reddy S.M. Saxey D.W., Erickson T.M., Kirkland C.L., Rickard W.D.A., Seydoux-Guillaume A.M., Clark C., Buick I.S. (2018) Nanoscale distribution of Pb in monazite revealed by atom probe microscopy. Chemical Geology 479, 251–258.

Förster H.J. (1998) The chemical composition of REE–Y–Th–U-rich accessory minerals from peraluminous granites of the Erzgebirge-Fichtelgebirge region, Germany.

Part I: The monazite-(Ce)–brabantite solid solution series. American Mineralogist 83, 259–272.

Förster H.J. (2006) Composition and origin of intermediate solid solutions in the system thorite–xenotime–zircon–coffinite. Lithos 88, 35–55.

Förster H.J., Harlov D.E. (1999) Monazite-(Ce)–huttonite solid solutions in granulite-facies metabasites from the Ivrea-verbano Zone, Italy. Mineralogical Magazine 63, 587–594.

Frondel C. (1953) Hydroxyl substitution in thorite and zircon. American Mineralogist 38, 1007–1018.

Gaft M., Reisfeld R., Panczer G. (2015) Modern Luminescence Spectroscopy of Minerals and Materials. Second Edition. Springer, pp. 220–221.

Geisler T., Pidgeon R.T., van Bronswijk W., Pleysier R. (2001) Kinetics of thermal recovery and recrystallization of partially metamict zircon a Raman spectroscopic study. European Journal of Mineralogy 13, 1163–1176.

Geisler T., Pidgeon R.T., van BronswijkW., Kurtz R. (2002) Transport of uranium, thorium and lead in metamict zircon under low-temperature hydrothermal conditions. Chemical Geology 191, 141–154.

Geisler T., Pidgeon R.T., Kurtz R., van Bronswijk W., Schleicher H. (2003a) Experimental hydrothermal alteration of partially metamict zircon. American Mineralogist 88, 1496–1513.

Geisler T., Trachenko K., Ríos S., Dove M.T., Salje E.K. (2003b) Impact of self-irradiation damage on the aqueous durability of zircon ($ZrSiO_4$): implications for its suitability as a nuclear waste form. Journal of Physics: Condensed Matter 15, L597–L605.

Geisler T., Rashwan A.A., Rahn M.K.W., Poller U., Zwingmann H., Pidgeon R.T., Tomaschek F. (2003c) Low-temperature hydrothermal alteration of natural metamict zircons from the Eastern Desert, Egypt. Mineralogical Magazine 67, 485–508.

Geisler T., Seydoux-Guillaume A.M., Wiedenbeck M., Wirth R., Berndt J., Zhang M., Mihailova B., Putnis A., Salje E.K.H., Schlüter J. (2004) Periodic precipitation pattern formation in hydrothermally treated metamict zircon. American Mineralogist 89, 1341–1347.

Geisler T., Schaltegger U., Tomaschek F. (2007) Re-equilibration of zircon in aqueous fluids and melts. Elements 3, 43–50.

Geisler T., Popa K., Konings R.J.M. (2016) Evidence for Lattice Strain and Non-ideal Behavior in the $(La_{1-x}Eu_x)PO_4$ Solid Solution from X-ray Diffraction and Vibrational Spectroscopy. Frontiers in Earth Sience 4, 1–12.

Ginster U., Reiners P.W., Nasdala L., Chanmuang C.N. (2019) Annealing kinetics of radiation damage in zircon. Geochimica et Cosmochimica Acta 249, 225–246.

Gordon S.M., Schneider D.A., Manecki M., Holm D.K. (2005) Exhumation and metamorphism of an ultrahigh-grade terrane: geochronometric investigations of the Sudete Mountains (Bohemia), Poland and Czech Republic. Journal of the Geological Society 162, 841–855.

Grand'Homme A., Janots E., Seydoux-Guillaume A.M., Guillaume D., Bosse V., Magnin V. (2016) Partial resetting of the U-Th-Pb systems in experimentally altered monazite: Nanoscale evidence of incomplete replacement. Geology 44, 431–434.

Grand'Homme A., Janots E., Seydoux-Guillaume A.M., Guillaume D., Magnin V., Hövelmann J., Höschen C., Boiron M.C. (2018) Mass transport and fractionation during monazite alteration by anisotropic replacement. Chemical Geology 484, 51–68.

Grapes R., Bucher K., Hoskin P.W.O. (2005) Monazite-epidote reaction in amphibolite grade blackwall rocks. European Journal of Mineralogy 17, 553–566.

Gratz R., Heinrich W. (1997) Monazite-xenotime thermobarometry: Experimental calibration of the miscibility gap in the binary system $CePO_4$–YPO_4. American Mineralogist 82, 7–8.

Grimes C.B., John B.E., Kelemen P.B., Mazdab F.K., Wooden J.L., Cheadle M.J., Hanghøj K.J., Schwartz J. (2007) Trace element chemistry of zircons from oceanic crust: A method for distinguishing detrital zircon provenance. Geology 35, 643–646.

Grimes C.B., Wooden J.L., Cheadle M.J., John B.E. (2015) “Fingerprinting” tectono-magmatic provenance using trace elements in igneous zircon. Contributions to Mineralogy and Petrology 170, 46.

Halden N.M., Hawthorne F.C., Campbell J.L., Teesdale W.J., Maxwell J.A., Higuchi D. (1993) Chemical characterization of oscillatory zoning and overgrowths in zircon using 3 MeV µ-PIXE. The Canadian Mineralogist 31, 637–647.

Harley S.L., Kelly N.M. (2007) Zircon: Tiny but Timely. Elements 3, 13–18.

Harlov D.E., Hetherington C.J. (2010) Partial high-grade alteration of monazite using alkali-bearing fluids: Experiment and nature. American Mineralogist 95, 1105–1108.

Harlov D.E., Wirth R. (2012) Experimental incorporation of Th into xenotime at middle to lower crustal P-T utilizing alkali-bearing fluids. American Mineralogist 97, 641–652.

Harlov D.E., Wirth R., Hetherington C.J. (2007) The relative stability of monazite and huttonite at 300–900 C and 200–1000 MPa: Metasomatism and the propagation of metastable mineral phases. American Mineralogist 92, 1652–1664.

Harlov D.E., Wirth R., Hetherington C.J. (2011) Fluid-mediated partial alteration in monazite: the role of coupled dissolution–reprecipitation in element redistribution and mass transfer. Contributions to Mineralogy and Petrology 162, 329–348.

Harlov D.E., Anczkiewicz R., Dunkley D.J. (2023) Metasomatic alteration of zircon at lower crustal P-T conditions utilizing al- kali- and F-bearing fluids: trace element incorporation, depletion, and reset- ting the zircon geochronometer. Geochimica et Cosmochimica Acta 352, 222–235.

Harrison T.M., Catlos E.J., Montel J.M. (2002) U-Th-Pb dating of phosphate minerals. In: Kohn J.K., Hughes J.M. (Eds.) Phosphates: Geochemical, Geobiological, and Materials Importance. Reviews in Mineralogy and Geochemistry 48, 523–558.

Hawkins D.P., Bowring S.A. (1999) U-Pb monazite, xenotime and titanite geochronological constraints on the prograde to post-peak metamorphic thermal history of Paleoproterozoic migmatites from the Grand Canyon, Arizona. Contribution to Mineralogy and Petrology 134, 150–169.

Hay D.C., Dempster T.J. (2009) Zircon alteration, formation and preservation in sandstones. Sedimentology 56, 2175–2191.

Hecht L., Cuney M. (2000) Hydrothermal alteration of monazite in the Precambrian crystalline basement of the Athabasca Basin (Saskatchewan, Canada): implications for the formation of unconformity-related uranium deposits. Mineralium Deposita 35, 791–795.

Heinrich W., Andrehs G., and Franz G. (1997) Monazite–xenotime miscibility gap thermometry. I. An empirical calibration. Journal of Metamorphic Geology 15, 3–17.

Hentschel F., Janots E., Trepmann C.A., Magnin V., Lanari P. (2020) Corona formation around monazite and xenotime during greenschist-facies metamorphism and deformation. European Journal of Mineralogy 32, 521–544.

Hetherington C.J., Harlov D.E. (2008) Metasomatic thorite and uraninite inclusion in xenotime and monazite from granitic pegmatites, Hidra anorthosite massif, southwestern Norway: Mechanics and fluid chemistry. American Mineralogist 93, 806–820.

Hetherington C.J., Jercinovic M.J., Williams M.L., Mahan K. (2008) Understanding geologic processes with xenotime: Composition, chronology, and a protocol for electron microprobe microanalysis. Chemical Geology 254, 133–147.

Hetherington C.J., Harlov D.E., Budzyń B. (2010) Experimental initiation of dissolution-reprecipitation reactions in monazite and xenotime: the role of fluid composition. Mineralogy and Petrology 99, 165–184.

Heuser J., Bukaemskiy A.A., Neumeier S., Neumann A., Bosbach D. (2014) Raman and infrared spectroscopy of monazite-type ceramics used for nuclear waste conditioning. Progress in Nuclear Energy 72, 149–155.

Hoskin P.W.O. (2000) Patterns of chaos: Fractal statistics and the oscillatory chemistry of zircon. Geochimica et Cosmochimica Acta 64, 1905–1923.

Hoskin P.W.O. (2005) Trace-element composition of hydrothermal zircon and the alteration of Hadean zircon from the Jack Hills, Australia. Geochimica et Cosmochimica Acta 69, 637–648.

Hoskin P.W.O., Schaltegger U. (2003) The composition of zircon and igneous and metamorphic petrogenesis. In: Hanchar, J.M., Hoskin P.W.O. (Eds.) Zircon. Reviews in Mineralogy and Geochemistry 53, 27–62.

Huminicki D., Hawthorne F. (2019) The crystal chemistry of the phosphate minerals. Phosphates: Geochemical, Geobiological and Materials Importance 48, 123–254.

Jahns R.H., Burnham C.W. (1969) Experimental studies of pegmatite genesis: I. A model for the derivation and crystallization of granitic pegmatites. Economic Geology 64, 843–864.

Janots E., Negro F., Brunet F., Goffé B., Engi M., Bouybaouène M.L. (2006) Evolution of the REE mineralogy in HP-LT metapelites of the Sebtide complex, Rif, Morocco: Monazite stability and geochronology. Lithos 87, 214–234.

Janots E., Engi M., Berger A., Allaz J., Schwarz J.O., Spandler C. (2008) Prograde metamorphic sequence of REE minerals in pelitic rocks of the Central Alps: implications for allanite–monazite–xenotime phase relations from 250 to 610 °C. Journal of Metamorphic Geology 26, 509–526.

Jastrzębski M., Budzyń B., Żelaźniewicz A., Konečný P., Sláma J., Kozub-Budzyń G.A., Skrzypek E., Jaźwa A. (2021) Eo-Variscan metamorphism in the Bohemian Massif: Thermodynamic modelling and monazite geochronology of gneisses and granulites of the Góry Sowie Massif, SW Poland. Journal of Metamorphic Geology 39, 751–779.

Jercinovic M.J., Williams M.L. (2005) Analytical perils (and progress) in electron microprobe trace element analysis applied to geochronology: background acquisition interferences, and beam irradiation effects. American Mineralogist 90, 526–546.

Ji L., Liu F., Harlov D.E., Wang F. (2021) Fluid-induced alteration of monazite, magnetite, and sulphides during the albitization of a Palaeoproterozoic granite from the Jiao-Liao-Ji orogenic belt, North China Craton. Contributions to Mineralogy and Petrology 176, 81.

Jian W., Mao J., Lehmann B., Wu S., Chen L., Song S., Xu J. (2023) Two discrete gold mineralization events recorded by hydrothermal xenotime and monazite, Xiaoqinling gold district, central China. American Mineralogist, doi: 10.2138/am-2022-8635

Jin G.B., Soderholm L. (2015) Solid-state syntheses and single-crystal characterizations of three tetravalent thorium and uranium silicates. Journal of Solid State Chemistry 221, 405–410.

Joseph C., Fougerouse D., Saxey D.W., Verberne R., Reddy S.M., Rickard W.D.A. (2021) Xenotime at the nanoscale: U-Pb geochronology and optimisation of analyses by atom probe tomography. Geostandards and Geoanalytical Research 45, 443–456.

Joseph C., Fougerouse D., Reddy S.M., Olierook H.K.H., Tacchetto T., Kennedy A., Saxey D.W., Rickard W.D.A., Denyszyn S., Dodd A. (2023) Radiogenic Pb in xenotime trapped in nanoscale inclusions of apatite during fluid alteration. Chemical Geology 630, 121444.

Kelly C.J., Harlov D.E., Schneider D.A. (2020) Experimental fluid-mediated alteration of zircon under lower greenschist facies conditions. The Canadian Mineralogist 58, 247–265.

Kelly N.M., Clarke G.L., Harley S.L. (2006) Monazite behaviour and age significance in poly-metamorphic high-grade terrains: A case study from the western Musgrave Block, central Australia. Lithos 88, 100–134.

Kingsbury J.A., Miller C.F., Wooden J.L., Harrison T.M. (1993) Monazite paragenesis and U-Pb systematics in rocks of the eastern Mojave Desert, California, U.S.A.; implications for thermochronometry. Chemical Geology 110, 147–167.

Krogh T.E. (1993) High precision U-Pb ages for granulite metamorphism and deformation in the Archean Kapuskasing structural zone, Ontario: implications for structure and development of the lower crust. Earth and Planetary Science Letters 119, 1–18.

Kröner A., Hegner E. (1998) Geochemistry, single zircon ages and Sm-Nd systematics of granitoid rocks from the Góry Sowie (Owl Mts.), Polish West Sudetes: evidence for early Palaeozoic arc-related plutonism. Journal of the Geological Society 155, 711–724.

Kryza R. (1981) Migmatization in gneisses of the northern part of the Sowie Góry, Sudetes. Geologia Sudetica 16, 7–91.

Kryza R., Fanning C.M. (2007) Devonian deep-crustal metamorphism and exhumation in the Variscan Orogen: evidence from SHRIMP zircon ages from the HT-HP granulites and migmatites of the Góry Sowie (Polish Sudetes). Geodinamica Acta 20, 159–175.

Kylander-Clark A.R.C. (2017) Petrochronology by laser-ablation inductively coupled plasma mass spectrometry. In: Kohn M.J., Engi M., Lanari P. (Eds.) Petrochronology: Methods and Applications. Reviews in Mineralogy and Geochemistry 83, 183–198.

Lalla E.A., Shkolyar S., Gilmour C.M., Lozano-Gorrín A.D., Konstantinidis M., Freemantle J., Daly M.G. (2021) Structural and vibrational analyses of $CePO_4$ synthetic monazite samples under an optimized precipitation process. Journal of Molecular Structure 1223, 129150.

Laurent A.T., Duchene S., Bingen B., Bosse V., Seydoux-Guillaume A.M. (2018) Two successive phases of ultrahigh temperature metamorphism in Rogaland, S. Norway: Evidence from Y-in-monazite thermometry. Journal of Metamorphic Geology 36, 1009–1037.

Lenz C., Talla D., Ruschel K., Škoda R., Götze J., Nasdala L. (2013) Factors affecting the Nd^{3+} (REE^{3+}) luminescence of minerals. Mineralogy and Petrology 107, 415–428.

Lenz C., Nasdala L., Talla D., Hauzenberger C., Seitz R., Kolitsch U. (2015) Laser-induced REE^{3+} photoluminescence of selected accessory minerals – An “advantageous artefact” in Raman spectroscopy. Chemical Geology 415, 1–16.

Linthout K. (2007) Tripartite division of the system $2REEPO_4$–$CaTh(PO_4)_2$–$2ThSiO_4$, discreditation of brabantite, and recognition of cheralite as the name for members dominated by $CaTh(PO_4)_2$. Canadian Mineralogist 45, 503–508.

London D. (2014) A petrologic assessment of internal zonation in granitic pegmatites. Lithos 184–187, 74–104.

London D. (2015) Reply to Thomas and Davidson on "A petrologic assessment of internal zonation in granitic pegmatites" (London, 2014a). Lithos 212–215, 469–484.

London D. (2021) Pegmatites. In: Alderton D., Elias S.A. (Eds.) Encyclopedia of Geology, 2nd Edition. Academic Press, pp. 184–195.

London D., Morgan G.B. (2012) The pegmatite puzzle. Elements 8, 263–268.

Lo Pò D., Braga R., Massonne H.-J., Molli G., Montanini A., Theye T. (2016) Fluid-induced breakdown of monazite in medium-grade metasedimentary rocks of the Pontremoli basement (Northern Apennines, Italy). Journal of Metamorphic Geology 34, 63–84.

Lumpkin G.R. (2006) Ceramic waste forms for actinides. Elements 2, 365–372.

Majka J., Budzyń B. (2006) Monazite Breakdown in Metapelites from Wedel Jarlsberg Land, Svalbard – Preliminary Report. Mineralogia Polonica 37, 61–69.

Majka J., Pršek J., Budzyń B., Bačik P., Barker A.K., Łodziński M. (2011) Fluorapatite-hingganite-(Y) coronas as products of fluid-induced xenotime-(Y) breakdown in the Skoddefjellet pegmatite, Svalbard. Mineralogical Magazine 75, 159–167.

Marfunin A. (1979) Luminescence. In: Marfunin A.S. (Ed.) Spectroscopy, Luminescence and Radiation Centers in Minerals. Springer, Berlin, Heidelberg, pp. 141–222.

Marheine D., Kachlík V., Maluski H., Patoçka F., Żelaźniewicz A. (2002) New ^{40}Ar/^{39}Ar ages in the West Sudetes (Bohemian Massif): constraints on the Variscan polyphase tectonothermal development. In: Winchester J.A., Pharaoh T.C., Verniers J. (Eds.) Palaeozoic Amalgamation of Central Europe. Geological Society, London, Special Publications 201, 133–156.

Marsello A.E., Garver J.I. (2010) Radiation damage and uranium concentration in zircon as assessed by Raman spectroscopy and neutron irradiation. American Mineralogist 95, 1192–1201.

Matte P., Maluski H., Rajlich P., Franke W. (1990) Terrane boundaries in the Bohemian Massif: Result of large-scale Variscan shearing. Tectonophysics 177, 151–170.

McDonough W., Sun S. (1995) The composition of the Earth. Chemical Geology 120, 223–253.

McNaughton N.J., Rasmussen B., Fletcher N.J. (1999) SHRIMP Uranium-Lead Dating of Diagenetic Xenotime in Siliciclastic Sedimentary Rocks. Science 285, 78–80.

McNaughton N.J., Rasmussen B. (2018) Geochemical characterisation of xenotime formation environments using U- Th. Chemical Geology 484, 109–119.

Meldrum A., Boatner L.A. (1997) Displacive radiation effects in the monazite- and zircon-structure orthophosphates. Physical Review B – Condensed Matter and Materials Physics 56, 13805–13814.

Meldrum A., Boatner L.A., Weber W.J., Ewing R.C. (1998) Radiation damage in zircon and monazite. Geochimica et Cosmochimica Acta 62(14), 2509–2520.

Morton A.C., Hallsworth C.R. (1999) Processes controlling the composition of heavy mineral assemblages in sandstones. Sedimentary Geology 124, 3–29.

Mullican D.F., Sappenfield E.L., Boatner L.A. (1996) Monazite- and zircon-type structures of seven mixed (Ln/Ln)PO_4 compounds. Inorganica Chimica 244, 247–252.

Nardi L.V.S., Formoso M.L.L., Müller I.F., Fontana E., Jarvis K., Lamarão C. (2013) Zircon/rock partition coefficients of REEs, Y, Th, U, Nb, and Ta in granitic rocks: Uses for provenance and mineral exploration purposes. Chemical Geology 335, 1–7.

Nasdala L., Irmer G., Wolf D. (1995) The degree of metamictization in zircon: a Raman spectroscopic study. European Journal of Mineralogy 7, 471–478.

Nasdala L., Pidgeon R.T., Wolf D., Irmer G. (1998) Metamictization and U-Pb isotopic discordance in single zircons: a combined Raman microprobe and SHRIMP ion probe study. Mineralogy and Petrology 62, 1–27.

Nasdala L., Wenzel M., Vavra G., Irmer G., Wenzel T., Kober B. (2001) Metamictization of natural zircon: accumulation versus thermal annealing of radioactivity-induced damage. Contributions to Mineralogy and Petrology 141, 125–144.

Nasdala L., Lengauer C.L., Hanchar J.M., Kronz A., Wirth R., Blanc P., Kennedy A.K., Seydoux-Guillaume A.M. (2002) Annealing radiation damage and the recovery of cathodoluminescence. Chemical Geology 191, 121–140.

Nasdala L., Hanchar J.M., Rhede D., Kennedy A.K., Váczi T. (2010) Retention of uranium in complexly altered zircon: an example from Bancroft, Ontario. Chemical Geology 269, 290–300.

Nasdala L., Akhmadaliev S., Artac A., Chanmuang C., Habler G., Lenz C. (2018) Irradiation effects in monazite–(Ce) and zircon: Raman and photoluminescence study of Au-irradiated FIB foils. Physics and Chemistry of Minerals 45, 855–871.

Nasdala L., Akhmadaliev S., Burakov B.E., Chanmuang C., Škoda R. (2020) The absence of metamictization in natural monazite. Scientific Reports 10, 1–9.

Nemchin A.A., Horstwood M.S.A., Whitehouse M.J. (2013) High-Spatial-Resolution Geochronology. Elements 9, 31–37.

Ni Y., Hughes J.M., Mariano A.N. (1995) Crystal chemistry of the monazite and xenotime structures. American Mineralogist 80, 21–26.

O'Brien P.J., Kröner A., Jaeckel P., Hegner E., Żelaźniewicz A., Kryza R. (1997) Petrological and isotopic studies on Palaeozoic high-pressure granulites, Góry Sowie Mts, Polish Sudetes. Journal of Petrology 38, 433–456.

Ondrejka M., Uher P., Pršek J., Ozdín D. (2007) Arsenian monazite-(Ce) and xenotime-(Y), REE arsenates and carbonates from the Tisovec-Rejkovo rhyolite, Western Carpathians, Slovakia: Composition and substitutions in the (REE,Y)XO_4 system (X = P, As, Si, Nb, S). Lithos 95, 116–129.

Ondrejka M., Uher P., Putiš M., Broska I., Bačík P., Konečný, P., Schmiedt I. (2012) Two-stage break down of monazite by post-magmatic and metamorphic fluids: An example from the Veporic orthogneiss, Western Carpathians, Slovakia. Lithos 142–142, 245–255.

Ondrejka M., Putiš M., Uher P., Schmiedt I., Pukaňcík L., Koněcný P. (2016) Fluid-driven destabilization of REE-bearing accessory minerals in the granitic orthogneisses of North Veporic basement (Western Carpathians, Slovakia). Mineralogy and Petrology 110, 561–580.

Ondrejka M., Molnárová A., Putiš M., Bačík P., Uher P., Voleková B., Milovská S., Mikuš T., Pukančík L. (2022) Hellandite-(Y)–hingganite-(Y)–fluorapatite retrograde coronae: a novel type of fluid-induced dissolution–reprecipitation breakdown of xenotime-(Y) in the metagranites of Fabova Hoľa, Western Carpathians, Slovakia. Mineralogical Magazine 86, 586–605.

Overstreet, W.C. (1967) The geologic occurrence of monazite. Geological Survey Professional Papers, Washington, D.C. 530, 327 pp.

Parrish R.R. (1990) U–Pb dating of monazite and its application to geological problems. Canadian Journal of Earth Sciences 27, 1435–1450.

Papoulis D., Tsolis-Katagas P., Katagas C. (2004) Monazite alteration mechanisms and depletion measurements in kaolins. Applied Clay Science 24, 271–285.

Paquette J.L., Monchoux P., Couturier M. (1995) Geochemical and isotopic study of a norite-eclogite transition in the European Variscan belt: Implications for U-Pb zircon systematics in metabasic rocks. Geochimica et Cosmochimica Acta 59, 1611–1622.

Pepin G.J., Vance E.R. (1981) Crystal data for rare earth orthophosphates of the monazite structure-type. Journal of Inorganic and Nuclear Chemistry 43(II), 2807–2809.

Perrault G., Szymanski J.T. (1982) Steacyite, a New Name, and a Re-evaluation of the Nomenclature of "Ekanite"-Group Minerals. The Canadian Mineralogist 20, 59–63.

Petrík I., Konečný P., Kováčik M., Holický I. (2006) Electron-microprobe dating of monazite from the nízke Tatry Mountains orthogneisses (Western Carpathians, Slovakia). Geologica Carpathica 57, 227–242.

Pidgeon R.T., O'Neil J.R., Silver R.T. (1966) Uranium and lead isotopic stability in a metamict zircon under experimental hydrothermal conditions. Science 154, 1538–1540.

Pidgeon R.T., O'Neil J.R., Silver R.T. (1995) The interdependence of U-Pb stability, crystallinity and external conditions in natural zircons – an early experimental study. (In: Leon T. Silver 70th Birthday Symposium and Celebration). Extended Abstracts, 225–231.

Pieczka A., Łodziński M., Szełęg E., Ilnicki S., Nejbert K., Szuszkiewicz A., Turniak K., Banach M., Michałowski P., Różniak R. (2012) The Sowie Mts. pegmatites (Lower Silesia, SW Poland): a current knowledge. Acta Mineralogia-Petrographica, Abstract Series 7, 105–106.

Pieczka A., Szuszkiewicz A., Szełęg E., Ilnicki S., Nejbert K., Turniak K. (2014) Samarskite-group minerals and alteration products: an example from the Julianna pegmatitic system, Piława Górna, SW Poland. The Canadian Mineralogist 52, 303–319.

Poitrasson F., Chenery S., Shepherd T.J. (2000) Electron microprobe and LA-ICP-MS study of monazite hydrothermal alteration: Implications for U-Th-Pb geochronology and nuclear ceramics. Geochimica et Cosmochimica Acta 64, 3283–3297.

Putnis A. (2002) Mineral replacement reactions: from macroscopic observations to microscopic mechanisms. Mineralogical Magazine 66, 689–708.

Putnis A. (2009) Mineral replacement reactions. In: Oelkers E.H., Schott J. (Eds.) Thermodynamics and Kinetics of Water-Rock Interaction. Reviews in Mineralogy and Geochemistry 70, 87–124.

Putnis A., Austrheim H. (2010) Fluid-induced processes: metasomatism and metamorphism. Geofluids 10, 254–269.

Putnis A., Austrheim H. (2013) Mechanisms of Metasomatism and Metamorphism on the Local Mineral Scale: The Role of Dissolution-Reprecipitation During Mineral Re-equilibration. In: Harlov D.E., Austrheim H. (Eds.) Metasomatism and the Chemical Transformation of Rock, Lecture Notes in Earth System Sciences. Springer-Verlag Berlin Heidelberg, pp. 141–170.

Putnis A., Putnis C.V. (2007) The mechanism of reequilibration of solids in the presence of a fluid phase. Journal of Solid State Chemistry 180, 1783–1786.

Putnis C.V., Tsukamoto K., Nishimura Y. (2005) Direct observations of pseudomorphism: compositional and textural evolution at a fluid-solid interface. American Mineralogist 90, 1909–1912.

Pyle J.M., Spear F.S. (2000) An empirical garnet (YAG) – xenotime thermometer. Contributions to Mineralogy and Petrology 138, 51–58.

Pyle J.M., Spear F.S. (2003) Four generations of accessory-phase growth in low-pressure migmatites from SW New Hampshire. American Mineralogist 88, 338–351.

Pyle J.M., Spear F.S., Rudnick R.L., McDonough W.F. (2001) Monazite–Xenotime–Garnet Equilibrium in Metapelites and a New Monazite–Garnet Thermometer. Journal of Petrology 42, 2083–2107.

Rafiuddin M.R., Seydoux-Guillaume A.M., Deschanels X., Mesbah A., Baumier C., Szenknect S., Dacheux N. (2020) An in-situ electron microscopy study of dual ion-beam irradiated xenotime-type $ErPO_4$. Journal of Nuclear Materials 539, 152265.

Raison P., Jardin R., Bouëxière D., Konings R.J.M., Geisler T., Pavel C.C., Rebizant J., Popa K. (2008) Structural investigation of the synthetic $CaAn(PO_4)_2$ (A*n* = Th and Np) cheralite-like phosphates. Physics and Chemistry Minerals 35, 603–609.

Rasmussen B. (2005) Radiometric dating of sedimentary rocks: the application of diagenetic xenotime geochronology. Earth-Science Reviews 68, 197–243.

Rasmussen B., Fletcher I.R., Muhling J.R., Wilde S.A. (2010) In situ U–Th–Pb geochronology of monazite and xenotime from the Jack Hills belt: Implications for the age of deposition and metamorphism of Hadean zircons. Precambrian Research 180, 26–46.

Rasmussen B., Fletcher I.R., Muhling J.R. (2011) Response of xenotime to prograde metamorphism. Contributions to Mineralogy and Petrology 162, 1259–1277.

Rubatto D. (2017) Zircon: The metamorphic Mineral. In: Kohn M.J., Engi M., Lanari P. (Eds.) Petrochronology: Methods and Applications. Reviews in Mineralogy and Geochemistry 83, 216–295.

Ruiz-Agudo E., Putnis C.V., Putnis A. (2014) Coupled dissolution and precipitation at mineral–fluid interfaces. Chemical Geology 383, 132–146.

Ruschel K., Nasdala L., Kronz A., Hanchar J.M., Többens D.M., Škoda R., Finger F., Möller A. (2012) A Raman spectroscopic study on the structural disorder of monazite–(Ce). Mineralogy and Petrology 105, 41–55.

Sales B.C., White C.W., Boatner L.A. (1983) A comparison of the corrosion characteristics of synthetic monazite and borosilicate glass containing simulated nuclear defense waste. Nuclear and Chemical Waste Management 4, 281–289.

Sarma D.S., Fletcher I.R., Rasmussen B., McNaughton N.J., Mohan M.R., Groves D.I. (2011) Archaean gold mineralization synchronous with late cratonization of the Western Dharwar Craton, India: 2.52 Ga U-Pb ages of hydrothermal monazite and xenotime in gold deposits. Mineralium Deposita 46, 273–288.

Schmidt C., Rickers K., Wirth R., Nasdala L., Hanchar J.M. (2006) Low-temperature Zr mobility: An in situ synchrotron-radiation XRF study of the effect of radiation damage in zircon on the element release in H_2O + HCl ± SiO_2 fluids. American Mineralogist 91, 1211–1215.

Schneider D.A., Zahniser S.J., Glascock J.M., Gordon S.M., Manecki M. (2006) Thermochronology of the west Sudetes (Bohemian Massif): Rapid and repeated eduction in the eastern Variscides, Poland and Czech Republic. American Journal of Science 306, 846–873.

Schulz B. (2021) Monazite Microstructures and Their Interpretation in Petrochronology. Frontiers in Earth Science 9, 668566.

Seydoux-Guillaume A.M., Paquette J.L., Wiedenbeck M., Montel J.M., Heinrich W. (2002a) Experimental resetting of the U–Th–Pb systems in monazite. Chemical Geology 191, 165–181.

Seydoux-Guillaume A.M., Wirth R., Heinrich W., Montel J.M. (2002b) Experimental determination of Thorium partitioning between monazite and xenotime using analytical electron microscopy and X-ray diffraction Rietveld analysis. European Journal of Mineralogy 14, 869–878.

Seydoux-Guillaume A.M., Wirth R., Nasdala L., Gottschalk M., Montel J.M., Heinrich W. (2002c) An XRD, TEM and Raman study of experimentally annealed natural monazite. Physics and Chemistry of Minerals 29, 240–253.

Seydoux-Guillaume A.M., Goncalves P., Wirth R., Deutsch A. (2003) Transmission electron microscope study of polyphase and discordant monazites: Site-specific specimen preparation using the focused ion beam technique. Geology 31, 973–976.

Seydoux-Guillaume A.M., Wirth R., Deutsch A., Schärer U. (2004) Microstructure of 24–1928 Ma concordant monazites; implications for geochronology and nuclear waste deposits. Geochimica et Cosmochimica Acta 68, 2517–2527.

Seydoux-Guillaume A.M., Montel J.M., Bingen B., Bosse V., De Parseval P., Paquette J., Janots E., Wirth R. (2012) Low-temperature alteration of monazite: Fluid mediated coupled dissolution–precipitation, irradiation damage, and disturbance of the U–Pb and Th–Pb chronometers. Chemical Geology 330–331, 140–158.

Seydoux-Guillaume A.M., Bingen B., Paquette J.-L., Bosse V. (2015) Nanoscale evidence for uranium mobility in zircon and the discordance of U-Pb chronometers. Earth and Planetary Science Letters 409, 43–48.

Seydoux-Guillaume A.M., Bingen B., Bosse V., Janots E., Laurent A.T. (2017) Transmission electron microscope imaging sharpens geochronological interpretation of zircon and monazite. Microstructural Geochronology: Planetary Records Down to Atom Scale. In: Moser D.E., Corfu F., Darling J.R., Reddy S.M., Tait K. (Eds.) Geophysical Monograph 232. First edition. Wiley & Sons, Inc., pp. 261–275.

Seydoux-Guillaume A.M., Deschanels X., Baumier C., Neumeier S., Weber W.J., Peuget S. (2018) Why natural monazite never becomes amorphous: Experimental evidence for alpha self-healing. American Mineralogist 103, 824–827.

Shannon R.D. (1976) Revised effective ionic radii and systematic studies of interatomic distances in halides and chalcogenides. Acta Crystallographica Section A: Crystal Physics, Diffraction, Theoretical and General Crystallography 32, 751–767.

Siégel C., Bryan S.E., Allen C.M., Gust D.A. (2018) Use and abuse of zircon-based thermometers: A critical review and a recommended approach to identify antecrystic zircons. Earth-Science Reviews 176, 87–116.

Silva E.N., Ayala A.P., Guedes I., Paschoal C.W.A., Moreira R.L., Loong C.K., Boatner L.A. (2006) Vibrational spectra of monazite-type rare-earth orthophosphates. Optical materials 29, 224–230.

Silver L.T., Deutsch S. (1963) Uranium lead isotopic variations in zircons: a case study. The Journal of Geology 71, 721–758.

Simmons W.B.S., Webber K.L. (2008) Pegmatite genesis: state of the art. European Journal of Mineralogy 20, 421–438.

Simpson, R.K., Parrish, R.R., Searle, M.P., Waters, D.J., 2000. Two episodes of monazite crystallization during metamorphism and crustal melting in the Everest region of the Nepalese Himalaya. Geology 28, 403–406.

Sinha A.K., Wayne D.M., Hewitt D.A. (1992) The hydrothermal stability of zircon: Preliminary experimental and isotopic studies. Geochimica et Cosmochimica Acta 56, 3551–3560.

Skrzypek E., Sakata S., Sorger D. (2020) Alteration of magmatic monazite in granitoids from the Ryoke belt (SW Japan): Processes and consequences. American Mineralogist 105, 538–554.

Smits G. (1989) (U-Th)-bearing silicates in reefs of the Witwatersrand, South Africa. The Canadian Mineralogist 27, 643–656.

Soman A., Geisler T., Tomaschek F., Grange M., Berndt J. (2010) Alteration of crystalline zircon solid solutions: A case study on zircon from an alkaline pegmatite from Zomba-Malosa, Malawi. Contributions to Mineralogy and Petrology 160, 909–930.

Spear F.S., Pyle J.M. (2002) Apatite, monazite, and xenotime in metamorphic rocks. In: Kohn M.J., Rakovan J., Hughes J.M. (Eds.) Phosphates: Geochemical, Geobiological, and Materials Importance. Reviews in Mineralogy and Geochemistry 48, 293–335.

Speer J.A. (1980) Zircon. In: Ribbe P.H. (Ed.) Orthosilicates. Reviews in Mineralogy and Geochemistry 5, 67–112.

Švecová E., Čopjaková R., Losos Z., Škoda R., Nasdala L., Cícha J. (2016) Multi-stage evolution of xenotime–(Y) from Písek pegmatites, Czech Republic: an electron probe micro-analysis and Raman spectroscopy study. Mineralogy and Petrology 110, 747–765.

Szuszkiewicz A., Szełęg E., Pieczka A., Ilnicki S., Nejbert K., Turniak K., Banach M., Łodziński M., Różniak R., Michałowski P. (2013) The Julianna pegmatite vein system at the Piława Górna mine, Góry Sowie Block, SW Poland–preliminary data on geology and descriptive mineralogy. Geological Quarterly 57, 467–484.

Tabaksblat R., Meier R.J., Kip B.J. (1992) Confocal Raman Microspectroscopy: Theory and Application to Thin Polymer Samples. Applied Spectroscopy 46, 60–68.

Tabaud A.S., Štípská P., Mazur S., Schulmann K., Míková J., Wong J., Sun M. (2021) Evolution of a Cambro-Ordovician active margin in northern Gondwana: Geochemical and zircon geochronological evidence from the Góry Sowie metasedimentary rocks, Poland. Gondwana Research 90, 1–26.

Thomas R., Davidson P. (2013) The missing link between granites and granitic pegmatites. Journal of Geosciences 58, 183–200.

Timmermann H., Parrish R.R., Noble S.R., Kryza R. (2000) New U–Pb monazite and zircon data from the Sudetes Mountains in SW Poland: evidence for a single-cycle Variscan orogeny. Journal of the Geological Society 157, 265–268.

Thomas R., Davidson P. (2015) Comment on "A petrologic assessment of internal zonation in granitic pegmatites" by David London (2014). Lithos 212–215, 462–468.

Tomaschek F., Kennedy A.K., Villa I.M., Lagos M., Ballhaus C. (2003) Zircons from Syros, Cyclades, Greece – recrystallization and mobilization of zircon during high- pressure metamorphism. Journal of Petrology 44, 1977–2002.

Trachenko K., Dove M.T., Salje E.K. (2002) Structural changes in zircon under α-decay irradiation. Physical Review B - Condensed Matter and Materials Physics 65, 180102.

Tramm F., Wirth R., Budzyń B., Sláma J., Schreiber A. (2021) LA-ICP-MS and TEM constraints on the magmatic and post-magmatic processes recorded by the zircon-xenotime intergrowth in pegmatite (Piława Górna, Góry Sowie Block, SW Poland). Lithos 404–405, 106480.

Tropper P., Manning C.E., Harlov D.E. (2011) Solubility of $CePO_4$ monazite and YPO_4 xenotime in H_2O and H_2O–NaCl at 800 °C and 1 GPa: Implications for REE and Y transport during high-grade metamorphism. Chemical Geology 282, 58–66.

Tunheng A., Hirata T. (2004) Development of signal smoothing device for precise elemental analysis using laser ablation-ICP-mass spectrometry. Journal of Analytical Atomic Spectrometry 19, 932–934.

Turniak K., Mazur S., Wysoczanski R. (2000) SHRIMP zircon geochronology and geochemistry of the Orlica–Snieznik gneisses (Variscan belt of Central Europe) and their tectonic implications. Geodinamica Acta 13, 293–312.

Turniak K., Pieczka A., Kennedy A.K., Szełęg E., Ilnicki S., Nejbert K., Szuszkiewicz A. (2015) Crystallisation age of the Julianna pegmatite system (Góry Sowie Block, NE margin of the Bohemian massif): evidence from U-Th-Pb SHRIMP monazite and CHIME uraninite studies. In: 7th International Symposium on Granitic Pegmatites, PEG 2015 Książ, Poland, pp. 111–112.

Turuani M.J., Laurent A.T., Seydoux-Guillaume A.-M. Fougerouse D., Saxey D., Reddy S.M., Harley S.L., Reynaud S., Rickard W.D.A. (2022) Partial retention of radiogenic Pb in galena nanocrystals explains discordance in monazite from Napier Complex (Antarctica). Earth and Planetary Science Letter 588, 117567.

Turuani M.J., Seydoux-Guillaume A.-M., Laurent A.T., Reddy S.M., Harley S.L., Fougerouse D., Saxey D., Gouy S., De Parseval P., Reynaud S., Rickard W.D.A. (2023) Nanoscale features revealed by a multiscale characterisation of discordant monazite highlight mobility mechanisms of Th and Pb. Contributions to Mineralogy and Petrology 178, 1–21.

Urusov V.S., Grechanovsky A.E., Eremin N.N. (2012) Radiation Resistance of the Xenotime YPO_4 from the Computer Simulation Data. Glass Physics and Chemistry 38, 55–62.

Valley J.W., Cavosie A.J., Ushikubo T., Reinhard D.A., Lawrence D.F., Larson D.J., Clifton P.H., Kelly T.F., Wilde S.A., Moser D.E., Spicuzza M.J. (2014) Hadean age for a post-magma ocean zircon confirmed by atom-probe tomography. Nature Geoscience 7, 219–223.

Valley J.W., Reinhard D.A., Cavosie A.J., Ushikubo T., Lawrence D.F., Larson D.J., Kelly T.F., Snoeyenbos D.R., Strickland A.A. (2015) Nano- and micro-geochronology in Hadean and Archean zircons by atom-probe tomography and SIMS: New tools for old minerals. American Mineralogist 100, 1355–1377.

Vallini D.A., Rasmussen B., Krapež B., Fletcher I.R., McNaughton N.J. (2005) Microtextures, geochemistry and geochronology of authigenic xenotime:

constraining the cementation history of a Palaeoproterozoic metasedimentary sequence. Sedimentology 52, 101–122.

van Achterbergh E., Ryan C.G., Jackson S.E., Griffin W.L. (2001) Data reduction software for LA-ICPMS: Appendix. In: Sylvester P.J. (Ed.) Laser Ablation ICP–MS in the Earth Sciences: Current Practices and Outstanding Issues. Mineralogical Association of Canada Short Course Series. Ottawa: Mineralogical Association of Canada. Vol. 29, pp. 239–243.

Vance E.R., Zhang Y., McLeod T., Davis J. (2011) Actinide valences in xenotime and monazite. Journal of Nuclear Materials 409, 221–224.

Vielreicher N.M., Groves D.I., Fletcher I.R., McNaughton N.J., Rasmussen B. (2003) Hydrothermal Monazite and Xenotime Geochronology: A New Direction for Precise Dating of Orogenic Gold Mineralization. SEG Discovery 53, 1–16.

Villa I. M., Hanchar J. M. (2017) Age discordance and mineralogy. American Mineralogist 102, 2422–2439.

Villa I.M., Williams M.L. (2013) Geochronology of Metasomatic Events. In: Harlov D.E., Austrheim H. (Eds.) Metasomatism and the Chemical Transformation of Rock. Springer-Verlag, Berlin Heidelberg, pp. 171–202.

Volante S., Collins W.J., Blereau E., Pourteau A., Spencer C., Evans N.J., Barrote V., Nordsvan A.R., Li Z.-X., Li J. (2020) Reassessing zircon-monazite thermometry with thermodynamic modelling: insights from the Georgetown igneous complex, NE Australia. Contributions to Mineralogy and Petrology 175, 110.

Watson E.B., Harrison T.M. (2005) Zircon Thermometer Reveals Minimum Melting Conditions on Earliest Earth. Science 308, 841–844.

Watson E.B., Cherniak D.J, Hanchar J.M., Harrison T.M., Wark D.A. (1997) The incorporation of Pb into zircon. Chemical Geology 141, 19–31.

Watson E.B., Wark D.A., Thomas J.B. (2006) Crystallization thermometers for zircon and rutile. Contributions to Mineralogy and Petrology 151, 413–433.

Wiedenbeck M.A.P.C., Alle P., Corfu F., Griffin W.L., Meier M., Oberli F.V., Roddic J.C., Spiegel W. (1995) Three natural zircon standards for U–Th–Pb, Lu–Hf, trace element and REE analyses. Geostandards Newsletter 19, 1–23.

Williams M.L., Jercinovic M.J. (2002) Microprobe monazite geochronology: putting absolute time into microstructural analysis. Journal of Structural Geology 24, 1013–1028.

Williams M.L., Jercinovic M.J., Hetherington C.J. (2007) Microprobe Monazite Geochronology: Understanding Geologic Processes by Integrating Composition and Chronology. Annual Review of Earth and Planetary Sciences 35, 137–175.

Williams M.L., Jercinovic M.J., Harlov D.E., Budzyń B., Hetherington C.J. (2011) Resetting monazite ages during fluid-related alteration. Chemical Geology 283, 218–225.

Williams M.L., Jercinovic M.J., Mahan K.H., Dumond G. (2017) Electron microprobe petrochronology. In: Kohn M.J., Engi M., Lanari P. (Eds.) Petrochronology: Methods and Applications. Reviews in Mineralogy and Geochemistry 83, 153–182.

Wing, B., Ferry, J.M., Harrison, T.M. (2003) Prograde destruction and formation of monazite and allanite during contact and regional metamorphism of pelites: petrology and geochronology. Contributions to Mineralogy and Petrology 145, 228–250.

Wirth R. (2004) Focused Ion Beam (FIB) A novel technology for advanced application of micro-and nanoanalysis in geosciences and applied mineralogy. European Journal of Mineralogy 16, 863–876.

Wirth R. (2009) Focused Ion Beam (FIB) combined with SEM and TEM: Advanced analytical tools for studies of chemical composition, microstructure and crystal structure in geomaterials on a nanometre scale. Chemical Geology 261, 217–229.

Wyckoff R.W.G. (1965) Crystal structures, 2nd edition Vol. III pp. 15 and 33

Yang S., Li C., Yokoyama K. (2006) Elemental compositions and monazite age patterns of core sediments in the Changjiang Delta: Implications for sediment provenance and development history of the Changjiang River. Earth and Planetary Science Letters 245, 762–776.

Zamyatin D.A., Shchapova Y.V., Votyakov S.L., Nasdala L., Lenz C. (2017) Alteration and chemical U-Th-total Pb dating of heterogeneous high-uranium zircon from a pegmatite from the Aduiskii massif, middle Urals, Russia. Mineralogy and Petrology 111, 475–497.

Żelaźniewicz A. (1990) Deformation and metamorphism in the Góry Sowie gneiss complex, Sudetes, SW Poland. Neues Jahrbuch für Paläontologie – Abhandlungen 179, 129–157.